Electron Beams with Orbital Angular Momentum

Sophia Marriott Lloyd

Submitted in accordance with the requirements
for the degree of
Doctor of Philosophy
in
Physics

Department of Physics
University of York
York, United Kingdom
August 2013

Abstract

Electron Beams with Orbital Angular Momentum

Electron vortex beams are beams of freely propagating electrons that possess orbital angular momentum. Recently predicted and experimentally verified, electron vortices are hoped to lead to new developments in several areas, in particular electron microscopy, as well as other areas as diverse as spintronics and quantum information. This thesis introduces and examines key concepts relating to electron vortices, and as an introduction, the major developments relating to electron vortices over the past few years are outlined and discussed.

The Bessel beam is derived as a suitable solution to the Schrödinger equation for an electron beam carrying orbital angular momentum. The linear and orbital angular momenta of such a beam are discussed alongside the use of electron vortices in manipulation of nanoparticles. Being a charged particle the electron vortex carries electromagnetic fields; the magnetic field is found to have an axial component, unique to the vortex beam. Coupling between the spin and orbital angular momentum of the electron propagating within its own field is found to be negligible in typical electron microscope contexts.

Electron vortices are found to have a similar form as the more widely known optical vortices, but key differences between electrons and photons lead to fundamentally different behaviour in many circumstances. The main differences between electron and optical vortices are outlined throughout this thesis. Interactions between the electron and optical vortices and matter, in the form of a hydrogenic atom, are considered. In contrast to the optical vortex, interactions between atomic matter and the electron vortex are found to lead to transfer of orbital angular momentum, opening the possibility of using electron vortices in the electron microscope to probe magnetism at nano- or atomic-scales. The premise and requirements of such experiments are discussed.

Table of Contents

Acknowledgements x

Author's Declaration xi

Publications xii

1 Introduction 1
- 1.1 Outline of Thesis Contents . . . 2
- 1.2 Vortices in Electron Beams . . . 3
  - 1.2.1 Vortices and Vortex Dynamics . . . 3
  - 1.2.2 Non-Relativistic and Relativistic Electron Vortices . . . 4
- 1.3 Generation of Electron Vortex Beams . . . 7
  - 1.3.1 Electron Optics . . . 7
  - 1.3.2 Spiral Phase Plates . . . 14
  - 1.3.3 Holographic Masks . . . 15
  - 1.3.4 Forked Masks . . . 21
  - 1.3.5 Spiral Masks . . . 22
  - 1.3.6 Other Methods of Generating Electron Vortices . . . 23
  - 1.3.7 Vortex Propagation through Electron Optics . . . 26
- 1.4 Applications of Electron Vortex Beams . . . 28
  - 1.4.1 Electron Energy Loss Spectroscopy with Vortex Beams . . . 28
  - 1.4.2 Vortex Propagation through Materials . . . 32
- 1.5 Dynamics and Fields . . . 33
  - 1.5.1 Motion and Collisions . . . 34
  - 1.5.2 Propagation through External Fields . . . 35

2 Vortex Solutions 38
- 2.1 Vorticity . . . 39
- 2.2 Bessel Function Vortex Solutions . . . 41
  - 2.2.1 Non-Relativistic Electron Vortex Solutions . . . 41
  - 2.2.2 Optical Vortex Solutions . . . 42
  - 2.2.3 General Properties of Bessel Beams . . . 43
- 2.3 Laguerre-Gaussian Vortex Solutions . . . 47
- 2.4 Beyond the Schrödinger and Paraxial Helmholtz Equations . . . 50

2.4.1 Relativistic Electron Vortices . . . 50
2.4.2 Non-Paraxial Optical Vortices . . . 52
2.5 Normalisation of the Electron Vortex Wavefunction . . . 52
2.5.1 Infinite Normalisation . . . 53
2.5.2 Semi-Infinite Normalisation . . . 54
2.5.3 Finite Normalisation . . . 55

3 Vortex fields 57
3.1 Charge and Current Density . . . 57
3.2 Electric Field . . . 58
3.3 Magnetic Field . . . 59
3.3.1 Azimuthal Component . . . 60
3.3.2 Axial Component . . . 61
3.3.3 Radial Component . . . 62
3.4 Simulation of Electric and Magnetic Fields for the Bessel Beam . . . 62
3.4.1 Infinite Beam . . . 62
3.4.2 Finite Beam . . . 63

4 Linear and Orbital Angular Momenta of the Vortex Beam 68
4.1 Optical Vortices . . . 69
4.2 Electron Vortices . . . 72
4.2.1 Mechanical Momentum . . . 72
4.2.2 Electromagnetic Momentum . . . 74
4.3 Mechanical Rotation of a Nanoparticle . . . 75

5 Interactions Between Optical Vortices and Atoms 78
5.1 The Coordinate System and Basis States . . . 78
5.2 Lagrangian and Hamiltonian Formalism . . . 81
5.2.1 Lagrangian formalism . . . 81
5.3 Matrix element and Selection Rules . . . 86
5.4 Conclusions . . . 88

6 Interactions Between Electron Vortices and Atoms 91
6.1 Lagrangian and Hamiltonian . . . 92
6.2 Multipolar Expansion of Hamiltonian . . . 94
6.2.1 Matrix Element in the Dipole Approximation . . . 96
6.3 Multipolar Effective Operator . . . 98
6.3.1 The Effective Operator . . . 101
6.3.2 Multipolar Expansion . . . 103
6.3.3 Zero Order Terms . . . 107
6.3.4 Dipole terms . . . 108
6.3.5 Spatial Dependence of the Dipole Matrix Element . . . 113

6.4 Comparison of the dipole interaction in the Hamiltonian and wavefunction expansions . . . 123
6.5 Analysis and application of the selection rules . . . 126
6.6 Comparison with optical vortex results . . . 130
6.7 Summary . . . 130

7 Spin-Orbit Coupling in the Electron Vortex 132
7.1 The Dirac Equation . . . 132
7.2 The Foldy-Wouthuysen Transformation . . . 136
7.2.1 The Form of the Foldy-Wouthyusen Transformation . . . 137
7.2.2 Expanding in Powers of $(mc^2)^{-1}$ . . . 138
7.2.3 The Foldy-Wouthyusen Hamiltonian . . . 140
7.3 Non-Relativistic Limit of the Dirac Equation . . . 142
7.4 Spin-orbit interaction . . . 143
7.4.1 Intrinsic Spin-Orbit Coupling . . . 144
7.4.2 Spin-Orbit Coupling in an External Field . . . 145

8 Discussion and Outlook 147
8.1 Outlook for Future Research Directions . . . 148
8.2 Closing Remarks . . . 150

A Optical Vortex Interactions 151
A.1 Expansion of vector potential about centre of mass . . . 151
A.2 Electric Dipole Matrix Element . . . 152
A.3 Vector Potential Matrix Element . . . 152
A.4 The Quadrupole Transition Matrix Element . . . 153
A.4.1 The Quadrupole Interaction Hamiltonian . . . 155
A.4.2 Quadrupole Selection Rules . . . 156

B Electron Vortex Interactions 159
B.1 Calculation of Dipole Selection Rules . . . 159
B.2 Calculation of Quadrupole Selection Rules . . . 161
B.3 Nucleus-Vortex Coulomb Interaction . . . 162
B.4 The Matrix Element After First Expansion . . . 163
B.5 Fourier Transform of Effective Operator . . . 165
B.6 Summation over p, p' and u . . . 166
B.7 Matrix element factors . . . 169
B.7.1 Integral Factors for Nucleus-Vortex Coulomb Interaction . . . 169
B.7.2 Integral factors for First Effective Operator . . . 169
B.7.3 Integral Factors for Zero Order Term . . . 170
B.7.4 Integral Factors for Dipole Term . . . 170

C Relativistic Quantum Mechanics 171
C.1 The Dirac γ Matrices . . . 171
C.2 Applying The Foldy-Wouthuysen Transformation . . . 173
C.3 The Foldy-Wouthuysen Hamiltonian . . . 174
C.4 Powers, time derivatives, commutators and anti-commutators . . . 175
C.4.1 Powers . . . 176
C.4.2 Time Derivatives . . . 176
C.4.3 Commutator and Anti-Commutator . . . 176

D Conferences 178

List of Abbreviations and Symbols 180
Abbreviations . . . 180
Mathematical Symbols . . . 180

References 193

List of Figures

1.2.1 Edge and screw dislocations in wavefronts . . . 6
1.3.1 Overview of the TEM . . . 8
1.3.2 The condenser lens system . . . 10
1.3.3 Focusing in the condenser lens system . . . 11
1.3.4 The objective aperture . . . 11
1.3.5 The spiral phase plate . . . 14
1.3.6 Interference patterns for an $l = 1$ Bessel beam interfering with a plane wave . . . 16
1.3.7 Binarised interference pattern for $l = 1$ Bessel beam . . . 17
1.3.8 The far field diffraction pattern and phase distribution of the continuous $l = 1$ holographic mask . . . 18
1.3.9 The far field diffraction pattern and phase distribution of the binary $l = 1$ holographic mask . . . 19
1.3.10 The far field diffraction pattern and phase distribution of the binary $l = 3$ holographic mask . . . 20
1.3.11 Interference patterns and masks of vortices interfering with spherical waves . . . 23
1.3.12 The experimental setup of a mode converter for an electron vortex. . . . 24
1.3.13 Electric and magnetic fields in q-filter device . . . 26
1.3.14 The evolution of the vortex beam passing through focus . . . 27
1.4.1 Set up and results of vortex dichroism experiment . . . 29
1.5.1 Dynamics of a ring vortex in a spherically symmetric trap . . . 34
1.5.2 Dynamics two vortex lines crossing or 'reconnecting' . . . 35
2.1.1 The phase character of $l = 1$ and $l = 3$ vortex beams . . . 40
2.2.1 Bessel functions of low order . . . 44
2.2.2 Bessel function intensity pattern . . . 45
2.2.3 The Bessel Beam as plane waves propagating on a cone . . . 47
2.3.1 Gaussian beam features . . . 48
2.3.2 Laguerre-Gaussian mode functions . . . 49
3.3.1 Caption Title . . . 60
3.4.1 Electric and magnetic field of infinite Bessel Beam . . . 64
3.4.2 Density plot of electric and magnetic field components of infinite Bessel Beam . . . 65
3.4.3 Electric and magnetic field of finite Bessel Beam . . . 66
3.4.4 Density plot of electric and magnetic field components of finite Bessel Beam . . . 67
4.3.1 Proposed experiments for nanoparticle rotation . . . 76

5.1.1 Coordinate frame of vortex-atom interaction 79
6.3.1 Expansion of Bessel wavefunction about atomic nucleus. 100
6.3.2 Expansion of Bessel wavefunction about atomic electron 102
6.3.3 p-mode modulation factors 111
6.3.4 Transitions in the expanded wavefunction formalism. 114
6.3.5 Spatial dependence of the dipole matrix element for $l = 0$ 115
6.3.6 Spatial dependence of the dipole matrix element for $l = +1$ 116
6.3.7 Spatial dependence of the dipole matrix element for $l = +1$ 117
6.3.8 Spatial dependence of the dipole matrix element for $l = +1$ 119
6.3.9 Comparison of dipole matrix element magnitudes for $l = 0, \pm 1$ 120
6.3.10 Suggested experimental set-up for dichroism experiments using electron vortices . 122
6.3.11 Contributions to the observable signal for $l = +1$ 124
6.3.12 Contributions to the observable signal for $l = -1$ 125
D.0.1 Group photo of SOILM13 179
D.0.2 Group photo of ICOAM 2013 179

List of Tables

4.2.1 Mechanical and electromagnetic contributions to the linear momentum of the electron vortex 75
4.2.2 Mechanical and electromagnetic contributions to the angular momentum of the electron vortex 75
6.3.1 Conditions on indices for Bessel functions of positive order 104
6.3.2 Conditions on indices for the zero-order interaction Hamiltonian 106
6.3.3 Conditions on indices for the dipole interaction Hamiltonian 106
6.3.4 Conditions on indices for the quadrupole interaction Hamiltonian 106
6.5.1 Allowed transitions in the L_2 and L_3 edges for atom-vortex interactions 128
7.4.1 Energy splitting due to spin-orbit coupling in the electron vortex 146

Acknowledgments

In writing this thesis I have of course relied heavily on the expertise and guidance of my supervisors, Prof. Mohamed Babiker and Prof. Jun Yuan, for which I am extremely grateful. Their support, advice and encouragement has shaped my understanding of the physics within this thesis (and beyond!), and helped me develop and grow from a shy student to a researcher with self-confidence. It is a testament to their mentorship skills that I never once questioned my passion for physics or my desire to continue research.

I have found the Department of Physics at the University of York to be an incredibly supportive and welcoming environment, and I have felt fully integrated since I arrived in October 2010. The administrative and academic staff have been extremely helpful and approachable at all times, and I am also grateful for the financial assistance provided in the form of a studentship from the Department. My fellow students have kept me sane throughout, especially the (thankfully few) particularly stressful times. The friendships forged during my time at York will remain with me.

Attending conferences and summer schools throughout my Ph.D. has enabled me to keep in touch with the frontiers of research in this area, and put my own work into a wider context, as well as being introduced to new concepts. I am grateful for the opportunities I have had to present my own work, and the many varied discussions I have had with people from many different fields have opened my interest in several different areas, both related and unrelated to my current research. Of particular note were the most recent two conferences I attended, Spin Orbit Interaction for Light and Matter Waves, Dresden and the Second Internation Conference on Optical Angular Momentum, Glasgow. Discussions at these conferences in particular allowed me to appreciate the ongoing study and subtleties of orbital angular momentum, greatly influencing the writing of this thesis.

I am also grateful to Dr. Claudia Eberlein, who was incredibly helpful with advice when I was searching for a suitable Ph.D studentship, and was kind enough to put me in touch with Mohamed.

Finally, the soundtrack to this thesis is provided by Mr. David Bowie. Listening to the entire back catalogue in chronological order kept the inspiration flowing during the final days of writing.

Author's Declaration

I DECLARE THAT, except where stated, the work contained within this thesis represents the original work of myself, including collaborative efforts between the members of the Electron Vortex Beam research group at the University of York. The extent of group collaboration is laid out below. Within the thesis references to the work of others are clearly stated and correctly referenced.

All original research contained herein was performed by myself under the direction and guidance of my supervisors, Prof. Mohamed Babiker and Prof. Jun Yuan. Suggestions for specific areas of research interest were made by my supervisors, who also aided in obtaining and interpreting the results. The experiment mentioned in Section 4.3 was performed by Dr. Gnanavel Thirunavukkarasu and Prof. Jun Yuan.

The investigation of the intrinsic electric and magnetic fields of the Bessel-type electron vortex given in Chapter 3 was performed in collaboration with Mr. Callum Kerr-Edwards, as part of his M.Phys. project work. These results have been presented by Callum in his M.Phys. dissertation. In particular, the derivations of the electric and magnetic field expressions for the infinite Bessel beam were obtained by Callum under my guidance.

Selected material from this thesis has been published in peer-reviewed journals, detailed overleaf. References to these works are supplied in the relevant chapters dealing with the particular topics.

Publications

1. S. Lloyd, M. Babiker, and J. Yuan, *Quantized Orbital Angular Momentum Transfer and Magnetic Dichroism in the Interaction of Electron Vortices with Matter*, Physical Review Letters **108**, 074802 (2012).

2. L. Clark, S. Lloyd, M. Babiker and J. Yuan, *Electron Beams with a Twist*, Journal of Physics: Conference Series **371**, 012005 (2012).

3. S. M. Lloyd, M. Babiker, and J. Yuan, *Interaction of electron vortices and optical vortices with matter and processes of orbital angular momentum exchange*, Physical Review A **86**, 023816 (2012).

4. S. M. Lloyd, M. Babiker, J. Yuan, and C. Kerr-Edwards, *Electromagnetic Vortex Fields, Spin, and Spin-Orbit Interactions in Electron Vortices*, Physical Review Letters **109**, 254801 (2012).

5. S. Lloyd, M. Babiker and J. Yuan, *Reply to 'Comment on "Quantized Orbital Angular Momentum Transfer and Magnetic Dichroism in the Interaction of Electron Vortices with Matter"'*, Physical Review Letters **110**, 189502 (2013).

6. J. Yuan, S. M. Lloyd, M. Babiker, *Chiral specific electron vortex beam spectroscopy*, Physical Review A **88**, 031801(R) (2013).

7. S. M. Lloyd, M. Babiker, J. Yuan, *Mechanical properties of electron vortices*, Physical Review A **88**, 031802(R) (2013).

1 Introduction

The term 'vortex beam' refers to a beam of particles - whether electrons, photons, or otherwise - that is freely propagating, and has the property of quantised orbital angular momentum about its axis of propagation. Optical vortices have been a subject of much interest over the last two decades, after the publication of the seminal work of Allen *et al.* in 1992 [1], in which the quantised orbital angular momentum of a Laguerre-Gaussian laser mode was examined, and a method for producing such beams proposed (the earlier discussion of optical vortices in laser modes by Coullet *et al.* [2] did not emphasise the quantisation of the orbital angular momentum about the propagation axis). Since then, optical vortices have led to many diverse applications [3, 4], including optical tweezers and spanners for various applications [5–8], including micromanipulation [9]; classical and quantum communications [10]; phase contrast imaging in microscopy [11, 12]; as well as further proposed applications in quantum information and metrology [10, 13]. The discussion of photonic spin and orbital angular momentum in various situations, and the similarities and differences between the two has led to new ways of thinking about, and examining orbital angular momentum in optics - the spin and vortex angular momentum can not be clearly separated outside of the paraxial approximation [14–16], which leads to the possibility of entanglement of the two degrees of freedom [17, 18].

The idea of particle vortices was first considered in 2001 by Bialynicki-Birula *et al.* [19–21], with the specific properties of electron vortices and methods of their generation considered in 2007, by Bliokh *et al.* [22], by analogy with the free orbital angular momentum of the optical vortex states. Orbital angular momentum is well known in electrons in bound states - such as the hydrogenic electron states and similar structures; the suggestion of freely propagating electron states with quantised orbital angular momentum was novel. The work [22] suggested several principles by which electron vortex beams may be generated - two examples are edge dislocations in crystals acting as diffraction gratings, and spiral-thickness wave plates. Both these methods were

demonstrated experimentally shortly afterwards, in electron microscopes [23–25].

Electron vortex beams are hoped to lead to applications in microscopial analysis, particularly for electron energy loss spectroscopy (EELS), in which the orbital angular momentum of the beam will provide new information about the crystallographic, electronic and magnetic composition of a sample [24, 25]. Magnetic EELS has already been demonstrated [24], and it is hoped that the high resolution achievable in the electron microscope will lead to the ability to map magnetic information at atomic or near-atomic resolution, as discussed in Chapter 6. Creating particular superpositions of vortex states could open possibilities of investigation of directional bonds through energy loss spectroscopy of crystalline materials [24]. Additionally, the phase structure of the vortex suggests applications in high resolution phase contrast imaging, as required for biological specimens with low absorption contrast [26]. Applications are not restricted to microscopy - the orbital angular momentum of the beam may also be used for manipulation of nanoparticles, [27, 28], leading to electron spanners analogous to the widely used optical tweezers and spanners. There may also be applications of the electron vortex that are relevant to quantum information, in particular the electron vortex may be used to impart angular momentum into vortices in Bose-Einstein condensates. Certain of these applications will be discussed in more detail in Section 1.4, and throughout this thesis.

The remainder of this chapter will provide an introduction to vortices and their general features, as well as an outline of the main experimental and theoretical developments that have occurred since 2010 in this fast expanding field. The properties of electron vortices will be specifically considered, along with methods of their generation. The growing literature relating to the application of electron vortices and additional considerations will also be reviewed.

1.1 Outline of Thesis Contents

This thesis is organised as follows: the remainder of this chapter constitutes an introduction to vortices, specifically electron vortices, with a discussion of the various methods generating electron vortices within the transmission electron microscope (TEM). Applications of electron vortices are discussed, in particular the growing body of literature concerning the use of vortex states in EELS for magnetic and other chiral information is reviewed. Other aspects of the evolution of the vortex state in different conditions are also presented, such as propagation in external fields and potentials, or vortex-vortex or vortex-plane wave collisions. Particular solutions and specific physical properties of the Bessel-type electron vortex are introduced in Chapter 2, and these normalised solutions are used throughout the thesis to estimate the magnitude of particular effects for a typical electron vortex, as would be created in a TEM. Also discussed are optical vortex solutions of a similar spatial distribution, so as to enable comparisons to be made between the behaviour of the electron and optical vortices in certain situations. Since the electron is a charged particle, the motion associated with the electron vortex will lead to electronic and magnetic fields, with characteristics particular to the vortex. These fields are discussed with estimated magnitudes in Chapter 3. The nature and origin of the linear and orbital angular momentum carried by both optical and electron vortices is explored in Chapter 4, with contributions to the momentum of the electron vortex due to the electromagnetic fields included.

Many of the potential applications of the electron vortex will rely on their interactions with matter. Inelastic interactions between a vortex and a hydrogenic atom are considered for the optical vortex and the electron vortex in Chapter 5 and Chapter 6 respectively. Comparison of the interactions shows that while the optical vortex may not exchange orbital angular momentum with the atomic electron, this is possible for the electron vortex, which opens up possibilities of using electron vortices for magnetic electron energy loss spectroscopy. The effect of the spin of the electron is considered in Chapter 7, in which the coupling of the spin and orbital angular momentum of single vortex electrons is considered. Finally in Chapter 8, the findings of this thesis are summarised with reference to their potential for applications, and further development of the field of electron vortex physics

1.2 Vortices in Electron Beams

Electron vortices exhibit the expected behaviour of a phase vortex as is common to the optical vortices, but also have their own unique properties that affect their interactions with matter and fields. The interaction of the electron vortex with atomic matter is described in detail in Chapter 6, and the influence of certain fields is considered in Chapter 7. Presented here are some of the general properties of the vortices, how they arise in wave interference, and an introduction to the specific properties of electron vortices.

1.2.1 Vortices and Vortex Dynamics

Vortices in beams and wavefronts were first described by Nye and Berry in 1974 [29] as dislocations in the wavefronts observed in interfering sound waves, though the analysis applies to all kinds of waves, including optical and matter waves. The dislocations are defined as points at which the amplitude of the wave is zero, with a phase change of a multiple of 2π along a circuit about the dislocation. For two interfering waves A and B travelling at an angle, two particular types of dislocations were described in [29], by analogy with defects in crystallography: the edge dislocation, in which the two travelling waves interfere so as to periodically generate an 'extra' phasefront, and the screw dislocation, in which lines of destructive interference arise parallel to the common axis of the beams. The phasefronts are shown schematically in Fig. 1.2.1 Mixed dislocations, in which both the edge and screw types are apparent, are also possible; however it is the screw dislocations that give rise to the helical wavefronts of the vortex beam of current interest. For a screw dislocation, the phase of the two travelling waves, A and B must be arranged such that there is destructive interference at the crossing of A and B, and the two waves are amplitude modulated in anti-phase in the direction perpendicular to their travel (the y direction for the waves in Fig. 1.2.1). The resulting interference pattern has a helicoid phasefront about each single dislocation line, given in a cylindrical geometry $\mathbf{r}(\rho, \phi, z)$ as:

$$\psi(\mathbf{r}) = k\rho e^{i(kz-\omega t-\phi)}, \tag{1.1}$$

where k is the momentum of the wave and ω is the angular frequency. The vortex beams discussed here take the form of a single screw dislocation line.

Such a screw dislocation may exist in the phase front of beams of particles or photons. The optical vortices studied for the past two decades [3, 10] have the same phase structure as particle vortices, such as the electron vortices that are the main focus of this thesis; since the specific properties of the beam will differ due to the different physical characteristics, the general dynamics of the vortex - such as creation and annihilation, motion and collisions - may not always have the same form. Vortices may be created and annihilated by wave interference, and a time dependence of the interfering fields will lead to motion of the vortex, for example if the wavelength of one of the waves A or B is much larger than other, then the vortex line will move in a continuous periodic fashion [29]. Additionally, the hydrodynamic formulation of quantum mechanics allows for the spontaneous creation and annihilation of pairs of vortices in the probability 'fluid' of the quantum particle [19–21]. More complicated vortex structures, involving looped and knotted vortex lines, may also be created, either spontaneously or through interference, and their behaviour has been discussed in [30, 31].

1.2.2 Non-Relativistic and Relativistic Electron Vortices

The possibility of vortices existing in freely propagating particle waves was put forward in 2000 by Bialynicki-Birula and collaborators [19–21]. Electron solutions to the Schrödinger equation were considered explicitly by Bliokh in 2007 [22], before the first observation of such electron vortices in 2010 [23–25]. The particle vortex is an eigenfunction of the angular momentum operator, with a helical current density trajectory, additionally the charged nature of the electron lends the electron vortex a magnetic moment $\boldsymbol{\mu} = g\mu_B l\hat{\mathbf{z}}$ with the gyromagnetic ratio $g = 1$ taking the classical value for an orbiting mass [32].

In an external magnetic field the magnetic moment $\boldsymbol{\mu}$ leads to a Zeeman interaction, splitting the energy of the vortex states having orbital angular momentum aligned or anti-aligned along the direction momentum of the beam. In any external field, the gross motion of the vortex electron follows the same curved trajectory as that of a plane-wave electron, and the vortex structure also curves so that the vortex axis follows this classical trajectory. As a result, an extra phase shift is necessary to describe the evolution of the vortex phase due to the curved trajectory distorting the vortex phasefront [32]. This distortion is described by the Berry curvature $\boldsymbol{\mathcal{B}}(\mathbf{p}) = \nabla \times \boldsymbol{\mathcal{A}}(\mathbf{p})$ where $\boldsymbol{\mathcal{A}}(\mathbf{p}) = i\langle\psi(\mathbf{p})|\nabla_p|\psi(\mathbf{p})\rangle$ is the associated gauge field, or Berry connection. The phase shift γ is termed the Berry phase, and is found by integrating the curvature over the relevant momentum surface:

$$\gamma = -\int_S \boldsymbol{\mathcal{B}}(\mathbf{p}) \cdot d\mathbf{S}_p = 2\pi l, \tag{1.2}$$

so that the phase γ has the form of a quantised 'flux' of the 'magnetic-monopole'-like field $\boldsymbol{\mathcal{B}}(\mathbf{p})$, for a 'monopole' of strength l [22].

Solutions to the Klein-Gordon and Dirac equations for electrons with orbital angular momentum have been written down for several situations - freely propagating relativistic vortices [32, 33], electrons in a cylindrically symmetric potential [34] and in a circularly polarised electromagnetic field [35]. The freely propagating relativistic vortices show spin dependent perturbations of the current density, leading to a non-zero intensity at the core for one spin polarisation, and a slight increase in the radius of the central dark core for the other [32]. In

principle, this is observable as a deviation of the intensity profile from the expected, scalar intensity, however the magnitude of the effect is such that in current microscopes such an effect is not measurable [36]. Additionally, in the paraxial limit, the relativistic effects become negligible [32], further hindering observation in the electron microscope. Unlike the solutions to the Schrödinger-Pauli equation the relativistic vortex is no longer an eigenstate of S_z and L_z separately, but instead the total angular momentum $J_z = S_z + L_z$. Selecting a particular J_z eigenstate using holographic or other methods to generate vortices (see below) is not possible, as the effect relies on discrimination between the two spin states - on passing through a typical electron optics system the two spin states behave the same way so that direct generation of a J_z eigenstate cannot be achieved for an un-polarised electron beam [36]. On the other hand, this is precisely the reason why the eigenvalues of L_z remain a good quantum number for electron vortices generated in electron microscopes - in the un-polarised beam $\langle L_z \rangle$ coincides with $\langle J_z \rangle$.

The effect of a strong, circularly polarised laser field on the dynamics of a relativistic particle described by either the Klein-Gordon or the Dirac equation has also been investigated [35], and it is found that although the average value of the orbital angular momentum is conserved, the effect of the laser causes spin precession and spin-flips, so that the beam is no longer an eigenstate state of $\langle J_z \rangle$. At high values of orbital angular momentum, the effect of spin precession on the total orbital angular momentum is less significant, and $\langle J_z \rangle \approx l$. The effect of strong laser fields on vortex electrons with large l has applications in both high-field non-linear quantum electrodynamics, such as in radiative processes due to the high magnetic moment, and also high energy particle physics, as the field provides a method by which vortex electrons or positrons could be accelerated to ultrarelativistic velocities to investigate the effects of orbital angular momentum in collisions [35].

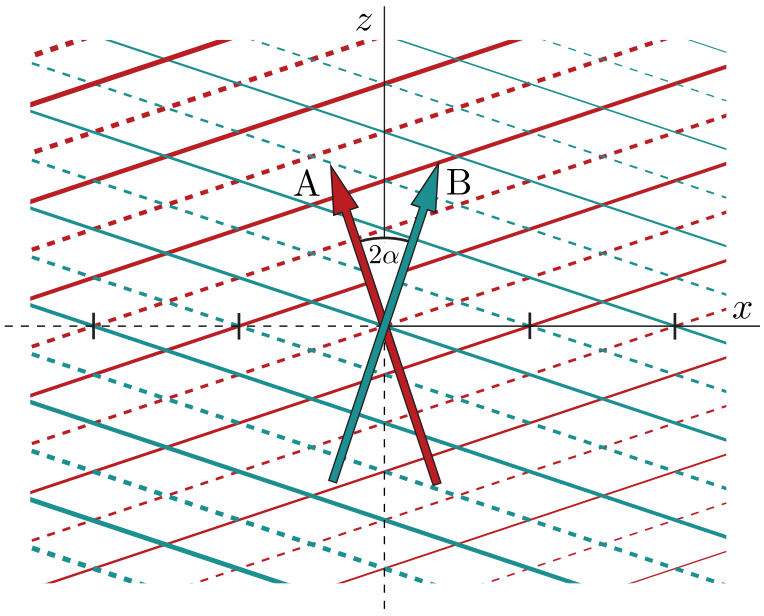

(a) Edge dislocations

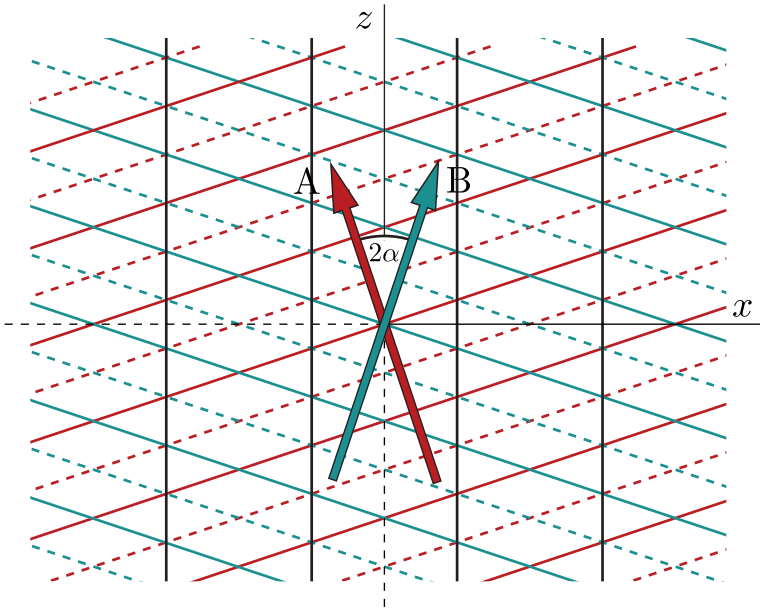

(b) Screw dislocations

Figure 1.2.1: Schematic representation of edge and screw dislocations in wavefronts resulting from interference of two waves A (red) and B (blue) propagating with a relative angle 2α in the z-x plane. Points of peak intensity are indicated by solid lines, minima by dashed lines. In (a) A and B are amplitude modulated (indicated by thickness of the lines) such that the amplitude of A increases along the propagation direction, while B decreases, such that the waves have the same amplitude along the x-axis. Above (below) the x-axis the amplitude of A (B) is greater than that of B (A), so that, due to the destructive interference of A and B along the axis, new wavefronts appear to be generated at the x-axis. These edge dislocations are indicated by ticks along the x-axis. In (b) the same two waves A and B are now amplitude modulated in the y direction, with A (B) increasing (decreasing) in the positive y direction so that their amplitudes match in the $y = 0$ plane, as shown. The vertical black lines indicate the screw dislocations; in the y=o plane the amplitude along these lines is zero, while the amplitude modulation causes the phasefront of the resulting interference pattern to wrap around these lines, in a corkscrew fashion.

1.3 Generation of Electron Vortex Beams

In the past few years several methods have been applied in the generation of electron vortices in a TEM, including spiral phase plates, holographic diffraction masks and mode converters. The principles of vortex generation using these methods will be outlined below. In order to illustrate the details of vortex generation and propagation though a physical electron optics system, some basic considerations of the optical system in the electron microscope are first discussed, with reference to points of specific importance for generation of coherent vortex states.

1.3.1 Electron Optics

The electron microscope system consists of three principal parts - the illumination system, the specimen stage and the imaging system. An overview of an electron beam propagating through these three stages is given in Fig. 1.3.1. Of principal importance for electron vortex microscopy is the illumination system, consisting of the electron source and a focusing condenser system, in which coherent, focused electron probes are generated. Some key points of the condenser lens and apertures are discussed in view of the concerns for the efficient production of tightly focused vortex probes of high quality.

The Electron Source

The electron source in an electron gun is a fine tip or filament cathode from which electrons are emitted through thermionic or field emission. The electrons generated at the gun are accelerated by a high voltage, usually between 50-300 keV, through a narrow aperture, in order to limit the angular spread of the beam. The beam current through the aperture is typically only 1% of the emission current [37]. The particular source determines several key beam properties such as current, brightness and energy spread. While a full discussion of the various beam sources is beyond the scope of this thesis, the effects of energy spread and finite source size will be discussed, as they are very important in the generation of high quality vortex probes, affecting the spatial and temporal coherence of the beam.

In the emission process, electrons with a range of kinetic energies are produced, due to thermal fluctuations of the source. For thermionic emission from heated cathodes this energy range is typically 1-3 eV, whereas for Schottky or field emission processes the range is much smaller, typically 0.2-0.7 eV [38]. The energy ranges stated refer to the full width at half maximum (FWHM) of the energy distribution of the emitted electrons, typically described by a Maxwell-Boltzman distribution [38]. The energy range leads to temporal incoherence within the beam, as the electrons do not all have the same frequency. Though values of the energy spreading is small compared to the acceleration voltage of the beam, this range causes deviations from the mean energy so that the electrons in the beam have varying speeds, and leads to a spread of the electron wavepacket along the optic axis [38]. This affects their transmission though the electron optics systems, which depends on the electron velocity, as well as leading to a smearing of interference patterns generated in diffraction, as various wavelengths are interfering. Another contribution to the partial-temporal coherence of the beam is the Boersch effect [38], in which electron-electron

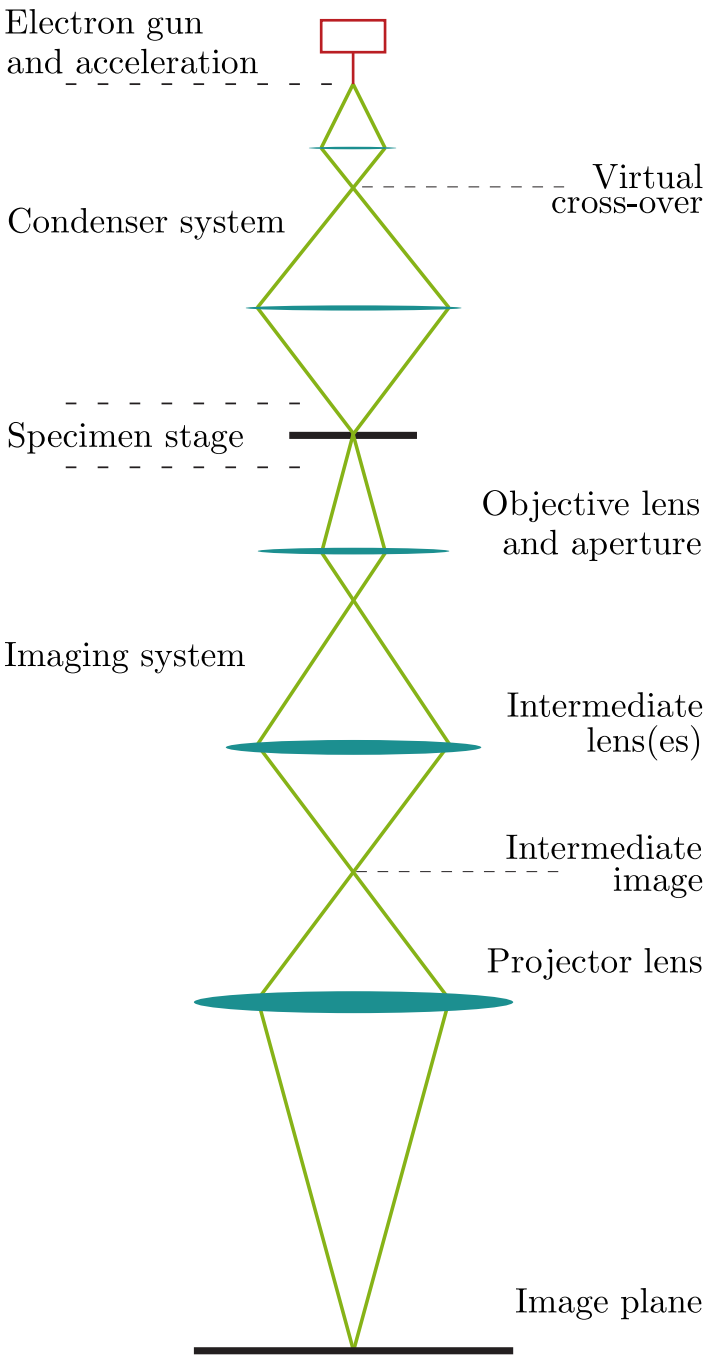

Figure 1.3.1: Schematic overview of the main elements of the transmission electron microscope operating in bright-field mode. Electrons are produced by an electron gun and accelerated into the microscope by voltages of 50-300 keV. The virtual cross over is the position of the virtual electron source. The beam of energetic electrons is then focused into a small probe, and projected onto a sample in the specimen stage. The electrons scattered through the sample at small angles are refocused by the objective lens, and magnified into an image.

repulsion in regions of high current density, such as close to the electron gun, leads to energy shifts within the beam. Any variations in the accelerating voltage will also lead to deviations from the mean electron energy.

An ideal electron source would be a point emitter, emitting a perfectly spatially coherent wave with a spherical wavefront profile. In practical electron microscopes the electron source has a finite size, leading to only partial spatial coherence of the beam, since the wavefronts emitted from different regions of the source are slightly out of phase. This is particularly important in diffractive effects, as any detail on the order of the source size cannot be resolved as the beam is not coherent over such length scales. The spatial distribution of the electron emission my be modelled as a Gaussian distribution, with the source width given by the FWHM of the distribution. [38–40]

Due to fringe field effects at the anode used for accelerating the electrons, the beam is bent through the aperture at the anode, and, for ray tracing purposes, may be considered to originate at a virtual source some 20 cm or so from the electron gun [37]. The size of this virtual source is typically 40 μm [37], and it is the imaging of this virtual source that affects the spatial coherence - the size of the virtual source relative to the size of the beam projected onto the sample - the probe size - determines the level of spatial coherence within the probe. If the probe is much larger than the virtual source then the beam is coherent; when the probe size is of the order of the size of the virtual source then the beam is incoherent [38].

The Condenser Lens System

The condenser lens deals with focusing the electron source onto the sample in the specimen plane, with a suitable probe current and area for the given application [38]. At least two lenses are employed for these purposes, allowing for very fine control of the size of the beam, and the magnification. The first lens is used to demagnify the virtual electron source, increasing the spatial coherence of the beam. This requires a strong magnetic field, and the focal length of the lens is as small as 2mm, resulting in a projected virtual source size of 0.1-1μm [37]. This virtual source is then the object for the second condenser lens, which projects the source onto the sample. A two-lens condenser system is shown in Fig. 1.3.2.

The second condenser lens and the condenser aperture are important for forming a probe of the required diameter and current. The focus of the lens and the size of the aperture determine the angle at which the electrons intersect the sample, with the correct focus giving the highest current density and smallest probe diameter [38]. This is required for high magnification imaging, and reduction of radiation damage to other areas of the sample. The focused situation is shown in Fig. 1.3.3b. The back focal plane of the lens coincides with the specimen plane, with the beam converging onto the sample at an angle of $2\alpha_c$. The convergence semi-angle α_c, often simply called the convergence angle, is the maximum angle of deviation of the beam from the optic axis. This is always measured at the sample plane, even if the focal plane of the image is elsewhere, as in the under- and over- focused situations depicted in Fig. 1.3.3a and Fig. 1.3.3c. From this it can be seen that a larger convergence angle results in a smaller beam size, as the largest α_c occurs for the fully focused condition. It can also be seen that the finite size of the source leads to a broadening of the

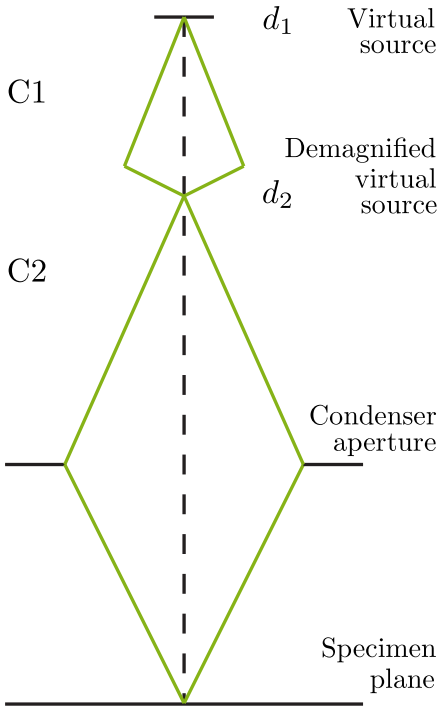

Figure 1.3.2: Schematic of a two-lens condenser system. The virtual electron source has a diameter d_1. The C1 lens demagnifies this virtual source to produce a smaller probe, focused by the C2 lens. The aperture in the C2 lens adjusts the convergence angle of the beam, and the size of the resulting probe in the specimen plane.

probe size even in the fully focused condition, leading to a limit on the probe diameter.

The Objective Lens System

The imaging system focuses the beam transmitted through the sample onto the imaging and viewing system of the microscope. The imaging system consists of a series of lenses, apertures and diaphragms that allows selected parts of the beam to be collected. The first lens, the objective lens, is the principal lens from which the image is formed, and must be very precise - subsequent lenses magnify the image formed by the objective lens onto the viewing system. The objective aperture is relatively large compared to the apertures of the successive lenses in the imaging system, since the high resolution requires a smaller aperture. This means that any aberrations in the objective lens must be corrected for, or they will significantly affect the image quality, whereas the smaller angles in the subsequent lenses allow for the introduction of fewer aberration effects.

The objective aperture is inserted into the back focal plane of the objective lens. The aperture blocks all electrons travelling along trajectories making an angle with the optic axis that is larger than the objective aperture angle α_o. This is illustrated in Fig. 1.3.4. Adjusting the aperture angle determines the allowed scattering angles of the observed electrons, such that a low α_o admits only those electrons that have been scattered along or close to the optic axis. A forked holographic mask (see below) may be placed inserted into the objective lens as the objective aperture, and the beam transmitted through the sample is then separated into vortex components [24].

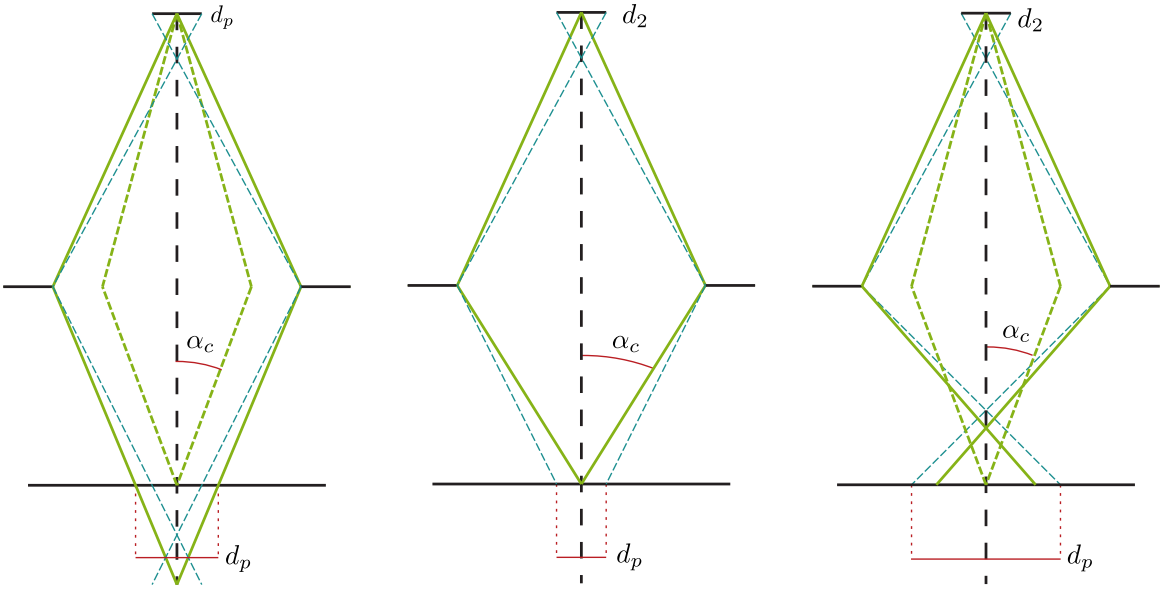

(a) Under-focus (b) Focus (c) Over-focus

Figure 1.3.3: Focusing in the second condenser lens. The situations of under-focus, focus and over-focus are shown in (a), (b) and (c) respectively. The convergence angle α_c is measured as the maximum angle of deviation from the optic axis of those electrons that converge on the axis at the specimen plane. The focused situation leads to the largest convergence angle and the smallest probes size d_p in the specimen plane. In the under- and over- focused situations the focal point does not coincide with the specimen plane, leading to smaller values of α_c, and a larger probe size d_p. Effects of finite source size broadening are indicated (blue dashed lines), for the demagnified source width d_2. Equivalently, reducing the aperture size gives a similar effect in decreasing α_c, and also reduces the current reaching the sample.

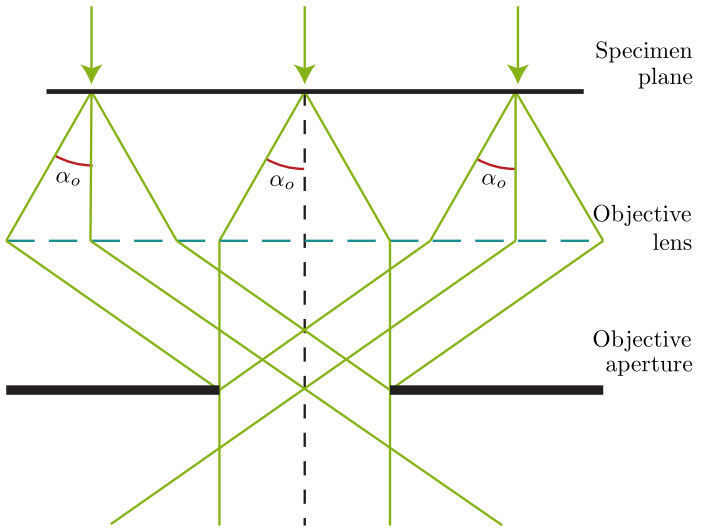

Figure 1.3.4: The objective aperture is placed in the back focal plane of the objective lens. The size of the aperture determines the maximum scattering angle α_o admitted to the imaging optics.

The lenses used to focus the electron beam use electric and magnetic fields to deflect and converge the beam, based on the Lorentz force. The main focusing lenses applied for the condenser and objective lenses are cylindrically symmetric magnetic fields, generated by current carrying wire coils with specially designed polepieces so that the field is inhomogeneous within a short length. Strong lenses, with short focal lengths, require high magnetic fields, up to 2 T [37]. The varying radial component of the inhomogeneous field causes the electrons to spiral in towards the z axis, focusing the beam along this axis. Changing the current in the coils changes the field strength and adjusts the focal length of the lens. Various aberrations cause deviation from the perfect lens behavior, which affect the probe size and the imaging resolution when they occur in the condenser and objective lenses respectively. A few examples of the main aberrations affecting production of vortex beams will be discussed below. It is also worth noting here that, similar to a Gaussian beam, after passing through a focal point the electron beam will acquire a Gouy phase shift of 2π [37, 38].

Since the focusing action relies on the Lorentz force, the velocity of the electrons is important, as electrons at different velocities will 'see' a lens with a different focal length. The partial temporal coherence of the beam will thus cause the beam to not be fully in focus, leading to a 'disk of minimum confusion', as opposed to a point of focus. This is known as chromatic aberration. The radius of the disk of confusion may be estimated for a beam with a certain energy spread ΔE passing through a lens with chromatic aberration coefficient C_c [38]

$$r_c^{\mathrm{C}} = \frac{1}{4}\alpha C_{\mathrm{C}}\frac{\Delta E}{E}\underbrace{\frac{1+\frac{E}{E_0}}{1+\frac{E}{2E_0}}}_{\text{Relativistic factor}} \tag{1.3}$$

where α is the maximum angle of deviation from the optic axis on entrance to the lens, E is the average beam energy, and E_0 is the rest energy of the electron. The relativistic factor indicated is approximately 1 for electrons of energy less than 200 keV. For weak lenses, $C_{\mathrm{C}} \approx f$, the focal length of the lens, with a minimum aberration coefficient of $C_{\mathrm{C}} \approx 0.6f$ for high field lenses [37, 38].

The temporal coherence of the beam is affected by the source, as discussed above, but chromatic aberrations are also important in the objective lens, due to scattering processes in the sample plane leading to a range of energies that must be focused onto the image plane.

Spherical aberrations describe the deviation of a lens from a perfect lens which focuses all parallel rays passing through the lens to a single point. Spherical wavefronts passing through a spherical lens remain spherical, though they are inverted; for example diverging spherical wavefronts are transformed to converging spherical wavefronts on exiting the lens. In a lens with spherical aberrations, rays passing through the outer edges of the lens tend to be over-focused, with the effect increasing farther away from the optic axis, so that the wavefronts are distorted from spherical. Like the chromatic aberrations, this causes the focal point to be broadened into a disk, as the rays originating from the edge of the lens are over-focused. The effect of spherical aberrations is described by an additional phase factor $e^{i\chi_S}$ [38, 40] with

$$\chi_S = \frac{C_S k_z r^4}{f^4}. \tag{1.4}$$

On focusing a beam with α the maximum angle of deviation from the optic axis on entrance to the lens, the radius of the disk of confusion at the focal point due to the spherical aberrations can be estimated as [38]

$$r_c^{\mathrm{S}} = \frac{1}{2} C_{\mathrm{S}} \alpha^3, \tag{1.5}$$

with C_{S} the coefficient of spherical aberrations, typically of the order of $0.5 - 2$ mm [37, 38]. In modern electron microscopes correction of spherical aberration is possible via the use of multipole lenses [37], which negate this broadening effect. Double aberration corrected microscopes have spherical aberration correcting components in both the probe forming condenser lenses as well as the image forming lens system.

The final lens aberration to be discussed here is axial astigmatism, which arises due to a breaking of the cylindrical symmetry of the lens field, due to imprecisions in machining of polepieces or other effects. This leads to there being different focal points along the optic axis for rays in the x-z and y-z planes. Between these two points will be a disc of minimum confusion, so that the width of the beam in the two planes is the same, and the beam is circular, rather than the elliptical profile expected elsewhere. The radius of this disk is given by

$$r_c^{\mathrm{A}} = \frac{1}{2} \Delta f \alpha \tag{1.6}$$

where Δf is the axial distance between the two focal points, of the order of 0.1-1 μm [38]. Axial astigmatism may be corrected for with the use of weak quadrupole lenses to deflect the beam back to a circular cross section. Using such a stigmator the deflection along the two axes may be adjusted independently, and in certain cases it may prove useful to have an astigmatic lens.

Coherent Illumination

As mentioned above, the energy spread at the source leads to a beam with only partial temporal coherence. The spatial coherence of the beams is also an important factor in electron imaging, particularly where diffraction effects are key. The electron source is small but finite, which leads to only partial spatial coherence within the beam, as the electron source is not truly point-like. The relative size of the condenser and objective apertures is important for determining the spatial coherency of the beam; for coherent conditions the convergence angle must be smaller than the aperture angle $\alpha_c << \alpha_o$ [38]. Alternatively, the diameter of the virtual source in the condenser aperture must be much smaller than the diameter of the beam probe, in order that the effects of partial coherence are minimised [40]. For the small demagnified virtual source diameter imaged onto the sample plane by the second condenser lens, the small angle approximation is valid, and the half-angle of incoherence θ_{Inc} is approximately the radius of the source. Magnification and demagnification of the source in the first condenser lens thus affects the spatial coherence of the beam.

The coherence of the beam is very important for the generation of probes with high quality vortex structure, particularly for the diffractive methods described below. If the beam is very incoherent, then the interference as the beam diffracts through the holographic mask will not lead to pure states, but mixed vortex states with ill-defined angular momenta. In order to quantify the

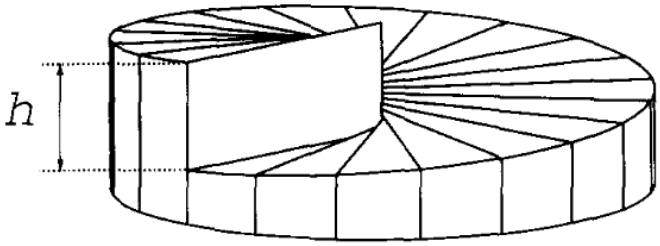

Figure 1.3.5: The spiral phase plate has a smoothly varying thickness in a helical shape, such that there is as step between the thinnest and thickest parts of the plate. The height of the step, and the material the plate is constructed from determine the change in orbital angular momentum for a given wavelength. Image adapted from [41].

partial-coherence of the beam, the source may be modelled as a Gaussian distribution with full width at half maximum of order 0.1 Å [38, 40].

1.3.2 Spiral Phase Plates

Spiral phase plates are constructed from refractive material having a thickness that changes continuously, giving a helical shape to the surface of the plate. Generation of optical vortices using spiral phase plates was first demonstrated in the mid-1990s [41, 42]. Spiral phase plates may be produced for millimeter wavelengths down to optical wavelengths [10, 42, 43], however due to precise refractive index and wavelength matching requirements the application of spiral phaseplates is not as versatile as the holographic masks discussed below.

The main fabrication considerations for the spiral phase plate production of the smoothly varying optical depth - usually by varying the thickness of the waveplate - since this is directly related to the angular momentum to be conferred to the beam. For a phase plate with spiral height h, as in Fig. 1.3.5, the change in orbital angular momentum between the incident and transmitted beam Δl is

$$\Delta l = (n_2 - n_1)\frac{h}{\lambda}, \tag{1.7}$$

where n_1 and n_2 are the refractive indices of the external and phase plate materials respectively, and λ the vacuum wavelength of the beam. As can be seen, it is therefore important to balance the phase plate material and the step height for the intended wavelength, so as to produce the desired orbital angular momentum change. This is the limiting factor for the fabrication of spiral phase plates suitable for electron beams; since the wavelength is so small - order of picometres - the step height must also be of this order.

The stepped phase plate used by Uchida and Tonomura was made of spontaneously stacked flakes of graphite, leading to a phase plate that changed thickness in steps - rather than continuously [23]. The edges of the steps cause extra phase features, such as phase jumps, to appear at different points in the beam cross-section - in addition to the sharp 2π phase change of the desired vortex structure. This was observed in Uchida and Tonomura's experimental results via interference patterns and in-plane phase profile. The transmitted beam thus did not demonstrate the required characteristics of a pure vortex state with integer orbital angular momentum, but was the first

experimental demonstration of a freely propagating (mixed) vortex state with a phase singularity and orbital angular momentum.

Due to the method of obtaining the phase plate, the defects in the phase structure of the beam cannot be well controlled. Thus the spiral phase plate for electrons does not lend itself well to reproducibility of results, as the particular arrangement of the graphene flakes cannot be properly controlled. Additionally, being made of carbon, under the influence of the high energy electron beam the flakes will be subject to damage and deformation, and the phase plate will lose its key structure. So, even if a suitable spot of graphene may be found, it will not remain useful for extended periods of beam illumination.

1.3.3 Holographic Masks

Holographic reconstruction is a well known technique in both optics and electron optics [37, 38, 44]. By interfering a wave diffracted from an object, and a non-diffracted component of that same wave, increased resolution is achieved by reconstructing the image from the interference pattern of the two waves [38]. The same principles of holography may be used to reconstruct an image or wavefunction from an input reference wave by passing the input wave though a hologram. The hologram consists of the interference pattern between the reference wave and the desired output, whether that output contains an image of an object, or a particular wave mode of interest. The holographic techniques employed in vortex optics and electron vortex optics rely on generating a vortex mode from an input plane wave, by passing the plane wave through a holographic mask consisting of the interference pattern between the vortex mode and the plane wave.

Wave interference patterns are often complicated, and very difficult to reproduce exactly, so that is it usually more practical to construct binarised holograms by selective clipping, resulting in a pattern of steps or rectangular fringes of varying widths, such that the phase and amplitude information may be encoded into the hologram in a variety of ways [45]. For the construction of vortex modes, we are interested in the phase variation of the wave, rather than any particular spatial variation of the mode, so the holograms to be generated concentrate on modifying the phase of the incident beam, though the aperture and the phase singularity ensure that the resulting beam has the desired Bessel-like or Laguerre-Gaussian-like amplitude profile.

The amplitude of a Bessel-type vortex mode travelling in the z direction with wavenumber k(ignoring any normalisation factors) is given by

$$\psi_l(\mathbf{r}) = J_l(k_\perp \rho) e^{il\phi} e^{ik_z z}, \tag{1.8}$$

where $J_l(x)$ is a Bessel function of the first kind. The hologram pattern is generated through interference of this mode with a reference plane wave travelling at an angle, where k_x is the component of the plane wave momentum orthogonal to the z direction:

$$\psi_p(\mathbf{r}) = e^{ik_x x}. \tag{1.9}$$

Any component of the plane wave momentum in the z direction does not contribute to the

interference pattern. The interference is constructed by superposition:

$$I(\mathbf{r}) = |\psi_l + \psi_p|^2. \tag{1.10}$$

This interference pattern is particular to the beam of interest. For the phase vortex, the characteristic pattern is a edge dislocation, with l edges - also known as a fork dislocation. The interference pattern may then be binarised by clipping the pattern, for example

$$I_{\text{holo}}(\mathbf{r}) = \begin{cases} 1 & I \geq 1, r \leq R_{\text{max}} or r > R_{\text{max}} \\ 0 & I < 1, r \leq R_{\text{max}} \end{cases} \tag{1.11}$$

for a maximum aperture radius R_{max}. The interference pattern and corresponding binary holographic mask for an $l = 1$ Bessel-type vortex are shown in Fig. 1.3.6. The binary mask for an $l = 3$ Bessel beam is given in Fig. 1.3.7, showing the corresponding three edge dislocations. This mask pattern is then embedded into something opaque to the radiation of interest - a printed film [46, 47] or a spatial light modulator [10] for optical beams; or focused ion beam (FIB) etching of metal or silicon nitride films for electrons [24, 25] - and placed into the path of a electron beam. Diffraction of the beam though the mask produces the desired vortex beams.

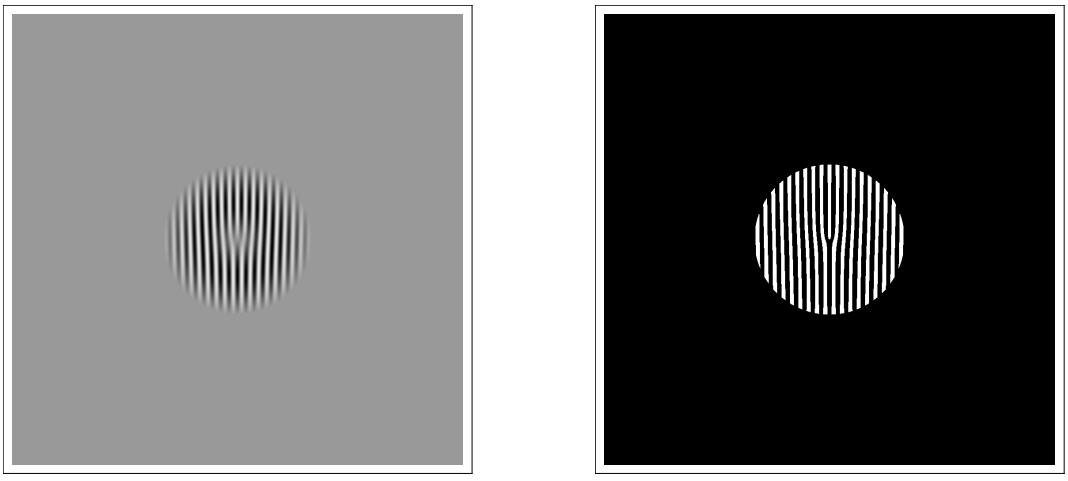

(a) (b)

Figure 1.3.6: Interference patterns for an $l = 1$ Bessel beam interfering with a plane wave. High intensity is indicated by black, zero by white. The characteristic interference fork can be seen in the centre of each image. (a) - the continuous interference pattern, within an aperture of radius R_{max}. (b) - the binarised, apertured interference pattern. For both masks, the parameters used are $R_{\text{max}} = \frac{\alpha_{1,1}}{k_\perp}$, and $k_x = 15k_\perp$, with $k_\perp = 2.3 \times 10^{10}$ m^{-1}. In each figure, high normalised intensity is indicated by black, zero by white.

The far-field diffraction pattern resulting from transmission of a plane wave through the holographic mask is given by the Fourier transform of the mask. This produces a non-diffracted, zero-order beam, along with the a series of vortex beams and their complex conjugates. The mask itself is not chiral, and so, unlike a phase plate, cannot impart orbital angular momentum to the

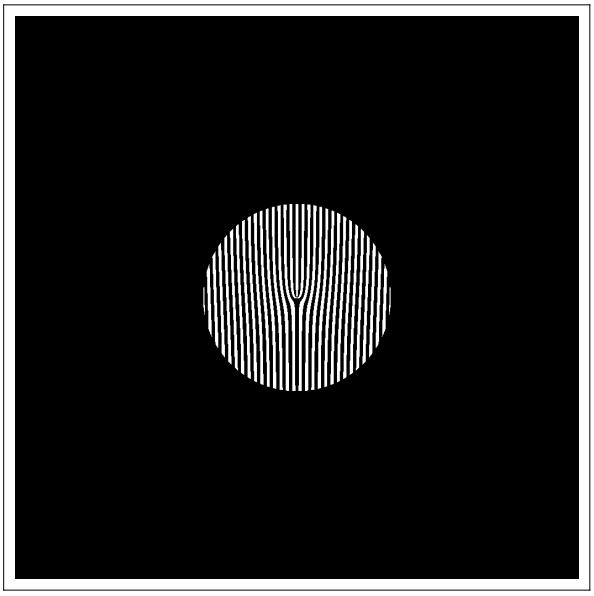

Figure 1.3.7: The binarised, apertured interference pattern for an $l = 3$ Bessel vortex interfering with a plane wave. High intensity is indicated by black, zero by white. The central fork dislocation has three prongs. the parameters used are $R_{\text{max}} = \frac{\alpha_{3,1}}{k_\perp}$, and $k_x = 15k_\perp$, with $k_\perp = 2.3 \times 10^{10}$ m^{-1}.

transmitted beam by directly modulating the phase of the wavefront. Instead, the mask decomposes the input plane wave into a basis of left-handed and right handed vortices, so that the total orbital angular momentum of the incident plane wave is conserved.

The Fourier transforms of the $l = 1$ continuous and binary masks of Fig. 1.3.6 and the binary $l = 3$ mask of Fig. 1.3.7 are given in Fig. 1.3.8, Fig. 1.3.9 and Fig. 1.3.10 respectively, along with the corresponding phase. The direct Fourier transform is given in Fig. 1.3.8a and Fig. 1.3.9a; plots of the logarithmic intensity display the inner features of the diffracted beams more clearly in Fig. 1.3.8b and Fig. 1.3.9b. It can be seen that the process of discretising the mask leads to a series of diffracted beams, with various orders of orbital angular momentum. The resulting phase indicates that the nth diffracted beam has orbital angular momentum $nl\hbar$, as is clear on looking at the phase of the second order diffracted beams of Fig. 1.3.10c, which have a phase change of 12π.

The various diffraction orders propagate from the mask at some angle ϕ_s to the centre of the mask, so that in the far-field the beams are well separated. The magnitude of k_x relative to k_z determines the angle that the diffracted beams exit the hologram, such that a large k_x increases the separation between the different diffracted orders [25, 46]. The angle of the first order diffracted beam is

$$\phi_s = \frac{\lambda}{d} = \frac{k_x}{k_z} \tag{1.12}$$

for grating separation d. The nth order diffracted beam emerges at an angle $n\phi$ while the zero-order beam propagates along the original axis of the incident wave. A particular diffraction order of interest may be realigned to this zero axis by illuminating the hologram with a beam with transverse momentum nk_x [40]. The transverse momentum of the vortex beam itself $k_\perp$ is determined by the

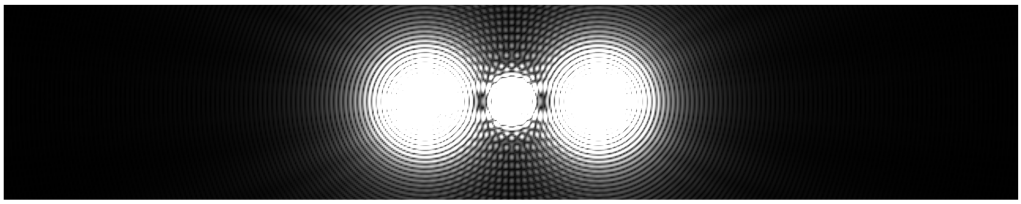

(a)

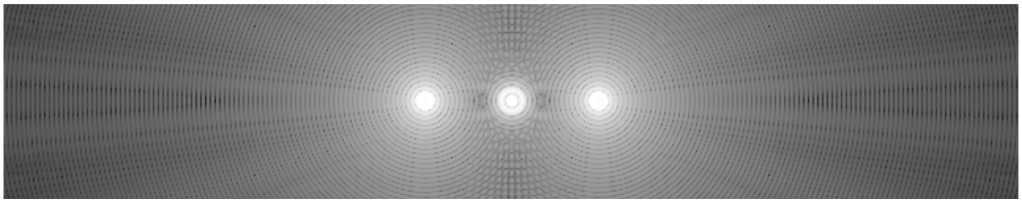

(b)

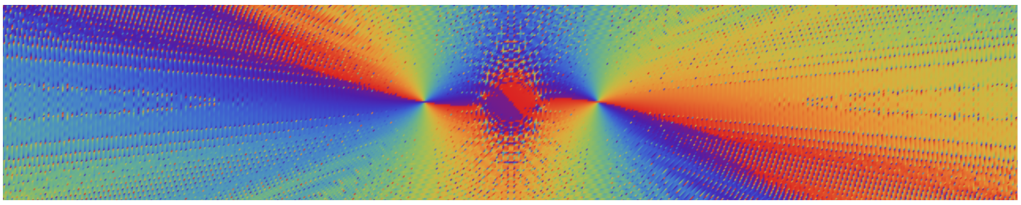

(c)

Figure 1.3.8: The far field diffraction pattern and phase distribution of the continuous $l = 1$ holographic mask of Fig. 1.3.6a. (a) shows the diffracted beams, only the zero and first order beams are apparent. The additional rings arise from diffractive effects, since the masks are designed using only the inner ring of the Bessel function. The log intensity plot of (b), show the fine structure of the centre of the diffracted beams, though at this scale the central minima of the first order beams are not apparent. The phase of the beams is shown in (c), the opposite direction of change of phase of the two sidebands can be seen. In (a) and (b) high intensity is indicated by white, zero by black; in (c) the rainbow scale indicates phase change from 0 (red) to 2π (purple).

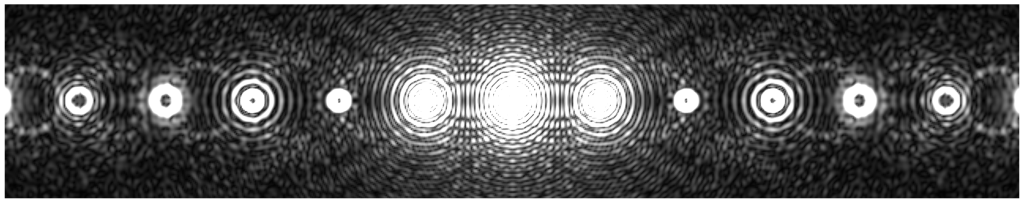

(a)

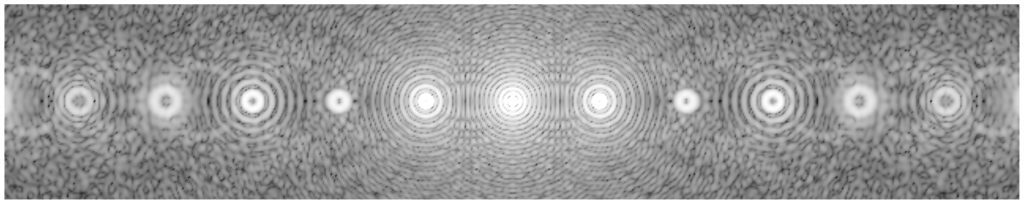

(b)

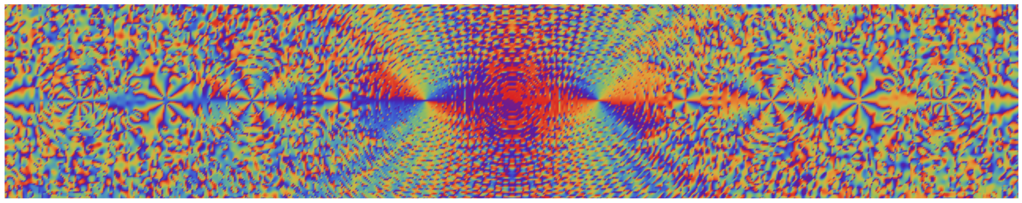

(c)

Figure 1.3.9: The far field diffraction pattern and phase distribution of the binary $l = 1$ holographic mask of Fig. 1.3.6b. (a) shows the diffracted beams, with several diffraction orders present. The log intensity plot of (b), shows the fine structure of the centre of the diffracted beams, the central minima of the higher order diffracted beams are apparent. The phase of the beams is shown in (c), the opposite direction of change of phase of the two sets of sidebands can be seen, with the nth order beams displaying a phase change of $2\pi n$. In (a) and (b) high intensity is indicated by white, zero by black; in (c) the rainbow scale indicates phase change from 0 (red) to 2π (purple).

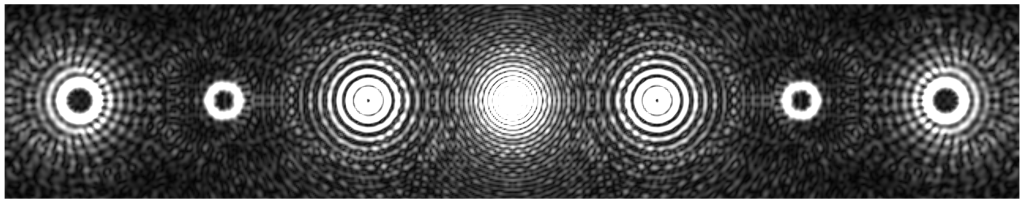

(a)

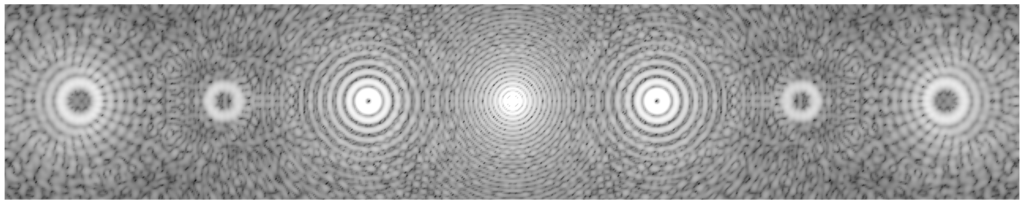

(b)

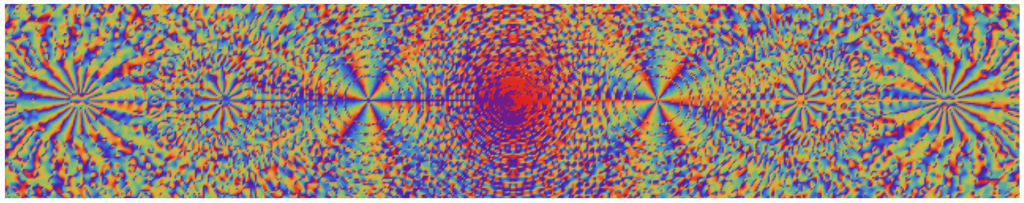

(c)

Figure 1.3.10: The far field diffraction pattern and phase distribution of the binary $l = 3$ holographic mask of Fig. 1.3.7. (a) shows the diffracted beams, with several diffraction orders present. The log intensity plot of (b), shows the fine structure of the centre of the diffracted beams, the central minima of the higher order diffracted beams are apparent. The phase of the beams is shown in (c), the opposite direction of change of phase of the two sets of sidebands can be seen, with the nth order beams displaying a phase change of $6\pi n$. In (a) and (b) high intensity is indicated by white, zero by black; in (c) the rainbow scale indicates phase change from 0 (red) to 2π (purple).

size of the mask aperture; for the Bessel beam we have

$$k_\perp = \frac{\alpha_{l,1}}{R_{\text{max}}} \tag{1.13}$$

with $\alpha_{l,1} \approx 3.81$ the first zero of the Bessel function $J_l(x)$. A similar relationship applies for the Laguerre-Gaussian modes, with $\alpha_{l,1}$ replaced by the relevant radius of the $p = 0$ Laguerre-Gaussian mode at $z = 0$.

The procedure described above may be used to produce holographic masks for Laguerre-Gaussian vortex modes; however the difference between the binary masks and Fourier transforms produced is very small [48]. The interference patterns have a slightly different spatial form, however the differences are mostly eradicated by the binarisation process. Whether the resulting beams are Bessel-like or Laguerre-Gaussian-like then depends on the diffraction characteristics as the beam propagates.

As can be seen, the production of phase holograms is much more versatile and controllable than the use of the spiral phase plates as described above. Even for the discrete binary masks, the beams produced have integer orders of angular momentum in all cases, as they are the vortex 'harmonics' of the incident beam - by definition they are phase vortices of $2\pi l$. The masks may be constructed out of materials that are resistant to beam damage, and will have a longer useful lifetime than a spiral phase plate of graphene - in addition the results are directly reproducible, and in principle any order of orbital angular momentum may be specified. On the other hand, it should be noted that the mask itself will block much of the incoming beam, so that only 50% of the incident intensity is transmitted. Approximately 25% of the incident intensity is channelled into the zero order beam, with the higher order beam decreasing in intensity. The first order diffracted beams have approximately $\frac{1}{8}$ of the incident intensity.

1.3.4 Forked Masks

Forked apertures as described above have been used to generate electron vortices in transmission electron microscopes (TEM) [24, 25, 39, 40]. The first proof of principle demonstration involved a $5\ \mu$m diameter mask cut from platinum foil, with a single fork dislocation generating left and right handed $l = 1$ beams. The second instance of this holographic vortex generation also involved a mask with a $5\ \mu$m aperture, but with a much reduced grating period d [25], corresponding to an order of magnitude increase in k_x of the plane wave used in calculating the interference pattern. The silicon nitride films used by McMorran *et al.* allowed for FIB milling of very fine features, so that the beam produced had a large angular separation, and also enabled the fine features of higher order masks to be reproduced - a forked mask of topological charge $l = 25$ was also demonstrated. For structural stability of the mask, the edge dislocations were not cut directly into the centre of the mask; instead the very centre of the mask was left solid, and the dislocations occurred at a small radius. This did not seem to significantly impair the function of the mask, and vortices with clear central dark cores were observed, with the fourth order diffracted beam carrying $100\hbar$ orbital angular momentum [25], demonstrating the versatility of the uses of holographic masks over spiral phase plates. The phase structure of the resulting beams was confirmed by observation of forked Fresnel interference fringes of opposite orientation for the two different vortex helicities [24], and

by the persistence of the central singular core of the vortex on propagation and diffraction [25]. A beam that simply has an annular profile will spread radially both inwards and outwards, obliterating the dark core at a certain distance from the focal point. A beam with a phase singularity must preserve this singularity through the length of the beam, as the orbital angular momentum must be conserved.

The first vortex beams produced using the forked masks were of the order of micrometre diameters [24, 25], however the forked mask holographic technique has been used to demonstrate that very small, atomic scale vortices may be generated in an electron microscope giving atomic resolution in scanning transmission electron microscopy (STEM) [39, 40]. As discussed above, the electron optics system is not perfectly coherent, so that the theoretical ideal of a point-like probe is not experimentally achievable, not to mention the necessity of a finite beam radius for the vortex beam. However, having a small spot size available for vortex beams is expected to be useful in STEM applications such as spatially resolved EELS, so that magnetic information can be accessed at the atomic scale. In a conventional TEM set-up, it is possible to make electron probes of diameter 0.8 Å [39, 49], using a highly coherent source with high convergence angle and corrective lenses adjusting for spherical aberrations. Such an arrangement was used to generate $l = 1$ vortices with a FWHM of 1.2 Å [39]. This diameter is larger than that for a similarly focused non-vortex probe, due to the presence of the vortex core singularity; however, analysis of the intensity profile of these Ångstrom beams shows that the intensity of the vortex core is significantly increased from zero intensity, and in the smallest beams the central minimum of the vortex is completely washed out [50]. This is due to finite sources size effects and a level of incoherence in the electron source [39, 40]. The effect of this is to degrade the integrity of the vortex produced - due to the relatively high level of incoherence at these small scales, the probe formed is a mixed state, rather than a pure, coherent vortex state. Defocusing the probe leads to an apparent reduction in the central intensity - however this is not an improvement of the vortex state, since the incoherence remains [40]. The Ångstrom scale vortices attainable in current generation TEM are as such not suitable for experiments that require high quality vortex states. On the other hand, the nanometre scale vortices achieved using a lower convergence angle show a diffraction-limited situation where the finite source size does not impair the vortex characteristics [39].

1.3.5 Spiral Masks

The holographic mask production techniques outlined above may also be applied with different reference waves. A common choice in optics is a wave with a spherical wavefront, sharing an axis with the desired mode. This also produces a characteristic interference pattern, a spiral with l arms, as shown for the $l = 1$ and $l = 3$ vortices in Fig. 1.3.11, alongside the corresponding binarised mask. The action of these holographic masks on an incident plane wave is very similar to that described above for the forked mask, however instead of the beams being separated by an angle, they are separated along the propagation direction. The reference spherical wave of Fig. 1.3.11a and Fig. 1.3.11d is a Fresnel zone plate function, with focal length f. The vortex and zero-order modes transmitted through the spiral hologram produced using this reference spherical wave will focus at different points separated by a distance f [47, 51] - when the beam as a whole is properly focused the zero-order beam will be in the focal plane, while the first order diffracted beams will also be

focused at a distance f in front and behind the focal plane. For electron microscopy, this has the advantage that over- or under-focusing the beam will enable the different vortices to be brought into focus onto the focal plane, where they may then be utilised with minimum interference from the other orders in the beam [51].

The use of a spiral holographic mask has been demonstrated for electron vortices [51]. In order to produce a stable structure, the binary mask created using FIB milling of platinum film was designed to have eight reinforcing struts subtending the diameter of the mask. It was found for simulations and experimental results that this did not significantly impair the integrity of the vortices produced [51]. However, one issue with the application of a spiral mask is that the coaxial presence of the different diffraction orders leads to a relatively large background signal, causing the intensity of the centre of the vortex to be increased from zero [51]. In order to reduce this effect as much as possible, the focal length of the reference Fresnel zone plate function must be very long. Achieving this requires very fine features in the holographic mask - similar to a large k_x giving a high diffraction angle ϕ_s, and decreasing the grating separation (Eq. (1.13)), a long focal length f requires the arms of the spiral to decrease in separation rapidly toward the edges of the aperture. Additionally a highly coherent beam with a large convergence angle is required, stretching the limits of current microscope and FIB technology.

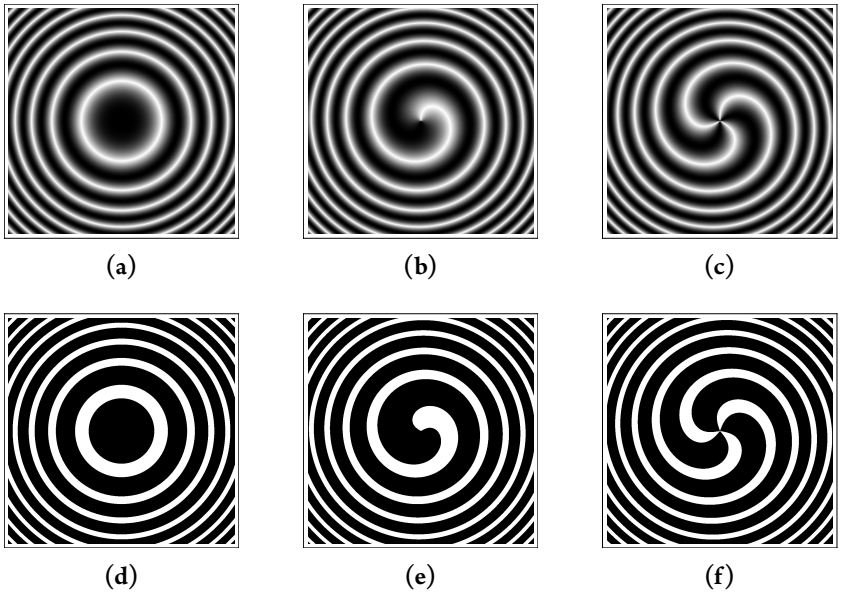

Figure 1.3.11: Interference patterns and masks of vortices interfering with spherical waves. (a) - in-plane intensity pattern for a spherical wave, with spherical wavefront propagating outwards; binarisation of this intensity pattern, forming a Fresnel zone plate, is shown in (d). (b) and (e) show the continuous and binarised interference patterns respectively for an $l = 1$ vortex interfering with the spherical wave. (c) and (f) show the same for the $l = 3$ vortex.

1.3.6 Other Methods of Generating Electron Vortices

Though the use of the holographic masks is currently the most widespread method for generating electron vortices, there are many other possible methods for producing electron beams with orbital

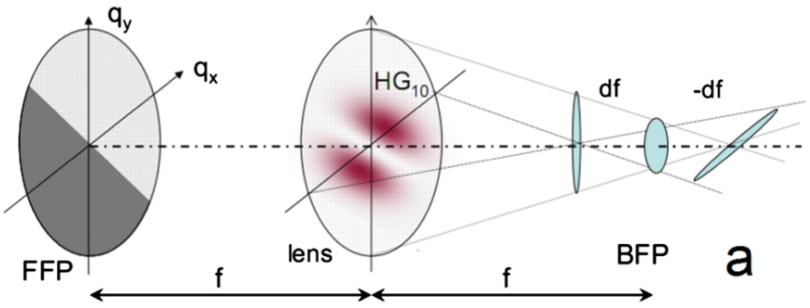

Figure 1.3.12: The experimental setup of a mode converter for an electron vortex. A Hilbert phase plate is place in the front focal plane (FFP) of the astigmatic lens, so that a rotated Hermite-Gaussian mode is projected through the lens. The astigmatic lens focuses the x component of the beam z_R in front of the back focal plan (BFP), and the y component z_R behind. The Laguerre-Gaussian beam profile is formed in the back focal plane, with the beam widths in the x and y directions the same at this point. Image from [52].

angular momentum. The holographic masks are versatile and relatively easy to produce; however, they also have their drawbacks, principally that the mask itself diminishes the intensity of the transmitted beam by 50%, resulting in the desired vortices having an intensity of ≈12% of the original plane wave - ≈25% of the remaining intensity is passed to the zero order, non-vortex mode, with the rest distributed between the various higher order modes. Additionally, since several modes are produced, it is difficult to isolate a particular mode of interest for further application. Other methods of generating vortices may overcome these limitations, leading to high intensity, single mode electron vortex sources suitable for various applications.

Electron Vortex Mode Converter

A mode converter for electron beams has been described [52], acting in an analogous way to laser mode converters in optics. The Laguerre-Gaussian optical vortex mode may be described as a linear superposition of two Hermite-Gaussian modes with a phase difference of $\frac{\pi}{2}$. The Hermite-Gaussian modes do not themselves carry orbital angular momentum, however by exploiting the difference in Gouy phase for astigmatic Hermite-Gaussian modes, such a superposition can be produced, resulting in a Laguerre-Gaussian mode with well defined orbital angular momentum and phase singularity [53]. The experimental procedure for electron vortices described by Schattschneider *et al.* [52] relies on a lens with variable astigmatism, so that the focal points of the x and y transverse parameters may be set independently. Setting one focus to a Rayleigh range z_R in front of the back focal plane, and one z_R behind leads to a circular beam profile in the back focal plane, where the vortex mode is to be observed, with a relative Gouy phase between the transverse beam profiles. This arrangement is shown in Fig. 1.3.12 This may then be used to generate a Laguerre-Gaussian mode from a Hermite-Gaussian mode. The transverse axes of the Hermite-Gaussian mode must be rotated by an angle of $45°$ to the transverse axes of the beam, so the astigmatism acts on the two x and y component modes.

An approximation to a Hermite-Gaussian mode is generated using a Hilbert phase plate, which imparts a phase-shift of π between the two halves of the beam, similar to the phase difference of π

between the two lobes of the Hermite-Gaussian mode. On passing through the astigmatic lens of the mode converter, the difference in Gouy phase between the two sides of the beam alters the phase shift to $\frac{\pi}{2}$, so that at the back focal plane, a Laguerre-Gaussian profile is obtained [52]. A proof-of-principle experimental result has been demonstrated, however though a phase singularity is apparent at the centre of the back focal plane, the resulting profile does not have rotational symmetry, and so is not a pure Laguerre-Gaussian mode. The discrepancy from the simulated results arises due to defocus effects and, importantly, strong beam absorption in transmission through the Hilbert plate [52]. Nevertheless, the electron vortex mode converter is an attractive prospect if these effects can be overcome, as it enables the generation of electron vortices of high intensity, of up to 90% of the incident plane wave intensity, as opposed to $\approx$12% using the holographic masks. Additionally, the mode converter may be applied in reverse, leading to a method of discriminating between the handedness of the incident vortex mode, by observing the relative rotation of the resulting Hermite-Gaussian mode. This will be useful in, for example, examining transfer of orbital angular momentum in experiments involving interactions with various forms of matter.

Spin to Orbital Angular Momentum Conversion

Another possibility is the generation of electron vortices from spin-polarised electron beams using so-called 'q-filters'. q-filters, or q-plates have been applied in optics since 2006 [54], and have applications in quantum information [55], The effect relies on a spatially varying optic axis, achievable by patterning of liquid crystal arrays. Passing circularly polarised light beam through the q-plate will result in a switch of the spin orientation of the beam, and a gain of orbital angular momentum $\pm q$. For electron beams, the q-filters work via a similar principle, requiring spatially varying electric and magnetic fields transverse to the beam propagation direction, in various multipolar configurations [56]. These fields must exist over a particular distance in the optics system, so that they act on the beam as it propagates. The direction and magnitude of the electric and magnetic fields vary according to the same pattern, with a relative angle of $\frac{\pi}{2}$, and field magnitudes matched so that the average Lorentz force is negated. The particular field patterns for some different values of q are shown in Fig. 1.3.13. If the length of the filter is correctly matched to the beam momentum then a spin polarised beam passing though the filter will attain orbital angular momentum of $l' = l \pm q$, depending on the input polarisation $\pm s$ [56, 57]. The filter works for annular beams, so that it is more efficient to add or subtract q units of orbital angular momentum from a vortex beam, rather than create a vortex beam from a plane wave.

High brightness spin polarised electron microscopes are currently being developed [58]; application in the current generation of electron microscopes would involve non-spin polarised states so that the beam produced will be a superposition of modes with $s = -1, l' = l + q$ and $s = +1, l' = l - q$. On the other hand, the fact that the change in orbital angular momentum $\pm q$ is correlated with the input spin polarisation opens the possibility of using such filters to produce spin-polarised vortices or plane waves from unpolarised input vortices [56].

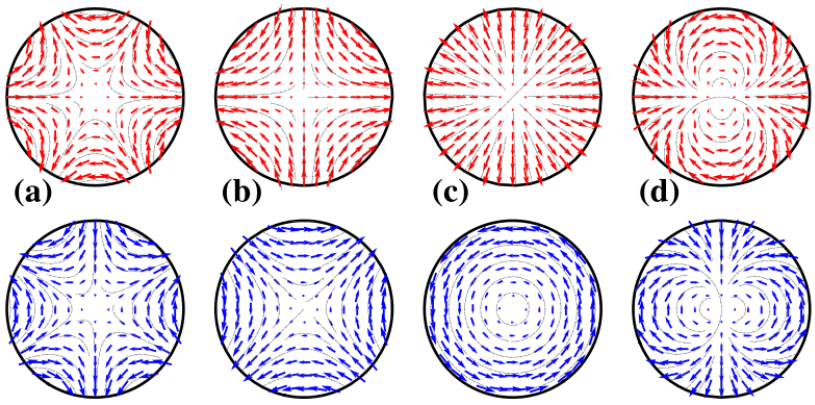

Figure 1.3.13: The spatial variation of the electric (upper, red) and magnetic field (lower, blue) vectors in a cross-section of a q-filter for some values of q. (a) - $q = -2$; (b) - $q = -2$; (c) - $q = 1$; (d) - $q = 2$. For a given q-filter the particular field pattern of the electric and magnetic field differs only in a rotation of $\frac{\pi}{2}$. Images from [56].

Diffraction Catastrophes

It has been shown that, under certain conditions in an electron microscope, the formation of caustics through diffraction catastrophes [59] leads to arrays of vortices - more specifically, vortex-antivortex pairs are formed in the presence of caustics [60]. Though this effect is highly unlikely to lead to an efficient method of producing pure electron vortex states, it allows for the possibility of creating topologically complex 3-dimensional phase structures, including loops and knots [61] in electron waves [60], in order to study the complex behaviour of the topological features, and how they behave under the influence of a periodic potential, such as in propagation through crystalline materials.

1.3.7 Vortex Propagation through Electron Optics

In order that useful analysis may be carried out using vortex beams in electron microscopy situations, it is necessary that the evolution of the vortex state as it passes through the various electron optical systems is well understood. This includes whether the state is preserved as it propagates, and the influences of the aberrations and other effects of the lenses and imaging systems.

The evolution of the vortex beam passing through the focal point was investigated in [25], and is shown in Fig. 1.3.14. The vortex state has a phase singularity through the beam axis, which has an indeterminate phase, so the beam intensity throughout the axis must be zero. As can be seen in the focal series of Fig. 1.3.14, the vortex beam produced using the holographic mask has a core null intensity that remains upon defocusing. As suggested above, the persistence of the dark core is indicative of a vortex state possessing orbital angular momentum, rather than simply an annular ring structure. The focal behaviour of the vortex appears to be Gaussian, with the radius of the vortex core increasing by a factor of approximately $\sqrt{2}$ over a Rayleigh range from the focal point [25], as expected for a Laguerre-Gaussian type beam, suggesting that the Gaussian beams and paraxial Gaussian optics used to describe the beam-lens systems to a first approximation [38]

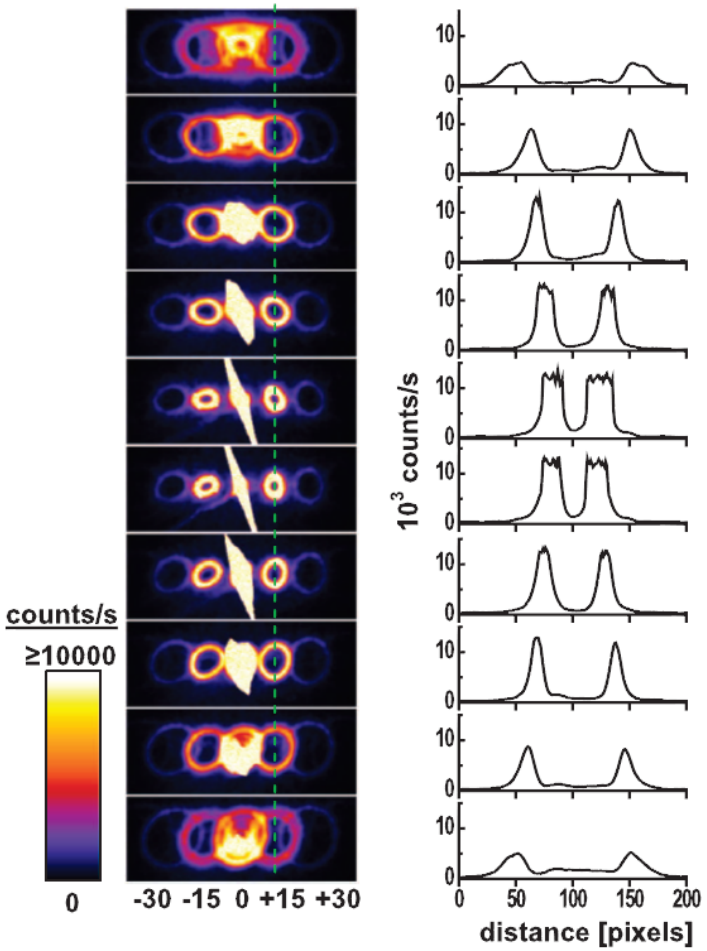

Figure 1.3.14: The evolution of the vortex beam passing through focus. The image of the left shows a focal series of the -1, 0 and 1 order beams of an $l = 15$ mask. The dotted green line shows the positions at which the line profiles were taken, shown in the image on the right. These line profiles show clearly that the centre of the beam contains a minimum, that is not washed out by defocus, which indicates a true vortex state. Image adapted from [25].

(i.e. without defects and aberrations) are also appropriate for the vortex beams.

The effect of spherical aberrations and partial spatial coherence on the vortex in the electron microscope has been determined both theoretically and experimentally [39, 40, 62]. Simulations of the resulting far field intensity profiles of a partially coherent electron beam diffracting through a forked mask in the aperture of a condenser lens with spherical aberrations have been performed [40, 62]. The effect of spherical aberrations is to increase the radius of the vortex, so that the intensity peak of the vortex ring occurs at a larger distance from the centre, and the peak itself is broadened [62]. This effect increases for larger mask apertures as expected, as more rays passing through the edges of the lens are admitted through the aperture [62].

As already discussed, the effect of incoherent illumination is to increase the intensity of the central dark core, and degrade the quality of the vortex state, resulting in a mixed, rather than pure, vortex [39, 62]. The effect of varying spatial coherence can be simulated by modelling the source as a Gaussian distribution, with the size of the source projected onto the aperture given by the standard deviation of the Gaussian distribution [40, 62]. When the radius of the projected source is over 10% of the aperture radius, the minimum of the vortex cannot be discerned [40], so that there is a trade-off between the narrow apertures that will reduce the effects of spherical aberrations, and the larger ones that reduce the effects of the finite source broadening. Simulations of the vortex state in the electron microscope incorporating spherical aberrations and partial spatial coherence show good agreement with experimental results, so that existing analytical techniques in TEM may be directly applied to the vortex beams [40].

1.4 Applications of Electron Vortex Beams

Several experimental applications have been suggested for the electron vortex, particularly in analytical TEM and STEM. These include obtaining magnetic and other chiral information from various samples with atomic resolution using EELS, and improvements in phase contrast microscopy. The experimental and theoretical progress towards such aims will be discussed, in particular the key aspects and considerations of magnetic imaging at nanometre to atomic scales. A significant issue affecting such a measurement is the contribution from atoms that are do not lie on the axis of the vortex. Further complicating matters is the fact that TEM and STEM samples, while necessarily thin, are typically on the order of 50nm thick, and propagation through crystalline structures significantly affects the vortex characteristics.

1.4.1 Electron Energy Loss Spectroscopy with Vortex Beams

The first demonstration of the forked holographic mask technique to generate electron vortices was accompanied by experimental results illustrating the possibility of using vortex beams to obtain magnetic information using EELS [24]. A dichroism effect was observed in a thin film (50nm) of magnetised iron, magnetised in the direction of the optic axis, due to positioning within the lens fields. The experiment involved a region of the film with a diameter of approximately 250nm. The incident electron beam was a plane beam, rather than a vortex; the beam transmitted through the sample is decomposed into vortex components by a forked mask placed at a small defocus from the back focal plane of the objective lens. This set up, and the resulting dichroism signal is shown in

Fig. 1.4.1. The defocus of the beam onto the mask allows a larger patch of coherent beam to diffract through the mask. Individually, the $l = 1$ and $l = -1$ beams are imaged on the detector by means of a selective aperture and a magnetic prism to separate the different energies from interaction with the sample. Comparing the energy loss spectra of the two $|l| = 1$ vortex components of the

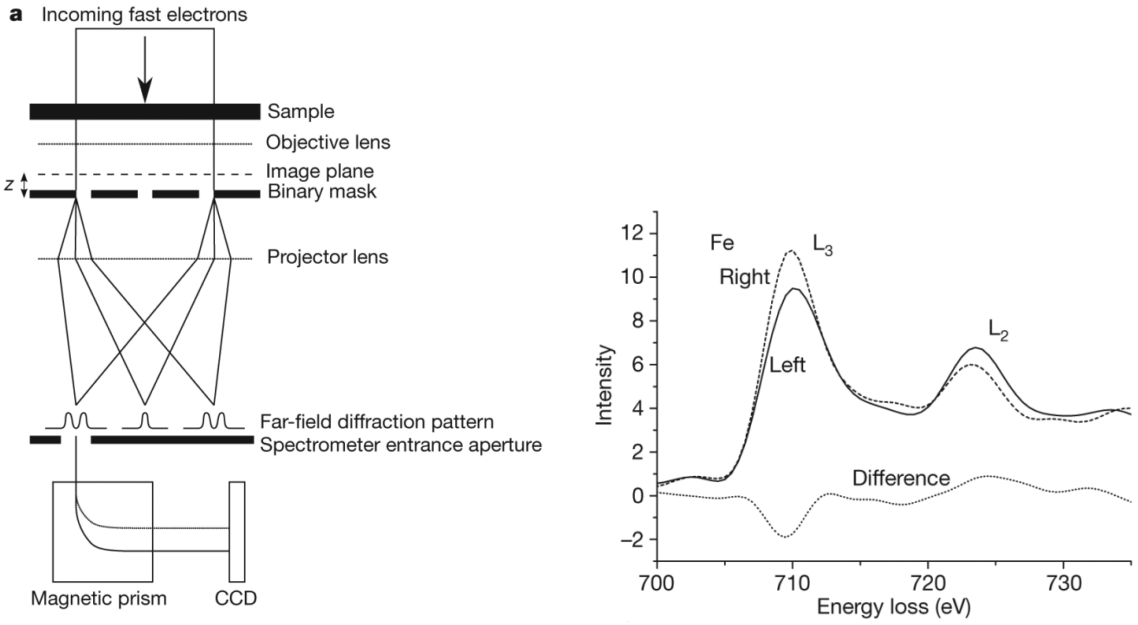

(a) (b)

Figure 1.4.1: The experimental arrangement and results of the dichroism experiment performed by Verbeeck *et al.* [24]. The experimental arrangement is shown in (a) The incident beam is a plane wave - after passing through the iron film sample the resulting beam is transmitted through a forked aperture in the objective lens, decomposing the post-interaction electrons into the vortex components. A second aperture selects a particular vortex component to be imaged, while the magnetic prism selects for electrons of particular energies to be detected, allowing a range of energies to be scanned, and the energy loss due to the interaction to be determined. Comparing the observed energy loss of the two different senses of rotation of vortex gives the dichroism signal of (b), where it can be seen that at different energies one or other of the two vortex components is absorbed preferentially. Images from [24].

transmitted electron beam shows a dichroism signal, in which one or other of the vortices is preferentially absorbed at particular energies. These energies correspond to the L_2 and L_3 edge transitions in iron [24], in which electrons in the iron are promoted from the 2p atomic states [63]. The vortex electron energy loss spectrum corresponds well to similar absorption spectra of circularly polarised x-rays, so that the magnetism of the sample is clearly indicated by the energy loss dichroism, as in x-ray magnetic circular dichroism (XMCD) experiments [64]. This experiment gave a proof-of-principle result that vortex beams may be used in magnetic dichroism experiments in the electron microscope.

In order to determine the mechanism and selection rules of the interactions involved in the experiment above, the interaction between an electron vortex and atomic matter was investigated [65–67] (see also Chapter 6). The principal contribution to the interaction was determined to be the Coulomb interaction between the atomic and vortex electrons, acting as a perturbation to the atomic electron state, and the selection rules for the interaction were found to take the same form

in the dipole approximation as those of the circularly polarised x-rays used in XMCD. Of note is the difference in selection rules between the optical vortex and the electron vortex - the mechanism of the interaction is very different in each case and as such the result that orbital angular momentum associated with the electron vortex may be directly transferred into the internal atomic motion is in contrast to the optical vortex case, in which only spin angular momentum may be transferred [14, 68–71] (see also Chapter 5).

Due to the extrinsic nature of the orbital angular momentum of the vortex state [16], a rigorous treatment taking into account the displacement of the atom from the vortex axis is necessary to interpret the results of vortex based EELS in terms of the change in orbital angular momentum of the incoming beam [67] (see also Section 6.3). This was not an issue in the experiment performed by Verbeeck *et al.* The magnetisation within the iron sample is along the optic axis, so that the orbital angular momentum of the vortex beams along the axis of magnetisation of the atom is the same as along the vortex axis[1]. Since these axes are parallel, the complications described in Chapter 6 regarding the extrinsic nature of the orbital angular momentum of the vortex beam are not apparent.

Since the demonstration of the possibility of the use of vortices for magnetic dichroism experiments there has been much discussion as to whether vortex based magnetic dichroism will soon be achievable in electron microscopes [67, 72–74]. Of particular interest is the use of vortices as atomic scale probes in STEM, the use of which will lead to the ability to map the magnetism (or other chiral activity) across the whole area of a sample with atomic resolution, potentially identifying the magnetic moment of single atoms or columns of atoms.

A major issue with such a goal is the size of the vortex relative to atomic scales. High resolution of 0.141 nm has been demonstrated using electron vortex beams in high angle annular dark field STEM [51], though the signal to noise ratio using vortex beams in this case was much worse than that of a non-vortex beam. In order to resolve magnetic information at atomic resolution is necessary to have probes that are able to address single atoms, so that high quality vortices of Ångstrom scale are necessary. The demonstration of vortex beams with Ångstrom diameter [39] is suggestive of the opportunities of producing vortex STEM probes with atomic resolution, however as discussed above source size effects significantly degrade the quality of the vortex. The smallest possible vortex beams are those consisting of a single ring (rather than several nodes) for which $|l| = 1$, with higher values of $k_\perp$, as determined by the size of the aperture with phase defect. The maximum resolution of a scanning vortex probe is given as $d \approx 2R_c + \Delta R$, where R_c is the radius of the peak intensity of the vortex beam, and ΔR is the FWHM of this peak. It has been suggested that for a vortex beam with typical scanning probe parameters - $\alpha_c = 30$ mrad and electron energy $E = 100$ keV - the aberration corrected resolution limit is $d \approx 1.14$ nm [72]. Increasing the electron energy to 300 keV, and $\alpha_c = 40$ mrad gives $d \approx 0.462$ nm. These values of d are an order of magnitude larger than similar non-vortex probes, and not low enough for atomic resolution, for

[1]The vortices measured in this experiment originate from the holographic mask, so that they are generated at an angle to the optic axis. In this particular set up this is not a problem, as the vortex components of the beam are separated *after* interaction with the sample - so that at the point of interaction, the axis of the iron magnetisation and the axis of the beam are the same, namely the optic axis of the microscope. If this experiment were to be performed with the mask before the sample, then the results would be different, as the change in axis leads to the breaking of rotational symmetry [16]. Is is therefore important to find a way to generate vortices aligned with the microscope axis, to avoid such issues

which an acceleration voltage of 2 MV is purportedly necessary [72]. Nevertheless, it may be possible to generate appropriately scaled vortices in the next generation of electron microscope with smaller source sizes and higher acceleration voltages.

The theoretical possibility of application of vortices to magnetic dichroism has been considered both on the 'medium' scale of 1-10 nm [74] and the atomic scale [67]. For both situations the spatial dependence of the atom-vortex interaction in which orbital angular momentum is exchanged has been considered in order to determine any observable dichroism due to magnetisation in the atom. In both the nanometre and atomic scales the interaction is found to be strongly dependent on the position of the atom relative to the axis of the vortex, due to previously indicated complications regarding the extrinsic nature of the orbital angular momentum of the vortex. It is found that when the atom is removed from the beam axis, there are several channels by which the interaction may proceed, involving various forms of orbital angular momentum exchange. This greatly complicates the interpretation of scattering results for an incident electron vortex beam.

For the medium, nanometre scale, simulations of a particular interaction channel using an incident vortex with a radius of 0.9 nm demonstrate that when the atom is on or near the beam axis, a clear difference is observed between the outgoing states of the $l = 1$ and $l = -1$ vortices. This difference is manifest in the spatial intensity of the scattered states. However, when the atom is displaced from the beam axis the effect of the dichroism is greatly reduced and the transmitted intensity profiles appear the same [74]. Additionally, when the vortex is incident on a homogeneous sample, contributions from the atoms all around the beam axis destroy the asymmetry observed in the intensity of the transmitted beams, and the dichroism is no longer apparent. Thus Schattschneider *et al.* conclude that this renders any dichroism unobservable on the nanometre scale, including nanoparticles larger than 1.5 nm [74].

The spatial dependence of the interaction between an atom and an atomic scale vortex does not present such an insurmountable problem for atomic resolution dichroism. The specifics of the inelastic interaction between an atom and an electron vortex are discussed in Chapter 6, but the key points are summarised as follows: the displacement of the atom from the beam axis leads to multiple channels by which orbital angular momentum may be exchanged between the beam and the atom, and each of these channels has a different strength and spatial dependence. The exchange of orbital angular momentum does not necessarily exhibit conservation of angular momentum about the beam axis, due to the extrinsic vortex angular momentum. However in examining the varying strengths of the different interaction channels it is found that the on-axis dipole interactions for which the orbital angular momentum is strictly conserved are the strongest, with the contributions from the other channels and higher multipoles an order of magnitude less. This leads us to suggest an experimental set up that could be used to perform STEM EELS of magnetic materials with atomic resolution, as detailed in Section 6.3.5. Using a confocal microscopy arrangement, to further reduce the off-axis contributions, an electron vortex is scattered through a magnetic sample. The resulting transmitted beam may then be passed through a vortex analyser in the form of a forked holographic mask or similar. This analyser allows the selection of a particular channel of interest, and an energy spectrum can be obtained through filtering though a magnetic prism. Using such an arrangement, the incident vortex probe may be scanned over the sample,

leading to an atomic resolution energy loss spectrum map that may be compared to the similar spectrum obtained using the vortex with opposite winding number. Further details regarding the experimental arrangement and expected observations are discussed in Section 6.3.5. It should be noted here that this experiment will be very demanding on the microscope specifications, requiring a highly coherent atomic scale beam in a scanning confocal arrangement in addition to the complications of energy filtering of the selected mode after the vortex analyser. Such an experiment will require development of the necessary technology. It is also worth noting that a post-sample vortex analyser could be used with the medium scale EELS experiment described above, to filter out the different channels and isolate the dichroic components of the transmitted beams. The spatial structure of the beam - which is significantly altered by the passage through the forked mask - is then not necessary to determine the relative strengths of the interaction with the two vortices. This experiment is slightly less demanding, since the vortex probe need not be atomic sized, however the issue with alignment and selection of the particular vortex modes for both scanning and spectrum collection remains.

Vortex EELS may also have potential in determining the magnetic response - susceptibility and permeability - of various materials, as a tool for characterisation of metamaterials [75]. The electrical response of a sample may be measured by examining surface plasmons using EELS [76, 77], and EELS with vortex beams would be a complementary technique, allowing both electric and magnetic responses to be measured in a single experiment. Simulations show that the magnetic signal obtained using a vortex beam is an order of magnitude smaller that typical EELS signals, which should still be measurable, and since the resonances occur at different energies the electric and magnetic information may be separated out [75]. Such a technique could be applied to study magnetic plasmon resonances of metallic nanostructures with high resolution.

Another method by which atomic resolution magnetic information might be achievable in the STEM involves the scattering of non-vortex probes through ultra-thin films, producing a phase gradient when the beam is transmitted through an atom with a non-zero magnetic moment [73]. The transmitted beam is then a mixed vortex state, which may be observed in the electron diffraction pattern by a shift and smearing of spots in the electron diffraction patterns; the direction and size of the shift is sensitive to spin polarisation of the atom. A proof-of principle experimental result has been obtained [73], allowing for the possibility of application of this method in the reconstruction of the single atom magnetic moments, subject to minimisation of drift, noise, aberrations and other factors that affect such a sensitive measurement.

1.4.2 Vortex Propagation through Materials

In order that experiments involving vortices be appropriately interpreted, it is necessary that the way the vortex propagates through crystalline structures is well understood. Any electron probe propagating through a crystal will experience strong elastic scattering from Coulomb interaction with the atomic nuclei, proportional to the thickness of the sample and tilt relative to the beam axis. Multislice simulations of the vortex state propagating through the crystal demonstrate the change in phase and amplitude of the beam as it passes through various thicknesses of material [78, 79]. It is found that the phase and amplitude of the resulting wave exiting the crystal depends not only on the thickness of the crystal, but also the location of the vortex axis relative to the atoms in the

crystal cell. The scattering potential of the atomic columns distorts the phase structure of the beam, and the beam is also channeled along the positive potential of the column [78], though the beam remains well localised [79]. The potential of the crystal nuclei perturbs the structure of the vortex, leading to tilts and shifts of the vortex axis [79].

The distortion of the phase front causes the orbital angular momentum of the beam to cease to be well defined, since the orbital angular momentum operator does not in general commute with the perturbing crystal potential, leading to local values of angular momentum that may be significantly different from that of the incident vortex [78, 79]. This leads to the generation of vortex loops within the crystal, originating along the atomic columns. These are manifest as vortex-anti-vortex pairs in the x-y plane as the vortex forming the loop propagates in the z-direction and then turns back on itself [79]. In addition to the loops formed in the propagating wave, it is found that higher order vortices with $l > 1$ may be decomposed into lower order vortices in propagation, with the particular splitting determined by the value of l and the symmetry of the scattering potential [79]. This is related to the extrinsic nature of the orbital angular momentum as discussed above, and indicates that atoms at different depths within the sample will be subject to modes with different orbital angular momentum [78], similar to the cases discussed for atoms that are far from the beam axis. For relatively thick samples then, particular care must be taken in analysis requiring direct observation of phase and intensity contrast; however filtering the separated scattered vortex states will go some way to ameliorating the phase complications.

1.5 Dynamics and Fields

The freely propagating vortex as introduced in Section 1.2.1 is the simplest example of a vortex state. In general, the vortex will move under the influence of external fields, in the presence of other vortices, or both [19–21, 80, 81]. The specific case of an electron vortex with magnetic moment μ in a magnetic field was mentioned above; here the effect of such a field, or other types of potential, on vortices with a general form is remarked upon.

Understanding the interaction and dynamics of the electron vortex in external fields is particularly important in electron microscopy applications, where various fields are required to focus the beam. Any shifts of the beam motion or distortion of the intensity due to interaction of the field must be accounted for in the interpretation of data collected using the vortex beam. The effects of the electron vortex in external fields typical of magnetic lenses has been discussed by several authors [82–84] and angular momentum dependant rotations due to the fields have been observed in the electron microscope [85].

In addition, the electron vortex is found to possess intrinsic electric and magnetic fields, due to the helical trajectory of the charge current density [86]. The orbital angular momentum of the beam leads to the presence of a component of the magnetic field in the z direction, as well as the azimuthal component and the radial electric field expected for a linearly propagating charge. Full details of the derivation and characteristics of the field of a Bessel-type electron vortex are given in Chapter 3.

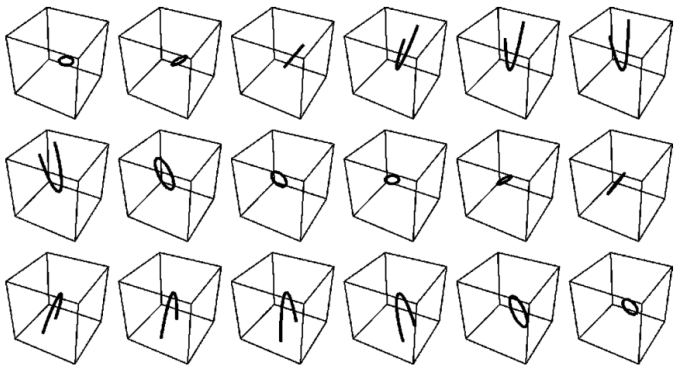

Figure 1.5.1: The dynamics of a ring shaped vortex line in a spherically symmetric harmonic trap. The vortex rotates at the trap frequency ω, and expands and contracts with a frequency of 2ω. Image from [19].

1.5.1 Motion and Collisions

The motion of charged vortices in a uniform magnetic field has been considered in a general case by Bialynicki-Birula *et al.* [19]. The rotation of the vortex line - described above as the classical electron trajectory in magnetic field - is observed as a precession of the vortex line about an axis parallel to the direction of the field. Vortices in other types of external fields have also been studied - in particular the harmonic and rotating harmonic traps [19–21] that are important for the confinement of Bose-Einstein condensates in which quantised vortices can be sustained [87]. The dynamics of vortices in such environments depend on the particular configurations of the vortices under study, for example it is found that a vortex ring in a spherically symmetric harmonic trap rotates and expands, as shown in Fig. 1.5.1. The behaviour of vortices in a rotating harmonic oscillator depends strongly on the configuration of the trap and the vortices. Examples given in [21] concern two parallel vortices, with co- and counter-circulation. In the first case, the vortex lines remain parallel and linear as they rotate with the trap, whereas the behaviour of the counter-circulating vortices is much more complicated - leading to distortion of the vortex lines [21]. The treatment of [19, 21] is quite general, concerning solutions to the Schrödinger equation that contain one or more vortex lines, rather than individual twisted particle states. For a Bose-Einstein condensate this description is appropriate, although interactions between the constituent particles modify this single wavefunction picture. Studying the behaviour of vortices in wavefields of particles with interactions - both long-range harmonic and short-range scattering interactions - shows that interatomic forces do not significantly alter the qualitative behaviour, displaying the universal features of vortex physics [20].

The evolution of wavefields containing several vortices may be very complex, even if there are otherwise no external potentials acting [19, 21, 80, 81]. Annihilation of two counter-circulating vortices may occur or, indeed, creation of a vortex and anti-vortex pair, while vortex lines taking the form of a ring may be spontaneously created or annihilated [19, 80]. Two vortices approaching each other will distort, and intersect - at the point of intersection the vortex lines 'swap' [19, 80, 81], as shown in Fig. 1.5.2, a process termed 'reconnection' of vortex lines by Berry *et al.* . For two vortices

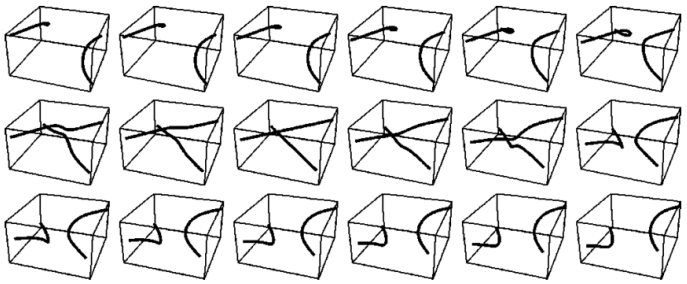

Figure 1.5.2: Dynamics two vortex lines crossing or 'reconnecting'. Two curved vortices approach each other; in the first panel of the second row one vortex is above the other, without intersecting. After the point of intersection (between fifth and sixth panels, second row) it can be seen that the separated vortices do not follow the same trajectories as before the collision. The two vortices swap sides, in a vortex reconnection. Image from [19].

existing in the same plane, the reconnection is final, and the two vortices propagate away from the collision having been apparently reflected at an angle of $\frac{\pi}{2}$. The more general case of non-coplanar vortices shows a double reconnection event, so that the net result is that after the collision, the vortices continue on their original trajectory [81]. Such reconnection events also occur in the collision of three vortex lines, in which reconnection leads to the creation of a ring vortex that is subsequently spontaneously annihilated; as well as collisions between a line and a ring, and two rings [21]. The result in each case is the apparently unperturbed motion of each of the vortices, except in the vicinity of the collision, where the multiple reconnection events make the behaviour very complicated indeed [81]. Such dynamics might have implications for the behaviour of the superpositions of vortices in fields, or motion of the electron vortex through a crystal potential.

Collisions between vortices and plane waves may also be considered [88]. In the general case, for scalar beams of particles or photons head on collision events between vortex beam and plane wave can be shown to result in scattered states consisting of a vortex and a plane wave, or two vortices [88]. The linear and angular momentum of the two scattered states is entangled, though since the orbital angular momentum of the vortex is an extrinsic quantity the total orbital angular momentum conservation of the two final states is non-trivial, and the resulting angular momentum depend strongly on the scattering angles involved. Such scattering events could potentially be useful in generating various species of entangled vortex pairs, including electron-electron and electron-photon entangled states. In addition it may be possible to generate vortex proton states by colliding a vortex electron beam with high energy protons, opening up the possibility of exploring vortex states in high energy particle physics [88].

1.5.2 Propagation through External Fields

Solving the Schrödinger equation in the presence of a magnetic field directed along z gives two possible results, depending on the particular field - a single line of flux along z gives a Bessel function [84], while a uniform field leads to a Laguerre-Gaussian solution [82–84]. The Laguerre-Gaussian solutions in the uniform field are of particular interest as they resemble the electron vortices propagating in microscope fields. The particular characteristics of the

Laguerre-Gaussian beam, such as the waist and Rayleigh range, depend on the strength of the field, such that [83, 84].

$$w_0 = w_B = 2\sqrt{\frac{\hbar}{|e\mathbf{B}|}}; \qquad z_R = z_B = \frac{2\sqrt{Em}}{|e\mathbf{B}|}. \tag{1.14}$$

In both field arrangements, the vector potential of the field $\mathbf{A}$ circulates about the z axis, having the form of a vortex. Depending on the direction of $\mathbf{B}$, the circulation of the vector potential may be in the same direction as, or counter to the direction of circulation of the vortex, which may either increase or diminish the orbital angular momentum relative to the freely propagating state. The canonical angular momentum of the Laguerre-Gaussian solutions in the presence of fields becomes [84]

$$\langle \mathcal{L}_z \rangle = \langle \mathbf{r} \times (\mathbf{p} - e\mathbf{A}) \rangle = \hbar \left(l \pm 2p \pm |l| \pm 1 \right), \tag{1.15}$$

where the $\pm$ relates to the direction of the magnetic field. Due to this, electron vortices of opposite topological charge l are affected quite differently by the presence of the field, and $\langle \mathcal{L}_z \rangle_{+l} \neq \langle \mathcal{L}_z \rangle_{-l}$.

The energy of the solutions in the magnetic field form Landau levels, determined by [83, 84]

$$E = \frac{\hbar^2 k_z^2}{2m} + \hbar\omega_L(2p + |l| + 1) - l\hbar\omega_L \tag{1.16a}$$

$$= \frac{\hbar^2 k_z^2}{2m} - \hbar\omega_L \langle \mathcal{L}_z \rangle \tag{1.16b}$$

with ω_L the Larmor frequency $\omega_L = \frac{|e|B}{2m}$. The second and third terms of Eq. (1.16a) are respectively the contributions from the Gouy phase and the Zeeman interaction between the electron magnetic moment and the external field. This effect can be combined into the effect of a Zeeman interaction between the field and the total angular momentum $\langle \mathcal{L}_z \rangle$, as shown in Eq. (1.16a). The Zeeman and Gouy terms lead to phase shifts $\Delta\theta$ acquired as the beam travels in the z direction, in addition to the usual propagation phase $k_z z$:

$$\Delta\theta = \hbar\omega_L \left((2p + |l| + 1) - l \right) z. \tag{1.17}$$

This phase shift results in rotation of the beam as it propagates through the field [82–84]. For the cylindrically symmetric vortex modes, such rotation is not observable; however the rotation is observable for superpositions of vortices, which in general have discrete rotational symmetry. There are two classes of vortex superposition - superpositions of vortices having opposing topological charge for which the net topological charge is zero, i.e. $l_1 + l_2 = 0$; and the more general case involving vortices having differing topological charges with $l_1 + l_2 \neq 0$.

The resulting intensity patterns of the superpositions of the $\pm l$ modes have a 'petal'-like structure, with $2|l|$ nodes forming a ring. As the beam propagates through the field, the two different $\pm l$ modes are affected differently by the field, leading to an l-dependent rotation $\phi_l = \frac{\Delta\theta}{z}$. The combined rotation of the two modes lead to a phase difference that varies with propagation [83, 84],

$$\Delta\phi = \pm\sqrt{\frac{m}{2E}}\omega_L z, \tag{1.18}$$

where the $\pm$ relates to the direction of the magnetic field. This causes the petal interference pattern to rotate as the mode propagates, with a longitudinal dependence characterised by the Larmor frequency. The situation for the superpositions with net topological charge displays different behavior depending on whether the resulting angular momentum is aligned or anti-aligned with the magnetic field. When the field is aligned the resulting rotation of the interference pattern is double that of Eq. (1.18), and characterised by the cyclotron frequency $\omega_c = 2\omega_L$, whereas for the anti-aligned case the combined effect of the Zeeman and Gouy phase contributions leads to no net rotation [84]. The three different cases of rotation - with characteristic frequencies ω_c, ω_L and zero - are experimentally observable [85].

In the lens system of the electron microscope, the effects of the Zeeman and Gouy phase shifts may be almost completely decoupled and independently adjusted [85]. As mentioned above, the Gouy phase is known as a phase shift when the Gaussian beam passes through focus, and has the strongest effect in the second condenser lens when the beam is sharply focused with a wide convergence angle and the Rayleigh range is small. This allows the effect of the Gouy phase to be observed by altering the defocus. The condenser lens does not produce significant magnification, so that the magnetic field is relatively weak compared to the high magnification imaging lens. Thus, while the Zeeman phase shift is not eliminated in the condenser lens, its effect is considerably smaller than within the imaging system, and is less significant than the Gouy phase. Similarly, the imaging system produces a strong Zeeman interaction due to the high field, but since the beam is projected at large magnification onto the image plane, the Gouy phase shift is negligible.

Superpositions of the different vortex modes may be created using specifically designed holographic masks as described above. In [85] the behaviour of the superposition of the $l = \pm 3$ modes was observed to show the expected rotation due to the Zeeman interaction (the Gouy phase does not contribute to the rotation in this case as it is equal for both the vortices). The non-zero orbital angular momentum superpositions were also observed using an aperture to block off half the mask - of the resulting three diffracted beams, one had net angular momentum of 3, one -3 and the other zero. Thus, the three different rotations with characteristic frequencies ω_c, ω_L and zero described above were confirmed [85].

If the Laguerre-Gaussian mode is not an eigenstate of the field, but instead has a width $w_0 \neq w_B$ then in addition to the rotation of the beam, the width of the beam may also be affected as it propagates through the field [83]. The waist of the beam oscillates with characteristic frequency w_c between w_0 and the field-characteristic width w_B. This oscillation is due to the interplay of diffractive effects acting to expand the beam, which are dominant at the small widths with $w < w_B$, and the constraining of the beam by the magnetic field, which is the dominant effect at $w > w_B$ [83]. For more complicated superpositions of eigenfunctions of the field, and for other modes that are not eigenmodes the rotation of the beam and such width oscillations will take more complicated forms, characterised by frequencies between $0 < \omega < w_c$ and possible distortion of the shape of the beam. [84].

2

Vortex Solutions

A THEORETICAL description of the behavior of the electron vortex requires a suitable wavefunction. Similarly, in order to make relevant comparisons between the electron and optical vortex, it is necessary to compare vortices of similar spatial distribution. The Bessel beam vortex is chosen as the particular distribution to compare the optical and electron vortices as it has the simplest spatial distribution suitable for carrying orbital angular momentum, so that the relevant behaviour will be due solely to the vortex. The electron and optical vortex solutions demonstrated here will be used throughout the rest of this thesis to compare the interaction between the two kinds of vortices and atomic matter, and determine the mechanical and electromagnetic properties of the electron vortex.

In this chapter the principal features of a vortex beam and some particular classes of vortex beams are discussed. Section 2.1 presents some general properties of vortex beams, and the necessary conditions for vorticity. The Bessel beam is derived as a suitable optical and electron vortex mode function in Section 2.2, and the specific properties of Bessel beams are discussed, with reference to the constraints of the paraxial approximation. The Laguerre-Gaussian beam is also a suitable mode function for paraxial electron and optical vortices, as shown in Section 2.3. The electron and optical solutions shown here, and applied throughout the rest of this thesis, are given within the paraxial approximation and, for the case of the electron vortex, the non-relativistic limit. These approximations are discussed in Section 2.4. At several points throughout this thesis, it will be useful to demonstrate results using a 'typical' electron vortex beam based on experimental parameters - a normalised wavefunction describing such a beam is defined in Section 2.5

2.1 Vorticity

Optical vortices were first described by Nye and Berry [29] in light reflected from a rough surface. Interference causes phase structure within the resulting wave that is topologically different to the incident plane wave. These phase structures were characterised as edge, screw, or mixed-dislocations, in analogy with crystal defects. The vortices described here in optical and electron waves are of a screw type - in which the phase front of the wave describes a helix about the axis of propagation [29] such that the phase is dependent on the angular position about the axis. The topological charge l quantises this winding such that there are l twists about the beams axis, or equivalently a phase change of $2\pi l$ during a full rotation about the axis, as shown in Fig. 2.1.1. The phase factor of $e^{il\phi}$ that gives rise to this helical phase structure is a characteristic feature of orbital angular momentum. The vortex beam propagating in the z direction then has the general form

$$\psi_l(\mathbf{r},t) = u(\rho,z)e^{il\phi}e^{ik_z z}e^{-i\omega t}, \tag{2.1}$$

where $\psi(\mathbf{r},t)$ may stand for the electron wavefunction in the case of electron vortices, or for the optical vortex the electric field mode function such that $\mathbf{E}(\mathbf{r},t) = \psi\hat{\boldsymbol{\varepsilon}}$ for some wave polarisation vector $\hat{\boldsymbol{\varepsilon}}$.

The helical phase structure leads to the phase at the core of the beam being indeterminate - since it is connected to all possible phases of the wave. This central phase singularity is not physically viable, and is compensated by the intensity of the wavefunction being zero at the location of the singularity - throughout the centre of the vortex. This has led to the nickname of 'doughnut' beams for a particular class of vortex beam - the Laguerre-Gaussian vortices with radial index $p = 0$, being a bright ring surrounding a central, dark core.

A zero-intensity at the centre of the beam is not sufficient to describe a vortex - there must be some topological difference between an area of the beam containing the vortex, and an area that does not [29]. For the present purposes, the topology of the vortex describes the connectedness of the phasefronts. The phasefront of the vortex is topologically distinct from that of a plane wave, as one cannot be transformed into the other through continuous deformations. Similarly, the $l = 1$ phasefront cannot be deformed into the $l = 2$ or any other l phasefront, so that the winding number l may also be termed the topological charge, characterising the 'strength' of the vortex. The phasefront of any vortex is characterised by $e^{il\phi}$, leading to a phase singularity along a line through the origin. A closed loop integration of the normalised probability current density $\mathbf{j}(\mathbf{r})$ along a path C encircling this line gives a quantised value [19]

$$\Gamma = \oint_C \mathbf{j}(\mathbf{r})\cdot d\mathbf{s} = \frac{2\pi\hbar}{m}l, \tag{2.2}$$

where m is the mass of the particle. For the vortex beam given in the form Eq. (2.1) we have the normalised probability current density

$$\mathbf{j}(\mathbf{r}) = \frac{i\hbar}{2m}\frac{\psi_l^*\nabla\psi_l - \psi_l\nabla\psi_l^*}{|\psi_l|^2} = -\frac{\hbar}{m}\left(\frac{l}{\rho}\hat{\boldsymbol{\phi}} + k_z\hat{\mathbf{z}}\right). \tag{2.3}$$

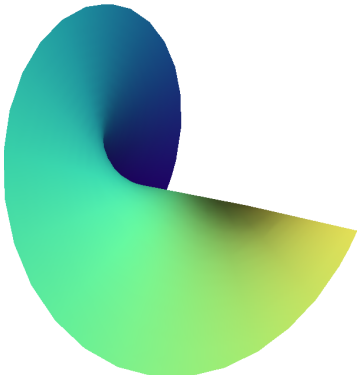

(a) Spiral phase front for $l = 1$

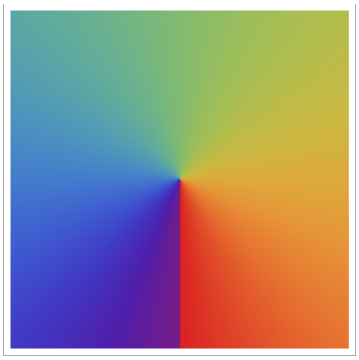

(b) Phase change in the plane for $l = 1$

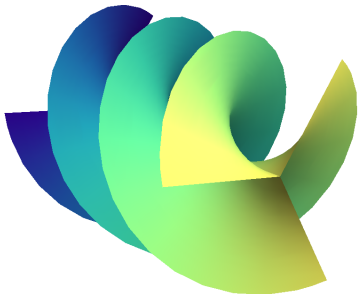

(c) Spiral phase front for $l = 3$

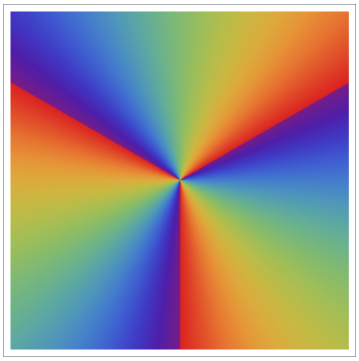

(d) Phase change in the plane for $l = 3$

Figure 2.1.1: The phase character of $l = 1$ and $l = 3$ vortex beams. (a) shows the phasefront of an $l = 1$ vortex - the phasefront wraps around the axis once. The phase change on rotation about the z axis is 2π, leading to a phase jump, as shown in the plane in (b). For the $l = 3$ vortex there are three surfaces of constant phase, each wrapping once around the axis as shown in (c). This leads to three phase discontinuities, as shown in (d).

Integrating this about a loop enclosing the z axis gives $-\frac{2\pi\hbar}{m}l$, while any other closed path gives zero, showing the topological distinction between a region of space containing the vortex and one that does not. Thus, on traversing the z-axis an additional phase of $2\pi l$ is acquired.

2.2 Bessel Function Vortex Solutions

The relevant equations of motion for electrons and photon in free space or linear media are the Schrödinger and vector Helmholtz equations respectively. Suitable vortex solutions will be derived for optical and electron vortices, and their properties discussed. The Schrödinger and Helmholtz equations have the same functional forms, so that the electron vortex wavefunctions will be found to have the same spatial dependence as the components of the electric field vector of the optical vortex. Suitable vortex solutions are described below in the paraxial approximation and, for the electron vortex, the non-relativistic limit.

The Bessel function is a solution to both the full Schrödinger and Helmholtz equations, and their paraxial forms. The Bessel beam will be derived as a solution to the full equation, with the specific requirements for the paraxial and non-paraxial solutions discussed below in Section 2.4.

2.2.1 Non-Relativistic Electron Vortex Solutions

The Schrödinger equation for a free electron of energy $\mathcal{E}$ reads

$$i\hbar\partial t\psi(\mathbf{r},t) = \mathcal{E}\psi(\mathbf{r},t) = -\frac{\hbar^2}{2m_e}\nabla^2\psi(\mathbf{r},t). \tag{2.4}$$

We look for freely propagating solutions having the phase factor $e^{il\phi}$, as associated with the vortex. It is natural to describe beam-like solutions in a cylindrical coordinate system, choosing propagation along the z-axis, such that the solutions will have the form

$$\tilde{\psi_l}(\mathbf{r},t) = N_l u(\rho,z)e^{il\phi}e^{ik_z z}e^{-i\omega t}, \tag{2.5}$$

with N_l a normalisation factor, and frequency $\omega = \frac{\mathcal{E}}{\hbar}$. The simplest solution exhibiting vortex structure will have $u(\rho,z) = u(\rho)$; applying Eq. (2.4) gives

$$\mathcal{E}u(\rho)e^{il\phi}e^{ik_z z}e^{-i\omega t} = -\frac{\hbar^2}{2m_e}\left(\frac{1}{\rho}\partial_\rho\left(\rho\partial_\rho\right) + \frac{1}{\rho^2}\partial_\phi^2 + \partial_z^2\right)u(\rho)e^{il\phi}e^{ik_z z}e^{-i\omega t} \tag{2.6}$$

$$= -\frac{\hbar^2}{2m_e}\left(u''(\rho) + \frac{1}{\rho}u'(\rho) - \frac{l^2}{\rho^2}u(\rho) - k_z^2 u(\rho)\right)e^{il\phi}e^{ik_z z}e^{-i\omega t}, \tag{2.7}$$

which reduces to the second order differential equation

$$u''(\rho) + \frac{1}{\rho}u''(\rho) + k^2 u(\rho) - \frac{l^2}{\rho^2}u(\rho) - k_z^2 u(\rho) = 0, \tag{2.8}$$

where the relationship $k^2 = \frac{2m_e\mathcal{E}}{\hbar^2}$ has been used. Additionally, the relationship between the longitudinal and transverse momenta of the particle is $k^2 = k_\perp^2 + k_z^2$, so that

$$u''(\rho) + \frac{1}{\rho}u''(\rho) + k_\perp^2 u(\rho) - \frac{l^2}{\rho^2}u(\rho) = 0. \tag{2.9}$$

This has the form of the differential equation

$$y''(x) + \frac{1-2a}{x}y'(x) + \left(\left(bcx^{c-1}\right)^2 + \frac{a^2 - p^2c^2}{x^2}\right)y(x) = 0, \tag{2.10}$$

with

$$a = 0, \qquad b = k_\perp, \qquad c = 0; \tag{2.11}$$

i.e. Bessel's differential equation. The solutions to Eq. (2.10) are of the form $y = x^a Z_p(bx^c)$ [89], giving

$$u(\rho) = Z_l(k_\perp \rho), \tag{2.12}$$

where $Z_l(k_\perp\rho)$ is a generic Bessel function of order l - either of the first kind $J_l(k_\perp\rho)$, or second kind $Y_l(k_\perp\rho)$, or a linear combination of the two. The Bessel functions of the second kind have a singularity at the origin and are therefore not suitable solutions for a physical beam wavefunction. The Bessel functions of the first kind, with the exception of $J_0(x)$, have a magnitude of zero at the origin, and so meet the criteria for carrying orbital angular momentum as described above. The full wavefunction of the Bessel-type electron vortex is then

$$\psi_l^{\mathrm{B}}(\mathbf{r}, t) = N_l J_l(k_\perp\rho)e^{il\phi}e^{ik_z z}e^{-i\omega t} \tag{2.13}$$

up to a normalisation factor. Normalisation of the electron vortex Bessel function is described in Section 2.5.

2.2.2 Optical Vortex Solutions

The full vector Helmholtz equation for the electric field in free space has the form

$$\nabla^2\mathbf{E}(\mathbf{r}, t) + k^2\mathbf{E}(\mathbf{r}, t) = 0. \tag{2.14}$$

For an optical vortex, the solutions $\mathbf{E}(\mathbf{r}, t)$ represent the electric field vector for a polarised electromagnetic wave. Choosing a Cartesian coordinate system, with transverse polarisation unit vector $\hat{\boldsymbol{\varepsilon}}$ and propagation along the z-axis, the vortex solutions take the form:

$$\tilde{\mathbf{E}}_l(\mathbf{r}, t) = u(x, y, z)e^{il\arctan(y,x)}e^{ik_z z}e^{-i\omega t}\hat{\boldsymbol{\varepsilon}}. \tag{2.15}$$

where we allow the polarisation vector to have the general form $\hat{\boldsymbol{\varepsilon}} = \alpha\hat{\mathbf{x}} + \beta\hat{\mathbf{y}}$. Again, it is possible to restrict the spatial mode function $u(x, y, z)$ to be a function of x and y only. Applying the

Helmholtz equation to the solution with mode function $u(x, y)$ gives

$$\nabla^2 \tilde{E}_x(\mathbf{r}, t) + k^2 \tilde{E}_x(\mathbf{r}, t) = 0; \tag{2.16}$$

$$\nabla^2 \tilde{E}_y(\mathbf{r}, t) + k^2 \tilde{E}_y(\mathbf{r}, t) = 0, \tag{2.17}$$

each describing a scalar Helmholtz equation. We are looking for cylindrically symmetric solutions such that $\tilde{E}_x(\mathbf{r}, t) = \tilde{E}_y(\mathbf{r}, t)$, and $|\alpha| = |\beta|$, allowing for the possibility of circular polarisation. From here it is more convenient to switch to cylindrical coordinates. The mode function is a function of ρ only, as the vortex structure requires ϕ dependence only in the phase factor $e^{il\phi}$. This gives

$$k^2 u(\rho) e^{il\phi} e^{ik_z z} e^{-i\omega t} = -\left(\frac{1}{\rho}\partial_\rho\left(\rho\partial_\rho\right) + \frac{1}{\rho^2}\partial_\phi^2 + \partial_z^2\right) u(\rho) e^{il\phi} e^{ik_z z} e^{-i\omega t} \tag{2.18}$$

$$= -\left(u''(\rho) + \frac{1}{\rho}u'(\rho) - \frac{l^2}{\rho^2}u(\rho) - k_z^2 u(\rho)\right) e^{il\phi} e^{ik_z z} e^{-i\omega t}, \tag{2.19}$$

which may be written in the same form as Eq. (2.8) above; thus the solutions take the same form as that of Eq. (2.12) to give the Bessel solutions:

$$\mathbf{E}_l^{\mathrm{B}}(\mathbf{r}, t) = E_0 J_l(k_\perp \rho) e^{il\phi} e^{ik_z z} e^{-i\omega t} \hat{\boldsymbol{\varepsilon}}, \tag{2.20}$$

where E_0 is the field amplitude. Since the orbital angular momentum of the optical vortex is quantised as $l\hbar$ per photon, it is sensible to quantise the optical field itself. With $\hat{a}^\dagger_{\mathbf{k},l}$ and $\hat{a}_{\mathbf{k},l}$ respectively the creation and annihilation operators for a Bessel photon of momentum $\mathbf{k}$, we may write

$$\hat{\mathbf{E}}_l^{\mathrm{B}} = \hat{\boldsymbol{\varepsilon}} E_0 J_l(k_\perp \rho)\left(e^{il\phi} e^{ik_z z} e^{-i\omega t} \hat{a}_{\mathbf{k},l} + e^{-il\phi} e^{-ik_z z} e^{i\omega t} \hat{a}^\dagger_{\mathbf{k},l}\right). \tag{2.21}$$

It will be useful to have the optical Bessel vortex in the form of a vector potential. The vector potential is found using

$$\mathbf{E}_l^{\mathrm{B}}(\mathbf{r}) = -\nabla\Phi(\mathbf{r}) - \partial_t \mathbf{A}_l^{\mathrm{B}}(\mathbf{r}), \tag{2.22}$$

as the scalar potential is zero for an optical field with no charges. Thus, the vector potential for the optical vortex can be written as

$$\mathbf{A}_l^{\mathrm{B}}(\mathbf{r}) = \frac{iE_0}{\omega} J_l(k_\perp \rho) e^{il\phi} e^{ik_z z} e^{-i\omega t}. \tag{2.23}$$

This vector potential field may also be quantised, so that we may now write

$$\hat{\mathbf{A}}_l^{\mathrm{B}}(\mathbf{r}) = \hat{\boldsymbol{\varepsilon}} \frac{iE_0}{\omega} J_l(k_\perp \rho)\left(e^{il\phi} e^{ik_z z} e^{-i\omega t} \hat{a}_{\mathbf{k},l} + e^{-il\phi} e^{-ik_z z} e^{i\omega t} \hat{a}^\dagger_{\mathbf{k},l}\right). \tag{2.24}$$

2.2.3 General Properties of Bessel Beams

Bessel beams have been known in optics since 1987; the zero order beam that carries no orbital angular momentum was first observed [90], and the higher order beams with angular momentum followed shortly after [91]. Since the spatial distribution does not change with propagation, such beams exhibit non-diffractive properties - there is no radial spread of the beam as it propagates in

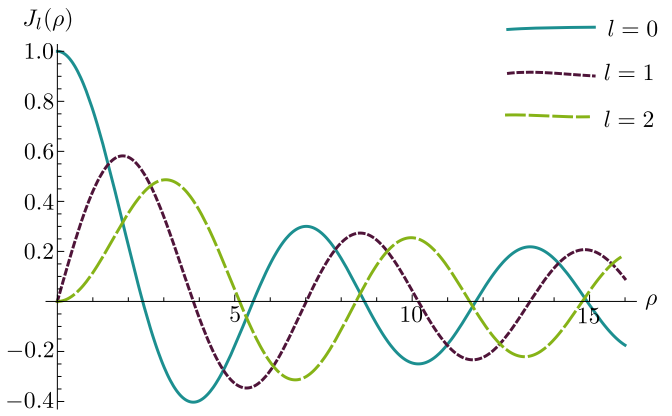

(a)

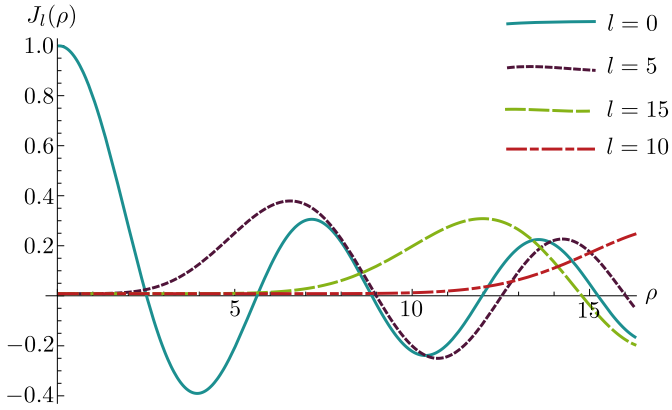

(b)

Figure 2.2.1: The behaviour of the first few Bessel functions. The Bessel function of the first kind $J_l(\rho)$ oscillates about zero with a decreasing amplitude. Bessel functions with $l = 0, 1, 2$ are shown in (a), and $l = 1, 5, 10, 15$ are shown in (b). The $l = 0$ Bessel function has a maximum at $\rho = 0$, and so is unsuitable for carrying orbital angular momentum. For $l \neq 0$, the Bessel function has a node at $\rho = 0$, with the maxima of successive $J_l(\rho)$ decreasing in magnitude with l and occurring at larger values of ρ.

the z-direction. The sense in which Bessel beams are non-diffracting is that the central maximum or minimum persists with very little spreading [91].

The Bessel functions of the first kind are a class of oscillatory functions denoted by $J_l(x)$, where the order l may take any value. Since we are interested in physical vortex solutions with well defined quantised orbital angular momentum, we concentrate on functions with integer l, as the Bessel function diverges at $x = 0$ for non-integer l and so does not satisfy vortex criteria. The order of the beam is identified with the angular momentum within the beam, as is made apparent in Chapter 4. The behaviour of the first few Bessel functions are shown in Fig. 2.2.1. Unlike the higher orders, the zeroth Bessel function does not meet the criteria for carrying orbital angular momentum, due to a maximum at the origin, $J_0(0) = 1$. The points at which are the magnitude of the function is zero are denoted the zeros of the Bessel function, so that $\alpha_{l,n}$ is the nth zero of the Bessel function, with $J_l(\alpha_{l,n}) = 0$. The oscillations about zero decrease in amplitude with x, so that $J_l(\infty) = 0$; however the integral between successive zeroes - or the area under each node - has the same value.

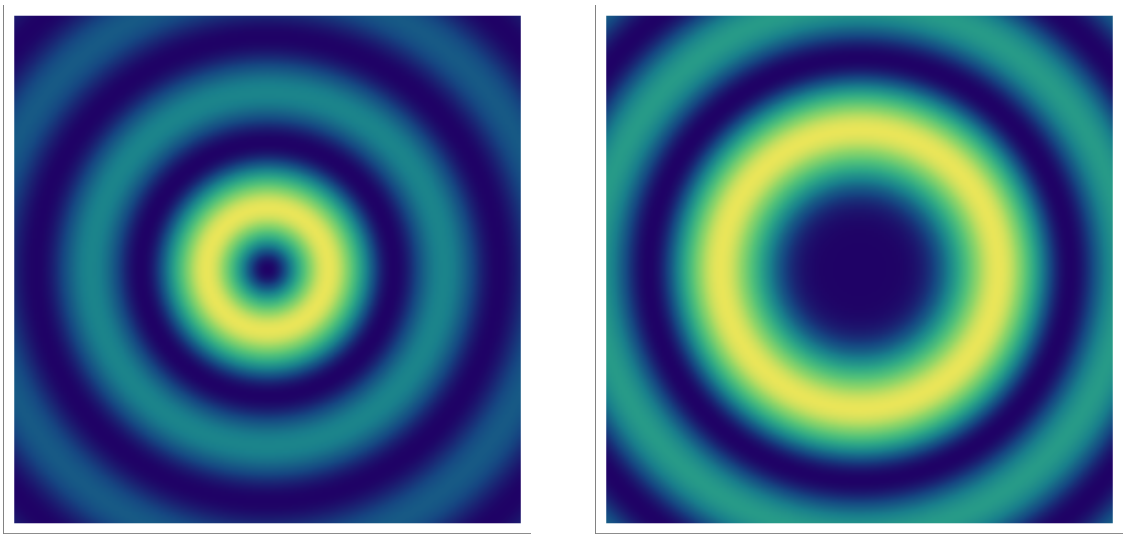

(a) $l = 1$ (b) $l = 3$

Figure 2.2.2: Plots of the intensity of a Bessel beam with (a) $l = 1$ and (b) $l = 3$. Intensity is given by $|\psi_l^{\mathrm{B}}(\mathbf{r})|^2$ for the electron wavefunction, or $|\mathbf{E}_l^{\mathrm{B}}(\mathbf{r})|^2$ for the optical Bessel vortex. For the electron Bessel beam with $k_\perp = 2.3 \times 10^{10}\,\mathrm{m}^{-1}$, as discussed in Section 2.5, the above plots have a scale of 0.66 nm to each side. The Bessel modes having $l < 0$ will have the same intensity distributions as shown above, however the phase (not shown) will have the opposite sign.

For a beam with intensity proportional to $J_l^2(x)$, the successive maxima and minima of the Bessel functions lead to a series of rings about the origin, with each ring carrying the same power, or current in the case of electrons [91]. This structure is depicted in Fig. 2.2.2. As can be seen, the magnitude of successive rings decreases, such that most of the power of such a beam will be concentrated in the first few inner rings about $\rho = 0$. However, the infinite number of rings within a Bessel function implies infinite power being carried by the beam, which is of course physically unrealistic. What is meant by a physical Bessel-type beam is a beam that has amplitude modulation similar to a Bessel function, over a finite radius, and whose core components behave non-diffractively over a reasonable, but finite, propagation length [91]. These are achievable by several methods in optics including axicon lenses, annular apertures and holograms [91]. Thus far, the observed electron vortex beams appear to be Laguerre-Gaussian in profile , with a well defined waist at the focal point [25] (Laguerre-Gaussian vortex beams are discussed in more detail below); however if the Rayleigh range is sufficiently large then the beam may be described as approximately Bessel-like.

The optical and electron Bessel beams given above each have the spatial distribution

$$u_l(\mathbf{r}) = J_l(k_\perp \rho) e^{il\phi} e^{ik_z z}. \tag{2.25}$$

The Fourier transform of the Bessel beam $u_l(\mathbf{r})$ will be found by applying the Fourier-Bessel transform for cylindrically symmetric functions [92]. Writing $\mathbf{r}(\rho, \phi, z)$ and $\mathbf{k}'(k'_\perp, \varphi, k'_z)$, the

Fourier transform of Eq. (2.25) is

$$\begin{aligned}\tilde{u}_l(\mathbf{k}') =& \frac{1}{(2\pi)^3}\int d^3r J_l(k_\perp\rho)e^{ik_z z}e^{il\phi}e^{-i\mathbf{k}'\cdot\mathbf{r}} \\ =& \frac{1}{(2\pi)^3}\int_0^{2\pi}d\phi\int_{-\infty}^{\infty}dz\int_0^{\infty}d\rho\rho J_l(k_\perp\rho)e^{il\phi}e^{i(k_z-k_z')z}e^{-ik_\perp'\rho(\cos\varphi\cos\phi+\sin\varphi\sin\phi)} \\ =& \frac{\delta(k_z-k_z')}{(2\pi)^2}\int_0^{2\pi}d\phi\int_0^{\infty}d\rho\rho J_l(k_\perp\rho)e^{il\phi}e^{-ik_\perp'\rho\cos(\phi-\varphi)};\end{aligned} \tag{2.26}$$

writing $-\cos(\varphi-\phi)=\cos(\pi-\phi+\varphi)$, and letting $\alpha=\pi-\phi+\varphi$

$$\begin{aligned}\tilde{u}_l(\mathbf{k}') =& \frac{\delta(k_z-k_z')}{(2\pi)^2}\int_0^{2\pi}d\alpha\int_0^{\infty}d\rho\rho J_l(k_\perp\rho)e^{ik_\perp'\rho\cos\alpha}e^{-il\alpha}e^{il\varphi}e^{il\pi} \\ =& \frac{\delta(k_z-k_z')i^{-l}}{(2\pi)}\int_0^{\infty}d\rho\rho J_l(k_\perp\rho)J_{-l}(k_\perp'\rho)e^{il\varphi}e^{il\pi}\end{aligned} \tag{2.27}$$

where we have made use of the Bessel function integral identity [93]

$$J_\nu(x)=\frac{1}{2\pi i^\alpha}\int_0^{2\pi}d\alpha e^{ix\cos\alpha}e^{i\nu\alpha}. \tag{2.28}$$

The Bessel function of order $-l$ may be written as a Bessel function of positive order using the following identity [93]:

$$J_{-\nu}(x)=e^{i\nu\pi}J_\nu(x); \tag{2.29}$$

so that we now have

$$\tilde{u}_l(\mathbf{k}')=\frac{\delta(k_z-k_z')i^{-l}}{(2\pi)}d\phi\int_0^{\infty}d\rho\rho J_l(k_\perp\rho)J_l(k_\perp'\rho)e^{il\varphi}. \tag{2.30}$$

Finally, the Bessel function orthogonality relation [94] is applied

$$\int_0^{\infty}J_\nu(\alpha x)J_\mu(\beta x)xdx=\frac{1}{\alpha}\delta(\alpha-\beta)\delta_{\nu,\mu}; \tag{2.31}$$

so that the Fourier transform of the Bessel beam function Eq. (2.25) is given as

$$\tilde{u}_l(\mathbf{k}')=\frac{i^{-l}}{2\pi}\frac{e^{il\varphi}}{k_\perp}\delta(k_z-k_z')\delta(k_\perp-k_\perp'). \tag{2.32}$$

The physical interpretation of this momentum representation is of a superposition of plane waves of varying $k_\perp$ such that $k=\sqrt{k_\perp^2+k_z^2}$ for each wave. For a given k_z the possible $k_\perp$ lie on a ring on the surface of constant k, so that there is a cone of plane waves that constitute the Bessel beam [32, 91], the phase of which is given by $e^{il\varphi}$. This is shown in Fig. 2.2.3. The picture of the Bessel beam as waves propagating on a cone relates nicely to the generation of vortices as screw dislocations discussed in Section 1.2.1. The interference pattern of two waves propagating at an angle 2θ to each other contains a series of screw dislocations parallel to the z axis. By having not merely two interfering waves but a cone, the zero-amplitude lines along the screw dislocation are swept out into cylinders, forming the nodes of the Bessel beam. This conical propagation leads to

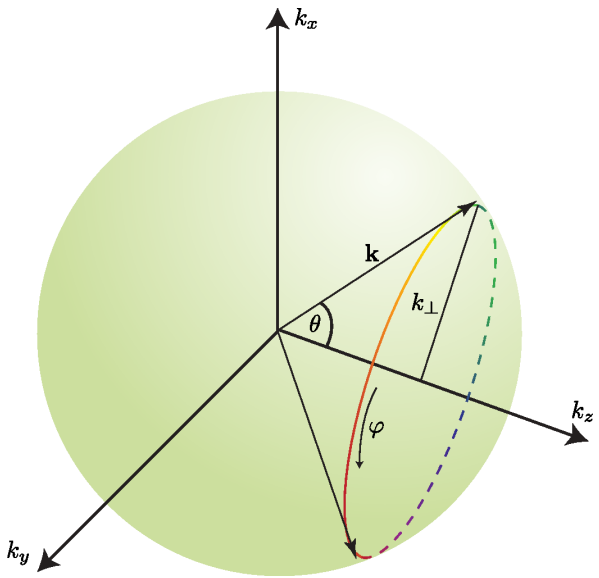

Figure 2.2.3: The Fourier transform of the Bessel beam results in a set of waves of fixed k_z and varying k_x and k_y, such that $k_\perp = \sqrt{k_x^2 + k_y^2}$. The vortex Bessel beam illustrated here has a phase factor $e^{il\varphi}$, so that the phase changes by $2\pi l$ on rotation about the k_z axis. This is illustrated for $l = 1$. The relationship between k_z and $k_\perp$ fixes the cone angle θ.

another interesting property of the Bessel beam; namely that the original spatial distribution is reconstructed after propagation past an obstruction [91, 95].

2.3 Laguerre-Gaussian Vortex Solutions

The Bessel beams described above are the simplest type of vortex beam, as their spatial distributions depend only on the transverse distance from the beam axis. In practise, this ideal is not the case in laser and electron optics systems that are described by Gaussian beams (up to aberration corrections) [38, 44]. The Laguerre-Gaussian beams have a Gaussian envelope, modified by a Laguerre polynomial distribution and a phase factor so that they are suitable for carrying orbital angular momentum. The Laguerre-Gaussian solutions will be given in the paraxial approximation for the electron vortex using the Schrödinger equation, but as before, these results will be directly applicable to the optical vortex solutions.

By analogy with the paraxial Helmholtz equation [96] we have the paraxial Schrödinger equation

$$(\nabla^2 + k^2)\psi_l \to (\nabla_\mathrm{T}^2 + 2ik\partial_z)\psi_l^\mathrm{LG} = 0 \tag{2.33}$$

with the Laguerre-Gaussian wavefunction taking the form

$$\psi_l^\mathrm{LG}(\mathbf{r}, t) = u(\rho, \phi, z)e^{ik_z z}e^{-i\omega t}. \tag{2.34}$$

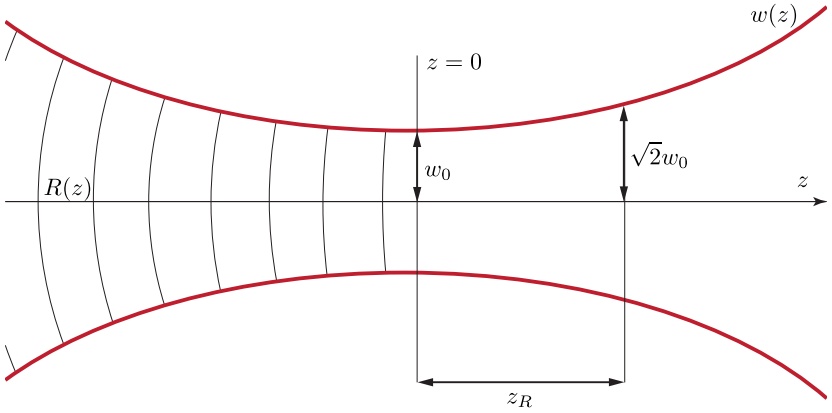

Figure 2.3.1: The general features of a Gaussian beam near focus. The beam has a characteristic width w_0, and the width increases away from the focal plan (here set at $z = 0$) according to $w(z)$. The Rayleigh range, z_R, is the distance at which the beam width has increased from w_0 to $\sqrt{2}w_0$. On the left hand side of the figure the curvature of the wavefronts is sketched - close to $z = 0$ the wavefronts are planar, i.e. $R(z) \to \infty$, while for large z the wavefronts approach a spherical profile, such that $R(z) \approx z$ for $z \gg z_R$. The minimum radius of curvature is $R(z_R) = 2z_R$.

The Gaussian beam parameters of beam width $w(z)$ and Rayleigh length z_R are defined as [44]

$$w(z) = w_0(z)\sqrt{1 - \left(\frac{2z}{k_z w_0^2}\right)^2}; \tag{2.35}$$

$$z_R = \frac{k_z w_0^2}{2}. \tag{2.36}$$

The beam width $w(z)$ describes the spread of the beam away from the focal point, or waist, at which the beam width has a minimum denoted by w_0. The width $w(z)$ is defined as the radius at which the intensity is $1/e$ of the maximum intensity in that plane. The Rayleigh length describes the distance from the focal point at which $w(z) = \sqrt{2}w_0$. The wavefronts associates with Gaussian beams are curved; at z_R from the beam waist, the radius of curvature of the beam is $2z_R$. These features are illustrated in Fig. 2.3.1. The Laguerre-Gaussian solution takes the form [1, 96]

$$\psi_l^{\mathrm{LG}}(\mathbf{r}, t) = \frac{N z_R}{\sqrt{z_R^2 + z^2}} \left(\frac{\sqrt{2}\rho}{w(z)}\right)^l L_p^l\left(\frac{2\rho^2}{w^2(z)}\right) e^{ik_z z} e^{-i\omega t} \times \exp\left\{-\frac{\rho^2}{w^2(z)} - \frac{ik_z\rho^2 z}{2(z_R^2 + z^2)} + il\phi + i(2p + l + 1)\arctan\left(\frac{z}{z_R}\right)\right\}, \tag{2.37}$$

where $L_p^l(x)$ is the generalised Laguerre polynomial, with azimuthal index l and radial index $p \geq 0$. These describe modes with the Gaussian beam profile in the z-direction, as depicted in Fig. 2.3.1, and a radial beam profile that varies with the indices p and l. The azimuthal index l indicates the orbital angular momentum of the beam, similar to the Bessel beam above, and may take any integer value. The radial index specifies the number of rings in the radial intensity distribution, such that the beam has $p + 1$ nodes, for $|l| > 0$ (for $l = 0$, the beam has a central spot, and p additional nodes). Laguerre-Gaussian distributions are shown in Fig. 2.3.2 for various orders of l and p. As can be seen, the modes with $|l| > 0$ have a central minimum, and Eq. (2.37)

has the appropriate $e^{il\phi}$ phase factor, indicating that the Laguerre-Gaussian modes are suitable vortex functions. Another phase factor of interest is the Gouy phase, given by the factor $\exp\left\{i(2p+l+1)\arctan\left(\frac{z}{z_R}\right)\right\}$, which describes the phase change of the Gaussian beam after passing through focus. The Gouy phase is common to all beams with Gaussian distributions, and reflects phase inversion on passing through the focal point [44]. Though the Gouy phase change is dependent on l, it does not contribute to the orbital angular momentum of the beam, and does not affect the vortex features of the beam.

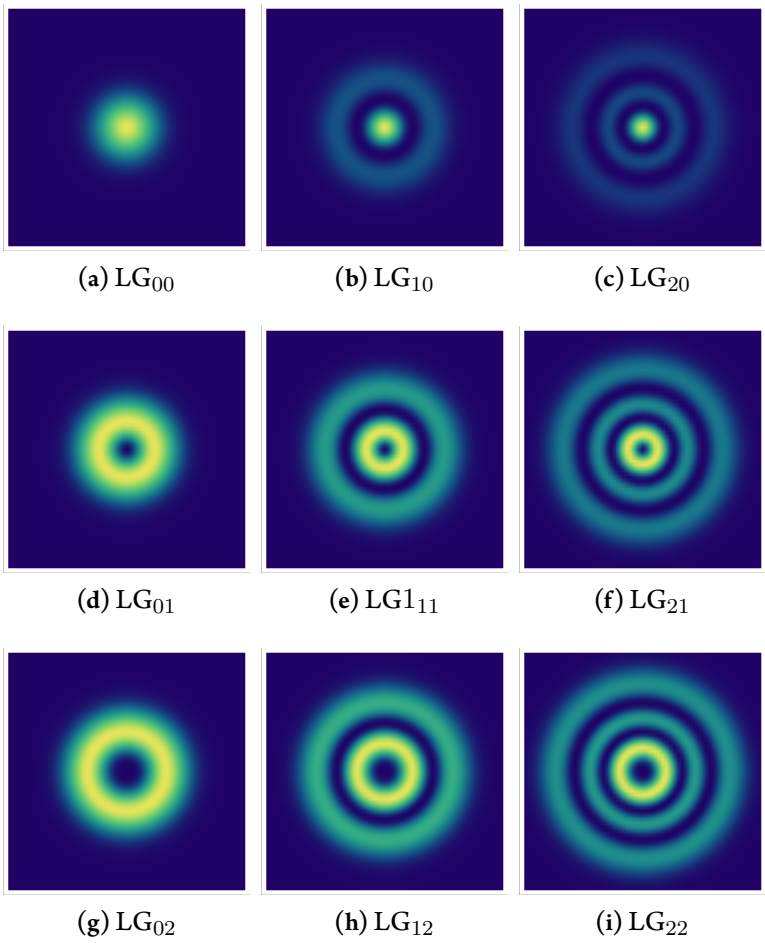

(a) LG_{00} (b) LG_{10} (c) LG_{20}

(d) LG_{01} (e) $LG1_{11}$ (f) LG_{21}

(g) LG_{02} (h) LG_{12} (i) LG_{22}

Figure 2.3.2: Intensity distribution patterns for the LG_{pl} modes, shown in the $z = 0$ plane. Intensity is given by $|\psi_l^{\mathrm{LG}}|^2$. The concentric ring structure of the orbital angular momentum carrying modes is clear, with $p+1$ nodes (or spots). Colour scale shows the intensity variation within individual modes (not the relative intensity variation across all modes). The Laguerre-Gaussian modes having $l < 0$ will have the same intensity distributions as shown above, however the phase (not shown) will have the opposite sign.

The Bessel mode electron wavefunction and electric field distribution will be used in the rest of the work presented within this thesis. The Bessel function is simpler to work with, as the z-dependence is restricted to the wave propagation factor. The features of interest are those arising due to the vortex phase factor of $e^{il\phi}$, which is the sole ϕ dependence of both mode functions, so the Bessel function will illustrate the appropriate vortex behavior. We note that, with one exception, the qualitative results of the following chapters will apply directly to the Laguerre-Gaussian optical and electron modes; application of the appropriate methods discussed will yield the correct

quantitative results for the Laguerre-Gaussian modes. However, the results of Section 6.3 rely on a particular property of the Bessel function, so that in order to extend this to the case of the Laguerre-Gaussian beam, the beam must be expanded as a series of the Bessel function basis states.

2.4 Beyond the Schrödinger and Paraxial Helmholtz Equations

The paraxial approximation of ray optics consists of rays travelling at a small angle to the propagation axis and polarised in the transverse direction, such that the variation of the beam's spatial distribution along the axis is small [96, 97]. For the optics case this leads to the paraxial Helmholtz equation

$$\left(\nabla_{\mathrm{T}}^2 + 2ik\partial_z\right) u(\mathbf{r}) = 0 \tag{2.38}$$

which, for the Bessel beam, is equivalent to the transverse variation restriction imposed on the mode function $u(\rho)$ and $u(x, y)$ for the electron and optics derivations above respectively. In optics, the problem with the paraxial approximation is that, for a mode polarised in, say, the x-direction, the spatial distribution should not then have any dependence on x in order to satisfy Maxwell's equations [97]. For Gaussian beams, this is resolved by considering the full mode function as an expansion in a small parameter, the beam width w_0, to find that the paraxial beams are the zeroth order terms in the expansion [97, 98]. Thus, the paraxial Helmholtz equation and its solutions are valid in this limit, and provide a very good approximation to the experimental intensity patterns of laser modes of Gaussian and Laguerre-Gaussian modes [97, 99].

The Bessel beams are not Gaussian, and so do not require the specific paraxial equations, being solutions to the full Schrödinger and Helmholtz equations as shown above. They satisfy the paraxial requirement that the distribution function vary slowly with z - indeed, the Bessel mode function is z-invariant - however the rays are not directed along the z-axis, as shown in Section 2.2.3. The momentum representation of the Bessel function in Fig. 2.2.3 gives a clear idea of the paraxial approximation for the Bessel beam - the angle θ of the cone of the k-vectors must be restricted to small angles such that $k_\perp \ll k_z$ [32].

2.4.1 Relativistic Electron Vortices

The electron vortex Bessel beam described above was found in the non-relativistic limit, via the Schrödinger equation. The full, non-paraxial, relativistic electron vortex wave solutions were described by finding vortex solutions to the Dirac equation [32] (the Dirac equation is discussed further in Chapter 7). For electrons with spin polarisation given by the 2-spinor $\mathbf{w}$, the relativistic

vortex solutions take the form

$$\Psi_l = \frac{1}{\sqrt{2}}\left[\begin{pmatrix}\sqrt{1+\frac{m}{E}}\mathbf{w}\\ \kappa\sigma_z\cos\theta\mathbf{w}\end{pmatrix}e^{il\phi}J_l(k_\perp\rho) + i\begin{pmatrix}0\\0\\-\beta\kappa\sin\theta\\0\end{pmatrix}e^{i(l-1)\phi}J_{l-1}(k_\perp\rho) + i\begin{pmatrix}0\\0\\0\\\alpha\kappa\sin\theta\end{pmatrix}e^{i(l+1)\phi}J_{l+1}(k_\perp\rho)\right]e^{ik_z z - i\omega t} \tag{2.39}$$

with

$$\mathbf{w} = \begin{pmatrix}\alpha\\ \beta\end{pmatrix}; \qquad \kappa = \sqrt{1-\frac{m}{E}}, \tag{2.40}$$

with $|\alpha| + |\beta| = 1$ and angle θ describing the opening angle of the cone of Bessel plane waves as discussed in Section 2.2.3. It can be seen that two 'extra' modes arise in the relativistic electron vortex solutions, making the relativistic electron vortex a mixed state of l and $l \pm 1$ Bessel modes for spin $s = \pm 1$. These modes give contributions in the small components of the Dirac spinor; in the non-relativistic limit $\kappa \to 0$, and in the paraxial limit we have $\sin\theta \to 0$ so that these modes vanish and the pure l mode is recovered.

Bliokh *et al.* describe the existence of these modes $J_{l\pm1}(k_\perp\rho)$ as a manifestation of coupling between the spin and orbital angular momenta of the electron, leading to a spin-dependent splitting of the beam energy states, but also a difference in spatial distribution of the charge and current densities [32]. However, this is not the traditional spin-orbit interaction of the electron in a radial field, as in the familiar spin-dependent energy splitting of the electron orbiting the hydrogen nucleus [100], though the symmetry properties under parity transformations remain the same [32]. The energy splitting of the non-relativistic electron vortex due to its intrinsic electric field is discussed in Chapter 7.

Instead, the spin-orbit coupling described in [32] arises from the electron motion through a gauge field - the Berry connection - associated with the adiabatic parallel transport of the electron state vector about a closed circuit in a parameter space [101, 102]. The Berry connection has a non-zero curl - the Berry curvature - which means that the gauge field has some circulation. If the Berry curvature turns out to be zero, then the 'Berry connection' is not a proper gauge field and can be compensated by an appropriate gauge transformation. Integration of the Berry curvature around the closed circuit in the parameter space yields extra phase factor which cannot be eradicated though choice of gauge - the Berry phase. The Berry connection leading to the spin-orbit coupling effect of [32] is a relativistic and non-paraxial effect, arising from the momentum dependence of the axis about which the spin and orbital angular momenta are defined.

2.4.2 Non-Paraxial Optical Vortices

The electric field of a non-paraxial light beam propagating in the z-direction should take the form [15, 97]

$$\begin{aligned}\mathbf{E}^{\mathrm{NP}} &= \left(\mathbf{E}_{\mathrm{T}}(x,y) + \mathbf{E}_z(x,y,z)\right) e^{ik_z z} \\ &= \left\{(\alpha\hat{\mathbf{x}} + \beta\hat{\mathbf{y}})\, E_{\mathrm{T}}(x,y) + \hat{\mathbf{z}} E_z(x,y,z)\right\} e^{ik_z z},\end{aligned} \tag{2.41}$$

with $E_{\mathrm{T}}(x,y)$ and $E_z(x,y,z)$ chosen such that $\nabla \cdot \mathbf{E}^{\mathrm{NP}} = 0$. Each component of Eq. (2.41) must satisfy the Helmholtz equation - solving this results in the Bessel mode solutions [15]

$$\begin{aligned}\mathbf{E}^{\mathrm{NP}} = \int_0^k dk_\perp \Bigg(&(\alpha\hat{\mathbf{x}} + \beta\hat{\mathbf{y}}) J_l(k_\perp\rho) e^{il\phi} \\ &+ \hat{\mathbf{z}} \frac{k_\perp}{2(k^2 - k_\perp^2)^{\frac{1}{2}}} \Big((i\alpha + \beta) J_{l-1}(k_\perp\rho) e^{i(l-1)\phi} \\ &- (i\alpha - \beta) J_{l+1}(k_\perp\rho) e^{i(l+1)\phi} \Big) \Bigg) K(k_\perp) e^{iz(k^2 - k_\perp^2)^{\frac{1}{2}}}.\end{aligned} \tag{2.42}$$

The integral over $k_\perp$ leads to non-paraxiality, as this is equivalent to varying the cone angle $0 \leq \theta \leq 2\pi$. These solutions show features similar to the non-paraxial, relativistic electron vortex Bessel modes, namely a coupling of the spin polarisation degree of freedom (controlled by α and β) and the orbital angular momentum. However, due to the transversality condition the z polarised waves propagate in the x-y plane, rather than along the z-axis as is the case for the electron modes. We note that the non-paraxial solutions for transverse magnetic modes have been demonstrated in [70] and that the non-paraxial Laguerre-Gaussian modes are also presented in [15]

2.5 Normalisation of the Electron Vortex Wavefunction

The electron vortex Bessel beam described above must be properly normalised in order to describe realistic electron vortices in an electron microscope. There are several ways of achieving normalisation, depending on the particular beam of interest. Firstly, the infinite Bessel beam is considered, which is taken to be a beam described by Eq. (2.13) that is of infinite radial and axial extent. Secondly, a semi-infinite beam of infinite axial extent but finite radial width is considered, and finally a finite beam restricted both radially and axially. The restriction of the radial extent of the beam implies a finite number of rings of high intensity - ignoring the creation of rings due to other factors in the electron optics, holographic masks may be designed to reproduce a certain number of rings of the Bessel beam.

The finite and semi-infinite beams may be related to the experimentally measurable beam parameters of energy and axial current. We define the 'typical' electron vortex beam to have the

following properties:

Beam energy:	$W = 200\,\text{keV};$
Beam current:	$I_z = 1\mu\,\text{A};$
Axial wavevector:	$k_z = 2.29104 \times 10^{12}\,\text{m}^{-1};$
Radial wavevector:	$k_\perp = 2.29104 \times 10^{10}\,\text{m}^{-1}.$

such that $k_\perp = 0.01 k_z$, well within the paraxial approximation. The normalisation is shown for beams having $l = 1$, but the same procedure may be applied for beams having $l > 1$, as is required in Chapter 3.

2.5.1 Infinite Normalisation

The infinite Bessel beam described by Eq. (2.13) is normalised using delta functions such that

$$\langle \psi_v(\mathbf{r}) \,|\, \psi'_v(\mathbf{r}) \rangle = \delta_{l,l'} \delta(k_\perp - k'_\perp) \delta(k_z - k'_z). \tag{2.43}$$

Applying this normalisation condition gives

$$\langle \psi_v(\mathbf{r}) \,|\, \psi'_v(\mathbf{r}) \rangle = |N|^2 \int_0^{2\pi} e^{i(l-l')\phi} d\phi \int_{-\infty}^{\infty} e^{i(k_z - k'_z)z} dz \int_0^{\infty} J_l(k_\perp \rho) J_{l'}(k'_\perp \rho) \rho d\rho \tag{2.44}$$

$$= |N|^2 4\pi^2 \delta_{l,l'} \delta(k_z - k'_z) \int_0^{\infty} J_l(k_\perp \rho) J_{l'}(k'_\perp \rho) \rho d\rho. \tag{2.45}$$

This last integral can be evaluated using the Bessel function orthogonality condition of Eq. (2.31), so that Eq. (2.45) becomes

$$\langle \psi_v(\mathbf{r}) \,|\, \psi'_v(\mathbf{r}) \rangle = |N|^2 \frac{4\pi^2}{k_\perp} \delta_{l,l'} \delta(k_z - k'_z) \delta(k_\perp - k'_\perp). \tag{2.46}$$

Comparing this with Eq. (2.43) gives

$$|N|^2 = \frac{k_\perp}{4\pi^2} \tag{2.47}$$

as the squared modulus of the normalisation factor. This factor must have the units of inverse volume - writing the delta functions in terms of dimensionless quantities will allow this to be checked. We have the relationship

$$\delta(\alpha x) = \frac{1}{|\alpha|} \delta(x), \tag{2.48}$$

which allows us to write

$$\delta(k_\perp - k'_\perp) = \frac{1}{\hat{k}_\rho} \delta(\kappa_\rho - \kappa'_\rho) \tag{2.49}$$

where $\kappa_\perp$ and $\hat{k_\perp}$ represent the magnitude and direction of the radial wavevector respectively. Similarly, for the axial wavevector

$$\delta(k_z - k_z') = \frac{1}{\hat{k_z}}\delta(\kappa_z - \kappa_z'). \tag{2.50}$$

Each of the delta functions now clearly has the units of a length $[L]$, so that the full vortex wavefunction is now given by

$$\psi_v(\mathbf{r}) = \frac{\sqrt{k_\perp}}{2\pi} J_l(k_\perp \rho) e^{il\phi} e^{ik_z z}, \tag{2.51}$$

with the appropriate dimension of $[L]^{-\frac{3}{2}}$.

2.5.2 Semi-Infinite Normalisation

As noted above, the infinite Bessel beam is unphysical. The normalisation process here will focus on a beam with a fixed diameter, but no constraint on the z-axis - i.e the single vortex electron stretches out to infinity. The beam diameter is given as $2\rho_{l,1}$, where

$$\rho_{l,1} = \frac{\alpha_{l,1}}{k_\perp} \tag{2.52}$$

and $\alpha_{l,1}$ is the first zero of the Bessel function of order l, so that only the single high intensity inner ring is present, physically similar to placing an aperture in front of the beam. The semi-infinite Bessel beam wavefunction is described as

$$\psi_v(\mathbf{r}) = N_l J_l(k_\perp \rho) e^{il\phi} e^{ik_z z} \Theta(\rho_{l,1}) \tag{2.53}$$

with $\Theta(x)$ the Heaviside step function. The normalization factor N_l is different to that of the infinite Bessel beam above, so that this apertured wavefunction must be now normalized. The normalization condition is now

$$\langle \psi_v \,|\, \psi_v' \rangle = \delta_{l,l'} \delta(k_z - k_z'); \tag{2.54}$$

substituting the wavefunction of Eq. (2.53) gives

$$\langle \psi_v \,|\, \psi_v' \rangle = |N_l|^2 \int_0^{2\pi} e^{i(l-l')\phi} d\phi \int_{-\infty}^{\infty} e^{i(k_z - k_z')z} dz \int_0^{\rho_{l,1}} J_l(k_\perp \rho) J_{l'}(k_\perp \rho) \rho d\rho \tag{2.55}$$

$$= |N_l|^2 4\pi^2 \delta_{l,l'} \delta(k_z - k_z') \int_0^{\rho_{l,1}} J_l^2(k_\perp \rho) \rho d\rho \tag{2.56}$$

$$= |N_l|^2 4\pi^2 \delta_{l,l'} \delta(k_z - k_z') \frac{1}{k_\perp^2} \mathcal{I}_l \tag{2.57}$$

where the last integral has been written in the dimensionless form

$$\mathcal{I}_l = \int_0^{\alpha_{l,1}} J_l^2(x) x dx, \tag{2.58}$$

to be evaluated numerically for an $l = 1$ beam:

$$\mathcal{I}_1 = 1.91. \tag{2.59}$$

The normalization factor for the beam with typical energy described above is thus

$$N_l = \frac{k_\perp}{2\pi\sqrt{\mathcal{I}_l}} \tag{2.60}$$

with correct units of $[L]^{-\frac{3}{2}}$ as before. Evaluating this for the $l = 1$ beam gives

$$N_1 = 3.34 \times 10^9 \,\mathrm{m}^{-\frac{3}{2}}. \tag{2.61}$$

2.5.3 Finite Normalisation

An electron vortex beam created in an electron microscope will have finite length, as well as width. The finite beam may be related to the axial electric current I_z, denoting the flux of the axial component of the current density through a cross section of radius $\rho_{l,1}$:

$$I_z = 2\pi e|N_l|^2 \frac{\mathcal{I}_l}{k_\perp^2}\left(\frac{\hbar k_z}{m}\right), \tag{2.62}$$

where $\mathcal{I}_l$ is the same as Eq. (2.58). Standard normalisation techniques give the result

$$N_l = \frac{k_\perp}{\sqrt{2\pi L\mathcal{I}_l}}, \tag{2.63}$$

where L is the finite linear extent of the electron wavefunction; however, rearranging Eq. (2.62) allows the normalisation factor N_l to be found in terms of the beam current I_z, a measurable quantity;

$$N_l^2 = \frac{I_z k_\perp^2 m}{2\pi e\mathcal{I}_l \hbar k_z}. \tag{2.64}$$

For the $l = 1$ beam this gives

$$N_1 = 4.06 \times 10^{10} \,\mathrm{m}^{-\frac{3}{2}}. \tag{2.65}$$

The axial extent of the electron may now be approximated by

$$L = \frac{e\hbar k_z}{m_e I_z}, \tag{2.66}$$

$$= 4.25 \times 10^{-2} \,\mathrm{m}. \tag{2.67}$$

This classical calculation indicates the spatial separation of point-like electrons travelling at approximately $0.8c$. In the transmission electron microscope the samples are of a typical thickness of $10 - 100$ nm, so that only one electron is interacting with the sample at any one time [103], and our single electron normalised wavefunction is an appropriate description of the beam in the region of the sample. As a first approximation, the full, multi-electron beam is viewed as a 'stack' of these single electron wavefuctions passing sequentially though the electron optics and the sample. Though the quantum nature of the electron leads to a spatial spread of the wavefunction - so that the

electron probability distribution is not the point-like Dirac delta distribution implicitly assumed in Eq. (2.67) - the relatively large separation of ≈ 4 cm indicates that the effects of electron-electron interactions, such as the repulsive Boersch effect, may be neglected at these currents.

The electron beam in an electron microscope is not truly monochromatic, and the electrons within the beam have an energy spread of order of 0.1-1 eV, depending on the electron source [103]. This energy spread affects the temporal coherence of the electron, leading to a broadened wavepacket with envelope spanning some length δz [38]. In the rest of this thesis we will assume monochromatic electron beams so as to simply illustrate the dynamics arising due to the existence of the vortex.

3 Vortex fields

The electron vortex beam consists of charged particles, with net motion in the z-direction of propagation. This implies that they should have associated electric and magnetic fields, as any linear current would, but there are also characteristics of the field that arise due to the specific vortex properties of the beam. These fields are explored for electron Bessel vortices of various values of l, in order to demonstrate the effect of winding number on the field characteristics, and illustrate those features arising due to the orbital angular momentum within the beam.

The electric and magnetic fields are found from the charge and current density of the electron wavefunction using Maxwell's equations. The general expressions for the charge and current densities of the vortex beam are shown in Section 3.1. Section 3.2 shows the derivation of the general form of the electric field of the Bessel vortex from the charge density, while the magnetic field is found from the beam's current density, as shown in Section 3.3. The expressions achieved for each field are then applied to specific cases of Bessel beam - varying the winding number l and the physical extent of the beam using the normalised wavefunctions of Section 2.5 - with the results shown in Section 3.4.

The expressions found for the electric and magnetic fields of the electron vortex, specifically the finite beam with $l = 1$, have been published in [86].

3.1 Charge and Current Density

The field of the electron vortex will be found from the charge and current density of the Bessel beam by careful application of Maxwell's equations. Using standard quantum mechanical

techniques [100] the electron vortex wavefunction has charge density $\tilde{\rho}_l(\mathbf{r})$ given by

$$\begin{aligned}\tilde{\rho}_l(\mathbf{r}) &= -e|\psi_v(\mathbf{r})|^2 \\ &= -e|N|^2 J_l^2(k_\rho \rho),\end{aligned} \tag{3.1}$$

and current density $\tilde{\mathbf{J}}(\mathbf{r})$ of the form

$$\begin{aligned}\tilde{\mathbf{J}}_l(\mathbf{r}) &= -e\frac{\hbar}{2m_e i}\left(\psi_v^*\nabla\psi_v - \psi_v\nabla\psi_v^*\right) \\ &= -e|N|^2\frac{\hbar}{m_e}J_l^2(k_\perp\rho)\left(\frac{l}{\rho}\hat{\boldsymbol{\phi}} + k_z\hat{\mathbf{z}}\right).\end{aligned} \tag{3.2}$$

The electric and magnetic fields of the vortex may now be found for the electron vortex described by the Bessel function of order l. The Bessel function distribution gives a cylindrically symmetric charge and current density, each varying only as a function of radial distance ρ. This indicates that the electric and magnetic fields will each also have such cylindrical symmetry.

These charge and current densities will be determined for the cases of the infinite, semi-infinite and finite Bessel beams discussed in Section 2.5, and expressions for the electric and magnetic fields found. For the infinite beam, the densities are given by the exact expressions above, however the beams of finite radial extent require slight modifications in order to convey the correct spatial distribution. This is accomplished by writing the wavefunction of the apertured beam in the form

$$\psi_l^\circ(\mathbf{r}) = \psi_l(\mathbf{r})\Theta(\rho_{l,1} - \rho) \tag{3.3}$$

where $\Theta(x)$ is the Heaviside step function representing the beam having a finite width, with a cut off at the first zero of the lth order Bessel function ensuring a smooth, continuous wavefunction. The corresponding charge and current densities have the similar form

$$\tilde{\rho}_l^\circ(\mathbf{r}) = \tilde{\rho}_l(\mathbf{r})\Theta(\rho_{l,1} - \rho); \tag{3.4}$$

$$\tilde{\mathbf{J}}_l{}^\circ(\mathbf{r}) = \tilde{\mathbf{J}}_l(\mathbf{r})\Theta(\rho_{l,1} - \rho), \tag{3.5}$$

so that the general methods shown below are applicable to each of the normalised vortex beams.

3.2 Electric Field

The electric field will be found from the charge density $\tilde{\rho}$ using Gauss' law:

$$\int_S \mathbf{E}(\mathbf{r})\cdot d\mathbf{S} = \frac{1}{\varepsilon_0}\int_V \tilde{\rho}(\rho)dV. \tag{3.6}$$

Due to the cylindrical symmetry of the beam, a suitable surface S will be a cylinder of constant radius ρ, and height L, centred on the origin. For the Bessel beam of infinite length it is clear that there will be no net field in the z direction[1] so that the electric field has a single component in the

[1]The beam of finite length described in Section 2.5 has a radius of order 10^{-10} m, and a length of order 10^{-2} m. Provided the area of interest is towards the centre of the beam, this ratio is sufficiently large to ensure that the z component of the resulting field is very small. Additionally, as described above, the beam in an electron microscope

radial direction, and we may write

$$\int_0^{2\pi}\int_{-\frac{L}{2}}^{\frac{L}{2}} \mathbf{E}(\rho)\rho dz d\phi = -\frac{e|N|^2}{\varepsilon_0}\int_0^{2\pi}\int_0^{L}\int_0^{\rho} J_l^2(k_\rho\rho')\rho' d\rho' dz d\phi. \tag{3.7}$$

The full electric field is thus given by

$$\mathbf{E}(\rho) = -\hat{\boldsymbol{\rho}}\frac{e|N|^2}{\varepsilon_0\rho}\int_0^{\rho} J_l^2(k_\rho\rho')\rho' d\rho'. \tag{3.8}$$

Evaluating this[2] gives the electric field for the infinite Bessel beam of order l:

$$\mathbf{E}(\rho) = -\hat{\boldsymbol{\rho}}\frac{e|N|^2}{2\varepsilon_0}\rho\left(J_l^2(k_\perp\rho) - J_{l-1}(k_\perp\rho)J_{l+1}(k_\perp\rho)\right) \tag{3.9}$$

as the electric field of the electron Bessel beam. This is valid for any l, so may also be applied to the non-vortex Bessel beam of $l = 0$.

3.3 Magnetic Field

Evaluation of the magnetic field is slightly more involved, and requires a more careful choice of limits in the use of the integral form of Ampère's law:

$$\oint_{\partial S}\mathbf{B}(\mathbf{r})\cdot d\mathbf{l} = \mu_0\int_S \tilde{\mathbf{J}}(\mathbf{r})\cdot d\mathbf{S} + \mu_0\epsilon_0\int_S \frac{\partial\mathbf{E}(\mathbf{r})}{\partial t}\cdot d\mathbf{S}. \tag{3.10}$$

The electric field has no time dependence, so the second term on the right hand side of Eq. (3.10) may be discarded. The remaining may now be split into three separate expressions, detailing the magnetic field arising from each component of the current. The current passing through each of the surfaces in Fig. 3.3.1 gives a contribution to the line integral of the component of magnetic field in the direction of the path, so that identifying the field and current components relevant to each surface allows us to write:

$$\mu_0\int_{S_1}\tilde{J}_z(\mathbf{r})\rho d\phi d\rho = \oint_{\partial S_1}[B_\phi(\mathbf{r})\rho d\phi + B_\rho(\mathbf{r})d\rho] \tag{3.11}$$

$$\mu_0\int_{S_2}\tilde{J}_\rho(\mathbf{r})\rho d\phi dz = \oint_{\partial S_2}[B_\phi(\mathbf{r})\rho d\phi + B_z(\mathbf{r})dz] \tag{3.12}$$

$$\mu_0\int_{S_3}\tilde{J}_\phi(\mathbf{r})d\rho dz = \oint_{\partial S_3}[B_\rho(\mathbf{r})d\rho + B_z(\mathbf{r})dz] \tag{3.13}$$

where the expressions on the right hand side of Eqs. (3.11), (3.12) and (3.13) indicate the line integrals sketched around the surfaces of Fig. 3.3.1. These expressions may now be evaluated piecewise, for chosen limits, to obtain the full magnetic field. The cylindrical symmetry of the situation allows us to infer that the magnetic field components, like the electric field, are functions

is considered to consist of a constant current of these electron wavefunctions of finite length, passing through the microscope in succession. Accordingly, the fields experienced by a thin TEM sample will be constant in the z direction, so that the results derived here are applicable to the physical case, necessitating only a suitable multiplicative factor.

[2] Evaluation of this expression is achieved though symbolic integration using Mathematica.

of ρ only. However, so as to define the line integrals clearly, the magnetic field components will be given as explicit functions of position, i.e. $\mathbf{B}(\rho, \phi, z)$.

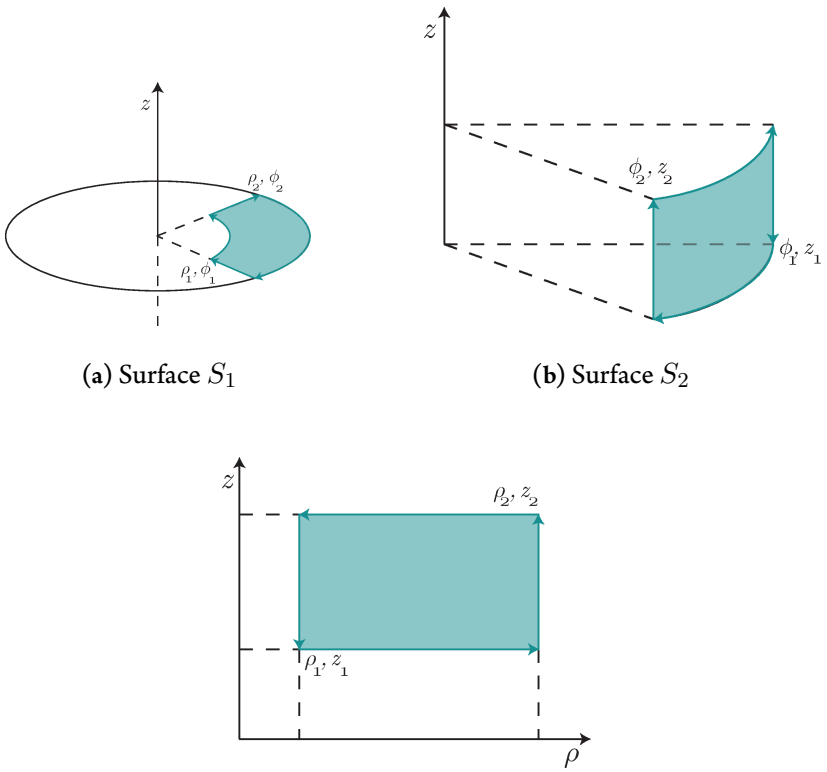

(a) Surface S_1

(b) Surface S_2

(c) Surface S_3

Figure 3.3.1: The surfaces (shaded) over which the current density components are integrated, bounded by the paths (blue, direction indicated with arrows) over which the magnetic field is integrated. (a) corresponds to Eq. (3.11), (b) corresponds to Eq. (3.12), and (c) corresponds to Eq. (3.13).

3.3.1 Azimuthal Component

Writing Eq. (3.11) in full gives:

$$\mu_0 \int_{\rho_1}^{\rho_2} \int_{\phi_1}^{\phi_2} \tilde{J}_z(\mathbf{r}) \rho d\rho d\phi = \int_{\phi_1}^{\phi_2} B_\phi(\rho_1, \phi, z_1) \rho_1 d\phi + \int_{\rho_1}^{\rho_2} B_\rho(\rho, \phi_2, z_1) d\rho \\ \int_{\phi_2}^{\phi_1} B_\phi(\rho_2, \phi, z_1) \rho_2 d\phi + \int_{\rho_2}^{\rho_1} B_\rho(\rho, \phi_1, z_1) d\rho. \quad (3.14)$$

Reversing the limits of the final integral over ρ, and recognising that $B_\rho(\rho, \phi_2, z_1) = B_\rho(\rho, \phi_1, z_1)$ due to the symmetry of the current density the two integrals over ρ on the right hand side cancel, leaving

$$\mu_0 \int_{\rho_1}^{\rho_2} \tilde{J}_z(\mathbf{r}) \rho d\rho = \rho_1 B_\phi(\rho_1, \phi, z_1) - \rho_2 B_\phi(\rho_2, \phi, z_1). \quad (3.15)$$

Choosing limits will allow B_ϕ to be found - choosing $\rho_1 = 0; \rho_2 = \rho$ is a natural choice, which gives the general form

$$B_\phi(\rho) = e\mu_0\hbar\frac{k_z|N_l|^2}{m_e}\frac{1}{\rho}\int_0^\rho J_l^2(k_\perp\rho')\rho' d\rho'. \tag{3.16}$$

The remaining integral is identical to that of Eq. (3.8); explicitly the azimuthal component of the magnetic field of the infinite beam is then

$$B_\phi(\rho) = e\mu_0\hbar\frac{k_z|N_l|^2}{2m_e}\rho\left(J_l^2(k_\perp\rho) - J_{l-1}(k_\perp\rho)J_{l+1}(k_\perp\rho)\right). \tag{3.17}$$

3.3.2 Axial Component

From Eq. (3.13), we have

$$\mu_0\int_{\rho_1}^{\rho_2}\int_{z_1}^{z_2}\tilde{J}_\phi(\mathbf{r})dzd\rho = \int_{\rho_1}^{\rho_2}B_\rho(\rho,\phi,z_1)d\rho + \int_{z_1}^{z_2}B_z(\rho_2,\phi,z)dz + \int_{\rho_2}^{\rho_1}B_\rho(\rho,\phi,z_2)d\rho + \int_{z_2}^{z_1}B_z(\rho_1,\phi,z)dz. \tag{3.18}$$

Once again, the contributions involving $B_\rho(\rho,\phi,z)$ may be eliminated to give

$$\mu_0\int_{\rho_1}^{\rho_2}\tilde{J}_\phi(\mathbf{r})d\rho = B_z(\rho_2,\phi,z)dz - B_z(\rho_1,\phi,z)dz. \tag{3.19}$$

Here, the limits are again chosen so as to eliminate one of the terms on the right hand side. The infinite Bessel beam may be thought of as a set of concentric infinite solenoids, so that the contribution to the field in the z direction at ρ comes from the circulating current $\tilde{J}_\phi$ enclosed within the radius ρ. The magnetic field should tend to zero as $\rho \to \infty$, since $J_\phi(\infty) \to 0$, giving a sensible limit as $\rho_1 = \rho; \rho_2 = \infty$. This gives

$$B_z(\rho) = e\mu_0\hbar\frac{l|N_l|^2}{m_e}\int_\rho^\infty\frac{J_l^2(k_\perp\rho')}{\rho}d\rho'. \tag{3.20}$$

Evaluating this[3] for an infinite Bessel beam of order l gives

$$B_z(\rho) = e\mu_0\hbar\frac{|N_l|^2}{2m_e}\left(1 - \frac{4^{-l}\rho^{2l}{}_2F_3\left[\{l, l+\frac{1}{2}\};\{l+1, l+1, 2l+1\};-\rho^2\right]}{l^2[\Gamma(l)]^2}\right), \tag{3.21}$$

where ${}_pF_q[\{a_1\ldots a_p\};\{b_1\ldots b_q\};z]$ is the generalised hypergeometric function, and $\Gamma(x)$ the gamma function. This general form reduces to a series of products of Bessel functions for particular values of l.

[3] Evaluation of this expression is achieved though symbolic integration using Mathematica.

3.3.3 Radial Component

In both the calculations above, the radial component of the magnetic field was neglected without issue. This suggests that there is no radial component to the net magnetic field generated by the vortex current; continuing the analogy of the vortex beam with a solenoid shows that this is the case. The current density of Eq. (3.2) has a helical form. A classical helical current carrying infinite wire is expected have a magnetic field directed through the centre of the helix in the z-direction due to the circulating current, as well as a field in the azimuthal direction, due to the linear charge transport. No radial component is expected, unless the helix itself is deformed, breaking the cylindrical symmetry.

3.4 Simulation of Electric and Magnetic Fields for the Bessel Beam

The electric and magnetic field expressions found above are used to find the quantitative electromagnetic fields of the normalised Bessel beam wavefunction of Section 2.5. The fields for each case of the infinite and finite beams (the semi-finite beams shows the same spatial variation, with reduced magnitudes due to the different normalisation factor) are evaluated for $l = 0, 1, 3$ and 10, so as to show how the characteristics of the field change with increasing orbital angular momentum. Comparison with $l = 0$ will indicate the specific characteristics that are unique to the vortex beam with orbital angular momentum.

3.4.1 Infinite Beam

The infinite beam has the straightforward spatial form

$$\psi_l(\mathbf{r}) = \frac{\sqrt{k_\perp}}{2\pi} J_l(k_\perp \rho) e^{ik_z z} e^{il\phi}. \tag{3.22}$$

The general results of Eq. (3.9), Eq. (3.17) and Eq. (3.21) are directly applicable to the infinite beam. The resulting fields for various values of l are plotted in Fig. 3.4.1 and Fig. 3.4.2, for each beam having transverse momentum $k_\perp = 2.3 \times 10^{10}$ m^{-1}. These plots were generated in Mathematica by straightforward substitution into the relevant expressions.

The electric field and the ϕ-component of the magnetic field have a similar spatial distribution - as can be seen each node of the beam leads to a local maximum of the field amplitude at a radius enclosing the node. This gives the fields an oscillatory character. It is clear that the amplitudes of E_ρ and B_ϕ tend to a finite value, due to the charge and current densities having a non-zero value everywhere except at $\rho \to \infty$. The z-component of the magnetic field exists only for those beams with $l > 0$ - as discussed above this field component arises due to the circulation of current within the beam, which requires vortex characteristics. This axial field has a maximum at the centre of the beam, dropping off quickly to approach zero. This field also shows oscillations; again, the total current contained within each node is the same, so that the local current density within each ring is greatly reduced with ρ, and the oscillations quickly become small.

The magnetic field plots of Fig. 3.4.1 show the two components of the magnetic field on the same graph. Note that $B_z(\rho)$ is two orders of magnitude smaller than B_ϕ for all values of l. The

field magnitudes are found to decrease with increasing l, due to the overall decrease in amplitude of the Bessel beam probability wavefunction, as shown in Fig. 2.2.1. The spatial variation of the fields is plotted in the $z = 0$ plane in Fig. 3.4.2; the electric field plots for each value of l are plotted with colour scale relative to the electric field for the $l = 0$ beam, and similarly the plots of both $B_\phi(\rho)$ are scaled to $B_\phi(\rho)$ for $l = 0$. The $B_z(\rho)$ plots are scaled to 1% of $B_\phi(\rho)$ for $l = 0$ in order to ensure that detail is visible. The magnitudes of the fields found for the infinite beam are very small, since the infinite beam represents a single electron wavefunction spread over all space, so the charge and current densities are very small. When the extent of the electron wavefunction is restricted, as with the finite beam, the magnitude of the field become more reasonable.

3.4.2 Finite Beam

As indicated above the wavefunction of a finite beam normalised with respect to a total axial current, I_z has the form

$$\psi_l^\circ(\mathbf{r}) = \sqrt{\frac{I_z k_\perp^2 m_e}{2\pi e\hbar k_z \mathcal{I}_l}} J_l(k_\perp \rho) e^{ik_z z} e^{il\phi} \Theta(\rho_{l,1} - \rho). \tag{3.23}$$

Evaluating the fields for such apertured Bessel beam of order $l = 0, 1, 3$ and 10 and $k_\perp = 2.3 \times 10^{10}$ m^{-1} gives the fields shown in Fig. 3.4.3 and Fig. 3.4.4. In order to obtain to correct spatial distributions for the fields, the expressions Eq. (3.8), Eq. (3.16) and Eq. (3.20) were re-evaluated using the charge and current densities for the apertured wavefunction, as given in Eq. (3.4) and Eq. (3.5).

The main difference compared to the infinite fields of Section 3.4.1 is that the fields are no longer oscillatory, and tend to zero since the current and charge density are both zero outside of $\rho_{l,1}$. The single node of the apertured Bessel beam leads to single maximum in each of the $E_\rho(\rho)$ and $B_\phi(\rho)$ fields, which then fall off to zero since no further change or current density is enclosed. Similarly, $B_z(\rho)$ is now exactly zero at $\rho_{l,1}$, as there is no current outside this radius to contribute to the field.

The relative magnitudes of the fields of the finite Bessel beam are shown in Fig. 3.4.4. Again, the increase in l leads to a decrease in the overall field strength; however the overall magnitude is much larger than that of the infinite fields, and closer to what would be expected for an experimentally realisable electron vortex. The magnetic fields are of the order of 10^{-6} T for the azimuthal field, and 10^{-8} T for the z-component. These fields are very small, but scale linearly with current, so that larger fields could be produced experimentally. The z-component is particularly interesting, as it is unique to the vortex beam, and is very localised in a region of Å order. This indicates that the vortex beam could potentially find applications in investigation quantum mechanical phase effects due to localised magnetic fields and flux quanta, such as the Aharonov-Bohm effect [104].

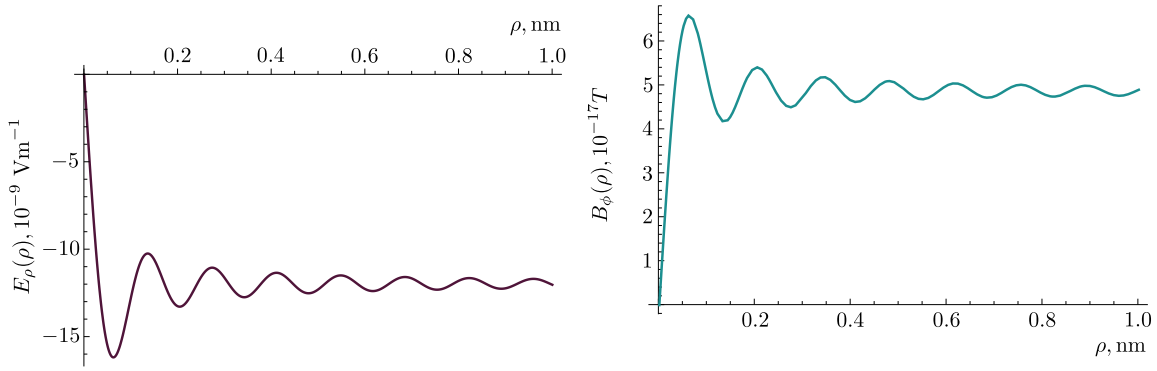

(a) $E_\rho(\rho), l = 0$

(b) $B_\phi(\rho), l = 0$

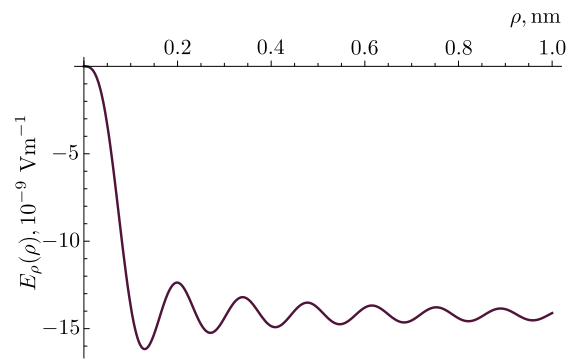

(c) $E_\rho(\rho), l = 1$

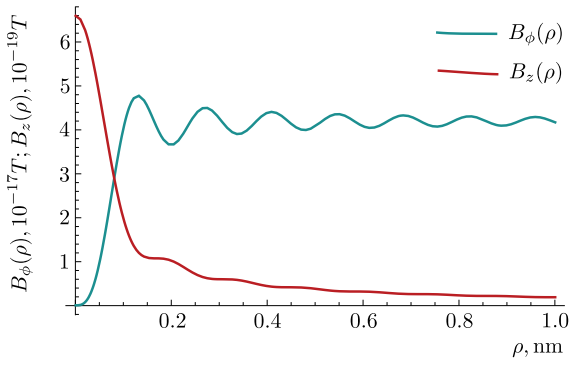

(d) $B_{\phi,z}(\rho), l = 1$

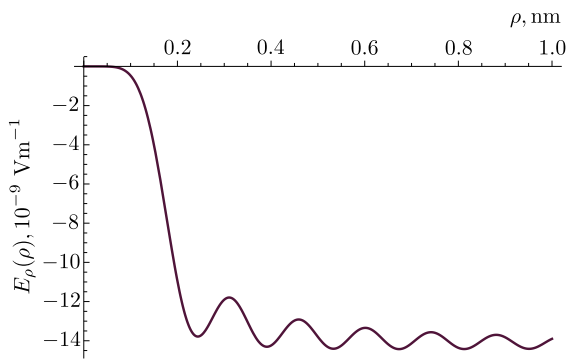

(e) $E_\rho(\rho), l = 3$

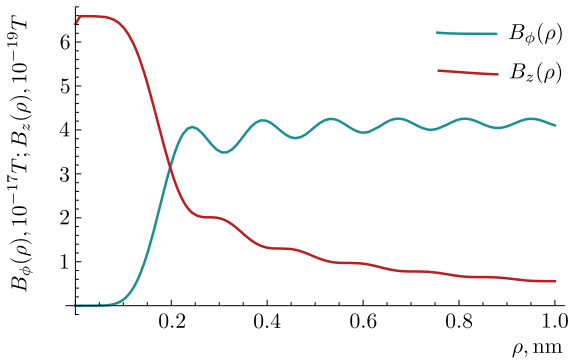

(f) $B_{\phi,z}(\rho), l = 3$

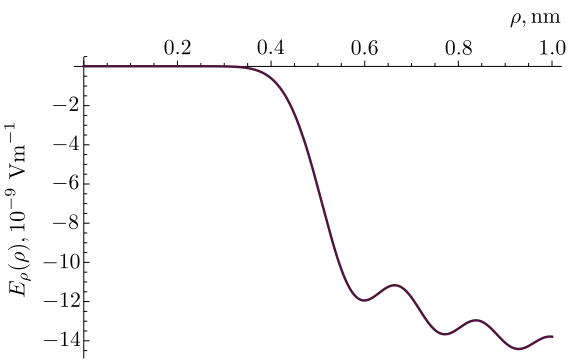

(g) $E_\rho(\rho), l = 10$

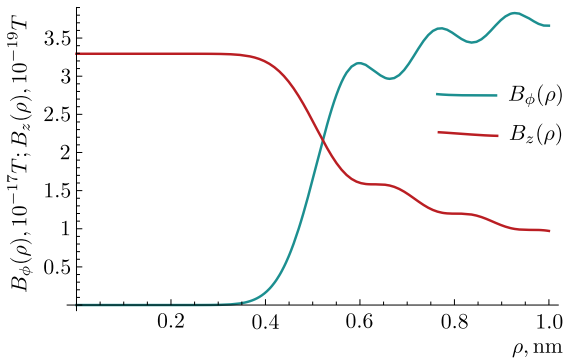

(h) $B_{\phi,z}(\rho), l = 10$

Figure 3.4.1: The electric and magnetic fields of the Bessel beam of infinite radial and axial extent. For beams with $l = 0, 1, 3$ and 10 the electric fields are shown in (a), (c),(e) and (g) respectively, with the magnetic fields shown in (b), (d),(f) and (h). Note that the z-components of the magnetic fields are two orders of magnitude smaller than the ϕ-component.

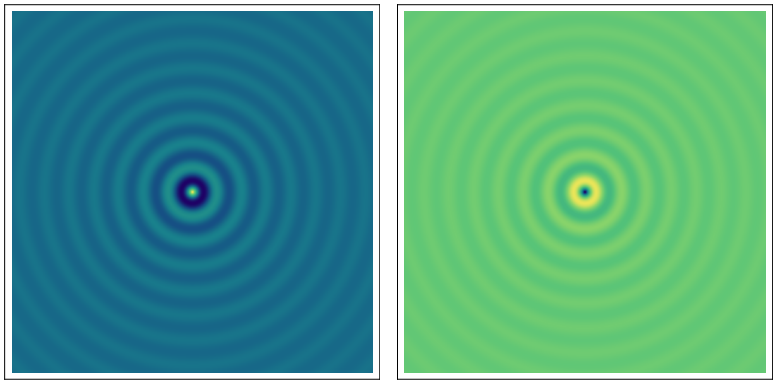

(a) $E_\rho(\rho), l = 0$ (b) $B_\phi(\rho), l = 0$

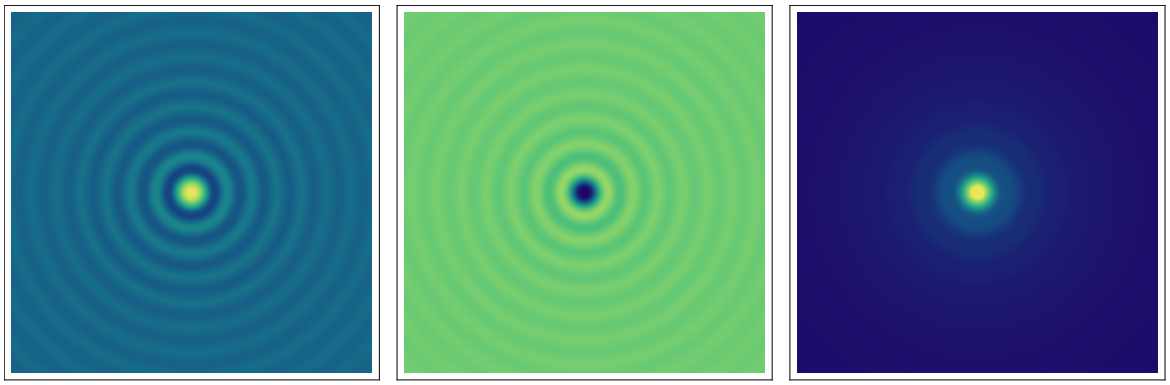

(c) $E_\rho(\rho), l = 1$ (d) $B_\phi(\rho), l = 1$ (e) $B_z(\rho), l = 1$

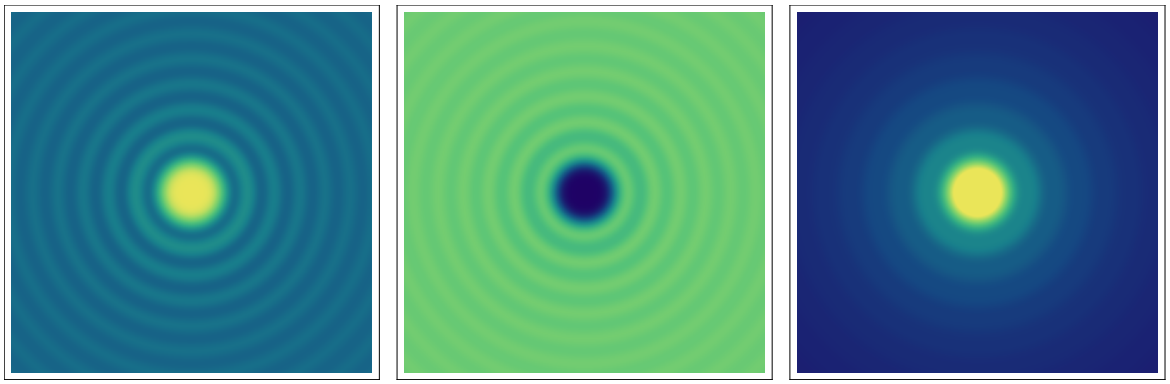

(f) $E_\rho(\rho), l = 3$ (g) $B_\phi(\rho), l = 3$ (h) $B_z(\rho), l = 3$

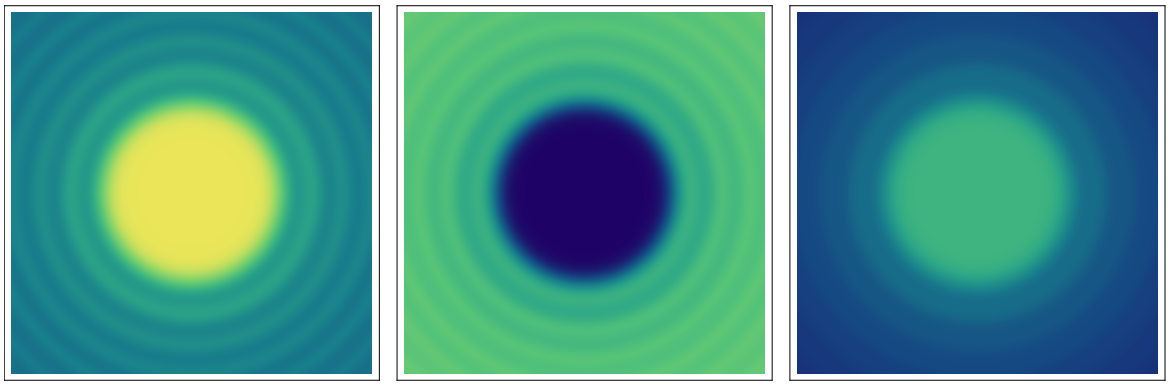

(i) $E_\rho(\rho), l = 10$ (j) $B_\phi(\rho), l = 10$ (k) $B_z(\rho), l = 10$

Figure 3.4.2: Density plots of the electric and magnetic fields for the infinite Bessel beam. Plot colour of $E_\rho(\rho)$ and $B_\phi(\rho)$ is scaled to the corresponding fields of the $l = 0$ beam, with high field shown as yellow, and low as dark blue (order reversed for negative electric field). $B_z(\rho)$ is plotted scaled to 1% in order to show detail.

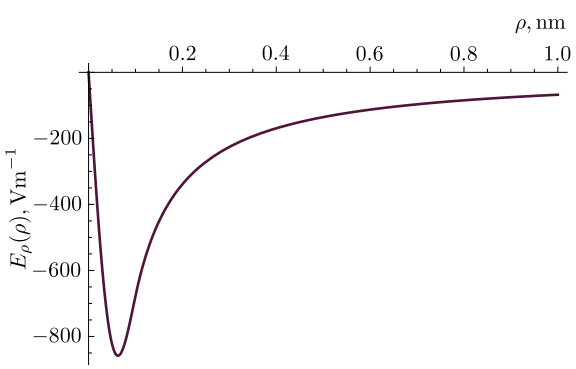

(a) $E_\rho(\rho), l = 0$

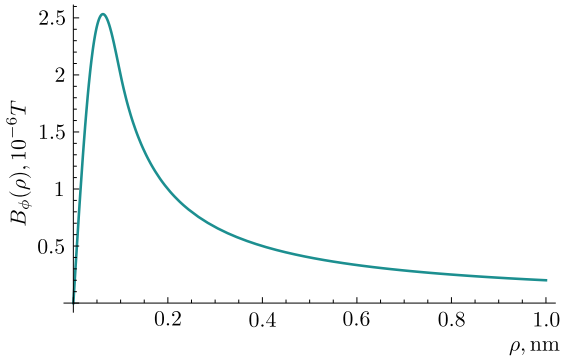

(b) $B_\phi(\rho), l = 0$

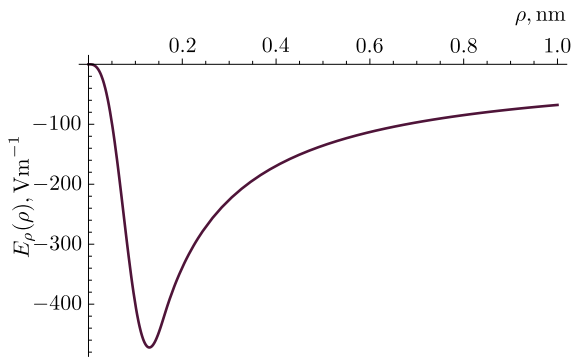

(c) $E_\rho(\rho), l = 1$

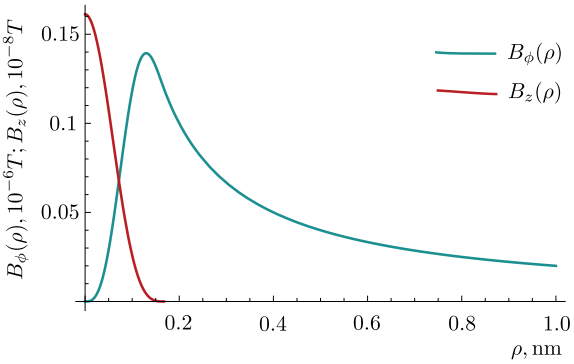

(d) $B_{\phi,z}(\rho), l = 1$

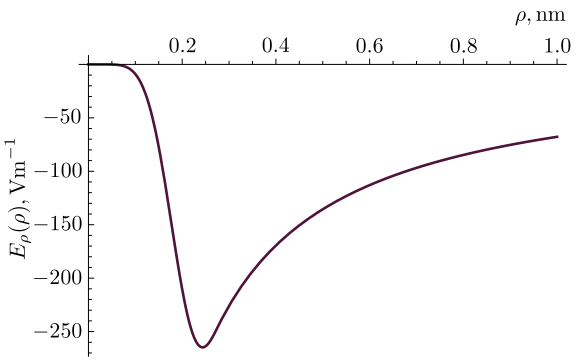

(e) $E_\rho(\rho), l = 3$

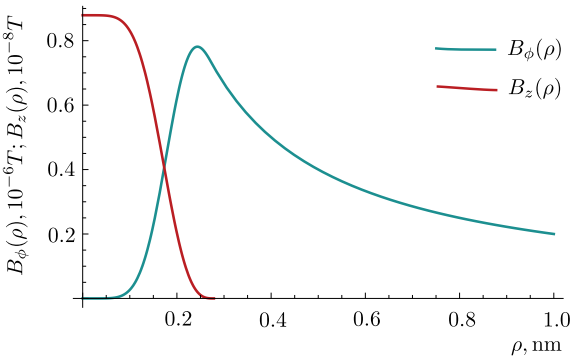

(f) $B_{\phi,z}(\rho), l = 3$

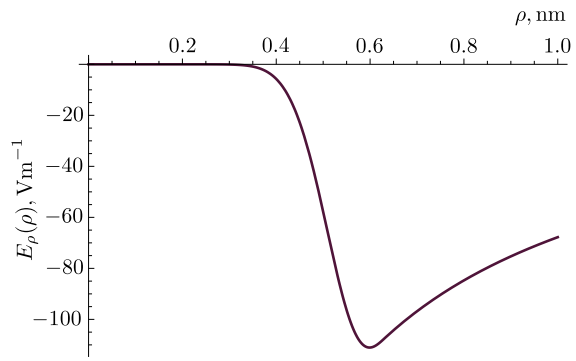

(g) $E_\rho(\rho), l = 10$

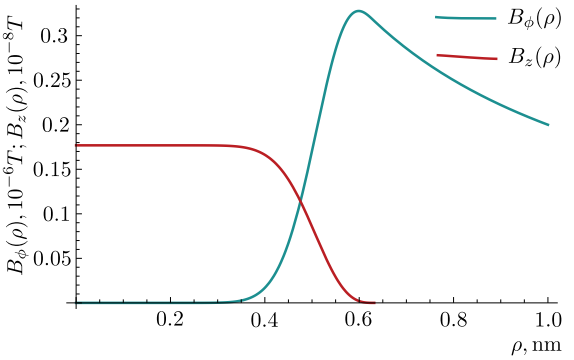

(h) $B_{\phi,z}(\rho), l = 10$

Figure 3.4.3: The electric and magnetic fields of the Bessel beam of finite radial and axial extent. For beams with $l = 0, 1, 3$ and 10 the electric fields are shown in (a), (c),(e) and (g) respectively, with the magnetic fields shown in (b), (d),(f) and (h). Note that the z-components of the magnetic fields are two orders of magnitude smaller than the ϕ-component.

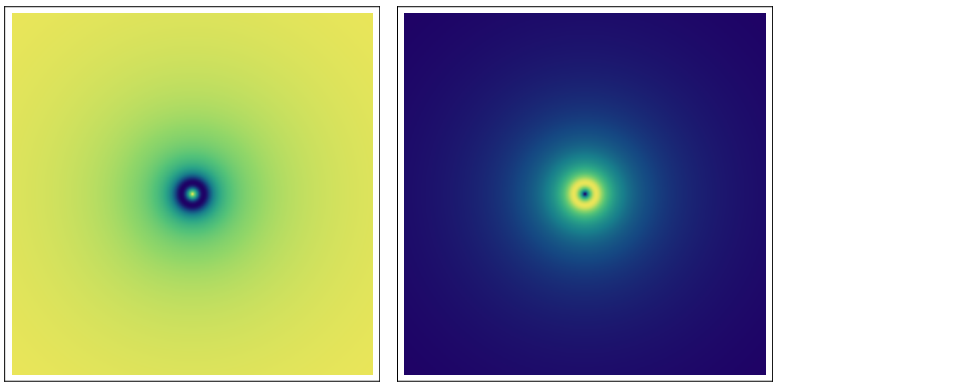

(a) $E_\rho(\rho), l = 0$ (b) $B_\phi(\rho), l = 0$

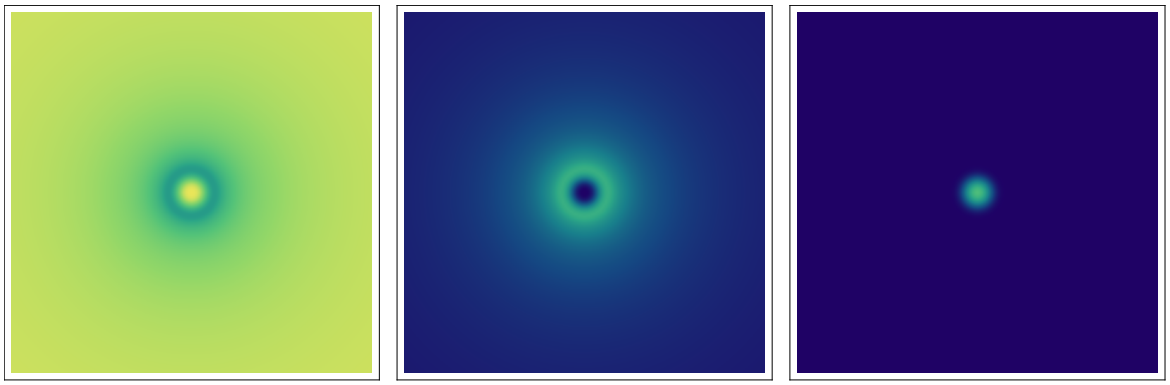

(c) $E_\rho(\rho), l = 1$ (d) $B_\phi(\rho), l = 1$ (e) $B_z(\rho), l = 1$

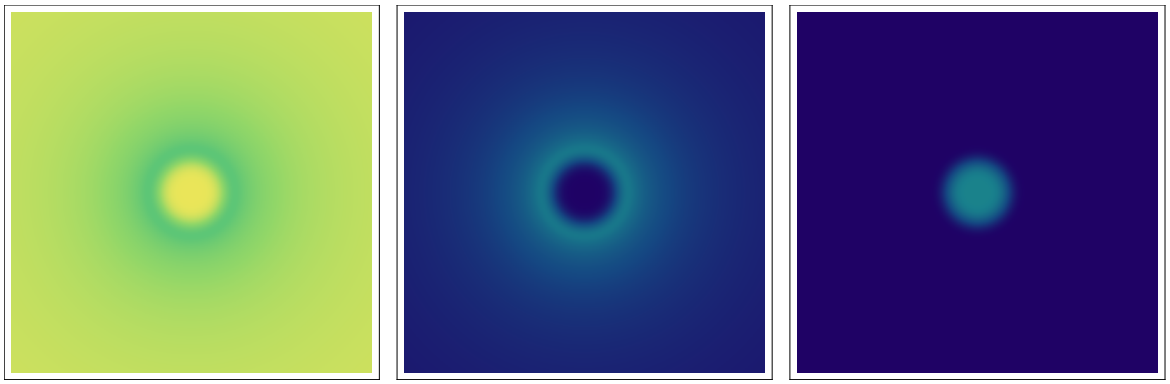

(f) $E_\rho(\rho), l = 3$ (g) $B_\phi(\rho), l = 3$ (h) $B_z(\rho), l = 3$

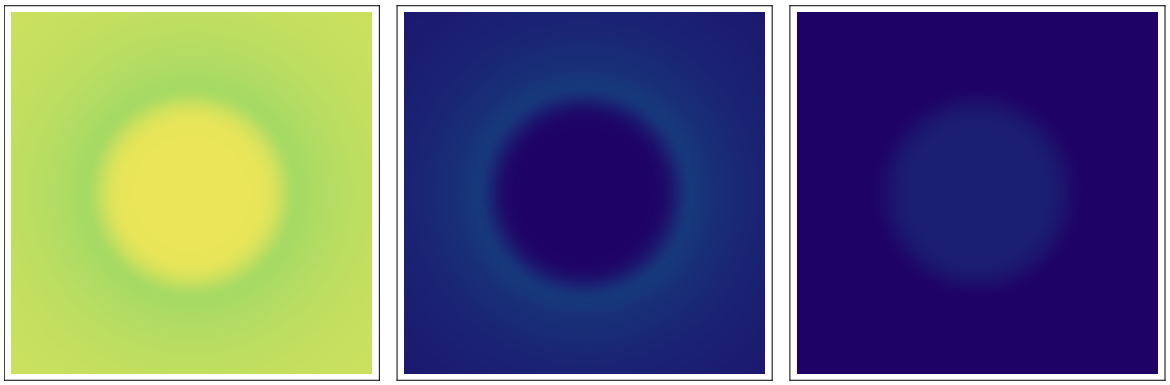

(i) $E_\rho(\rho), l = 10$ (j) $B_\phi(\rho), l = 10$ (k) $B_z(\rho), l = 10$

Figure 3.4.4: Density plots of the electric and magnetic fields for the infinite Bessel beam. Plot colour of $E_\rho(\rho)$ and $B_\phi(\rho)$ is scaled to the corresponding fields of the $l = 0$ beam, with high field shown as yellow, and low as dark blue (order reversed for negative electric field). $B_z(\rho)$ is plotted scaled to 1% in order to show detail.

4

Linear and Orbital Angular Momenta of the Vortex Beam

Electron and optical vortex beams both possess quantised orbital angular momentum. The precise density distribution of this orbital angular momentum depends on the structure of the beam, and its distribution. In this chapter, the linear and angular momenta of the electron and optical Bessel and Laguerre-Gaussian vortices are derived and discussed. It is found that for an optical vortex beam with either the Bessel or Laguerre-Gaussian distribution has *total* momenta - both linear and axial - in the z-direction only, despite the presence of other components in the momentum density. This is also found for the electron vortex beam case. Since both the optical and electron vortices are shown to induce rotational motion, in particles acting under their influence [5, 27, 28, 105] the conclusion must be that the momentum density of each vortex is important. For the optical spanner effect, it is the momentum density of the fields penetrating the particle that produces the rotation [105], whereas for the electron vortex, the rotation is thought to be a mechanical effect arising due to elastic collisions between the object and the vortex mass current density [27].

Knowledge of the momentum densities of the electron and optical vortices is therefore important for discussion of the rotation of particles in such fields. The linear and angular momentum densities of an optical vortex of general distribution are given in Section 4.1, leading to the total linear and angular momenta. The linear and angular momentum densities of the electron vortex are also found, however the electron vortex is found to have two contributions - one mechanical, due to the mass flux, and one electromagnetic, due to the fields associated with the electron vortex. These are evaluated and compared in Section 4.2. Finally, the magnitude of the rotation of a nanoparticle induced by the mechanical influence of the electron vortex is estimated in Section 4.3, and the potential use for electron vortices to investigate friction forces on nanoscale

particle is discussed.

4.1 Optical Vortices

The momentum density of an electromagnetic field can be found from the energy flux density of the field, the Poynting vector $\mathbf{S}$. For a periodically varying field, such as the case of the optical vortices considered here, the Poynting vector must be averaged over a wave-cycle

$$\boldsymbol{\mathcal{S}} = \frac{1}{\mu_0} \langle \mathbf{E} \times \mathbf{B} \rangle . \tag{4.1}$$

For the linear momentum density, we have

$$\begin{aligned} \boldsymbol{\mathcal{P}} &= \frac{1}{c^2} \boldsymbol{\mathcal{S}} && (4.2) \\ &= \varepsilon_0 \langle \mathbf{E} \times \mathbf{B} \rangle . && (4.3) \end{aligned}$$

Similarly, the angular momentum density is found to be

$$\begin{aligned} \boldsymbol{\mathcal{L}} &= \mathbf{r} \times \boldsymbol{\mathcal{P}} && (4.4) \\ &= \varepsilon_0 \mathbf{r} \times \langle \mathbf{E} \times \mathbf{B} \rangle . && (4.5) \end{aligned}$$

The total linear and angular momenta of the beam will be found by integrating the corresponding density over the extent of the beam. This will be applied to the optical vortex solutions of Chapter 2, here given in the form:

$$\mathbf{E}(\mathbf{r}, t) = E_0 u(\rho, z) e^{il\phi} e^{ik_z z} e^{-i\omega t} \hat{\boldsymbol{\varepsilon}}, \tag{4.6}$$

for some polarisation $\hat{\varepsilon}$. The functions $u(\rho, z)$ may be either the Bessel or the Laguerre-Gaussian mode functions without the phase factor $e^{il\phi + ik_z z}$:

$$u_{\mathrm{B}}(\rho) = J_l(k_\perp \rho); \tag{4.7}$$

$$\begin{aligned} u_{\mathrm{LG}}(\rho, z) =& \frac{z_R}{\sqrt{z_R^2 + z^2}} \left(\frac{\sqrt{2}\rho}{w(z)} \right)^l L_p^l \left(\frac{2\rho^2}{w^2(z)} \right) \\ & \times \exp \left\{ -\frac{\rho^2}{w^2(z)} - \frac{ik_z \rho^2 z}{2(z_R^2 + z^2)} + i(2p + l + 1) \arctan \left(\frac{z}{z_R} \right) \right\} . \end{aligned} \tag{4.8}$$

The linear and angular momentum densities will be found for optical vortices of the form given in Eq. (4.6) for circularly polarised fields having spin $\sigma = \pm 1$. The polarisation vector $\boldsymbol{\varepsilon}$ is then

$$\begin{aligned} \hat{\boldsymbol{\varepsilon}} &= \frac{\hat{\mathbf{x}} + i\sigma \hat{\mathbf{y}}}{2} && (4.9) \\ &= \frac{e^{i\sigma\phi} \hat{\boldsymbol{\rho}} - i\sigma e^{-i\sigma\phi} \hat{\boldsymbol{\phi}}}{2}. && (4.10) \end{aligned}$$

giving

$$\mathbf{E}(\mathbf{r},t) = \frac{E_0}{2}u(\rho,z)e^{ik_z z}e^{-i\omega t}\left(e^{i(l+\sigma)\phi}\hat{\boldsymbol{\rho}} - i\sigma e^{i(l-\sigma)\phi}\hat{\boldsymbol{\phi}}\right). \tag{4.11}$$

The magnetic field of the optical vortex is found from the electric field vector using Faraday's law

$$\nabla \times \mathbf{E} = -\frac{\partial \mathbf{B}}{\partial t}; \tag{4.12}$$

giving the corresponding magnetic field as

$$\begin{aligned}\mathbf{B} = \frac{E_0 e^{ik_z z}e^{-i\omega t}}{2\omega}\Bigg[&\hat{\boldsymbol{\rho}}\sigma e^{i(l-\sigma)\phi}\left(ik_z u + \partial_z u\right) - i\hat{\boldsymbol{\phi}}e^{i(l+\sigma)\phi}\left(ik_z u + \partial_z u\right)\\ &- \hat{\mathbf{z}}\left(\frac{\sigma}{\rho}e^{i(l-\sigma)\phi}u + \sigma e^{i(l-\sigma)\phi}\partial_\rho u + \frac{(l+\sigma)}{\rho}e^{i(l+\sigma)\phi}u\right)\Bigg].\end{aligned} \tag{4.13}$$

The electric and magnetic fields may now be used to find the momentum density, using

$$\boldsymbol{\mathcal{P}} = \frac{\varepsilon_0}{2}\left(\mathbf{E}^* \times \mathbf{B} + \mathbf{E} \times \mathbf{B}^*\right). \tag{4.14}$$

The linear momentum density of the optical vortex is found to be

$$\begin{aligned}\boldsymbol{\mathcal{P}}_{\mathrm{OV}} = \frac{\varepsilon_0 E_0^2}{4\omega}\Bigg[&\hat{\boldsymbol{\phi}}\left\{2\frac{(l+\sigma)}{\rho}u^*u + \frac{\sigma}{\rho}u^*u\left(e^{2i\sigma\phi} + e^{-2i\sigma\phi}\right) + \sigma u^*\partial_\rho u\left(e^{2i\sigma\phi} + e^{-2i\sigma\phi}\right)\right\}\\ &- \hat{\boldsymbol{\rho}}i\sigma\frac{(l+\sigma)}{\rho}u^*u\left(e^{2i\sigma\phi} - e^{-2i\sigma\phi}\right) + 4\hat{\mathbf{z}}k_z u^*u\Bigg],\end{aligned} \tag{4.15}$$

which simplifies to become

$$\begin{aligned}\boldsymbol{\mathcal{P}}_{\mathrm{OV}} = \frac{\varepsilon_0 E_0^2}{2\omega}\Bigg[&\hat{\boldsymbol{\rho}}\frac{(l+\sigma)}{\rho}u^*u\sin(2\phi)\\ &+ \hat{\boldsymbol{\phi}}\left\{\frac{(l+\sigma)}{\rho}u^*u + \frac{\sigma}{\rho}u^*u\cos(2\phi) + \sigma u^*\partial_\rho u\cos(2\phi)\right\} + 2\hat{\mathbf{z}}k_z u^*u\Bigg].\end{aligned} \tag{4.16}$$

From this, we may now find the total linear momentum, by integrating over all space. However, the momentum density must first be given in a fully independent coordinate representation, as the precise directions $\hat{\boldsymbol{\rho}}$ and $\hat{\boldsymbol{\phi}}$ depend on position. It will be convenient to express the unit directions in independent Cartesian coordinates, but perform the integration using cylindrical polar coordinates. The unit direction $\hat{\boldsymbol{\rho}}$ can be expressed in Cartesian coordinates as

$$\begin{aligned}\hat{\boldsymbol{\rho}} &= \frac{x}{\sqrt{x^2+y^2}}\hat{\mathbf{x}} + \frac{y}{\sqrt{x^2+y^2}}\hat{\mathbf{y}},\\ &= \cos\phi\hat{\mathbf{x}} + \sin\phi\hat{\mathbf{y}};\end{aligned} \tag{4.17}$$

similarly, the unit $\hat{\boldsymbol{\phi}}$ direction is written as

$$\begin{aligned}\hat{\boldsymbol{\phi}} &= -\frac{y}{\sqrt{x^2+y^2}}\hat{\mathbf{x}} + \frac{x}{\sqrt{x^2+y^2}}\hat{\mathbf{y}}, \\ &= -\sin\phi\hat{\mathbf{x}} + \cos\phi\hat{\mathbf{y}}. \end{aligned} \tag{4.18}$$

The total linear momentum of the beam is now given as

$$\mathbf{P} = \int dV \hat{\mathbf{x}}\left(\mathcal{P}_\rho\cos\phi - \mathcal{P}_\phi\sin\phi\right) + \hat{\mathbf{y}}\left(\mathcal{P}_\rho\sin\phi + \mathcal{P}_\phi\cos\phi\right) + \hat{\mathbf{z}}\mathcal{P}_x. \tag{4.19}$$

It can be seen that, regardless of the specific functional form of $\mathcal{P}_\rho$ or $\mathcal{P}_\phi$, the integration over ϕ will yield zero for all $\hat{\mathbf{x}}$ and $\hat{\mathbf{y}}$ terms. Thus the linear momentum is found to be in the $\hat{\mathbf{z}}$ direction only:

$$\mathbf{P}_{\text{OV}} = \hat{\mathbf{z}}\frac{\varepsilon_0 E_0^2}{\omega}k_z\int u^* u dV, \tag{4.20}$$

which, for a properly normalised single photon wavefunction gives the result

$$\mathbf{P}_{\text{OV}} = \hat{\mathbf{z}}\hbar k_z. \tag{4.21}$$

The angular momentum density of the beam may also now be found, by applying Eq. (4.5) to the linear momentum density of Eq. (4.16),

$$\boldsymbol{\mathcal{L}}_{\text{OV}} = -\hat{\boldsymbol{\rho}}z\mathcal{P}_\phi + \hat{\boldsymbol{\phi}}\left(z\mathcal{P}_\rho - \rho\mathcal{P}_z\right) + \hat{\mathbf{z}}\rho\mathcal{P}_\phi. \tag{4.22}$$

The angular momentum density then has the form

$$\begin{aligned}\boldsymbol{\mathcal{L}}_{\text{OV}} = \frac{\varepsilon_0 E_0^2}{2\omega}\Bigg[&-\hat{\boldsymbol{\rho}}z\left\{\frac{(l+\sigma)}{\rho}u^*u + \frac{\sigma}{\rho}u^*u\cos(2\phi) + \sigma u^*\partial_\rho u\cos(2\phi)\right\} \\ &+\hat{\boldsymbol{\phi}}\left\{z\frac{(l+\sigma)}{\rho}u^*u\sin(2\phi) - 2\rho k_z u^*u\right\} \\ &+\hat{\mathbf{z}}\rho\left\{\frac{(l+\sigma)}{\rho}u^*u + \frac{\sigma}{\rho}u^*u\cos(2\phi) + \sigma u^*\partial_\rho u\cos(2\phi)\right\}\Bigg].\end{aligned} \tag{4.23}$$

This may now be integrated over the beam volume to find the total angular momentum within the beam. Again, the $\hat{\boldsymbol{\phi}}$ and $\hat{\boldsymbol{\rho}}$ unit directions must be transformed to Cartesian unit vectors; it can be seen that neither the $\hat{\boldsymbol{\rho}}$ or the $\hat{\boldsymbol{\phi}}$ components will contribute to the total angular momentum after integration. As for the $\hat{\mathbf{z}}$ component, due to the presence of factors of $\cos(2\phi)$ in the second and third terms, only the first term will contribute to the total angular momentum. Thus, the total angular momentum within the beam is given as

$$\mathbf{L}_{\text{OV}} = \hat{\mathbf{z}}\frac{\varepsilon_0 E_0^2}{2\omega}(l+\sigma)\int u^* u dV; \tag{4.24}$$

for the normalised single photon wavefunction this gives

$$\mathbf{L}_{\text{OV}} = \hat{\mathbf{z}}\hbar(l+\sigma). \tag{4.25}$$

Similar to the linear momentum, this is in the axial direction only despite there being transverse components to the angular momentum density. These results are consistent with the results of previous investigations into the momentum density of Bessel beams of various transverse polarisations [105].

4.2 Electron Vortices

The electron vortex has two sources of momentum, both linear and angular. The mechanical motion of the electrons within the beam gives rise to the momenta associated with the mass flux of the beam, including the orbital angular momentum $l\hbar$; however since the beam is charged it also possesses an electric field, and a magnetic field due to its motion, as shown in Chapter 3. As shown above, the electromagnetic fields also have associated linear and angular momenta. For the Bessel electron vortex, these field contributions to the beam momenta will be evaluated, and compared to their mechanical counterparts.

4.2.1 Mechanical Momentum

The total linear and angular momenta associated with the mass flux of the electron vortex solutions of Chapter 2 will be found from the corresponding momentum densities. Similar to above, the electron vortex wavefunction is written in the form

$$\psi(\mathbf{r},t) = N_l u(\rho,z) e^{il\phi} e^{ik_z z} e^{-i\omega t}, \tag{4.26}$$

where again $u(\rho,z)$ stands for either the Bessel or the Laguerre-Gaussian beam mode functions, given in Eq. (4.7) and Eq. (4.8) respectively, and each mode is assumed to be properly normalised. Using standard quantum mechanical techniques, the probability current density is given by

$$\mathbf{J} = -\frac{i\hbar}{2m_e}\left(\psi^*\nabla\psi - \psi\nabla\psi^*\right). \tag{4.27}$$

Applying this to the electron vortex beam of Eq. (4.26) gives the general vortex current density in the form

$$\mathbf{J} = -\frac{i\hbar|N_l|^2}{2m_e}\left[\hat{\boldsymbol{\rho}}\left(u^*\partial_\rho u - u\partial_\rho u^*\right) + \hat{\boldsymbol{\phi}}\frac{2il}{\rho}u^*u + \hat{\mathbf{z}}\left(u^*\partial_z u - u\partial_z u^* + 2ik_z u^*u\right)\right]. \tag{4.28}$$

For the electron vortex the linear momentum density is given by the mass current density, found from the probability current density by

$$\boldsymbol{\mathcal{P}}_{\text{EV}} = m_e\mathbf{J}. \tag{4.29}$$

Similar to above, the angular momentum density is found using

$$\boldsymbol{\mathcal{L}}_{\text{EV}} = \mathbf{r} \times \boldsymbol{\mathcal{P}}_{\text{EV}}. \tag{4.30}$$

The total linear momentum of the general electron vortex wavefunction of Eq. (4.26) is found to be

$$\mathbf{P}_{\text{EV}} = \frac{\hbar|N_l|^2}{2} \int \left(iu\partial_z u^* - iu^*\partial_z u + 2k_z u^* u\right) dV; \tag{4.31}$$

once again, only the $\hat{\mathbf{z}}$ component contributes, due to the vanishing integral over ϕ. For the Bessel beam of Eq. (2.13) the total angular momentum is

$$\begin{aligned} \mathbf{P}^{\text{B}}_{\text{EV}} &= 2\pi\hbar k_z L\mathcal{I}_l |N_l|^2 \hat{\mathbf{z}} \\ &= \hbar k_z \hat{\mathbf{z}}, \end{aligned} \tag{4.32}$$

using the normalisation of the electron vortex in Section 2.5. For the Laguerre-Gaussian beam, the situation is a little more complicated, due to the complex z-dependence of the mode function $u_{\text{LG}}(\rho, z)$. The linear momentum becomes

$$\mathbf{P}^{\text{LG}}_{\text{EV}} = \frac{\hbar|N_l|^2}{2} \int \left(-\frac{k_z\rho^2}{2} \frac{(z^2 - z_R^2)}{(z^2 - z_R^2)^2} - 2(2p + l + 1)\frac{z_R}{z_R^2 + z^2} + 2k_z \right) u^* u dV. \tag{4.33}$$

In the limit of a Laguerre-Gaussian beam with infinite length the contribution of the first term and second terms goes to zero, recovering the expected momentum of $\hbar k_z$. We note here that the Bessel beam is an eigenstate of the momentum operator $\hat{\mathbf{p}}_z = -i\hbar\partial_z$, while the Laguerre-Gaussian beam is not.

The angular momentum density of the Bessel beam is found from the linear momentum density in the same way as before; we have

$$\begin{aligned} \boldsymbol{\mathcal{L}}_{\text{EV}} = \frac{\hbar|N_l|^2}{2} \Bigg[\hat{\boldsymbol{\phi}} \left\{ iz \left(u^*\partial_\rho u - u\partial_\rho u^*\right) + i\rho(u\partial_z u^* - u^*\partial_z u + 2k_z u^* u) \right\} \\ + \frac{2l}{\rho}(\hat{\mathbf{z}} - \hat{\boldsymbol{\rho}}) u^* u \Bigg]. \end{aligned} \tag{4.34}$$

Again, the unit vectors $\hat{\boldsymbol{\rho}}$ and $\hat{\boldsymbol{\phi}}$ are replaced by the Cartesian vectors Eq. (4.17) and Eq. (4.18), so that the total orbital angular momentum of the beam is found to be

$$\begin{aligned} \mathbf{L}_{\text{EV}} &= l\hbar|N_l|^2 \int u^* u dV \\ &= \hbar l \hat{\mathbf{z}} \end{aligned} \tag{4.35}$$

for both the Bessel and Laguerre-Gaussian electron vortices, as expected. Both modes are eigenfunctions of the angular momentum operator $\hat{L}_z$.

4.2.2 Electromagnetic Momentum

The electromagnetic fields of the Bessel vortex were shown in Chapter 3 to have the following form

$$\mathbf{E}(\rho) = \hat{\boldsymbol{\rho}}\frac{1}{\varepsilon_0 \rho}\int_0^{\rho} \tilde{\rho}_l(\rho')\rho' d\rho', \tag{4.36}$$

for the electric field, and

$$\mathbf{B}(\rho) = \mu_0\left[\hat{\boldsymbol{\phi}}\frac{1}{\rho}\int_0^{\rho} \tilde{J}_z(\rho')\rho' d\rho' + \hat{\mathbf{z}}\int_{\rho}^{\infty} \tilde{J}_{\phi}(\rho')d\rho'\right] \tag{4.37}$$

for the magnetic field. We will now apply the same treatment as in Section 4.1, using the Poynting vector to determine the linear and angular momentum densities. For the linear momentum density, we have

$$\boldsymbol{\mathcal{P}}_{\text{EM}} = \varepsilon_0\left(-\hat{\boldsymbol{\phi}}E_\rho B_z + \hat{\mathbf{z}}E_\rho B_\phi\right), \tag{4.38}$$

which implies for the angular momentum density

$$\boldsymbol{\mathcal{L}}_{\text{EM}} = -\varepsilon_0\left(\hat{\boldsymbol{\rho}}zE_\rho B_z + \hat{\boldsymbol{\phi}}\rho E_\rho B_\phi - \hat{\mathbf{z}}\rho E_\rho B_z\right). \tag{4.39}$$

Once again, the $\hat{\boldsymbol{\rho}}$ and $\hat{\boldsymbol{\phi}}$ components vanish after integration over ϕ, leaving

$$\mathbf{P}_{\text{EM}} = \hat{\mathbf{z}}\varepsilon_0\int E_\rho B_\phi dV; \tag{4.40}$$

$$\mathbf{L}_{\text{EM}} = \hat{\mathbf{z}}\varepsilon_0\int \rho E_\rho B_z dV. \tag{4.41}$$

These may now be evaluated for the typical electron vortex beam of Section 2.5, using the relevant electric fields of Chapter 3. This is carried out for the beams of finite radius and length, having $l = 0, 1, 3$ and 10, using the expressions for electric and magnetic fields obtained using the finite wavefunction of Eq. (3.23). The integrals of $\mathbf{P}_{\text{EM}}$ and $\mathbf{L}_{\text{EM}}$ should be evaluated over all space; however, as described in Section 2.5.3 the beam is considered to consist of a 'stack' of single electron wavefunctions, so the integral over z may be restricted to the beam length $L \approx 4$cm, in order to find the contribution per electron. It is not sensible to evaluate the total momentum of the beam of infinite radial extent; since the Bessel beam contains an infinite number of nodes, with each node carrying the same total current. Thus, the electric and magnetic fields approach a non-zero value at infinity, leading to an infinite total linear or angular momentum within the beam.

The results of the total linear and angular momenta for the finite beams[1] are summarised in Table 4.2.1 and Table 4.2.2 respectively. For the linear momentum, it is found that each beam carries approximately the same linear momentum in its field, and the minor discrepancies are considered

[1] In order to obtain the linear and angular momenta, the integrals of Eq. (4.40) and Eq. (4.41) were performed numerically using Mathematica. For the linear momentum the upper limit of the radial of Eq. (4.40) integral should be infinity, however it was found that the expression $E_\rho B_\phi \rho$ did not converge sufficiently quickly to obtain a sensible result. Instead, the limits for each integral have been set to $10^8\rho_{l,1}$, which is of the order of cm. Extrapolation of the fields to this point shows that they are effectively zero, being 10^8 times smaller than the field maximum, so that this limit is sufficient to show the order of magnitude of the electromagnetic momentum. For the angular momentum, this is no longer a problem, as the relevant magnetic field is identically zero outside of the beam radius, so that setting the upper limit to $\rho_{l,1}$ yields an exact result.

	$\mathbf{P}_{\mathrm{M}}(\mathrm{kg\,m\,s^{-1}})$	$\mathbf{P}_{\mathrm{EM}}(\mathrm{kg\,m\,s^{-1}})$	$\mathbf{P}_{\mathrm{EM}}/\mathbf{P}_{\mathrm{M}}$
$l = 0$	$\hbar k_z$	-6.12×10^{-34}	-2.53×10^{-12}
$l = 1$	$\hbar k_z$	-6.04×10^{-34}	-2.50×10^{-12}
$l = 3$	$\hbar k_z$	-6.00×10^{-34}	-2.48×10^{-12}
$l = 10$	$\hbar k_z$	-5.95×10^{-34}	-2.31×10^{-12}

Table 4.2.1: Magnitude of the mechanical and electromagnetic contributions to the total linear momenta of the electron vortex Bessel beams with $l = 0, 1, 3$ and 10.

	$\mathbf{L}_{\mathrm{M}}(\mathrm{J\,s})$	$\mathbf{L}_{\mathrm{EM}}(\mathrm{J\,s})$	$\mathbf{L}_{\mathrm{EM}}/\mathbf{L}_{\mathrm{M}}$
$l = 0$	0	0	–
$l = 1$	$\hbar$	-1.59×10^{-48}	-1.51×10^{-14}
$l = 3$	$3\hbar$	-3.53×10^{-48}	-1.12×10^{-14}
$l = 10$	$10\hbar$	-3.52×10^{-48}	-3.34×10^{-15}

Table 4.2.2: Magnitude of the mechanical and electromagnetic contributions to the total angular momenta of the electron vortex Bessel beams with $l = 0, 1, 3$ and 10.

to arise from the approximation made in the numerical calculation, since the total charge and current contained in each Bessel beam is the same. The ratio of electromagnetic to mechanical angular momentum appear to decrease with an increase in orbital angular momentum. Both $\mathbf{P}_{\mathrm{EM}}$ and $\mathbf{L}_{\mathrm{EM}}$ are extremely small compared to their mechanical counterparts; at these currents of $1\ \mu$A they are negligible.

4.3 Mechanical Rotation of a Nanoparticle

The electron vortex has been shown to cause rotation of nanoparticle placed within the beam, however the precise mechanism causing the rotation is as yet unclear [27, 28]. The exact mechanism of interaction will depend on the particularities of the nanoparticle, such as its shape and composition. For a dielectric medium, extra effects due to the fields of the vortex may arise, while for metallic particles excitations such as plasmon resonances may modify the interaction, though these effects will be small relative to the mechanical effects of elastic collisions between the electrons and the particle, since the probability of inelastic interactions is small for small particles.

The observations of Verbeeck *et al.* and Gnanavel *et al.* show conclusively the electron vortex induced rotation of nanoparticles [27, 28]. The confirmation of rotation in both cases was achieved by observation of the rotation of the crystal planes of the nanoparticle, however due to frictional forces the observed rates of rotation were very small, so that the particle achieved a rotation rate of the order of a few mrads^{-1} to tens of mrads^{-1}. Though the effect is small, the influence of the electron vorticity is clear, as the direction of rotation changes for beams with opposite vorticity. However, (unpublished) experimental observations at York show that the net rotation is accompanied by oscillations in both directions such that on small timescales the direction of rotation switches. It is also noted that in order to obtain any rotation, the nanoparticles must be

subject to the beam for some time, so that the support on which the particles are resting is damaged, making minimal contact with the particle [28]. These observations suggest that friction plays large role in these experiments. Since friction on the nanoscale is not well understood, it is difficult to obtain quantitative results regarding the elastic interaction of electron vortices with particles.

Two possible experiments for observation of nanoparticle rotation in the absence of friction are sketched below in Fig. 4.3.1. Both experiments involve a nanoparticle suspended in the field of the electron vortex - in the first scenario, depicted in Fig. 4.3.1a this is accomplished by laser trapping, while the particle in the second scenario is levitated by the combined action of two counter-propagating beams, as shown in Fig. 4.3.1b. The magnitude of possible rotation induced may now be estimated for both cases.

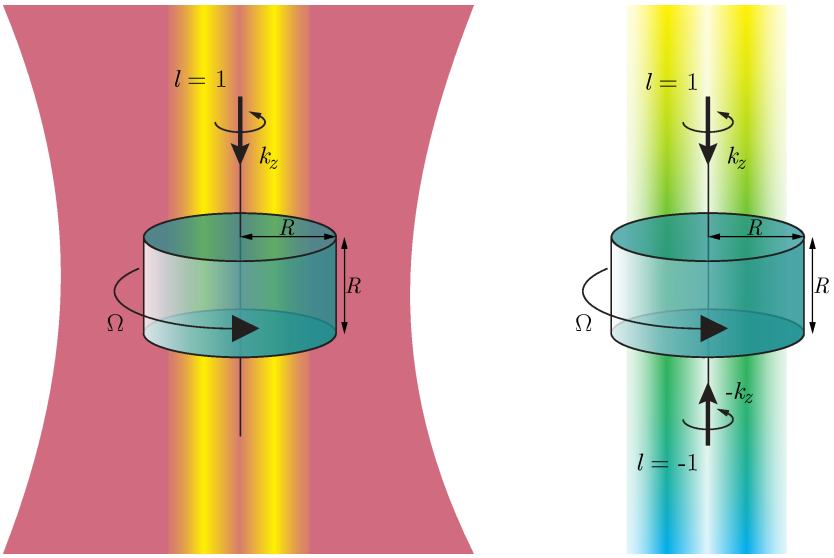

Figure 4.3.1: Proposed experiments to explore electron vortex induced rotation of nanoparticles in the absence of friction. (a) shows a cylindrical nanoparticle of radius and height R suspended in the laser field of optical tweezers (red), illuminated from above by an electron vortex (yellow). (b) shows the same nanoparticle balanced in the centre of two counter-propagating electron beams, one approaching the particle from above (yellow) the other from below (blue). The opposite orbital angular momentum of the counter-propagating beams gives a total angular momentum of $l_T = 2$. In both cases, the effect of elastic collisions with the beam induces a rotation with angular frequency Ω.

The laser-levitated particle of Fig. 4.3.1a is taken to be made of silica, with

$$R = 10^{-8}\,\mathrm{m} \qquad M = \rho_\mathrm{m}\pi R^3 \tag{4.42}$$

with the mass density of fused silica approximately $\rho_\mathrm{m} = 2.2 \times 10^3\,\mathrm{kg\,m^{-3}}$. The particle is placed into an optical trap, so that it is suspended in free space, and there are no friction forces acting. Illumination of the nanoparticle with an electron vortex will induce rotation with angular frequency

$$\Omega = \frac{L_\mathrm{TR}}{I}, \tag{4.43}$$

with L the total angular momentum transferred to the particle, and I the moment of inertia of the cylindrical particle. The angular frequency of the particle will increase with the continuous transfer of angular momentum from the beam, and the angular acceleration can be estimated by assuming a certain rate of transfer from the beam with a particular current I_z. Simulations indicate that a typical transfer would be expected to be approximately $0.1\hbar$ per electron [51], this suggests an average angular momentum transfer rate of

$$L_{\mathrm{TR}} = \frac{0.1\hbar I_z}{e}. \tag{4.44}$$

The angular acceleration is then

$$\alpha = \frac{0.1\hbar I_z}{eI}. \tag{4.45}$$

For the silica nanoparticle the angular momentum transfer gives an angular frequency of approximately 30 Hz after interaction with a single electron. In a beam with a current of $I_z = 1$ nA this suggests an angular acceleration of 1.9×10^{11} s^{-2}. This is extremely large, as despite the small beam current a large number of electrons pass through the beam in a second. This in line with the 'in principle infinite rotational energy' mentioned in [27], though in practice this will be limited by experimental factors.

This analysis may also be applied to the scenario involving counter-propagating beams depicted in Fig. 4.3.1b, in which the particle is constrained by the oppositely acting axial forces of the two beams. Assuming the beams are otherwise identical (same current, energy, momentum), and if the forward propagating beam has a winding number of l and the reverse propagating beam $-l$ then the total angular momentum of the beam will be $2l$. Assuming the same transfer of $0.1\hbar$ per electron suggests the resulting angular velocity and angular acceleration will be double those found above, namely 60 Hz and 3.8×10^{11} s^{-2} respectively for the silica nanoparticle, or 3.5H z and 2.2^{10} s^{-3} for a gold nanoparticle of the same dimensions.

Experiments of this type could be used to explore the effect of nanoscale friction, by providing a control environment in which to measure the unhindered motion to compare with the effect of interactions with various surfaces. Similar experiments may also be considered to explore viscous forces, for example by using nanoparticles suspended in liquids in a liquid-cell sample holder. The electron vortex provides a method by which particles may be moved transverse to a surface, so that friction between various surfaces and particles may be investigated directly; this transverse motion may also find application in nanomanipulation for various uses. In addition, such experiments may provide an opportunity to explore the effects of the transverse components of the linear and angular momentum densities, by slightly displacing the particle from the beam axis and studying the subsequent motion.

5

Interactions Between Optical Vortices and Atoms

The influence of optical vortices on matter has been investigated by several authors [14, 66, 68–71, 106] via several different methods. It is accepted that to leading order interactions, the optical vortex cannot couple to the internal degrees of freedom, including the atomic electron motion, via exchange of orbital angular momentum [14, 66, 68, 69, 71], and these results have been confirmed experimentally [107, 108], in both the paraxial and non-paraxial regimes.

The mechanism of an interaction between an optical vortex and atomic-type matter is considered here, in the paraxial approximation. The coordinate frame of the interaction and basis states of the vortex and atomic system is introduced in Section 5.1, before the full Lagrangian of the interacting system is presented in Section 5.2 and used to find the full system Hamiltonian, including vortex-atom interactions. In Section 5.3 the matrix element of the interaction Hamiltonian is used to determine the orbital angular momentum selection rules, and these results are discussed with reference to the theoretical and experimental literature in Section 5.4

The schematic of the interaction described here will form the basis for investigation of the similar interaction between atomic matter and an electron vortex. As such, the coordinate system introduced here will be common to both optical and electron vortex interactions, though we will show that the mechanism and results are drastically different.

5.1 The Coordinate System and Basis States

The coordinate frame of the interaction has its origin at the centre of the vortex beam, and is the cylindrical frame used previously to describe the vortex. The atom is free to move within the beam, and it is assumed that the electric field is approximately uniform over scales of the order of the atomic radius so that the dipole expansion is valid (as is shown in Section A.4 the gradient of the

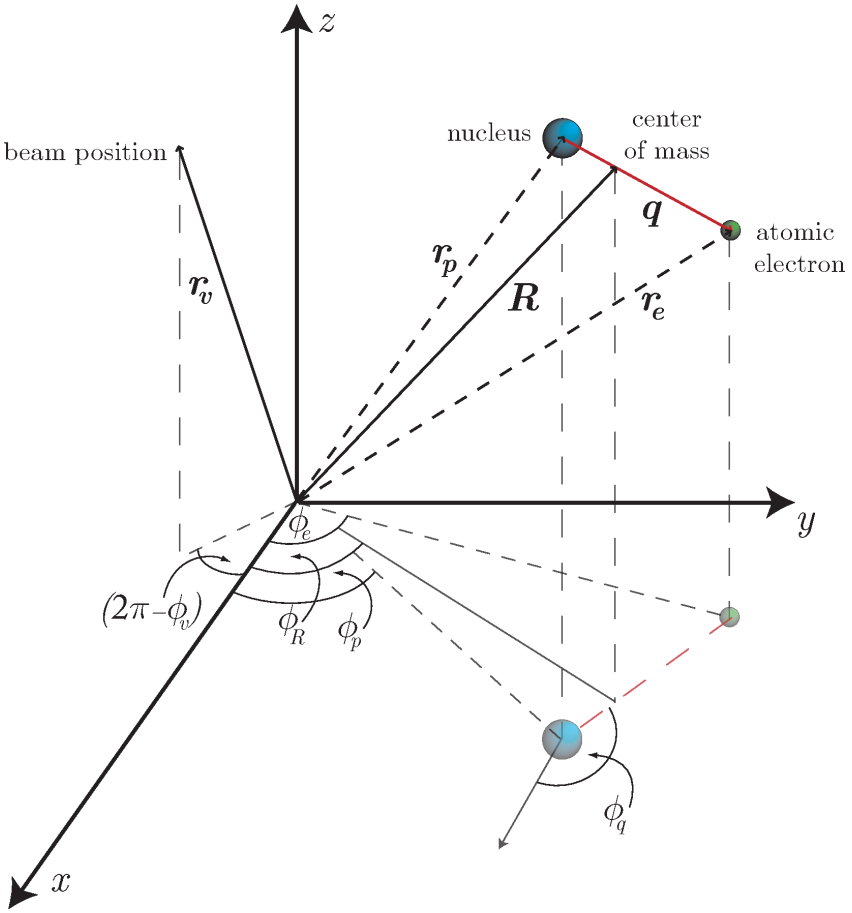

Figure 5.1.1: The relevant coordinate frames in the description of the interaction between a two-particle neutral system and Bessel-type optical or electron vortex beam (schematic). The vortex position variable, $\mathbf{r}_v$ relative to the laboratory frame is given in cylindrical coordinates; $\mathbf{R}$ is the position variable of the atomic center of mass, and $\mathbf{q}$ stands for the position variable of the internal (electron-type) motion, described in cylindrical coordinates about $\mathbf{r}_p$. The projections of the three position vector variables on the xy plane are seen to have azimuthal angular coordinates ϕ_v, ϕ_R, and ϕ_q respectively.

field contributes to the quadrupole interaction). The centre of mass of the atom is located at position $\mathbf{R}(\rho_R, \phi_R, z_R)$ relative to the origin, while the nuclear and atomic electron positions are denoted by $\mathbf{r}_p(\rho_p, \phi_p, z_p)$ and $\mathbf{r}_e(\rho_e, \phi_e, z_e)$ respectively. Position within the beam is indicated by $\mathbf{r}_v(\rho_v, \phi_v, z_v)$. The atomic electron is described slightly differently - with respect to a spherical coordinate system centered on the nucleus as is usual for the hydrogen atom. The position in this atomic frame is denoted by $\mathbf{q}(\rho_q, \phi_q, \theta_q)$, such that

$$\mathbf{r}_p + \mathbf{q} = \mathbf{r}_e. \tag{5.1}$$

The centre of mass position is defined as

$$\mathbf{R} = \frac{m_e \mathbf{r}_e + m_p \mathbf{r}_p}{M} \tag{5.2}$$

where $M = m_e + m_p$ is the total mass of the atom. The particle position variables are given in terms of $\mathbf{q}$ and $\mathbf{R}$ by

$$\mathbf{r}_e = \mathbf{R} + \frac{m_p}{M}\mathbf{q}; \qquad \mathbf{r}_p = \mathbf{R} - \frac{m_e}{M}\mathbf{q}. \tag{5.3}$$

Additionally, in this frame of reference the two-particle system possesses a total charge density given by

$$\tilde{\rho}_{\mathrm{A}}(\mathbf{r}) = e\delta(\mathbf{r} - \mathbf{r}_p) - e\delta(\mathbf{r} - \mathbf{r}_e). \tag{5.4}$$

This set up is demonstrated in Fig. 5.1.1, and is common to the atomic interactions of both the optical and electron vortex, and will be referred to in Chapter 6.

The quantum state of the atom is taken to be a product state of the eigenstates of the motion of both the atomic electron and atomic centre of mass:

$$|\psi_{\mathrm{atom}}\rangle = |\psi_q(\mathbf{q}); \psi_R(\mathbf{R})\rangle\,, \tag{5.5}$$

where $\psi_q(\mathbf{q})$ and $\psi_R(\mathbf{R})$ are the electronic and centre of mass eigenstates respectively. The internal electronic type motion is considered to be in a well defined hydrogenic state,

$$|\psi_q(\mathbf{q})\rangle = |\psi_q(\rho_q, \theta_q, \phi_q)\rangle = N_{n,\ell,m} Q_n(\rho_q) P_\ell^m(\cos(\theta_q)) e^{im\phi_q}, \tag{5.6}$$

where the integer ℓ is the internal orbital angular momentum (not to be confused with l, the vortex orbital angular momentum quantum number about the beam axis); m is the internal magnetic quantum number (such that $-\ell \leq m \leq \ell$), and n is the principal quantum number of the internal motion. $\mathcal{Q}_n(\rho_q)$ describes the radial part of the hydrogenic wavefunction.

The eigenstates of the centre of mass are taken to be product states of both its translational and rotational motion

$$|\psi_R(\mathbf{R})\rangle = N_R\,|\psi_R(\rho_R, \phi_R, z_R)\rangle = R(\rho_R) e^{iK_\perp \rho_R} e^{iK_z z_R} e^{iL\phi_R}, \tag{5.7}$$

where the subscript R indicates centre of mass coordinates relative to the laboratory frame. K_R and K_z are centre of mass wavevectors for the in-plane translational motion and motion along the z-axis, such that the total linear momentum of the centre of mass is given by $K^2 = K_z^2 + K_\perp^2$. L is

the orbital angular momentum quantum number of the centre of mass about the beam axis, such that the atom is free to rotate about the beam.

Treatment of the interaction proceeds from a Lagrangian formalism, from which the full Hamiltonian H, including the interaction Hamiltonian $H_{\text{int}}^{\text{OV}}$, is derived. The transition matrix element $\mathcal{M}_{\text{OV}}^{fi}$ is found from:

$$\mathcal{M}_{\text{OV}}^{fi} = \left\langle \psi_f \left| H_{\text{int}}^{\text{OV}} \right| \psi_i \right\rangle . \tag{5.8}$$

and will yield the orbital angular momentum selection rules of the interaction. From these selection rules it is possible to determine which final states are accessible from a specified initial state, from which it will be seen whether it is possible to access a final state in which orbital angular momentum is transferred between the vortex and the atom.

5.2 Lagrangian and Hamiltonian Formalism

In the coupling of initial and final atomic states by the optical vortex field we consider a minimum coupling prescription such that the interaction Hamiltonian takes the form $\mathbf{p} \cdot \mathbf{A}$. The interaction here will be fully quantised such that the magnetic vector potential $\mathbf{A}(\mathbf{R})$ takes the form of Eq. (2.24)

$$\hat{\mathbf{A}}(\mathbf{r}, t) = \mathbf{A}(\mathbf{r}, t)\hat{a}_{k_\perp, k_z} + \mathbf{A}^*(\mathbf{r}, t)\hat{a}^\dagger_{k_\perp, k_z}. \tag{5.9}$$

with $\hat{a}^\dagger_{\mathbf{k},l}$ and $\hat{a}_{\mathbf{k},l}$ respectively the creation and annihilation operators for a vortex photon with $k = \sqrt{k_\perp^2 + k_z^2}$ and orbital angular momentum $l\hbar$. For notational brevity, the hat notation for operators will be dropped.

5.2.1 Lagrangian formalism

The full Lagrangian of the atomic system coupled to the optical vortex may be written as

$$L = L_0^{\text{atom}} + L_0^{\text{OV}} + L_{\text{int}}^{\text{OV}}. \tag{5.10}$$

where L_0 is the component of the Lagrangian associated with the kinetic energy of free particles, L_0^{OV} the component associated with the existence of the electromagnetic field, and L_{int} that associated with the interaction of the charged particles with the field. Following standard Langrangian techniques such as [109] the full Lagrangian of any system of particles and electromagnetic fields may be written as

$$L = \underbrace{\frac{1}{2}\sum_\alpha m_\alpha \dot{\mathbf{r}}_\alpha{}^2}_{L_{\text{K}}} + \underbrace{\frac{\varepsilon_0}{2}\int \sum_\gamma \left(\mathbf{E}_\gamma^2(\mathbf{r}) - c^2\mathbf{B}_\gamma^2(\mathbf{r})\right) d^3r}_{L_{\text{EM}}} + \underbrace{\sum_{\alpha,\gamma} \left(q_\alpha \dot{\mathbf{r}}_\alpha \cdot \mathbf{A}\gamma(\mathbf{r}_\alpha) - q_\alpha \phi_\gamma(\mathbf{r}_\alpha)\right)}_{L_{\text{Int}}}, \tag{5.11}$$

for collection of particles indexed by α, and fields indexed by γ. L_{K} denotes the kinetic energy from the particle motion, L_{EM} the energy associated with the presence of the electromagnetic fields, and L_{Int} the interaction energy between the particle and fields. This general form will be applied to the atomic-optical vortex system described in Section 5.1. For our purposes here we consider a system of bound charges, rather than free, so we also require a term associated with the Coulomb potential

between the charged particles, which we write as $V_\beta(\mathbf{r}_\alpha)$, indicating the Coloumb potential at position $\mathbf{r}_\alpha$ due to charge q_β at $\mathbf{r}_\beta$. The standard Lagrangian of Eq. (5.11) then becomes

$$L = \frac{1}{2}\sum_\alpha m_\alpha \dot{\mathbf{r}}_\alpha{}^2 - \sum_{\alpha<\beta} q_\alpha V_\beta(\mathbf{r}_\alpha) + \frac{\varepsilon_0}{2}\int \sum_\gamma \left(\mathbf{E}_\gamma^2(\mathbf{r}) - c^2\mathbf{B}\gamma^2(\mathbf{r})\right) d^3r + \sum_{\alpha,\gamma}\left(q_\alpha \dot{\mathbf{r}}_\alpha \cdot \mathbf{A}\gamma(\mathbf{r}_\alpha) - q_\alpha \phi_\gamma(\mathbf{r}_\alpha)\right). \quad (5.12)$$

The scalar potentials $V_\beta(\mathbf{r}_\alpha)$ are given by

$$V_\beta(\mathbf{r}_\alpha) = \frac{1}{4\pi\varepsilon_0}\frac{q_\beta}{|\mathbf{r}_\beta - \mathbf{r}_\alpha|}. \quad (5.13)$$

This is responsible for the binding potential that holds the particle system together (i.e. the Coulomb potential within the atom), and is distinct from the scalar potential of the external electromagnetic field, $\phi(\mathbf{r})$ (in this case the vortex potential). The Lagrangians L_0^{atom}, L_0^{OV} and $L_{\text{int}}^{\text{OV}}$ may now be separated as

$$L_0^{\text{atom}} = \frac{1}{2}\sum_\alpha m_\alpha \dot{\mathbf{r}}_\alpha{}^2 - \sum_{\alpha<\beta} q_\alpha V_\beta(\mathbf{r}_\alpha); \quad (5.14)$$

$$L_0^{\text{OV}} = \frac{\varepsilon_0}{2}\int \sum_\gamma \left(\mathbf{E}_\gamma^2(\mathbf{r}) - c^2\mathbf{B}_\gamma^2(\mathbf{r})\right) d^3r; \quad (5.15)$$

$$L_{\text{int}}^{\text{OV}} = \sum_{\alpha,\gamma}\left(q_\alpha \dot{\mathbf{r}}_\alpha \cdot \mathbf{A}_\gamma(\mathbf{r}_\alpha) - q_\alpha \phi_\gamma(\mathbf{r}_\alpha)\right). \quad (5.16)$$

The electric and magnetic fields $\mathbf{E}_\gamma(\mathbf{r})$ and $\mathbf{B}_\gamma(\mathbf{r})$ may be written instead in terms of the associated scalar and vector potentials, $\phi_\gamma(\mathbf{r})$ and $\mathbf{A}_\gamma(\mathbf{r})$.

$$\mathbf{B}_\gamma(\mathbf{r}) = \nabla \times \mathbf{A}_\gamma(\mathbf{r}); \quad (5.17)$$

$$\mathbf{E}_\gamma(\mathbf{r}) = -\dot{\mathbf{A}}_\gamma(\mathbf{r}) - \nabla\phi_\gamma(\mathbf{r}), \quad (5.18)$$

which allows Eq. (5.15) to be written

$$L_0^{\text{OV}} = \frac{\varepsilon_0}{2}\int \sum_\gamma \left(\left(\dot{\mathbf{A}}_\gamma(\mathbf{r}) + \nabla\phi_\gamma(\mathbf{r})\right)^2 - c^2\left(\nabla \times \mathbf{A}_\gamma(\mathbf{r})\right)^2\right) d^3r. \quad (5.19)$$

Finally, the full Lagrangian of the system is

$$\begin{aligned} L^{\text{OV}} &= L_0^{\text{atom}} + L_0^{\text{OV}} + L_{\text{int}}^{\text{OV}} \\ &= \frac{1}{2}\sum_\alpha m_\alpha \dot{\mathbf{r}}_\alpha{}^2 - \sum_{\alpha<\beta} q_\alpha V_\beta(\mathbf{r}_\alpha) \\ &\quad + \frac{\varepsilon_0}{2}\int \sum_\gamma \left(\left(\dot{\mathbf{A}}_\gamma(\mathbf{r}) + \nabla\phi_\gamma(\mathbf{r})\right)^2 - c^2\left(\nabla \times \mathbf{A}_\gamma(\mathbf{r})\right)^2\right) d^3r \\ &\quad + \sum_{\alpha,\gamma}\left(q_\alpha \dot{\mathbf{r}}_\alpha \cdot \mathbf{A}_\gamma(\mathbf{r}_\alpha) - q_\alpha \phi_\gamma(\mathbf{r}_\alpha)\right). \end{aligned} \quad (5.20)$$

This general form is now applied to the specific case of the optical vortex and the hydrogenic system. The two particles $\alpha = 1, 2$ are the atomic electron and proton, with the familiar properties, and position vectors defined as in Fig. 5.1.1, while the single electromagnetic field $\gamma = 1$ in this case is that of the optical vortex. Applying this to Eq. (5.20) gives

$$\begin{aligned} L = \frac{1}{2}m_p\dot{\mathbf{r}}_p^2 + \frac{1}{2}m_e\dot{\mathbf{r}}_e^2 + \frac{1}{4\pi\varepsilon_0}\frac{e^2}{|\mathbf{q}|} \\ + \frac{\varepsilon_0}{2}\int\left(\left(\dot{\mathbf{A}}_{\mathrm{OV}}(\mathbf{r}) + \nabla\phi_{\mathrm{OV}}(\mathbf{r})\right)^2 - c^2\left(\nabla\times\mathbf{A}_{\mathrm{OV}}(\mathbf{r})\right)^2\right)d^3r \\ + -e\dot{\mathbf{r}}_e\cdot\mathbf{A}_{\mathrm{OV}}(\mathbf{r}_e) + e\phi_{\mathrm{OV}}(\mathbf{r}_e) \\ + e\dot{\mathbf{r}}_p\cdot\mathbf{A}_{\mathrm{OV}}(\mathbf{r}_p) - e\phi_{\mathrm{OV}}(\mathbf{r}_p), \end{aligned} \tag{5.21}$$

with

$$L_0^{\mathrm{atom}} = \frac{1}{2}m_p\dot{\mathbf{r}}_p^2 + \frac{1}{2}m_e\dot{\mathbf{r}}_e^2 + \frac{1}{4\pi\varepsilon_0}\frac{e^2}{|\mathbf{q}|} \tag{5.22}$$

$$L_0^{\mathrm{OV}} = \frac{\varepsilon_0}{2}\int\left(\left(\dot{\mathbf{A}}_{\mathrm{OV}}(\mathbf{r}) + \nabla\phi_{\mathrm{OV}}(\mathbf{r})\right)^2 - c^2\left(\nabla\times\mathbf{A}_{\mathrm{OV}}(\mathbf{r})\right)^2\right)d^3r \tag{5.23}$$

$$L_{\mathrm{int}}^{\mathrm{OV}} = -e\dot{\mathbf{r}}_e\cdot\mathbf{A}_{\mathrm{OV}}(\mathbf{r}_e) + e\phi_{\mathrm{OV}}(\mathbf{r}_{\mathrm{OV}}) + e\dot{\mathbf{r}}_p\cdot\mathbf{A}_{\mathrm{OV}}(\mathbf{r}_p) - e\phi_{\mathrm{OV}}(\mathbf{r}_p) \tag{5.24}$$

Writing the Lagrangian of Eq. (5.21) in terms of the centre of mass of the hydrogenic system will make it simpler to determine any transitions involving centre of mass states. Making use of Eq. (5.3), this gives

$$\begin{aligned} L = \frac{1}{2}m_p\left(\dot{\mathbf{R}} - \frac{m_e}{M}\dot{\mathbf{q}}\right)^2 + \frac{1}{2}m_e\left(\dot{\mathbf{R}} + \frac{m_p}{M}\dot{\mathbf{q}}\right)^2 + \frac{1}{4\pi\varepsilon_0}\frac{e^2}{|\mathbf{q}|} \\ + \frac{\varepsilon_0}{2}\int\left(\left(\dot{\mathbf{A}}_{\mathrm{OV}}(\mathbf{r}) + \nabla\phi_{\mathrm{OV}}(\mathbf{r})\right)^2 - c^2\left(\nabla\times\mathbf{A}_{\mathrm{OV}}(\mathbf{r})\right)^2\right)d^3r \\ - e\left(\dot{\mathbf{R}} + \frac{m_p}{M}\dot{\mathbf{q}}\right)\cdot\mathbf{A}_{\mathrm{OV}}(\mathbf{r}_e) + e\phi_{\mathrm{OV}}(\mathbf{r}_e) \\ + e\left(\dot{\mathbf{R}} - \frac{m_e}{M}\dot{\mathbf{q}}\right)\cdot\mathbf{A}_{\mathrm{OV}}(\mathbf{r}_p) - e\phi_{\mathrm{OV}}(\mathbf{r}_p), \end{aligned} \tag{5.25}$$

where the relevant field dependencies have been left in terms of $\mathbf{r}_e$ and $\mathbf{r}_p$ for ease of reading. Expanding:

$$\begin{aligned} L = \frac{1}{2}M\dot{\mathbf{R}}^2 + \frac{1}{2}\mu\dot{\mathbf{q}}^2 + \frac{1}{4\pi\varepsilon_0}\frac{e^2}{|\mathbf{q}|} \\ + \frac{\varepsilon_0}{2}\int\left(\left(\dot{\mathbf{A}}_{\mathrm{OV}}(\mathbf{r}) + \nabla\phi_{\mathrm{OV}}(\mathbf{r})\right)^2 - c^2\left(\nabla\times\mathbf{A}_{\mathrm{OV}}(\mathbf{r})\right)^2\right)d^3r \\ - e\dot{\mathbf{R}}\cdot\Delta_A - e\dot{\mathbf{q}}\cdot\Sigma_A + e\Delta_\phi \end{aligned} \tag{5.26}$$

where μ is the reduced mass of the atomic system, and the following shorthand has been introduced

$$\Delta_A = \mathbf{A}_{\mathrm{OV}}(\mathbf{r}_e) - \mathbf{A}_{\mathrm{OV}}(\mathbf{r}_p); \tag{5.27}$$

$$\Sigma_A = \frac{m_p}{M}\mathbf{A}_{\mathrm{OV}}(\mathbf{r}_e) + \frac{m_e}{M}\mathbf{A}_{\mathrm{OV}}(\mathbf{r}_p); \tag{5.28}$$

$$\Delta_\phi = \phi_{\mathrm{OV}}(\mathbf{r}_e) - \phi_{\mathrm{OV}}(\mathbf{r}_p). \tag{5.29}$$

The dynamical coordinates are now those of the centre of mass motion, $\mathbf{R}$, and internal coordinate $\mathbf{q}$. This is now a suitable Lagrangian from which to construct a Hamiltonian relevant to the states Eq. (5.7) and Eq. (5.6), such that the states are eigenfunctions of the Hamiltonian without interactions.

The full Hamiltonian is defined from the Lagrangian as

$$H = \sum_\alpha \mathbf{p}_\alpha \cdot \dot{\mathbf{r}}_\alpha + \int \sum_\gamma \mathbf{\Pi}_\gamma(\mathbf{r}) \cdot \dot{\mathbf{A}}_\gamma(\mathbf{r})\, d^3r - L, \tag{5.30}$$

where $\mathbf{p}_\alpha$ is the generalised momentum of the particle coordinates $\mathbf{r}_\alpha$,

$$\mathbf{p}_\alpha \equiv \frac{\partial L}{\partial \dot{\mathbf{r}}_\alpha}, \tag{5.31}$$

and $\Pi_\gamma(\mathbf{r})$ is the generalised coordinate momentum for the continuous field $\mathbf{A}_\gamma(\mathbf{r})$

$$\mathbf{\Pi}_\gamma(\mathbf{r}) \equiv \frac{\partial \mathcal{L}}{\partial \dot{\mathbf{A}}_\gamma(\mathbf{r})} \tag{5.32}$$

with $\mathcal{L}$ the Lagrangian density, such that $L = \int \mathcal{L} d^3r$. For the Lagrangian of Eq. (5.25) we find that the generalised momenta $\mathbf{p}_R$ and $\mathbf{p}_q$ are in the form

$$\mathbf{p}_R = M\dot{\mathbf{R}} - e\Delta_A; \tag{5.33}$$

$$\mathbf{p}_q = \mu\dot{\mathbf{q}} - e\Sigma_A. \tag{5.34}$$

This allows the Hamiltonian to be written as

$$H = \mathbf{p}_R \cdot \dot{\mathbf{R}} + \mathbf{p}_q \cdot \dot{\mathbf{q}} - \frac{1}{4\pi\varepsilon_0}\frac{e^2}{|\mathbf{q}|} - e\Delta_\phi + \varepsilon_0 \int \left(\dot{\mathbf{A}}^2_{\mathrm{OV}}(\mathbf{r}) + \left(\nabla\phi_{\mathrm{OV}}(\mathbf{r})\right)^2 + c^2\nabla \times \mathbf{A}_{\mathrm{OV}}(\mathbf{r})\right) d^3r \tag{5.35}$$

It can be seen that this Hamiltonian includes the interactions of the optical vortex field with the centre of mass and the atomic electron by eliminating the velocities $\dot{\mathbf{R}}$ and $\dot{\mathbf{q}}$ in favour of the generalised momenta:

$$H = \frac{\left[\mathbf{p}_R + e\Delta_A\right]^2}{2M} + \frac{\left[\mathbf{p}_q + e\Sigma_A\right]^2}{2\mu} - \frac{1}{4\pi\varepsilon_0}\frac{e^2}{|\mathbf{q}|} - e\Delta_\phi + \varepsilon_0 \int \left(\dot{\mathbf{A}}^2_{\mathrm{OV}}(\mathbf{r}) + \left(\nabla\phi_{\mathrm{OV}}(\mathbf{r})\right)^2 + c^2\nabla \times \mathbf{A}_{\mathrm{OV}}(\mathbf{r})\right) d^3r. \tag{5.36}$$

Finally, expanding gives

$$H = \frac{\mathbf{p}_R^2}{2M} + \frac{\mathbf{p}_q^2}{2\mu} + \frac{e}{M}\mathbf{p}_R \cdot \Delta_A + \frac{e}{\mu}\mathbf{p}_q \cdot \Sigma_A + e^2\Delta_A^2 + e^2\Sigma_A^2 - \frac{1}{4\pi\varepsilon_0}\frac{e^2}{|\mathbf{q}|} - e\Delta_\phi + \varepsilon_0 \int \left(\dot{\mathbf{A}}_{\text{OV}}^2(\mathbf{r}) + \left(\nabla\phi_{\text{OV}}(\mathbf{r})\right)^2 + c^2\nabla \times \mathbf{A}_{\text{OV}}(\mathbf{r})\right) d^3r, \quad (5.37)$$

and we may now write the Hamiltonian in the form

$$H = H_0^{(q)} + H_0^{(R)} + H_0^{\text{OV}} + H_{\text{int}}^{\text{OV}(q)} + H_{\text{int}}^{\text{OV}(R)}, \quad (5.38)$$

identifying the following terms in Eq. (5.37) with the ground state and interaction Hamiltonians:

$$H_0^{(q)} = \frac{\mathbf{p}_q^2}{2\mu} - \frac{1}{4\pi\varepsilon_0}\frac{e^2}{|\mathbf{q}|}; \quad (5.39)$$

$$H_0^{(R)} = \frac{\mathbf{p}_R^2}{2M}; \quad (5.40)$$

$$H_0^{\text{OV}} = \varepsilon_0 \int \left(\dot{\mathbf{A}}_{\text{OV}}^2(\mathbf{r}) + \left(\nabla\phi_{\text{OV}}(\mathbf{r})\right)^2 + c^2\nabla \times \mathbf{A}_{\text{OV}}(\mathbf{r})\right) d^3r; \quad (5.41)$$

$$H_{\text{int}}^{\text{OV}(q)} = \frac{e}{\mu}\mathbf{p}_q \cdot \Sigma_A + e^2\Sigma_A^2 - e\phi_{\text{OV}}(\mathbf{r}_e); \quad (5.42)$$

$$H_{\text{int}}^{\text{OV}(R)} = \frac{e}{M}\mathbf{p}_R \cdot \Delta_A + e^2\Delta_A^2 + e\phi_{\text{OV}}(\mathbf{r}_p). \quad (5.43)$$

The terms involving the vector potential, Δ_A and Σ_A, are defined in terms of the value of $\mathbf{A}(\mathbf{r})$ at the location of the atomic constituents, i.e. $\mathbf{A}(\mathbf{r}_e)$ and $\mathbf{A}(\mathbf{r}_p)$ have been left in terms of the position vectors of the electron and proton, instead of the center of mass and atomic coordinate relations of Eq. (5.3). When these relations are substituted, the vector potential may be expanded about the centre of mass position $\mathbf{R}$. Up to second order this gives

$$\mathbf{A}(\mathbf{r}_e) \approx \mathbf{A}(\mathbf{R}) + \frac{m_p}{M}(\mathbf{q} \cdot \nabla)\mathbf{A}(\mathbf{R})... \quad (5.44)$$

$$\mathbf{A}(\mathbf{r}_p) \approx \mathbf{A}(\mathbf{R}) - \frac{m_e}{M}(\mathbf{q} \cdot \nabla)\mathbf{A}(\mathbf{R})... \quad (5.45)$$

(see Appendix A.1 for full details). The leading order terms lead to the dipole approximation - it will be shown that only this term will give first order in $\mathbf{q}$, the atomic coordinate, in the interaction Hamiltonian of Eq. (5.42). Thus, in the dipole approximation, the relevant interaction Hamiltonians that will affect the atomic states are[1]

$$H_{\text{dip}}^{\text{OV}(q)} = \frac{2e}{\mu}\mathbf{p}_q \cdot \mathbf{A}(\mathbf{R}); \quad (5.46)$$

$$H_{\text{dip}}^{\text{OV}(R)} = \frac{e}{M}\mathbf{p}_R \cdot (\mathbf{q} \cdot \nabla)\mathbf{A}(\mathbf{R}). \quad (5.47)$$

The interaction Hamiltonian $H_{\text{dip}}^{\text{OV}(q)}$ will induce transitions between the atomic internal states, so this will be the focus hereafter. The Hamiltonian $H_{\text{dip}}^{\text{OV}(R)}$ will affect the centre of mass motion of the atom, due to its dipole moment [110], though this interaction is typically much smaller than

[1] Neglecting the potential $\phi_{\text{OV}}(\mathbf{r})$, as this will simply introduce an energy shift, and neglecting also terms non-linear in $\mathbf{A}(\mathbf{r})$, as we are interested in single-photon processes only.

the coupling of Eq. (5.46) [111].

5.3 Matrix element and Selection Rules

The matrix element of this interaction will now be evaluated, to determine the selection rules of the internal atomic interactions induced by the optical vortex field. The matrix element for this process is given by

$$\mathcal{M}^{fi}_{\mathrm{OV}} = \left\langle \psi^f_q(\mathbf{q}); \psi^f_{\mathrm{R}}(\mathbf{R}); n^f_{\mathrm{OV}} \middle| H^{\mathrm{OV}(q)}_{\mathrm{dip}} \middle| \psi^i_q(\mathbf{q}); \psi^i_{\mathrm{R}}(\mathbf{R}); n^i_{\mathrm{OV}} \right\rangle . \tag{5.48}$$

where the superscripts i and f denote initial and final states respectively and $n^{i,f}_{\mathrm{OV}}$ the number state of the optical vortex field. The interaction operator $H^{\mathrm{OV}(q)}_{\mathrm{dip}}$ couples different atomic states via the atomic momentum operator, $\mathbf{p}_q$. In the Coulomb gauge, $\mathbf{A}(\mathbf{R})$ and $\mathbf{p}_q$ commute. Additionally, we have the standard relationship $\mathbf{p}_q = \frac{im_e}{\hbar}[H^{(q)}_0, \mathbf{q}]$; this allows the interaction Hamiltonian to be written

$$H^{\mathrm{OV}(q)}_{\mathrm{dip}} = \frac{2iem_e}{\hbar\mu}\mathbf{A}(\mathbf{R}) \cdot [H^{(q)}_0, \mathbf{q}]. \tag{5.49}$$

This commutator operator acts on the atomic electron wavefunction only - applying this yields

$$\left\langle \psi^f_q(\mathbf{q}) \middle| [H^{(q)}_0, \mathbf{q}] \middle| \psi^i_q(\mathbf{q}) \right\rangle = \left\langle \psi^f_q(\mathbf{q}) \middle| H^{(q)}_0\mathbf{q} - \mathbf{q}H^{(q)}_0 \middle| \psi^i_q(\mathbf{q}) \right\rangle \tag{5.50}$$

$$= (\mathcal{E}_f - \mathcal{E}_i) \left\langle \psi^f_q(\mathbf{q}) \middle| \mathbf{q} \middle| \psi^i_q(\mathbf{q}) \right\rangle , \tag{5.51}$$

where $\mathcal{E}_f$ and $\mathcal{E}_i$ are respectively the initial and final energies of the atomic electron. This allows the full matrix element of Eq. (5.48) to be split into two parts, one acting on the atomic electron wavefunction, and the other acting on the centre of mass and optical vortex states:

$$\mathcal{M}^{fi}_{\mathrm{OV}} = \frac{2i(\mathcal{E}_f - \mathcal{E}_i)(m_e + m_p)}{\hbar m_p} \langle \psi^f_q(\mathbf{q}) | \hat{\boldsymbol{\epsilon}} \cdot \mathbf{d} | \psi^i_q(\mathbf{q}) \rangle \langle \psi^f_{\mathrm{R}}(\mathbf{R}); n^f_{\mathrm{OV}} | A(\mathbf{R}) | \psi^i_{\mathrm{R}}(\mathbf{R}); n^i_{\mathrm{OV}} \rangle . \tag{5.52}$$

The first part of the matrix element is simply the atomic transition dipole moment, with $\mathbf{d} = e\mathbf{q}$, the electric dipole moment. $A(\mathbf{R})$ is the scalar operator of the vortex vector potential, the optical polarisation vector $\hat{\boldsymbol{\epsilon}}$ being incorporated into the dipole matrix element, $\langle \hat{\boldsymbol{\epsilon}} \cdot \mathbf{d} \rangle_{fi}$. This separation of the optical vortex potential from the atomic electron states shows that the optical vortex will not be able to induce internal transition of the atom, at least in the dipole approximation.

Both parts of Eq. (5.52) must be evaluated to determine the selection rules for the full interaction. The details of this evaluation are given in Appendix A.2 and Appendix A.3. The full

matrix element of this dipole interaction is now

$$\begin{aligned}\mathcal{M}^f i_{\mathrm{OV}} =& \frac{2eE_0(\mathcal{E}_f - \mathcal{E}_i)(m_e + m_p)}{\hbar\omega m_p} N_i N_f \mathcal{A}_R \\ &\times \left[\sqrt{n^i_{\mathrm{OV}}}\delta(K_z - K'_z + k_z)\delta_{(L,L'-l)}\delta_{(n^f_{\mathrm{OV}},n^i_{\mathrm{OV}}-1)} \right. \\ &\left. - \sqrt{n^i_{\mathrm{OV}}+1}\delta(K_z - K'_z - k_z)\delta_{(L,L'+l)}\delta_{(n^f_{\mathrm{OV}},n^i_{\mathrm{OV}}+1)} \right] \\ &\times \hat{\boldsymbol{\varepsilon}} \cdot \left[\frac{\hat{\mathbf{x}} + i\hat{\mathbf{y}}}{2}\mathcal{A}^{\pm}_q \delta_{m,m'-1} + \frac{\hat{\mathbf{x}} - i\hat{\mathbf{y}}}{2}\mathcal{A}^{\pm}_q \delta_{m,m'+1} + \hat{\mathbf{z}}\mathcal{A}^0_q \delta_{m,m'} \right], \end{aligned} \tag{5.53}$$

with the factors $\mathcal{A}_R$, $\mathcal{A}^{\pm}_q$, and $\mathcal{A}^0_q$ arising from the full space integration, and defined in Appendix A.2 and Appendix A.3. For this interaction, there are two possible sources of orbital angular momentum exchange between the atom and the optical vortex field. Firstly, angular momentum may be transferred between the optical vortex and the centre of mass, by absorption or emission of a vortex photon, leading to changes in the rotational state of the centre of mass. Conservation of orbital angular momentum is ensured by the Kronecker deltas $\delta_{(L,L'-l)}$ and $\delta_{(L,L'+l)}$, giving an exchange of $l\hbar$. Total linear momentum is also conserved in the interaction, such that absorption or emission of a vortex photon changes the linear momentum of the centre of mass by $\pm\hbar k_z$.

Secondly, the internal state of the atomic electron may exchange orbital angular momentum with the light field, but this is only possible if the optical vortex is circularly polarised. In this case, the orbital angular momentum may change by $\pm\hbar$, due to the spin polarisation of the photon. This electric dipole interaction is the standard optical dipole interaction, as exploited in measurement techniques such as x-ray magnetic circular dichroism, and is not an effect of the vortex features of the light. It is found that it is not possible to transfer orbital angular momentum from the vortex directly to the internal electronic motion, even via quadrupole interactions (as shown in Appendix A.4).

In the case of the quadrupole interaction, the orbital angular momentum of both the electron and the centre of mass may couple together, such that a change of $\Delta m = \pm 1$ is possible, and the internal motion may also couple to the spin angular momentum of the light field so that a total change of up to $\pm 2\hbar$ is possible. However, the orbital angular momentum of the photon again only directly affects the centre of mass. This is the same result as that achieved by van Enk [14] and Babiker *et al.* [68]. The position of the centre of mass is required to act as a dynamical variable in order for any orbital angular momentum (distinct from the photon spin angular momentum) to be transferred to the internal electronic motion. We note also that, in the dipole approximation, the centre of mass must be free to rotate in order that any interaction occur. Thus the conclusion is that, barring transfer of photonic spin angular momentum, any angular momentum transfer between atomic matter and the optical vortex hinges on the rotational freedom of the centre of mass motion.

This result is consistent with previous theoretical calculations of interactions between atomic and molecular matter and Laguerre-Gaussian optical modes [14, 68–71, 106], using a variety of methods of analysis. The minimal coupling scheme applied here is similar to that used in [14], in which interaction between cold atoms and optical vortices were found to induce centre of mass motion, but not internal transitions. These same results are shown using a Power-Zienau-Woolley interaction formalism [68, 71], and also derived via symmetry considerations [69]. These results all show that the interactions mechanisms pertaining to the spin and orbital angular momenta of the beam are quite distinct, and in the dipole approximation it is solely the spin angular momentum of the beam that affects the internal motion, rather than the total spin and angular momenta combined. The full and meaningful separation of spin and orbital angular momentum is valid only within the paraxial approximation [15], however even beyond this approximation it is also found that a hydrogenic atom may emit (and therefore absorb) a Bessel photon such that only the orbital angular momentum of the atomic centre of mass is changed [70]. Even outside of the paraxial limit it is the field polarisation, rather than the photon orbital angular momentum, that affects the internal motion of the atom.

In contrast to those results discussed above, results found by Alexandrescu *et al.* for ionised molecular matter show that, in the dipole approximation, it is possible to couple the internal electronic orbital angular momentum with the other rotational degrees of freedom of the molecule [106], though the optical vortex angular momentum still does not directly couple to the internal motion. It is found that, for ionised molecules such as H_2^+, orbital angular momentum may be transferred between the optical vortex and the three molecular angular momentum subsystems - internal electronic motion, centre of mass motion, and rotation of the molecule about the centre of mass axis - such that the internal angular momentum changes by one unit, with a corresponding reverse change in the rotational angular momentum, assisted by the centre of mass motion [106]. This result displays a similar mechanism to that of the quadrupole interaction discussed above for the hydrogenic atom - in the molecular case the rotational degree of freedom may couple directly to the vortex angular momentum, alongside coupling between the internal and rotational angular momentum. The existence of the extra degree of freedom in the molecular rotation allows the interaction to occur in the dipole interaction. This result is yet to be shown experimentally.

To date, experimental results have shown that orbital angular momentum cannot be transferred from the optical field to the internal electronic motion [107, 108]. Optical vortices do not allow for observation of optical activity of chiral materials, as demonstrate by Araoka *et al.* in the comparison of absorption of light by chiral molecules having various spin and orbital angular momentum polarisations [107]. The samples chosen for the investigation were the $(+)$- and $(-)$-enantiomers[2] of a helicene bisquinone derivative that exhibits significant chiral optical activity at a wavelength of 514.5nm, giving a chiral dichroism signal of $\mathrm{CD} = 60 - 90$ mdeg [3] [107]. In this experiment, the

[2] An enantiomer being one of the particular forms of a the two spatial structures available for a chiral compound.

[3] Here, a chiral dichroism signal, indicates a difference in absorption of the two different spin polarisations of light [107],

$$\mathrm{CD} = \frac{I_{\sigma=+1} - I_{\sigma=-1}}{I_{\sigma=+1} + I_{\sigma=-1}} C_\theta, \tag{5.54}$$

chiral dichroism CD is measured for both enantiomers for light with orbital angular momentum $l = 0, \pm 1$. The total angular momentum flux of the light has contributions from both the spin and orbital angular momentum, such that the CD signal will be significantly altered if the chiral molecule interacts with the *total* angular momentum of the light. This is due to the presence of orbital angular momentum breaking the symmetry of the total orbital angular momentum on the exchange of left and right circular spin polarisations.

The results of this experiment found no such symmetry breaking. For both $(+)$- and $(-)$-enantiomers the measured (spin) chiral dichroism signals were the same for the non-chiral Hermite-Gaussian HG_{00} and the Laguerre-Gaussian $l = 1$ vortex beams, LG^{+}_{01} and LG^{-}_{01}. This result indicates that only the spin polarisation of the beam is relevant for the optical activity of the sample, and confirms the theoretical predictions that the optical orbital angular momentum does not couple to the internal degrees of freedom responsible for molecular chirality [69].

The later experiment by Löffler *et al.* [108] sought to determine whether this still holds in the non-paraxial regime, in which spin and orbital angular momentum are inseparable from the total orbital angular momentum [15]. The investigated samples in this case were cholesteric polymer films of a mixture of chiral and achiral polymers, which are arranged in helical planes of parallel molecules, so that the overall structure has spatial chirality, in addition to the molecular chirality. This cholesteric structure arises from alignment of polymer molecules in layers, the orientation of which changes layer by layer such that eventually a full, 2π rotation of orientation occurs. The presence of the chiral polymers allows this to happen in this case - cholesteric films are not formed by achiral molecules. For such a film, the optical activity is such that light of a particular circular polarisation will be reflected, and the other transmitted, leading to 50% transmission of linearly polarised light. The reflection wavelength at which this effect occurs is tunable by the ratio of chiral to achiral polymers [108].

The optical vortex light was generated by a spatial light modulator acting on linearly polarised light, and was then focused through a high numerical aperture lens, to ensure non-paraxiality. The normalised transmission signal was then measured:

$$\Delta = \frac{\mathrm{CD}_{l=+p} - \mathrm{CD}_{l=-1}}{\mathrm{CD}_{l=+p} + \mathrm{CD}_{l=-1}} \tag{5.55}$$

and it was found that $\Delta = 0$ for all frequencies, including the chiral dichroism reflection resonance frequency. Thus, no effect of the orbital angular momentum on the spin optical activity was observed, in agreement with the earlier experiment of Araoka *et al.* . The experiment of Löffler *et al.* confirmed these previous results with an order of magnitude increase in precision, and also showed that the spin to orbital angular momentum conversion in a high numerical aperture lens is not a reversible process [112].

Further to the experimental verification that, to leading order, orbital angular momentum may not be transferred to internal degrees of freedom, it is now experimentally established that coupling

where $I_{\sigma=\pm 1}$ is the light intensity transmitted by the sample, with conversion coefficient C_θ, having units mdegs. The chiral dichroism signal effectively represents the degree of elliptical polarisation that will be induced in a beam of initially unpolarised light transmitted through the sample, and as such has the units of an angle. The two enantiomers will respond oppositely to each polarisation, so that their chiral dichroism signals should be, barring other effects, equal in magnitude, and opposite in sign.

the rotation of a particle's centre of mass to an optical vortex beam is possible [5]. This fact has formed the basis for the application of optical vortex beams to optical tweezers, producing optical spanners that rotate the particle in the light field. These optical spanners have found applications in micromanipulation [8, 9] as well as in fundamental experimental studies of the action of optical vortices on matter [5–7].

O God, I could be bounded in a nut shell and count myself a king of infinite space, were it not that I have bad dreams.

W. Shakespeare, *Hamlet*, Act II Scene II

6

Interactions Between Electron Vortices and Atoms

The results of EELS in magnetised iron published by Verbeeck *et al.* [24] are very interesting, as they indicate an electronic transition induced by the vortex beam acting on the atoms in the sample, in contrast to the optics interaction shown in Chapter 5. We seek here to explain the underlying interaction, and to investigate the conclusion of Verbeeck *et al.* that the interaction dipole-like, as in the XMCD case. This is achieved by the study of the simplest possible interacting system - the Bessel electron beam and a hydrogen-like atom. Additionally, the interaction mechanism considered is the Coulomb interaction only; as the energy of an electron in an electron microscope is much greater than that within the atom, exchange effects can be neglected. As indicated above, we find that the interaction may indeed proceed via a dipole transition, unlike the case of an optical vortex [14, 66, 68–70, 106]. In the following analysis, we look predominantly at the angular effects of the interaction - to determine whether, in principle, orbital angular momentum may be exchanged between the vortex beam and atom.

Using a similar method as in Chapter 5, the interaction Hamiltonian is derived from the full Lagrangian of the interacting system and presented in Section 6.1. Two different methods are used to obtain the dipole selection rules of the interaction Hamiltonian. Firstly, a direct multipolar expansion of the Hamiltonian is considered in Section 6.2. This method proceeds similarly to the analysis of the optical interaction of Chapter 5 and the selection rules obtained by this method my be directly compared with those for the interaction with the optical vortex. Secondly, the selection rules are obtained by constructing an effective Hamiltonian incorporating an expansion of the electron vortex wavefunction itself, shown in Section 6.3. This method has the advantage that the spatial dependence of the interaction is clear, leading to a suggestion of a novel application of electron vortex beams to EELS chiral dichroism experiments. In Section 6.5 the selection rules obtained in each case are used to analyse the results of the Verbeeck experiment, by explicit analysis of the specific core-level transitions in the iron L_2 and L_3 edges. A comparison of the results

obtained via the two expansion methods is made in Section 6.4, while the selection rules of the electron vortex interaction are compared with those of the optical vortex interaction of the previous chapter in Section 6.6.

The results obtained via the Hamiltonian expansion have been published [65, 66]. A comparison of the electron and optical vortex-atom interactions, and the explicit analysis of the particular transitions in magnetised iron were also included in [66].

6.1 Lagrangian and Hamiltonian

The theoretical framework here is similar to that described in Section 5.1. The physical system is again described as a vortex beam interacting with a hydrogenic atom, with well defined electronic and centre of mass states. Rather than the vector potential of the optical vortex, the electon vortex is described by a wavefunction; the Coulomb interaction between the vortex and the hydrogenic atom is evaluated as an interaction Hamiltonian meidating the transition between two distinct initial and final product states of the vortex, atomic electron and atomic centre of mass system. In order to find the interaction Hamiltonian, we describe the system by first writing directly the Lagrangian of the system, as was the case for the interaction with the optical vortex. The atomic part of the Lagrangian takes the same form, however the vortex and interaction components now become

$$L^{\mathrm{EV}} = \frac{1}{2}m_e\dot{\mathbf{r}}_e^2 + \frac{1}{2}m_p\dot{\mathbf{r}}_p^2 + \frac{e^2}{4\pi\varepsilon_0}\frac{1}{|\mathbf{r}_p - \mathbf{r}_e|} + \frac{1}{2}m_e\dot{\mathbf{r}}_v^2 - \int \tilde{\rho}_{\mathrm{A}}(\mathbf{r})\Phi(\mathbf{r})d^3r, \tag{6.1}$$

where $\tilde{\rho}_{\mathrm{A}}(\mathbf{r})$ is the atomic charge density given by

$$\tilde{\rho}_{\mathrm{A}}(\mathbf{r}) = e\delta(\mathbf{r} - \mathbf{r}_p) - e\delta(\mathbf{r} - \mathbf{r}_e), \tag{5.4}$$

and the Coulomb potential, $\Phi(\mathbf{r})$ is

$$\Phi(\mathbf{r}) = -\frac{e}{4\pi\epsilon_0}\frac{1}{|\mathbf{r}_v - \mathbf{r}|}, \tag{6.2}$$

such that

$$\int \tilde{\rho}_{\mathrm{A}}(\mathbf{r})\Phi(\mathbf{r})d^3r = \frac{e^2}{4\pi\epsilon_0}\left(\frac{1}{|\mathbf{r}_v - \mathbf{r}_e|} - \frac{1}{|\mathbf{r}_v - \mathbf{r}_p|}\right). \tag{6.3}$$

As we are interested in the effects of the interaction on the atomic electron, the atomic electron coordinate $\mathbf{r}_e = \mathbf{r}_p + \mathbf{q}$ may be substituted to give

$$L^{\mathrm{EV}} = \frac{1}{2}m_e(\dot{\mathbf{r}}_p+\dot{\mathbf{q}})^2+\frac{1}{2}m_p\dot{\mathbf{r}}_p^2+\frac{1}{2}m_e\dot{\mathbf{r}}_v^2+\frac{e^2}{4\pi\epsilon_0}\left(\frac{1}{|\mathbf{r}_v - \mathbf{r}_p|} - \frac{1}{|\mathbf{r}_v - \mathbf{r}_p - \mathbf{q}|} + \frac{1}{|\mathbf{q}|}\right). \tag{6.4}$$

As before, we find the interaction Hamiltonian using standard Lagrangian techniques [109]

$$H = \sum_i \mathbf{p}_i \cdot \dot{\mathbf{r}}_i - L, \tag{6.5}$$

where conjugate momenta in this case are

$$\mathbf{p}_p = \frac{\partial L}{\partial \dot{\mathbf{r}}_p} = m_e(\dot{\mathbf{r}}_p + \dot{\mathbf{q}}) + m_p\dot{\mathbf{r}}, \tag{6.6}$$

$$\mathbf{p}_q = \frac{\partial L}{\partial \dot{\mathbf{q}}} = m_e(\dot{\mathbf{r}}_p + \dot{\mathbf{q}}), \tag{6.7}$$

$$\mathbf{p}_v = \frac{\partial L}{\partial \dot{\mathbf{r}}_v} = m_e\dot{\mathbf{r}}_v. \tag{6.8}$$

This gives the full Hamiltonian as

$$H^{\text{EV}} = \frac{1}{2}M\dot{\mathbf{r}}_p^2 + \frac{1}{2}m_e\dot{\mathbf{q}}^2 + \frac{1}{2}m_e\dot{\mathbf{r}}_v^2 - \frac{e^2}{4\pi\epsilon_0}\left(\frac{1}{|\mathbf{r}_v - \mathbf{r}_p|} - \frac{1}{|\mathbf{r}_v - \mathbf{r}_p - \mathbf{q}|} + \frac{1}{|\mathbf{q}|}\right), \tag{6.9}$$

where $M = m_p + m_e$, the total atomic mass. The interaction Hamiltonian is thus

$$\hat{H}^{\text{B}}_{\text{Int}} = \frac{e^2}{4\pi\varepsilon_0}\left(\frac{1}{|\mathbf{r}_v - \mathbf{r}_p - \mathbf{q}|} - \frac{1}{|\mathbf{r}_v - \mathbf{r}_p|}\right), \tag{6.10}$$

The interaction Hamiltonian found in this way is precisely the Coulomb interaction between the three particles in the system, as can be written directly from the relative positions of the particles. However, this is not a 'good' Hamiltonian to apply to the centre of mass states of Eq. (5.7), as it is not given in terms of the centre of mass position, but rather the nuclear position. As before, we may find a suitable Hamiltonian by writing the atomic electron and nucleus positions as in Eq. (5.3):

$$\mathbf{r}_e = \mathbf{R} + \frac{m_p}{M}\mathbf{q}; \qquad \mathbf{r}_p = \mathbf{R} - \frac{m_e}{M}\mathbf{q}. \tag{5.3}$$

Applying this to the Lagrangian of Eq. (6.1) gives a Lagrangian of the form

$$L^{\text{CM}} = \frac{1}{2}m_e(\dot{\mathbf{R}} + \frac{m_p}{M}\dot{\mathbf{q}})^2 + \frac{1}{2}m_p(\dot{\mathbf{R}} - \frac{m_e}{M}\dot{\mathbf{q}})^2 + \frac{1}{2}m_e\dot{\mathbf{r}}_v^2 + \frac{e^2}{4\pi\epsilon_0}\left(\frac{1}{|\mathbf{r}_v - \mathbf{R} + \frac{m_e}{M}\mathbf{q}|} - \frac{1}{|\mathbf{r}_v - \mathbf{R} - \frac{m_p}{M}\mathbf{q}|} + \frac{1}{|\mathbf{q}|}\right). \tag{6.11}$$

The canonical momenta of the generalised coordinates $\mathbf{r}_v$, $\mathbf{R}$ and $\mathbf{q}$ are then

$$\mathbf{p}_R = m_e\dot{\mathbf{R}}; \tag{6.12}$$

$$\mathbf{p}_q = \mu\dot{q}; \tag{6.13}$$

$$\mathbf{p}_v = m_e\dot{\mathbf{r}}_v; \tag{6.14}$$

so that the Hamiltonian is then given by

$$H^{\text{CM}} = \frac{1}{2}m_e\dot{\mathbf{R}}^2 + \frac{1}{2}\mu\dot{q}^2 + \frac{1}{2}m_e\dot{\mathbf{r}}_v^2 - \frac{e^2}{4\pi\epsilon_0}\left(\frac{1}{|\mathbf{r}_v - \mathbf{R} + \frac{m_e}{M}\mathbf{q}|} - \frac{1}{|\mathbf{r}_v - \mathbf{R} - \frac{m_p}{M}\mathbf{q}|} + \frac{1}{|\mathbf{q}|}\right), \tag{6.15}$$

with

$$H_{\text{Int}}^{\text{CM}} = -\frac{e^2}{4\pi\epsilon_0}\left(\frac{1}{|\mathbf{r}_v - \mathbf{R} + \frac{m_e}{M}\mathbf{q}|} - \frac{1}{|\mathbf{r}_v - \mathbf{R} - \frac{m_p}{M}\mathbf{q}|}\right). \tag{6.16}$$

We now have two distinct Hamiltonians for the same interaction. $H_{\text{Int}}^{\text{CM}}$, the Hamiltonian involving the centre of mass coordinate, is the appropriate Hamiltonian for finding the selection rules via multipolar expansion of the interaction Hamiltonian, and can be compared directly to the optical vortex results of the previous chapter; while it will be shown that for the second approach, involving multipolar expansions of the wavefunctions themselves, the basic Coulomb Hamiltonian of Eq. (6.9) is appropriate.

As before, we evaluate the transition matrix element of the interaction Hamiltonian, in order to determine the selection rules of the interaction. In this case, the initial and final wavefunctions are product states of the electron vortex wavefunction as well as the atomic electron and the wavefunctions of either the centre of mass or nucleus, so that the matrix element is found from

$$\mathcal{M}_{fi} = \left\langle \psi_v^f; \psi_e^f; \psi_{R,p}^f \middle| \hat{H}_{\text{int}}^{\text{B, CM}} \middle| \psi_v^i; \psi_e^i; \psi_{R,p}^i \right\rangle. \tag{6.17}$$

The wavefunctions of the electron vortex beam are those described above in Section 2.2: the Bessel beam vortex functions of (2.13). In the current notation, as developed in Section 5.1, the vortex wavefunctions are written (the time dependent factor of $e^{-i\omega t}$ is irrelevant to current purposes, and can be dropped),

$$\psi_v(\rho_v, \phi_v, z_v) = N_l J_l(k_\perp \rho_v) e^{il\phi_v} e^{ik_z z_v}. \tag{6.18}$$

We now proceed to evaluate the above matrix element by expansion into a multipolar series. This will allow the dipole and other multipoles to be identified and compared to the dipole interaction of the optical vortex in Section 5.3. Two methods for doing so are here presented: firstly, the Hamiltonian is expanded in a multipolar series and secondly, an effective Hamiltonian is constructed by expanding the vortex wavefunction about the atomic nucleus. The first case is a general treatment, as it does not depend on the nature of the vortex wavefunctions, while the second relies on specific properties of the Bessel function. The advantage of the second method is that the variation of the interaction strength with location of the atom relative to the beam axis is more readily apparent.

6.2 Multipolar Expansion of Hamiltonian

The Hamiltonian of Eq. (6.16) may be expanded about the atomic centre of mass, expressing the interaction as a series of multipolar interaction terms in powers of the dipole length of the atomic electron, ρ_q. The first term in Eq. (6.16) can be written as

$$\frac{1}{|\mathbf{r}_v - \mathbf{R} + \frac{m_e}{M}\mathbf{q}|} = \frac{1}{\sqrt{(\mathbf{r}_v - \mathbf{R})^2 + 2\frac{m_e}{M}\mathbf{q}\cdot(\mathbf{r}_v - \mathbf{R}) + \frac{m_e^2}{M^2}\mathbf{q}^2}} \tag{6.19}$$

$$= \frac{1}{|\mathbf{r}_v - \mathbf{R}|} \cdot \frac{1}{\sqrt{1 - 2\frac{m_e}{M}\frac{\mathbf{q}\cdot(\mathbf{r}_v - \mathbf{R})}{|\mathbf{r}_v - \mathbf{R}|^2} + \frac{m_e^2}{M^2}\frac{\mathbf{q}^2}{|\mathbf{r}_v - \mathbf{R}|^2}}}. \tag{6.20}$$

The square root in (6.20) can now be expanded as a Taylor series. Expanding up to second order we have

$$\frac{1}{|\mathbf{r}_v - \mathbf{R} + \frac{m_e}{M}\mathbf{q}|} \approx \frac{1}{|\mathbf{r}_v - \mathbf{R}|}\left[1 - \frac{1}{2}\left(\frac{m_e^2}{M^2}\frac{\mathbf{q}^2}{|\mathbf{r}_v - \mathbf{R}|^2} + 2\frac{m_e}{M}\frac{\mathbf{q}\cdot(\mathbf{r}_v - \mathbf{R})}{|\mathbf{r}_v - \mathbf{R}|^2}\right) + \frac{3}{8}\left(\frac{m_e^4}{M^4}\frac{\mathbf{q}^4}{|\mathbf{r}_v - \mathbf{R}|^4} + 4\frac{m_e^4}{M^4}\frac{(\mathbf{q}\cdot(\mathbf{r}_v - \mathbf{R}))^2}{(\mathbf{r}_v - \mathbf{R})^4} + 2\frac{m_e^3}{M^3}\frac{\mathbf{q}^2(\mathbf{q}\cdot(\mathbf{r}_v - \mathbf{R}))}{|\mathbf{r}_v - \mathbf{R}|^4}\right)\right]. \tag{6.21}$$

Similar expansion of the second term yields

$$\frac{1}{|\mathbf{r}_v - \mathbf{R} - \frac{m_p}{M}\mathbf{q}|} \approx \frac{1}{|\mathbf{r}_v - \mathbf{R}|}\left[1 - \frac{1}{2}\left(\frac{m_p^2}{M^2}\frac{\mathbf{q}^2}{|\mathbf{r}_v - \mathbf{R}|^2} - 2\frac{m_p}{M}\frac{\mathbf{q}\cdot(\mathbf{r}_v - \mathbf{R})}{|\mathbf{r}_v - \mathbf{R}|^2}\right) + \frac{3}{8}\left(\frac{m_p^4}{M^4}\frac{\mathbf{q}^4}{|\mathbf{r}_v - \mathbf{R}|^4} + 4\frac{m_p^4}{M^4}\frac{(\mathbf{q}\cdot(\mathbf{r}_v - \mathbf{R}))^2}{|\mathbf{r}_v - \mathbf{R}|^4} - 2\frac{m_p^3}{M^3}\frac{\mathbf{q}^2(\mathbf{q}\cdot(\mathbf{r}_v - \mathbf{R}))}{|\mathbf{r}_v - \mathbf{R}|^4}\right)\right]; \tag{6.22}$$

subtracting Eq. (6.22) from Eq. (6.21) gives

$$H_{\text{Int}}^{\text{CM}} = \frac{e^2}{4\pi\varepsilon_0}\frac{1}{|\mathbf{r}_v - \mathbf{R}|}\left[-\frac{1}{2}\left(\frac{(m_e^2 - m_p^2)}{M^2}\frac{\mathbf{q}^2}{|\mathbf{r}_v - \mathbf{R}|^2} + 2\frac{(m_e - m_p)}{M}\frac{\mathbf{q}\cdot(\mathbf{r}_v - \mathbf{R})}{|\mathbf{r}_v - \mathbf{R}|^2}\right) + \frac{3}{8}\left(\frac{(m_e^4 - m_p^4)}{M^4}\frac{\mathbf{q}^4}{|\mathbf{r}_v - \mathbf{R}|^4} + 4\frac{(m_e^4 - m_p^4)}{M^4}\frac{(\mathbf{q}\cdot(\mathbf{r}_v - \mathbf{R}))^2}{|\mathbf{r}_v - \mathbf{R}|^4} + 2\frac{(m_e^3 - m_p^3)}{M^3}\frac{\mathbf{q}^2(\mathbf{q}\cdot(\mathbf{r}_v - \mathbf{R}))}{|\mathbf{r}_v - \mathbf{R}|^4}\right)\right]. \tag{6.23}$$

The Hamiltonian of Eq. (6.16) has now been expanded in powers of $\mathbf{q}$, allowing us to write

$$\hat{H}_{\text{int}} = \hat{H}_{\text{int}}^{\text{dip}} + \hat{H}_{\text{int}}^{\text{quad}} + \hat{H}_{\text{int}}^{\text{hex}} \ldots, \tag{6.24}$$

where the dipole terms have been identified as those of first order in q, the quadrupole as those of second order etc., so that

$$\hat{H}_{\text{Int}}^{\text{dip}} = \frac{e^2}{4\pi\varepsilon_0}\frac{(m_p - m_e)}{M}\frac{\mathbf{q}\cdot(\mathbf{r}_v - \mathbf{R})}{|\mathbf{r}_v - \mathbf{R}|^3}; \tag{6.25}$$

$$\hat{H}_{\text{Int}}^{\text{quad}} = \frac{e^2}{8\pi\varepsilon_0}\left[\frac{(m_p^2 - m_e^2)}{M^2}\frac{\mathbf{q}^2}{|\mathbf{r}_v - \mathbf{R}|^3} + 3\frac{(m_e^4 - m_p^4)}{M^4}\frac{(\mathbf{q}\cdot(\mathbf{r}_v - \mathbf{R}))^2}{|\mathbf{r}_v - \mathbf{R}|^5}\right]. \tag{6.26}$$

We can now look at the possibility of an atomic electron transition being induced by the interaction with the vortex beam, and the selection rules of such an interaction, using Eq. (6.17). Here, the key piece of information we are looking for is whether any exchange of orbital angular momentum between the components of the system is possible. In order to determine this, we can

look simply at the azimuthal angular parts of the matrix element, since it is these that are affected by the angular momentum in the system.

6.2.1 Matrix Element in the Dipole Approximation

Here, we focus on the vortex interaction with the atom via the dipole interaction Hamiltonian of Eq. (6.25). This will enable clear comparisons to be made with the results of the optical vortex interaction of the previous chapter and previous investigations [14, 68].

Similar to the optical vortex interaction, the dipole matrix element may be written as a scalar product of two separate matrix elements - splitting the Hamiltonian into the factors that affect the atomic electron, and those that affect the vortex and the centre of mass states:

$$\mathcal{M}^{fi}_{\mathrm{EV}} = \frac{e^2}{4\pi\varepsilon_0}\frac{(m_p - m_e)}{M}\left\langle \psi^f_q(\mathbf{q}) \,\middle|\, \mathbf{q} \,\middle|\, \psi^i_q(\mathbf{q})\right\rangle \cdot \left\langle \psi^f_v(\mathbf{r}_v);\psi^f_p(\mathbf{R}) \middle| \frac{\mathbf{r}_v - \mathbf{R}}{|\mathbf{r}_v - \mathbf{R}|^3} \middle| \psi^i_v(\mathbf{r}_v);\psi^i_R(\mathbf{R})\right\rangle . \quad (6.27)$$

The first part of this matrix element may be expressed as the electric dipole matrix element,

$$\boldsymbol{\mathcal{D}} = \left\langle \psi^f_q(\mathbf{q}) \,\middle|\, \mathbf{q} \,\middle|\, \psi^i_q(\mathbf{q})\right\rangle , \quad (6.28)$$

This electric dipole matrix element is well understood for the hydrogen atom [113], and other atoms treated in a hydrogenic approximation [63]. The dipole matrix element is also a component of the full matrix element for the interaction of the optical vortex with the hydrogenic atom, as in Section 5.3. The form of the dipole matrix element gives the atomic selection rules, and is dependant on circular polarisation in the atomic electron position vector (see Appendix A.2 for details):

$$\boldsymbol{\mathcal{D}} = N_n N_{n'}\left(\frac{\hat{\mathbf{x}} + i\hat{\mathbf{y}}}{2}\mathcal{A}^{\pm}_q\delta_{m,m'-1} + \frac{\hat{\mathbf{x}} - i\hat{\mathbf{y}}}{2}\mathcal{A}^{\pm}_q\delta_{m,m+1} + \hat{\mathbf{z}}\mathcal{A}^0_q\delta_{m,m'}\right). \quad (6.29)$$

As can be seen, this matrix element allows unit changes in the atomic orbital angular momentum projection via circular fields. The strengths of the forward and reverse transitions, $\Delta m = \pm 1$ are the same, provided there are suitable final states available.

The second matrix element of Eq. (6.27) may now be evaluated; expressing the result in Cartesian coordinates will allow direct calculation of the product with $\boldsymbol{\mathcal{D}}$;

$$\frac{(\mathbf{r}_v - \mathbf{R})}{|\mathbf{r}_v - \mathbf{R}|^3} = \frac{(\rho_v\cos(\phi_v) - \rho_R\cos(\phi_R))\hat{\mathbf{x}} + (\rho_v\sin(\phi_v) - \rho_R\sin(\phi_R))\hat{\mathbf{y}} + (z_v - z_R)\hat{\mathbf{z}}}{[\mathcal{F}(\rho_v, z_v, \rho_R, z_R) - \mathcal{G}(\rho_v, \rho_R)\cos(\phi_v - \phi_R)]^{\frac{3}{2}}}, \quad (6.30)$$

with the functions $\mathcal{F}$ and $\mathcal{G}$ do not contain azimuthally relevant factors (see Appendix B.1). the operator Eq. (6.30) may now be inserted between the initial and final states of the electron vortex and the centre of mass states. Expressing the sines and cosines of Eq. (6.30) as exponentials, and making the substitution $y = (\phi_v - \phi_R)$ allows the matrix element to be written in terms of generic

integrals of the form

$$\mathcal{Y}_{\alpha}^{(\beta)} = \int_0^{2\pi} \frac{e^{i(l-l'+\alpha)y}}{\left(\mathcal{F}(\rho_v, z_v, \rho_R, z_R) - \mathcal{G}(\rho_v, \rho_R)\cos(\phi_v - \phi_p)\right)^{\frac{\beta}{2}}} dy, \tag{6.31}$$

before integrating between the initial and final states to find (see Appendix B.1 for full details)

$$\left\langle \frac{\mathbf{r}_v - \mathbf{R}}{|\mathbf{r}_v - \mathbf{R}|^3} \right\rangle_{fi} = \mathcal{B}_l^{(-1)} \left(\hat{\mathbf{x}} + i\hat{\mathbf{y}}\right) \delta_{[(L+l),(L'+l'+1)]} + \mathcal{B}_l^{(+1)} \left(\hat{\mathbf{x}} - i\hat{\mathbf{y}}\right) \delta_{[(L+l),(L'+l'-1)]} + \mathcal{B}_l^{(0)} \hat{\mathbf{z}} \delta_{[(L+l),(L'+l')]} \tag{6.32}$$

The factors $\mathcal{B}_l^{(-1)}$, $\mathcal{B}_l^{(+1)}$ and $\mathcal{B}_l^{(0)}$ are numerical factors arising from the integration over the non-azimuthal degrees of freedom. The superscripts refer to the induced change in orbital angular momentum of the combined vortex-centre of mass system. For a given l, we find the relationship $|\mathcal{B}_l^{+1}| = |\mathcal{B}_{-l}^{-1*}|$.

From here, we may now examine the full matrix element, by combining Eq. (6.32) with the electric dipole matrix element,

$$\mathcal{M}_{\mathrm{EV}}^{fi} = \frac{e}{4\pi\varepsilon_0} \frac{(m_p - m_e)}{M} \boldsymbol{\mathcal{D}} \cdot \left\langle \frac{\mathbf{r}_v - \mathbf{R}}{|\mathbf{r}_v - \mathbf{R}|^3} \right\rangle_{fi}. \tag{6.33}$$

Putting this together we have

$$\mathcal{M}_{\mathrm{EV}}^{fi} = \frac{e}{4\pi\varepsilon_0} \frac{(m_p - m_e)}{M} \big(\mathcal{C}_{+1} \delta_{[(L+l),(L'+l'+1)]} \delta_{m,m'-1} + \mathcal{C}_{-1} \delta_{[(L+l),(L'+l'-1)]} \delta_{m,m'+1} + \mathcal{C}_0 \delta_{[(L+l),(L'+l')]} \delta_{m,m'}\big), \tag{6.34}$$

with

$$\mathcal{C}_l^{+1} = \mathcal{B}_l^{+1} \mathcal{A}_q^{\pm}; \tag{6.35a}$$

$$\mathcal{C}_l^{-1} = \mathcal{B}_l^{-1} \mathcal{A}_q^{\pm}; \tag{6.35b}$$

$$\mathcal{C}_l^{0} = \mathcal{B}_l^{0} \mathcal{A}_q^{0}. \tag{6.35c}$$

Interpretation of the selection rules brings us to the conclusion that orbital angular momentum may be transferred between the electron vortex beam and the atom. In the dipole approximation, transfer of a single unit, $\hbar$ is possible. The delta functions indicate conservation of angular momentum quanta, and allow for the forward (gain of $\hbar$) and reverse (decrease of $\hbar$) transfer of orbital angular momentum into the atom. The forward transition is accompanied by the loss of a unit of angular momentum from either the electron vortex, or the orbital motion of the centre of mass, which combine to form a single orbital angular momentum system. Likewise, the reverse transition indicates a gain of orbital angular momentum for the vortex-centre of mass motion. Additionally, there are possible interactions in which no orbital angular momentum is exchanged at all. Since $|\mathcal{B}_l^{+1}| = |\mathcal{B}_{-l}^{-1*}|$, we have $|\mathcal{C}_l^{+1}| = |\mathcal{C}_{-l}^{-1*}|$, so a forward transition induced by a beam with orbital angular momentum l will have the same strength as a reverse transition induced by a beam

of $-l$.

The quadrupole Hamiltonian has also been analysed, and is presented in Appendix B.2. The quadrupole selection rules found in Appendix B.2 show very similar features - they show the possibility of transitions in which one unit of angular momentum is exchanged between the atomic electron and the beam or the centre of mass, as well as those transitions in which no angular momentum is exchanged. Additionally, there is also the possibility of the exchange of two units of angular momentum. This is expected - the quadrupole approximation allows for quadrupole-like transitions in which the orbital angular momentum projection of the atom changes by $2\hbar$. It is apparent that higher orders multipole terms of Eq. (6.23) of order n will allow for interactions in which up to n units of orbital angular momentum may be transferred.

These selection rules may be compared directly with those obtained in Chapter 5 for the interaction with the optical vortex. In both cases, the atom is described by the wavefunction relating to the internal motion of the atomic electron and that relating to the centre of mass motion. The dipole and quadrupole selection rules have been explicitly demonstrated in each case. The selection rules for the interaction of this atom with an optical and electron vortex are found to be quite different - the electron vortex interaction directly allows for the change of the orbital angular momentum of the internal state as well as the centre of mass motion, while the optical vortex may only directly affect the centre of mass.

6.3 Multipolar Effective Operator

The selection rules obtained above are useful for determining the general features of the interaction, but further information - such as the spatial dependence of the interaction and the relative strengths of the multipolar terms - is not readily apparent. In order to make these features clearer, a second analysis of the interaction is carried out via an expansion of the wavefunctions themselves. This is possible due to certain properties of the Bessel function - however these results may be generalised to other types of vortex through expansion of the particular vortex into a Bessel-mode basis.

As mentioned above, the interaction Hamiltonian applied here is the direct Coulomb Hamiltonian of the system's constituent particles,

$$H_{\text{Int}}^{\text{B}} = \frac{e^2}{4\pi\varepsilon_0}\left(\frac{1}{|\mathbf{r}_v - \mathbf{r}_e|} - \frac{1}{|\mathbf{r}_v - \mathbf{r}_p|}\right). \tag{6.36}$$

where here $\mathbf{r}_e$ has been left, rather than $\mathbf{r}_e = \mathbf{r}_p + \mathbf{q}$. Rather than centre of mass states, this will now be applied to atomic wavefunctions involving the nuclear kinetic states. For notational simplicity, these states will take the same form as those given in Eq. (5.7), so that we have let $\mathbf{R} \to \mathbf{r}_p$:

$$|\psi_p(\mathbf{r}_p \to \mathbf{R})\rangle = |\psi_p(\rho_R, \phi_R, z_R)\rangle = \mathcal{R}_p(\rho_R)e^{iK_R\rho_R}e^{iK_z z_R}e^{iL\phi_R}. \tag{6.37}$$

The transition matrix element is then

$$\mathcal{M} = \left\langle \psi_q^i; \psi_p^i; \psi_{EV}^i \middle| \frac{e^2}{4\pi\varepsilon_0}\left(\frac{1}{|\mathbf{r}_v - \mathbf{r}_e|} - \frac{1}{|\mathbf{r}_v - \mathbf{R}|}\right) \middle| \psi_q^f; \psi_p^f; \psi_{EV}^f \right\rangle. \tag{6.38}$$

The first term of the Hamiltonian may lead to internal transitions within the atom as well as transitions between states of the centre of mass, while the second may only lead to transitions of the centre of mass wavefunctions.

The second term is relatively simple to evaluate (see Appendix B.3), since both position vectors $\mathbf{r}_v$ and $\mathbf{R}$ and the relevant wavefunctions are properly specified about the same reference frame - that of the beam's origin. It is apparent that this term will affect only the centre of mass, and will not lead to transitions between the internal atomic states. For the first term, we again have the problem that the wavefunction of the atomic electron and the beam electron are naturally described about very different frames. We now seek to find the influence of the electron vortex on the atomic states $|\psi_q(\mathbf{q});\psi_p(\mathbf{R})\rangle$, through the matrix element

$$\mathcal{M} = \left\langle \psi_q^i;\psi_p^i;\psi_{EV}^i \right| \frac{e^2}{4\pi\varepsilon_0}\frac{1}{|\mathbf{r}_v-\mathbf{r}_e|}\left|\psi_q^f;\psi_p^f;\psi_{EV}^f\right\rangle . \tag{6.39}$$

The aim is to write this in terms of some effective multipolar operator $\mathcal{O}$ acting on the atomic states

$$\mathcal{M} = \left\langle \psi_q^i;\psi_p^i \right| \mathcal{O} \left| \psi_q^f;\psi_p^f \right\rangle \tag{6.40}$$

This is achieved by considering the Neumann addition theorem for Bessel functions [114]. This addition theorem describes a Bessel function about a certain origin in terms of a series of Bessel functions about another, displaced axis, with appropriate weighting:

$$e^{i\nu\Psi}J_\nu(z) = \sum_{m=-\infty}^{\infty} J_{\nu+m}(x)J_m(y)e^{im\Phi}. \tag{6.41}$$

Here, the original Bessel function (on the left hand side) is $J_\nu(z)$, and on the right hand side the expansion is given about the new axis by the Bessel functions $J_m(y)$ with weighting functions $J_{\nu+m}(x)$.

Applying the theorem to our situation, we take the triangle made by the origin, the position vectors of the atomic nucleus and the vortex position $\mathbf{r}_v$, shown in the plane in Fig. 6.3.1. Applying the addition theorem to the electron vortex spatial distribution function $J_l(k_\perp\rho_v)$ gives

$$J_l(k_\perp\rho_v) = e^{-il\Psi}\sum_{p=-\infty}^{\infty} J_{l+p}(k_\perp\rho_R)J_p(k_\perp\rho_v')e^{ip\Phi}. \tag{6.42}$$

so that the spatial distribution function is now described about an origin centered on the atomic nucleus - i.e. the vortex and the atomic electron are now described in the same coordinate frame. The angles ψ and ϕ are the inner triangle angles as shown in Fig. 6.3.1. Application of simple

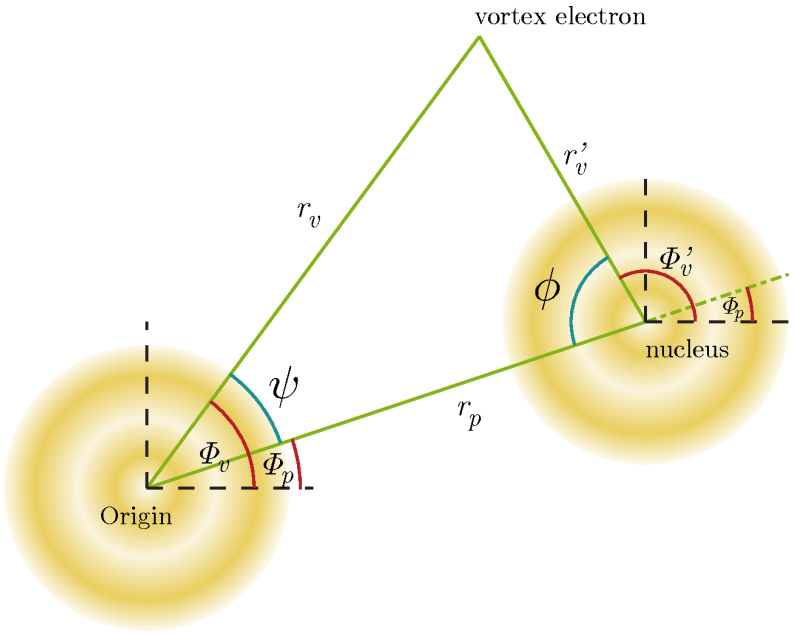

Figure 6.3.1: The triangle formed in applying the Neumann addition theorem for Bessel functions. The expansion angles ψ and ϕ are shown - these are expressed in terms of the relevant angles as $\Psi = \phi_v - \phi_R$ and $\Phi = \pi - \phi_v' + \phi_R$, where ϕ_v' denotes the angle between the vortex electron and the x-axis at the new pole, centred on the atomic nucleus. After expansion, the wavefunction is expressed in terms of a sum of $J_p(k_\perp \rho_v')$, about the nucleus. The original and expanded beams are shown schematically.

trigonometry allows these angles to be related to the known angles in the interacting system [1]:

$$\Psi = \phi_v - \phi_R; \tag{6.43}$$

$$\Phi = \pi - \phi_v' + \phi_R. \tag{6.44}$$

where the new angle ϕ_v' is the azimuthal angle of the new position vector $\mathbf{r}_v'$ about the atomic nucleus. Applying this to Eq. (6.42) gives

$$J_l(k_\perp \rho_v) = e^{-il\phi_v} \sum_{p=-\infty}^{\infty} J_{l+p}(k_\perp \rho_R) J_p(k_\perp \rho_v') e^{ip\pi} e^{i(l+p)\phi_R} e^{-ip\phi_v'}. \tag{6.45}$$

Now, since p runs from positive to negative infinity, we may reverse the sign of p without loss of generality. Letting $p \to -p$ gives

$$J_l(k_\perp \rho_v) = e^{-il\phi_v} \sum_{p=-\infty}^{\infty} J_{l-p}(k_\perp \rho_R) J_{-p}(k_\perp \rho_v') e^{-ip\pi} e^{i(l-p)\phi_R} e^{ip\phi_v'}. \tag{6.46}$$

Using Eq. (2.29), the relationship between Bessel functions of positive and negative order, we may

[1] The angle definition is dependant on the orientation of this triangle within the external coordinate frame of the vortex beam. There are two principal choices, effectively the right-handed and left-handed orientations - both are valid. We choose the angles here such that the factor $e^{il\phi_v}$ may be eliminated (rather than squared) in the final expanded Bessel wavefunction of Eq. (6.48).

finally write the expanded Bessel function as

$$J_l(k_\perp \rho_v) = e^{-il\phi_v} \sum_{p=-\infty}^{\infty} J_{l-p}(k_\perp \rho_R) J_p(k_\perp \rho'_v) e^{i(l-p)\phi_R} e^{ip\phi'_v}, \tag{6.47}$$

where the original Bessel function is now expressed as a sum of Bessel functions centered about the centre of mass, i.e. a shift in origin.

This new shifted Bessel function may now be incorporated into the electron vortex wavefunction of Section 2.2 to give

$$\psi_{\text{EV}} = N_l e^{ik_z(z_R+z'_v)} e^{-i\omega t} \sum_{p=-\infty}^{\infty} J_{l-p}(k_\perp \rho_R) J_p(k_\perp \rho'_v) e^{i(l-p)\phi_R} e^{ip\phi'_v}. \tag{6.48}$$

The Bessel functions $J_p(k_\perp \rho'_v)$ describe the new vortex wavefunctions that the atomic electron 'sees' in its coordinate frame, such that the atomic electron may now interact with the new vortex wavefunction having p units of orbital angular momentum. The other Bessel function $J_{l-p}(k_\perp \rho_R)$ gives the weighting factor of the shifted vortex, describing its strength as a function of distance from the origin of the initial vortex beam $J_l(k_\perp \rho_v)$. As expected, if $\rho_R \to 0$ then $\rho'_v \to \rho_v$, and the only contribution comes from $p = l$, since at $\rho_R = 0$ the only non-zero Bessel function is that of the zero order. Otherwise, all terms in the expansion must be considered. Note that the full wavefunction has been expressed about the new centre of mass origin, including the z dependence, so that $z_v \to z_R + z'_v$.

6.3.1 The Effective Operator

This transformed wavefunction may now be used to find the an effective operator and selection rules for the interaction between the vortex and the hydrogen atom when the atom is situated a distance from the beam origin. As suggested above, we have

$$\mathcal{M}_{fi} = \left\langle \psi_q^i; \psi_R^i \middle| \mathcal{O} \middle| \psi_q^f; \psi_R^f \right\rangle, \tag{6.40}$$

where the effective operator $\mathcal{O}$ is the product of the new, shifted initial and final wavefunctions, and the Coulomb interaction operator, integrated over the vortex electron degrees of freedom:

$$\begin{aligned} \mathcal{O} = \frac{e^2}{4\pi\varepsilon_0} N_l^i N_{l'}^f e^{-i(\omega-\omega')t} \int d^3\mathbf{r}'_v e^{i(k_z-k'_z)(z_R+z'_v)} \\ \times \sum_{p,p'=-\infty}^{\infty} J_{l-p}(k_\perp \rho_R) J_{l'-p'}(k'_\perp \rho_R) \frac{J_p(k_\perp \rho'_v) J_{p'}(k'_\perp \rho'_v)}{|\mathbf{r}'_v - \mathbf{q}|} e^{i(l-l'-p+p')\phi_R} e^{i(p-p')\phi'_v}, \end{aligned} \tag{6.49}$$

where the distance between the atomic electron and the vortex electron $|\mathbf{r}_v - \mathbf{r}_e|$ has been rewritten as the equivalent vector $|\mathbf{r}'_v - \mathbf{q}|$ in the centre of mass frame, and the distance between the vortex electron and the centre of mass has $|\mathbf{r}'_v - \mathbf{R}|$ been replaced with $|\mathbf{r}'_v|$. This is written in the form

$$\mathcal{O} = N_l^i N_{l'}^f \frac{e^2}{4\pi\varepsilon_0} e^{-i(\omega-\omega')t} \sum_{p,p'=-\infty}^{\infty} F_R^{l,l',p,p'} I_q^{p,p'}, \tag{6.50}$$

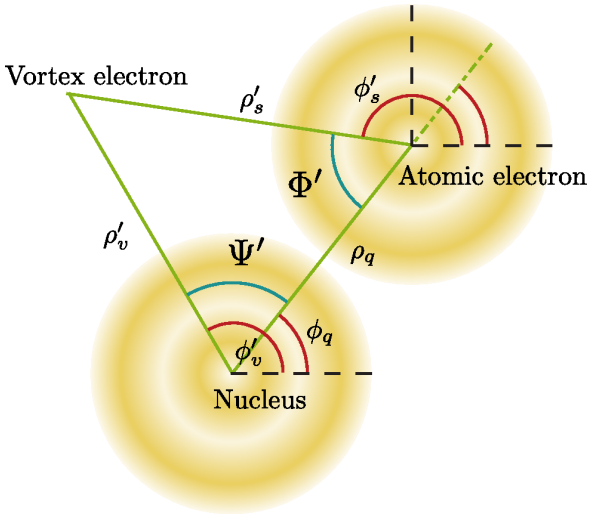

Figure 6.3.2: The triangle formed in applying the Neumann addition theorem a second time. The expansion angles ψ and ϕ are shown - these are expressed in terms of the relevant angles as $\Psi' = \phi'_v - \phi_q$ and $\Phi' = \pi - \phi'_s + \phi_q$, where ϕ'_s denotes the angle between the vortex electron and the x-axis at the new pole, centred on the atomic electron. After expansion, the wavefunction is expressed in terms of a sum of $J_u(k_\rho \rho'_s)$, about the atomic electron, allowing the series to be expanded in terms of q, making the multipolar nature of each contribution to the interaction clear. The original and expanded beams are shown schematically.

where we have introduced the shorthand

$$F_R^{l,l',p,p'} = e^{i(k_z - k'_z)z_R} J_{l-p}(k_\perp \rho_R) J_{l'-p'}(k'_\perp \rho_R) e^{i(l-l'-p+p')\phi_R}, \tag{6.51}$$

and

$$I_q^{p,p'} = \int e^{i(k_z - k'_z)z'_v} \frac{J_p(k_\perp \rho'_v) J_{p'}(k'_\perp \rho'_v)}{|\mathbf{r}'_v - \mathbf{q}|} e^{i(p-p')\phi'_v} d^3\mathbf{r}'_v. \tag{6.52}$$

The first term, $F_R^{l,l',p,p'}$, relates to the centre of mass motion, and may be integrated in the context of the Dirac brackets of Eq. (6.40) in the usual fashion. The second term, $I_q^{p,p'}$, relates to the Coulomb interaction between the atomic and vortex electrons. The matrix element of this effective operator may be directly evaluated (see Appendix B.4). When $\mathbf{R}$ is considered as a dynamical variable, and the atom is free to move about the beam axis we find the selection rule

$$\Delta l + \Delta L = -\Delta m. \tag{6.53}$$

This demonstrates general orbital angular momentum conservation at all $\mathbf{R}$, and encompasses all possible transitions, from all multipolar contributions, since as yet, no information regarding the multipolar nature of the transition has been obtained. This general expression of orbital angular momentum conservation does not specify which transitions are dipole allowed. In order to determine this, a further wavefunction expansion is made, in a similar manner to above.

6.3.2 Multipolar Expansion

As shown in Fig. 6.3.2, the centre of mass, the atomic electron and the vortex electron make a triangle similar to that shown in Fig. 6.3.1. Expansion of the Bessel functions within this triangle allows the multipolar expansion of the interaction to be found. In the above, the original Bessel function was expanded into a summation of Bessel functions about a new origin, with new position vector r'_v. We may now use the same technique to expand these Bessel functions in terms of the electron position from the centre of mass, q, leading to an intuitive multipolar interpretation.

Returning to the matrix element as described in Eq. (6.50), (6.51) and (6.52), we define a new vector $\mathbf{r}_s$ as the separation between the atomic and vortex electrons, such that

$$\mathbf{r}'_s = \mathbf{r}'_v - \mathbf{q}; \tag{6.54}$$

$$|\mathbf{r}'_s| = \left(\rho'^2_v + z'^2_v + q^2 - z'_v q\cos\theta_q - \rho'_v q\sin\theta_q\cos(\phi'_v - \phi_q)\right)^{\frac{1}{2}}. \tag{6.55}$$

Using this, the Bessel functions $J_p(k_\perp r'_v)$ may now be expanded in terms of r'_s, in the same way as before. In this case the expansion angles are found to be

$$\Psi = \phi'_v - \phi_q; \tag{6.56}$$

$$\Phi = \pi - \phi'_s + \phi_q, \tag{6.57}$$

so that performing the expansion gives [2]

$$J_p(k_\perp\rho'_v) = e^{-ip\phi'_v}\sum_{u=-\infty}^{\infty} J_{p-u}(k_\perp q_\perp)J_u(k_\perp\rho'_s)e^{i(p-u)\phi_q}e^{iu\phi'_s}, \tag{6.58}$$

with $q_\perp$ the magnitude of the atomic position vector in the plane, i.e.

$$q_\perp = \rho_q\sin\theta_q. \tag{6.59}$$

The full wavefunction of the Bessel vortex, after both expansions is now

$$\psi_{\text{EV}} = Ne^{ik_z(z_R+z_q+z'_s)}e^{-i\omega t}\sum_{p=-\infty}^{\infty} J_{l-p}(k_\perp\rho_R)e^{i(l-p)\phi_R} \times \sum_{u=-\infty}^{\infty} J_{p-u}(k_\perp q_\perp)J_u(k_\perp\rho'_s)e^{i(p-u)\phi_q}e^{iu\phi'_s}, \tag{6.60}$$

[2] At this point the reason for using the Hamiltonian $H^{\text{B}}_{\text{Int}}$ rather than the centre of mass Hamiltonian $H^{\text{CM}}_{\text{Int}}$ will be made clear. In the centre of mass formalism, the atomic electron coordinate relative to the centre of mass is $\frac{m_p}{M}\mathbf{q}$, and the first wavefunction expansion may be made either about the centre of mass, or about the atomic nucleus, with the relevant position $\frac{m_e}{M}\mathbf{r}_p$. For notational simplicity then, this expansion is carried out in the limit that the centre of mass is coincident with the nuclear position. In either case, the main features of the selection rules will be the same, with the addition of multiplicative factors involving the particle masses. In the centre of mass formalism $|\mathbf{r}'_v - \mathbf{q}|^{-1} \to |\mathbf{r}'_v - \frac{m_p}{M}\mathbf{q}|^{-1}$, and there are two options for the wavefunction expansions, since the original wavefunction may be expanded about either the centre of mass or the atomic nucleus. In the first case, the first expansion takes the same form as that given above, and the second expansion about the atomic electron takes the form $J_{p-u}(k_\perp\rho_q) \to J_{p-u}(k_\perp\frac{m_p}{M}\rho_q)$. The alternate method involves the first expansion being made about the atomic nucleus, so that $J_{l-p}(k_\perp\rho_R) \to J_{l-p}(k_\perp\frac{m_e}{M}\rho_p)$, and the second expansion has the same form as shown above.

p, p'	u	$p, p' - u$
$0 \leq p, p' < \infty$	$0 \leq u < \infty$	positive if $p, p' \geq u$
		negative if $p, p' < u$
	$-\infty < u < -1$	positive for all p, p', u
$-\infty < p, p' < 0$	$0 \leq u < \infty$	negative for all p, p', u
	$-\infty < u < -1$	positive if $p, p' \geq u$
		negative if $p, p' < u$

Table 6.3.1: Summary of the separate conditions on the indices p, p' and u, and the sign of the order of the Bessel function given by $J_{p,p'-u}(k_\perp q_\perp)$.

where again, the z-dependence has been changed to reflect the new centre of expansion so that $z_v \to z_R + z_q + z'_s$.

Putting this into the matrix element of Eq. (6.40) gives an effective operator $\mathcal{O}$ of the form

$$\mathcal{O}' = N_l^i N_{l'}^f \frac{e^2}{4\pi\varepsilon_0} e^{i(k_z - k'_z)z_q} e^{-i(\omega-\omega')t} \sum_{p,p'=-\infty}^{\infty} \sum_{u,u'=-\infty}^{\infty} F_R^{l,l',p,p'} I_q^{p,p',u,u'}, \tag{6.61}$$

with

$$I_q^{p,p',u,u'} = \int e^{i(k_z - k'_z)z'_s} J_{p-u}(k_\perp q_\perp) J_{p'-u'}(k'_\perp q_\perp) \times \frac{J_u(k_\perp \rho'_s) J_{u'}(k'_\perp \rho'_s)}{|\mathbf{r}'_s|} e^{i(p-u-p'+u')\phi_q} e^{i(u-u')\phi'_s} d^3\mathbf{r}'_s. \tag{6.62}$$

This expression may be simplified, using the Fourier transform for the Coulomb potential (see Appendix B.5) to give

$$I_q^{p,p',u,u} = J_{p-u}(k_\perp q_\perp) J_{p'-u}(k'_\perp q_\perp) e^{i(p-p')\phi_q} \frac{\delta_{u,u'}}{\sqrt{2\pi^3}} \int_0^{2\pi} d\beta \frac{e^{-iu\beta}}{Q^2(\beta)}, \tag{6.63}$$

where $Q(\beta)$ is the total linear momentum transfer between the initial and final states of the electron vortex wavefunction, as a function of the angle β between the incoming and outgoing states. This leads to the condition that $u = u'$, so that the full effective operator is now

$$\mathcal{O}' = N_l^i N_{l'}^f \frac{e^2}{4\pi\varepsilon_0} e^{i(k_z - k'_z)z_q} e^{-i(\omega-\omega')t} \sum_{p,p'=-\infty}^{\infty} \sum_{u=-\infty}^{\infty} F_R^{l,l',p,p'} I_q^{p,p',u,u}. \tag{6.64}$$

In order to see clearly the multipolar nature of this expression, the Bessel functions of ρ_q may be Taylor expanded. Since our interest lies in the dipole term, expansion to first order is sufficient, giving the asymptotic limit of the Bessel function. This is valid for small arguments $0 < z << \sqrt{\alpha + 1}$ [93, 115]:

$$J_\alpha(z) \approx \frac{1}{\Gamma(\alpha+1)} \left(\frac{z}{2}\right)^\alpha \text{ for } \alpha \in \mathbb{N} \tag{6.65}$$

We have $z = k_\perp \rho_q \sin\theta_q \approx k_\perp a_0$. For the typical electron vortex described in Section 2.5 we have

$k_\perp = 2.3 \times 10^{10}\,\mathrm{m}^{-1}$, so that z is of order unity. The dominant terms in the expansion will have $\alpha = 0$, so that this is not a good approximation, nevertheless, $k_\perp$ is a tunable parameter (for example, by changing the widths of the bars in the forked masks). However, reducing $k_\perp$ corresponds to increasing the radius of the beam, so that atomic resolution may not then be possible. A $k_\perp \approx 10^{-9}\,\mathrm{m}^{-1}$ would produce a beam satisfying Eq. (6.65), and suitable for probing atomic transitions at the nanoscale, with good resolution.

The expression Eq. (6.65) is valid for Bessel functions of positive integer order only, which occurs under certain conditions of p,p' and u (see Table 6.3.1). For the remaining cases of p,p' and u we apply the relationship between Bessel functions of positive and negative order of Eq. (2.29), i.e. for the case when both p, p' and u are positive, but $p, p' < u$, then $p, p' - u < 0$, we must write

$$J_{p-u}(k_\perp q_\perp) = (-1)^{|p-u|} J_{|p-u|}(k_\perp q_\perp). \tag{6.66}$$

In this way, the triple sum over p, p' and u is divided into eighteen individual terms, with strict conditions, and we may write the full effective operator as

$$\mathcal{O}' = N_l^i N_{l'}^f \frac{e^2}{4\pi\varepsilon_0} e^{i(k_z - k_z')z_q} e^{-i(\omega-\omega')t} \Sigma_{p,p',u} F_R^{l,l',p,p'} K_q^{p,p',u,u}, \tag{6.67}$$

with $F_R^{l,l',p,p'}$ given by Eq. (6.51), and

$$K_q^{p,p',u} = \frac{e^{i(p-p')\phi_q}}{\sqrt{2\pi^3}} \int_0^{2\pi} d\beta \frac{e^{-iu\beta}}{Q^2(\beta)}, \tag{6.68}$$

with $\Sigma_{p,p',u}$ representing the eighteen sums over the different combinations of p, p' and u, displayed in full in Appendix B.6. We may now apply the asymptotic limit of Eq. (6.65), and then explicitly examine the conditions that lead to the individual terms in the multipolar expansion of the effective Hamiltonian $\mathcal{O}'$. The zero order terms are those for which the power of $q_\perp$ is zero, while the dipole and quadrupole terms contain $q_\perp^1$ and $q_\perp^2$ respectively. This leads to particular conditions on p, p' and u, which are summarised in Tables 6.3.2 - 6.3.4. The effective operator is now expressed in terms of a multipolar series

$$\mathcal{O}' = \mathcal{O}'_{\mathrm{ZO}} + \mathcal{O}'_{\mathrm{dipole}} + \mathcal{O}'_{\mathrm{quadrupole}} \cdots \tag{6.69}$$

where the matrix element of each can now be evaluated carefully to see the orbital angular momentum selection rules suggested for l and m. We note here that the identification of 'dipole' and 'quadrupole' etc. relates to the in-plane excitations, such as angular momentum transfer only, as this $q_\perp = \rho_q \sin\theta_q$ is not the only source of ρ_q dependence - the out of plane excitation factor $e^{i(k_z - k_z')z_q} = e^{i(k_z - k_z')\rho_q \cos\theta}$ will also affect the atomic electron states. However, since we are interested in the transfer of orbital angular momentum it is sufficient to consider the in-plane factors, and for convenient nomenclature these are identified as the multipolar terms, since they will affect the orbital angular momentum in a similar way. Below, the zero order and dipole terms are explicitly considered.

Zero Order

	$\lvert p-u\rvert = 0 \,\&\, \lvert p'-u\rvert = 0$	$p-u = 0 \,\&\, \lvert p'-u\rvert = 0$
	$\lvert p-u\rvert = 0 \,\&\, p'-u = 0$	$p-u = 0 \,\&\, p'-u = 0$
$\Delta p = 0$	$p = p' = u$	

Table 6.3.2: Conditions on p,p' and u for contributions to the zero order term of the interaction matrix element. These conditions lead to terms with q^0. In the interaction with the atom, the orbital angular momentum of the p-wavefunction does not change.

Dipole

	$\lvert p-u\rvert = 1 \,\&\, \lvert p'-u\rvert = 0$	$p-u = 1 \,\&\, \lvert p'-u\rvert = 0$	$\lvert p-u\rvert = 0 \,\&\, \lvert p'-u\rvert = 1$	$\lvert p-u\rvert = 0 \,\&\, p'-u = 1$
	$\lvert p-u\rvert = 1 \,\&\, p'-u = 0$	$p-u = 1 \,\&\, p'-u = 0$	$p-u = 0 \,\&\, \lvert p'-u\rvert = 1$	$p-u = 0 \,\&\, p'-u = 1$
$\Delta p = +1$	$p = u+1, p' = u$	$p = u+1, p' = u$	$p = u, p' = u-1$	
$\Delta p = -1$	$p = u-1, p' = u$		$p = u, p' = u+1$	$p = u, p' = u+1$

Table 6.3.3: Conditions on p,p' and u for contributions to the dipole term of the interaction matrix element. These conditions lead to terms with q^1. In the interaction with the atom, the orbital angular momentum of the p-wavefunction may increase or decrease by one unit.

Quadrupole

	$\lvert p-u\rvert = 1 \,\&\, \lvert p'-u\rvert = 1$	$p-u = 1 \,\&\, \lvert p'-u\rvert = 1$	$\lvert p-u\rvert = 1 \,\&\, p'-u = 1$	$p-u = 1 \,\&\, p'-u = 1$
$\Delta p = 0$	$p = u+1, p' = u+1$	$p = u+1, p' = u+1$	$p = u+1, p' = u+1$	$p = u+1, p' = u+1$
	$p = u-1, p' = u-1$			
$\Delta p = +2$	$p = u+1, p' = u-1$	$p = u+1, p' = u-1$		
$\Delta p = +2$	$p = u-1, p' = u+1$		$p = u-1, p' = u+1$	

	$\lvert p-u\rvert = 2 \,\&\, \lvert p'-u\rvert = 0$	$p-u = 2 \,\&\, \lvert p'-u\rvert = 0$	$\lvert p-u\rvert = 0 \,\&\, \lvert p'-u\rvert = 2$	$\lvert p-u\rvert = 0 \,\&\, p'-u = 2$
	$\lvert p-u\rvert = 2 \,\&\, p'-u = 0$	$p-u = 2 \,\&\, p'-u = 0$	$p-u = 0 \,\&\, \lvert p'-u\rvert = 2$	$p-u = 0 \,\&\, p'-u = 2$
$\Delta p = +2$	$p = u+2, p' = u$	$p = u+2, p' = u$	$p = u, p' = u-2$	
$\Delta p = -2$	$p = u-2, p' = u$		$p = u, p' = u+1$	$p = u, p' = u+2$

Table 6.3.4: Conditions on p,p' and u for contributions to the quadrupole term of the interaction matrix element. These conditions lead to terms with q^2. In the interaction with the atom, the orbital angular momentum of the p-wavefunction may increase or decrease by two units, or remain unchanged.

6.3.3 Zero Order Terms

The zero terms are those having $q_\perp^{(p-u)} q_\perp^{(p'-u)} = q_\perp^0$ (and similar, see Appendix B.6 and Table 6.3.2), and this gives directly the condition $p = p' = u$. These zero order terms cannot lead to orbital angular momentum exchange between the vortex and the atom, however since there is dependence on ρ_q in the out-of plane excitation factor $e^{i(k_z - k'_z)z_q}$ transitions between different initial and final states of the atomic electron are possible.

The zero order term cannot lead to exchange of orbital angular momentum between the atomic electron and the p state that the atom interact with, so the difference in orbital angular momentum between the ingoing and outgoing Bessel beam must be zero, i.e.:

$$\Delta p = p - p' = 0. \tag{6.70}$$

For all sets of conditions on p and u this gives that $p = p' = u$. This condition is valid for just two terms in Eq. (B.34) and all indices cancel, leaving only one term in each sum. Thus, the zero order terms are

$$\begin{aligned}\mathcal{O}'_{\text{ZO}} &= N_l^i N_{l'}^f \frac{e^2}{4\pi\varepsilon_0} e^{i(k_z - k'_z)z_q} e^{-i(\omega-\omega')t} \\ &\quad \times \left(\frac{1}{\Gamma(1)\Gamma(1)} \sum_{p=0}^{\infty} F_R^{l,l',p,p} K_q^{p,p,p,p} + \frac{1}{\Gamma(1)\Gamma(1)} \sum_{p=-\infty}^{-1} F_R^{l,l',p,p} K_q^{p,p,p,p} \right) \\ &= N_l^i N_{l'}^f \frac{e^2}{4\pi\varepsilon_0} e^{i(k_z - k'_z)z_q} e^{-i(\omega-\omega')t} \sum_{p=-\infty}^{\infty} F_R^{l,l',p,p} K_q^{p,p,p,p}. \end{aligned} \tag{6.71}$$

The sums over p do not disappear completely - there are further factors in $K_q^{p,p',u,u'}$ and $F_R^{l,l',p,p'}$ involving the indices and these must still be summed over. However, the sums have now been collapsed by these conditions to give $K_q^{p,p,p,p}$ and $F_R^{l,l',p,p}$.

Writing the functions $F_R^{l,l',p,p}$ and $K_q^{p,p,p,p}$ explicitly, we find

$$\begin{aligned}\mathcal{O}'_{\text{ZO}} = \frac{N_l^i N_{l'}^f}{\sqrt{2\pi^3}} \frac{e^2}{4\pi\varepsilon_0} e^{i(k_z - k'_z)(z_q + z_R)} e^{-i(\omega-\omega')t} \sum_{p=-\infty}^{\infty} J_{l-p}(k_\perp \rho_R) J_{l'-p}(k'_\perp \rho_R) \\ \times \underbrace{e^{i(l-l'-p+p)\phi_R} e^{i(p-p)\phi_q}}_{\text{azimuthal factors}} \int_0^{2\pi} d\beta \frac{e^{-ip\beta}}{Q^2(\beta)}. \end{aligned} \tag{6.72}$$

The factors that will affect orbital angular momentum transfer are indicated as the azimuthal terms. It is clear here that in general the orbital angular momentum of the beam directly affects the motion of the centre of mass, while the atomic electron is affected by the shifted Bessel beam - in this zero order interaction $p = p'$ so it is obvious there is no orbital angular momentum transferred to the atom, as expected. Incorporating these azimuthal factors into the relevant part of the full matrix element $\mathcal{M}_{\text{ZO}}^{l,l'}$ gives the selection rules:

$$\mathcal{M}_{\text{ZO}}^{l,l'} = \frac{e^2}{\varepsilon_0 \sqrt{2\pi}} \sum_{p=\infty}^{\infty} \Theta_R^{l,l',p} \Theta_q^{\text{ZO}} \int_0^{2\pi} d\beta \frac{e^{-ip\beta}}{Q^2(\beta)} \delta_{[m,m']} \delta_{[(l+L),(l'+L')]}, \tag{6.73}$$

such that the zero term allows transfer of orbital angular momentum between the electron vortex and the nuclear rotation only. The factors $\Theta_R^{l,l',p}$ and Θ_q^{ZO} contain the integrals over the remaining degrees of freedom, and are stated in full in Appendix B.7.3.

6.3.4 Dipole terms

The dipole interaction Hamiltonian that is single order in ρ_q will allow the transfer of orbital angular momentum to the atom, and the z component of the electron angular momentum may change [113]:

$$\Delta m = 0, \pm 1. \tag{6.74}$$

Accordingly, for present purposes we identify the dipole terms as being single order in q and have the following selection rule for p,

$$\Delta p = \pm 1, 0. \tag{6.75}$$

Since orbital angular momentum is conserved when the atomic electron interacts with the vortex wavefunction, so that $\Delta m = \Delta p$. The conditions for p, p' and u obtained by these requirements are indicated in Table 6.3.3. Applying these conditions leads to[3]

$$\begin{aligned}
\mathcal{O}'_{\text{dipole}} = {} & N_l^i N_{l'}^f \frac{e^2}{4\pi\varepsilon_0} e^{i(k_z - k'_z)z_q} e^{-i(\omega-\omega')t} \left(\frac{q_\perp}{2}\right) \\
& \times \Bigg(k_\perp \sum_{p=0}^{\infty} \frac{1}{\Gamma(2)\Gamma(1)} F_R^{l,l',p,p-1} K_q^{p,p-1,p-1,p-1} + k'_\perp \sum_{p=0}^{\infty} \frac{1}{\Gamma(1)\Gamma(2)} F_R^{l,l',p,p+1} K_q^{p,p+1,p,p} \\
& + k'_\perp \sum_{p=0}^{\infty} \frac{(-1)}{\Gamma(1)\Gamma(0)} F_R^{l,l',p,p-1} K_q^{p,p-1,p,p} + k_\perp \sum_{p=0}^{\infty} \frac{(-1)}{\Gamma(2)\Gamma(1)} F_R^{l,l',p,p+1} K_q^{p,p+1,p+1,p+1} \\
& + k_\perp \sum_{p=-\infty}^{-1} \frac{1}{\Gamma(2)\Gamma(1)} F_R^{l,l',p,p-1} K_q^{p,p-1,p-1,p-1} + k'_\perp \sum_{p=-\infty}^{-1} \frac{1}{\Gamma(1)\Gamma(2)} F_R^{l,l',p,p+1} K_q^{p,p+1,p,p} \\
& + k'_\perp \sum_{p=-\infty}^{-1} \frac{(-1)}{\Gamma(1)\Gamma(2)} F_R^{l,l',p,p-1} K_q^{p,p-1,p,p} + k_\perp \sum_{p=-\infty}^{-1} \frac{(-1)}{\Gamma(2)\Gamma(1)} F_R^{l,l',p,p+1} K_q^{p,p+1,p+1,p+1} \Bigg),
\end{aligned} \tag{6.76}$$

which reduces to

$$\begin{aligned}
\mathcal{O}'_{\text{dipole}} = {} & N_l^i N_{l'}^f \frac{e^2}{4\pi\varepsilon_0} e^{i(k_z - k'_z)z_q} e^{-i(\omega-\omega')t} \left(\frac{q_\perp}{2}\right) \\
& \times \Bigg(k_\perp \sum_{p=-\infty}^{\infty} F_R^{l,l',p,p-1} K_q^{p,p-1,p-1,p-1} - k_\perp \sum_{p=-\infty}^{\infty} F_R^{l,l',p,p+1} K_q^{p,p+1,p+1,p+1} \\
& + k'_\perp \sum_{p=-\infty}^{\infty} F_R^{l,l',p,p+1} K_q^{p,p+1,p,p} - k'_\perp \sum_{p=-\infty}^{\infty} F_R^{l,l',p,p-1} K_q^{p,p-1,p,p} \Bigg).
\end{aligned} \tag{6.77}$$

Once again, we may expand the functions $K_q^{p,p',u,u'}$ and $F_R^{l,l',p,p'}$, and isolate the relevant

[3] Note that certain terms of Eq. (B.34) fulfill the requirements of Table 6.3.3 for very specific numerical conditions of p, p' and u, leading to a single term with no summation. These contributions have been excluded, as they are found to lead to double counting when the sums are contracted to a single variable.

azimuthal factors. This gives

$$\begin{aligned}\mathcal{O}'_{\text{dipole}} = &\frac{N_l^i N_{l'}^f}{\sqrt{2\pi^3}}\frac{e^2}{4\pi\varepsilon_0}e^{i(k_z-k'_z)(z_q+z_R)}e^{-i(\omega-\omega')t}\left(\frac{q_\perp}{2}\right)\\
&\times\Bigg(k_\perp\sum_{p=-\infty}^{\infty}J_{l-p}(k_\perp\rho_R)J_{l'-p+1}(k'_\perp\rho_R)\underbrace{e^{i(l-l'-p+p-1)\phi_R}e^{i(p-p+1)\phi_q}}_{\text{azimuthal factors}}\int_0^{2\pi}d\beta\frac{e^{-i(p-1)\beta}}{Q^2(\beta)}\\
&-k_\perp\sum_{p=-\infty}^{\infty}J_{l-p}(k_\perp\rho_R)J_{l'-p-1}(k'_\perp\rho_R)\underbrace{e^{i(l-l'-p+p+1)\phi_R}e^{i(p-p-1)\phi_q}}\int_0^{2\pi}d\beta\frac{e^{-i(p+1)\beta}}{Q^2(\beta)}\\
&+k'_\perp\sum_{p=-\infty}^{\infty}J_{l-p}(k_\perp\rho_R)J_{l'-p-1}(k'_\perp\rho_R)\underbrace{e^{i(l-l'-p+p+1)\phi_R}e^{i(p-p-1)\phi_q}}\int_0^{2\pi}d\beta\frac{e^{-i(p)\beta}}{Q^2(\beta)}\\
&-k'_\perp\sum_{p=-\infty}^{\infty}J_{l-p}(k_\perp\rho_R)J_{l'-p+1}(k'_\perp\rho_R)\underbrace{e^{i(l-l'-p+p-1)\phi_R}e^{i(p-p+1)\phi_q}}\int_0^{2\pi}d\beta\frac{e^{-i(p)\beta}}{Q^2(\beta)}\Bigg).\end{aligned}\tag{6.78}$$

Applying this to the matrix element of Eq. (6.40) is more difficult than in the zero order case, and specific circumstances must be considered. We will first focus on the case when the atom is located on the axis of the beam, such that $\mathbf{R}=0$, so as to illustrate the general features of the interaction. When the atom is displaced from the beam axis other effects are apparent due to the presence of the p modes about the atom. The general properties of this off-axis interaction are discussed below, with a quantitative treatment of the full dipole interaction give in Section 6.3.5.

Atom On-Axis

When the atom is on axis, we have $\mathbf{R}=0$, so the Bessel function factors in Eq. (6.78) are non-zero only when they are of order 1. This gives conditions on the relationship between l, l' and p, and each of the summations over p collapses into a single term:

$$\begin{aligned}\mathcal{O}'_{\text{dipole}} = &\frac{N_l^i N_{l'}^f}{\sqrt{2\pi^3}}\frac{e^2}{4\pi\varepsilon_0}e^{i(k_z-k'_z)(z_q+z_R)}e^{-i(\omega-\omega')t}\left(\frac{q_\perp}{2}\right)\\
&\times\Bigg[\delta_{[l,l'+1]}e^{i(0)\phi_R}e^{i\phi_q}\left(k_\perp\int_0^{2\pi}d\beta\frac{e^{-i(l-1)\beta}}{Q^2(\beta)}-k'_\perp\int_0^{2\pi}d\beta\frac{e^{-il\beta}}{Q^2(\beta)}\right)\\
&+\delta_{[l,l'-1]}e^{i(0)\phi_R}e^{-i\phi_q}\left(k'_\perp\int_0^{2\pi}d\beta\frac{e^{-il\beta}}{Q^2(\beta)}-k_\perp\int_0^{2\pi}d\beta\frac{e^{-i(l+1)\beta}}{Q^2(\beta)}\right)\Bigg].\end{aligned}\tag{6.79}$$

This can be expressed as

$$\mathcal{O}'_{\text{dipole}} = N_i N_f\frac{e^2}{(2\pi)^{\frac{5}{2}}\varepsilon_0}\left(\mathcal{A}_l^{+1}\rho_q e^{i(0)\phi_R}e^{i\phi_q}\delta_{[l,l'+1]}+\mathcal{A}_l^{-1}\rho_q e^{i(0)\phi_R}e^{-i\phi_q}\delta_{[l,l'-1]}\right),\tag{6.80}$$

with

$$\mathcal{A}_l^{+1} = k_\perp \int_0^{2\pi} d\beta \frac{e^{-i(l-1)\beta}}{Q^2(\beta)} - k'_\perp \int_0^{2\pi} d\beta \frac{e^{-il\beta}}{Q^2(\beta)} \tag{6.81}$$

$$\mathcal{A}_l^{-1} = k'_\perp \int_0^{2\pi} d\beta \frac{e^{-il\beta}}{Q^2(\beta)} - k_\perp \int_0^{2\pi} d\beta \frac{e^{-i(l+1)\beta}}{Q^2(\beta)}. \tag{6.82}$$

Note that for this on-axis case, no orbital angular momentum may be transferred between the vortex and the centre of mass, as expected. For the special case when $l = 0$, it can be seen that $\mathcal{A}_0^{+1} = -\mathcal{A}_0^{-1*}$. For the general case, with $l \neq 0$, we find that $\mathcal{A}_l^{+1} = -\mathcal{A}_{-l}^{-1*}$, so that the forward and reverse transitions induced by oppositely polarised vortices have the same strength.

This operator may now be applied to find the full matrix element of the on-axis dipole interaction:

$$\mathcal{M}_{\text{dip}}^{\text{on-axis}} = \frac{e^2}{\varepsilon_0\sqrt{2\pi}} \Theta_R \Theta_q^{\text{dip}} \left(\mathcal{A}_l^{+1} \delta_{[m,m'-1]} \delta_{[l,l'+1]} + \mathcal{A}_l^{-1} \delta_{[m,m'+1]} \delta_{[l,l'-1]} \right), \tag{6.83}$$

with expressions for Θ_R and Θ_q^{dip} given in Appendix B.7.4. It can be seen that again, the dipole term admits interaction in which the magnetic quantum number of the atom may change by 0 or 1 units. In this case, no dipole interactions are possible in which the orbital angular momentum of the atomic electron does not change.

Atom Off-Axis

When the atom is off-axis, there are contributions from the expanded wavefunction having $p \neq l$ and $p' \neq l'$, and for a given atom location $p = l$ is not necessarily the dominant term. The factors $F_R^{l,l',p,p'}$ of Eq. (6.51) give the weighting of each p-mode at different positions ρ_R, with the relevant spatial dependence given by $J_{l-p}(k_\perp \rho_R)$. Plotted in Fig. 6.3.3 are these Bessel function prefactors for the first few p modes about $p = l$, for the $E = 200$ keV vortex beam with $k_\perp = 2.23 \times 10^{10}$ m^{-1}, described in Section 2.5. Since the Bessel function of order zero has the largest maximum, with the successive decrease of the maxima of the higher order Bessel functions, those modes close to $p = l$ will always be the most significant in the interaction with the atomic electron - however, depending on the actual atomic position, the other modes may not be negligible. For the $l = \pm 1$ the first zero $\rho_{1,1}$ occurs at approximately 0.17 nm. It is clear from Fig. 6.3.3 that within this radius other orders of orbital angular momentum are not negligible, so that these extra channels of orbital angular momentum transfer will become significant.

The full spatial dependence of the dipole interaction is given in Eq. (6.78). Each p mode contributes a channel for orbital angular momentum exchange to the interaction, in which one unit of orbital angular momentum is transferred. However, this also opens up channels in which orbital angular momentum about the beam z-axis does not appear to be conserved; since the atom and vortex are described about different axes the orbital angular momentum of each cannot be simultaneously conserved. The full matrix element may again be written in the form

$$\mathcal{M}_{\text{dip}}^{l,l'} = \frac{e^2}{\varepsilon_0\sqrt{2\pi}} \Theta_q^{\text{dip}} \left(\mathcal{A}_{l,\Sigma p,l'}^{+1} \delta_{[m,m'-1]} + \mathcal{A}_{l,\Sigma p,l'}^{-1} \delta_{[m,m'+1]} \right), \tag{6.84}$$

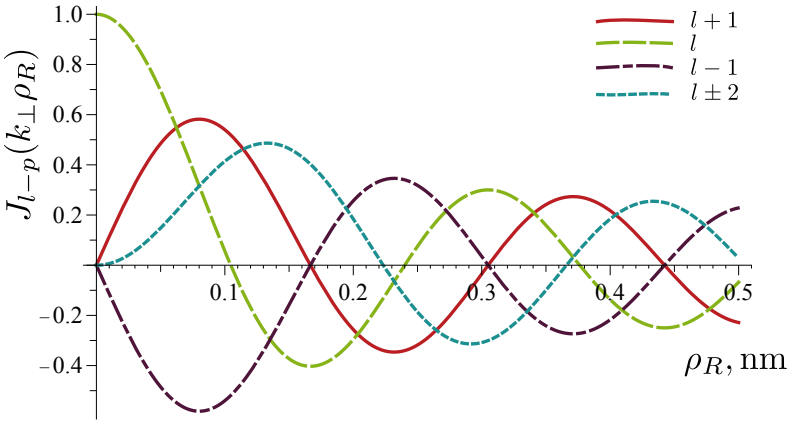

Figure 6.3.3: The vortex modes $J_p(k_\perp \rho'_v)$ about the atomic centre of mass are modulated by the prefactor $J_{l-p}(k_\perp \rho_R)$. This prefactor is plotted above for the indicated values of p, showing the relative significance of the various modes as the atom is moved away from the beam axis. Near the beam axis, the mode $p = l$ dominates, while it can be seen that farther from the axis, several p-modes must be taken into account in the analysis of vortex-atom interactions.

where now the factors affecting the transition strengths consist of sums over p and the final beam angular momentum l':

$$\mathcal{A}^{+1}_{l,\Sigma p,l'} = \sum_{p=-\infty}^{\infty} \sum_{l'-\infty}^{\infty} \mathcal{A}^{+1}_{l,l',p}; \tag{6.85}$$

$$\mathcal{A}^{-1}_{l,\Sigma p,l'} = \sum_{p=-\infty}^{\infty} \sum_{l'=-\infty}^{\infty} \mathcal{A}^{-1}_{l,l',p}; \tag{6.86}$$

with

$$\mathcal{A}^{+1}_{l,l',p} = \Theta_R^{l,l',p,+} \left(k_\perp \int_0^{2\pi} d\beta \frac{e^{-i(p-1)\beta}}{Q^2(\beta)} - k'_\perp \int_0^{2\pi} d\beta \frac{e^{-ip\beta}}{Q^2(\beta)} \right); \tag{6.87}$$

$$\mathcal{A}^{-1}_{l,l',p} = \Theta_R^{l,l',p,-} \left(k'_\perp \int_0^{2\pi} d\beta \frac{e^{-ip\beta}}{Q^2(\beta)} - k_\perp \int_0^{2\pi} d\beta \frac{e^{-i(p+1)\beta}}{Q^2(\beta)} \right), \tag{6.88}$$

with $\Theta_R^{l,l',p,\pm}$ given in Appendix B.7.4, and we have $|\Theta_R^{l,l',p,+}| = |\Theta_R^{l,l',p,-}|$. Since the sums over p and l' are symmetric about zero, and $\mathcal{A}^{+1}_{l,l',p} = -\mathcal{A}^{-1*}_{-l,-l',-p}$, we have that $|\mathcal{A}^{+1}_{l,\Sigma p,l'}| = |\mathcal{A}^{-*1}_{-l,\Sigma p,l'}|$. Note that the delta functions relating l and l' are no longer present, and the factor pertaining to the centre of mass states is included in the sum over l', as the azimuthal factor $e^{i(l-l'\pm 1)\phi_R}$ in Eq. (6.78) affects the nucleus rotation. In the case when the interaction occurs off axis the resulting l' modes are not restricted to $l' = \pm 1$. This point is important for experimental considerations, since it means that a dipole transition, in which $\Delta m = \pm 1$, contributes to signals in *all* l' channels, not simply the $l' = \pm 1$ as would be expected from simple conservation of angular momentum about the beam axis. However, when the nuclear position vector is taken to be a dynamical variable orbital angular momentum conservation about the vortex axis is apparent.

In the situation when the atom is free to rotate about the beam axis, and the nucleus is in a well defined rotational eigenstate, the conservation of orbital angular momentum is straightforward,

and the transfer of orbital angular momentum to the atom may be inferred by looking at the l' states. As an example, the $p = l - 1$ mode may be scattered to the state $p' = p + 2$, via a quadrupole or higher order interaction. Relating this p state to the final beam state, l' requires some knowledge of the atomic orbital angular momentum eigenstate, characterised by L, or at least ϕ_R is required to be a dynamical variable. Assuming $L = L'$, we have

$$\mathcal{M}^{l,l'}_{\text{dip}} \propto \int d^3\rho_R J_{+1}(k_\perp \rho_R) J_{l'-l-1}(k'_\perp \rho_R) e^{i(l-l'+2)\phi_R}, \tag{6.89}$$

as the part of the matrix element dependent on the distance of the atom from the beam axis. Performing the azimuthal integration here indicates $l' = l + 2$, as expected for the atomic change of $\Delta m = -2$. However, it will not be clear through examination of the l' states the *type* of transition induced in the atom. Tables 6.3.2 - 6.3.4 show that both the zero order and the quadrupole interactions may occur with no transfer of orbital angular momentum. It is clear that even orders of q - such as the zero order and quadrupole etc. - will allow transfer of even integer units of orbital angular momentum, while odd orders - dipole, octopole, etc. - will allow odd integer units of angular momentum to be transferred.

As mentioned above, in the case when the atom is fixed off axis the orbital angular momentum about the beam axis is not necessarily a conserved quantity. A consequence of this is that when the atom is situated off-axis the change in magnetic quantum number of the atomic state is not necessarily reflected in the change of orbital angular momentum of the electron vortex. This is illustrated in Fig. 6.3.4, in comparison to the simpler case of the atom on-axis. For the on-axis case, the only contribution to the interaction is from the p-modes having $p = l$ and the resulting final state must have $p' = l'$, and so the atomic change is directly reflected in the exiting beam. However, for the off-axis case, the contributions from several different p-modes induce transitions within the atom causing exchange of orbital angular momentum of different orders. The resulting p' modes may be re-cast as l' modes, by expanding back to the vortex beam axis, such that each l' mode contains contributions from several different p' modes. This makes it very difficult to determine the change in orbital angular momentum of the atom by examining the orbital angular momentum of the beam about the original z-axis.

For experimental applications, it is important to understand the relative strengths of the different possible interactions and determine the most probable change in orbital angular momentum of the atomic electron. This is affected by the relative strengths of the incoming p-modes, and the relative strengths of the multipole transitions, $\left\langle \psi^f_q \middle| q^n e^{\pm in\phi_q} \middle| \psi^i_q \right\rangle$. For an atom in an $m = 0$ state, i.e. with no net magnetic moment, the transitions with $\pm n$ are of equal strength, with the interactions of lowest order in q having the highest strength [113]. It can be seen from Fig. 6.3.3 that the modes having $p = l \pm s$ have equal strength, so illuminating the atom with an $l = 0$ beam will show dichroism in the resulting l' states only when the atom has a net magnetic moment. However, if the atom is allowed to interact with a beam with $l \neq 0$, there will be a difference in distribution of the resulting states l'. This is because, although the modulating factor $J_{l-p}(k_\perp \rho_R)$ will be the same, the Bessel functions describing the p-modes are not symmetric about $l \neq 0$, so the modes $p_1 = l + s$ and $p_2 = l - s$ will not have the same spatial distribution for $l \neq 0$. Since we have $\mathcal{A}^{+1}_{l,\Sigma p,l'} = -\mathcal{A}^{+1*}_{-l,\Sigma p,l'}$, it will be possible to observe dichroism effects by comparing the

resulting l' distributions of beams with $\pm l$ as, barring density of states considerations in the atomic dipole matrix element, the distribution of final modes l' should be the same. For certain values of l and l' the relative magnitude of the different contributions to particular l' modes is discussed quantitatively in Section 6.3.5.

The apparent breaking of orbital angular momentum conservation is due to the extrinsic nature of the orbital angular momentum in this case [16], and the effect may be viewed as a mode broadening. Simply transforming the beam from one axis to another, parallel axis is not enough to make the extrinsic nature of the orbital angular momentum apparent, however. The orbital angular momentum of a vortex beam about a displaced axis is found to be [116]

$$L_z \to L_z + \hat{\mathbf{z}} \cdot \mathbf{R} \times \langle \mathbf{P}_\perp \rangle \tag{6.90}$$

where $\langle \mathbf{P}_\perp \rangle$ is the total transverse momentum (or current), measured about the new axis. In the situation here, the two axes are parallel, and as shown in Chapter 4 the total momentum of the electron vortex has a component only in the z direction. Thus $\langle \mathbf{P}_\perp \rangle = 0$, and the angular momentum of the beam about the new axis is simply $l\hbar$. On the other hand, the interaction with the atom at this new axis makes the extrinsic nature of the vortex orbital angular momentum apparent - due to its spherical symmetry the z-axis of the atom is arbitrary[4], so that the transverse momentum of the beam about the z-axis is not necessarily zero, leading to a change in the orbital angular momentum of the beam about the atomic axis. This is responsible for the apparent non-conservation of the beam orbital angular momentum.

6.3.5 Spatial Dependence of the Dipole Matrix Element

For the dipole term, the full spatial dependence of the matrix element is contained in Eq. (6.78). The first and fourth terms represent interaction in which the orbital angular momentum of the atom may increase by one unit, while the second and third terms represent interactions in which it may decrease by one unit. For both these interactions the change in the orbital angular momentum of the beam may be either $+\hbar$ or $-\hbar$, with the two possibilities having different spatial dependence. These spatial dependence of $|\mathcal{M}^{l,l'}_{\text{dip}}|^2$ are plotted for electron vortex beams having $l = 0, \pm 1$, for the different combinations of $\Delta m = \pm 1$ and $\Delta l = \pm 1$ in Fig. 6.3.5, Fig. 6.3.6 and Fig. 6.3.7. The plots of $|\mathcal{M}^{l,l'}_{\text{dip}}|^2$ show the strength of a given interaction process at different positions within the beam, such that the centre of the beam is always at the centre of the plot. The beams are modelled using the same parameters of the typical Ångstrom size electron vortex as described in Section 2.5, with $k_z = 2.3 \times 10^{12}\ \text{m}^{-1}$ and $k_\perp = 2.3 \times 10^{10}\ \text{m}^{-1}$ for the incoming beam, and $k'_z = k_z$, $k'_\perp = 0.5 k_\perp$ in each case[5].

[4] In making the transformation shown in Fig. 6.3.2 it appears that we 'fix' the atomic electron angle ϕ_q to lie in a plane transverse to the beam axis. In doing this we have rotated the atomic coordinate system to the frame that best suits our purposes - the 'natural' z-axis of the atom may be quite different - so that ϕ_q and θ_q in this rotated frame are different to those in the natural atomic basis.

[5] The plots were generated using Mathematica 8. For each forward or reverse atomic transition, the relevant terms in Eq. (6.78) were calculated over a 256×256 sample grid of atomic positions $\mathbf{R}$. For each individual calculation (one

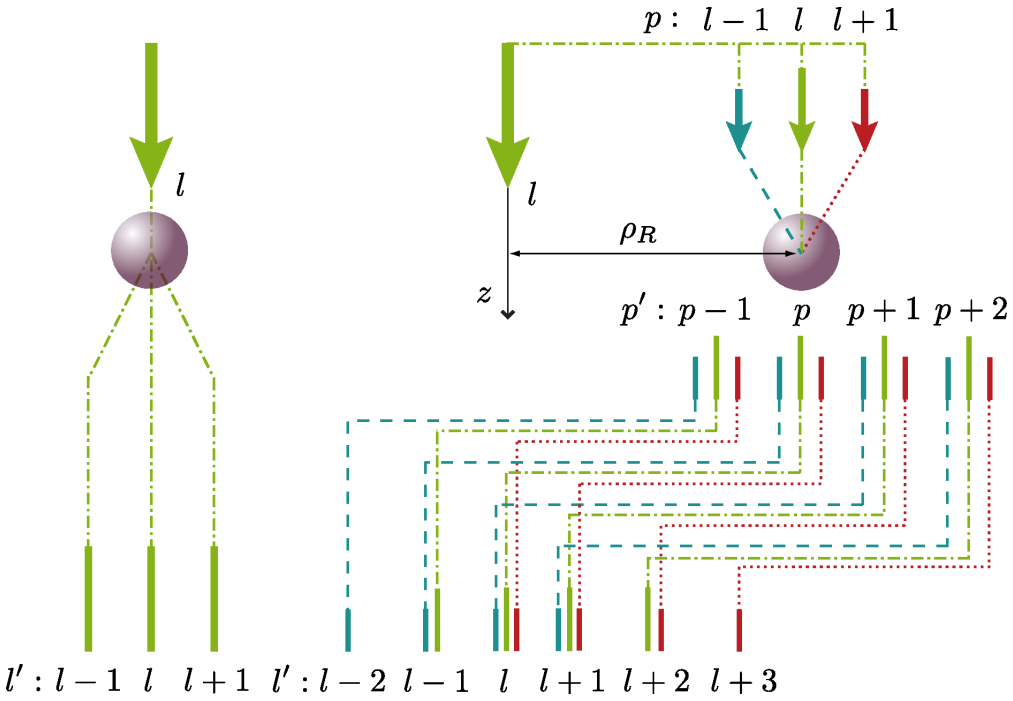

Figure 6.3.4: Schematic showing contributions of the expanded wavefunctions to transitions of an off-axis atom, compared to those in the atom lying on the axis. In the on-axis case the change in orbital angular momentum of the atom is directly reflected in the change in the orbital angular momentum of the beam. In the off axis case, the atom interacts with the p-vortex modes arising after the expansion of the beam about an axis through the atomic nucleus. The p-modes may interact via a multipolar transition, leading to a change in the atomic orbital angular momentum $\Delta p = -\Delta m$. However, when the orbital angular momentum of the vortex is measured after the interaction, it is measured about the original beam axis - in transforming the post interaction p' states back to this axis the direct connection to the atomic states is lost. However, by examining the relative strengths of the atomic multipolar transitions the change in the atom can be determined.

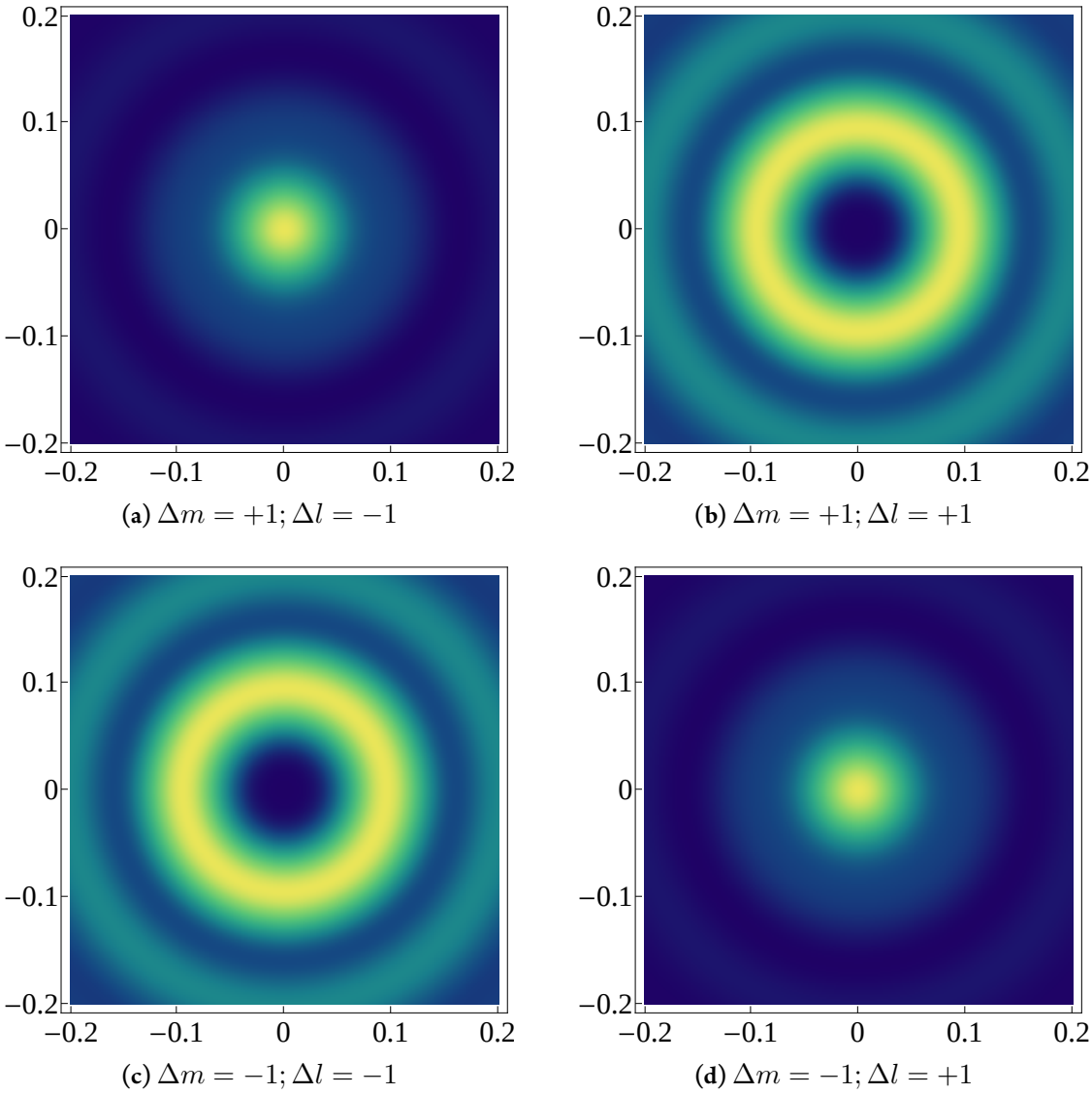

(a) $\Delta m = +1; \Delta l = -1$ (b) $\Delta m = +1; \Delta l = +1$

(c) $\Delta m = -1; \Delta l = -1$ (d) $\Delta m = -1; \Delta l = +1$

Figure 6.3.5: The spatial dependence of the strength of the matrix element for the interaction between a hydrogen-like atom and the electron vortex beam with $l = 0$, across a nanometre scale (see text for relevant parameters). (a) and (b) show the interaction for which $\Delta m = +1$, with $\Delta l = -1$ and $\Delta l = +1$ respectively. (c) and (d) show the interaction for which $\Delta m = -1$, with $\Delta l = -1$ and $\Delta l = +1$ respectively. Plots are normalised such that for each individual plot blue is the lowest value (zero) and yellow is the highest. The relative strengths for each plot may be seen in the line graphs of 6.3.8a

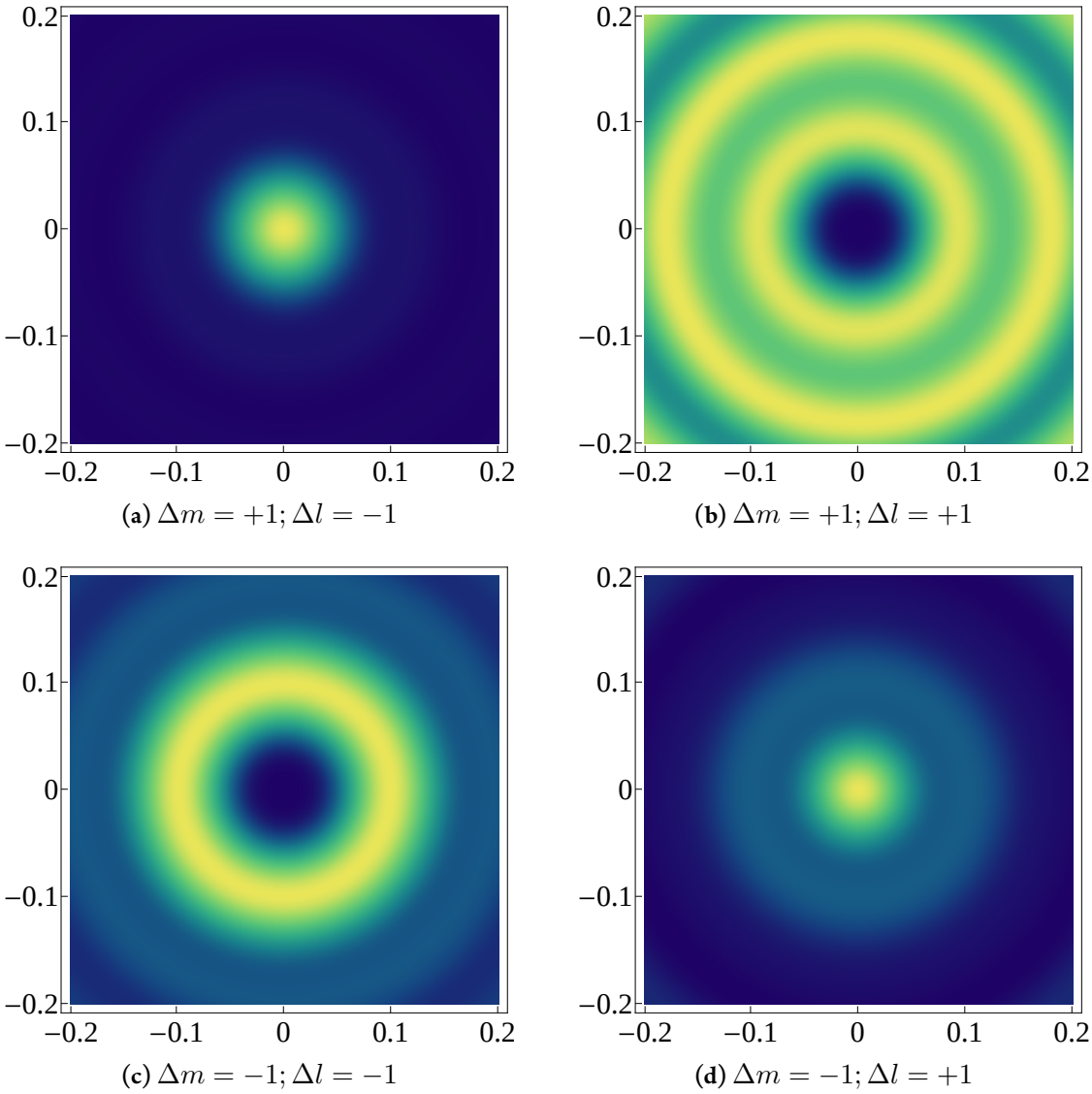

(a) $\Delta m = +1; \Delta l = -1$

(b) $\Delta m = +1; \Delta l = +1$

(c) $\Delta m = -1; \Delta l = -1$

(d) $\Delta m = -1; \Delta l = +1$

Figure 6.3.6: The spatial dependence of the strength of the matrix element for the interaction between a hydrogen-like atom and the electron vortex beam with $l = +1$, across a nanometre scale (see text for relevant parameters). (a) and (b) show the interaction for which $\Delta m = +1$, with $\Delta l = -1$ and $\Delta l = +1$ respectively. (c) and (d) show the interaction for which $\Delta m = -1$, with $\Delta l = -1$ and $\Delta l = +1$ respectively. Plots are normalised such that for each individual plot blue is the lowest value (zero) and yellow is the highest. The relative strengths for each plot may be seen in the line graphs of 6.3.8b

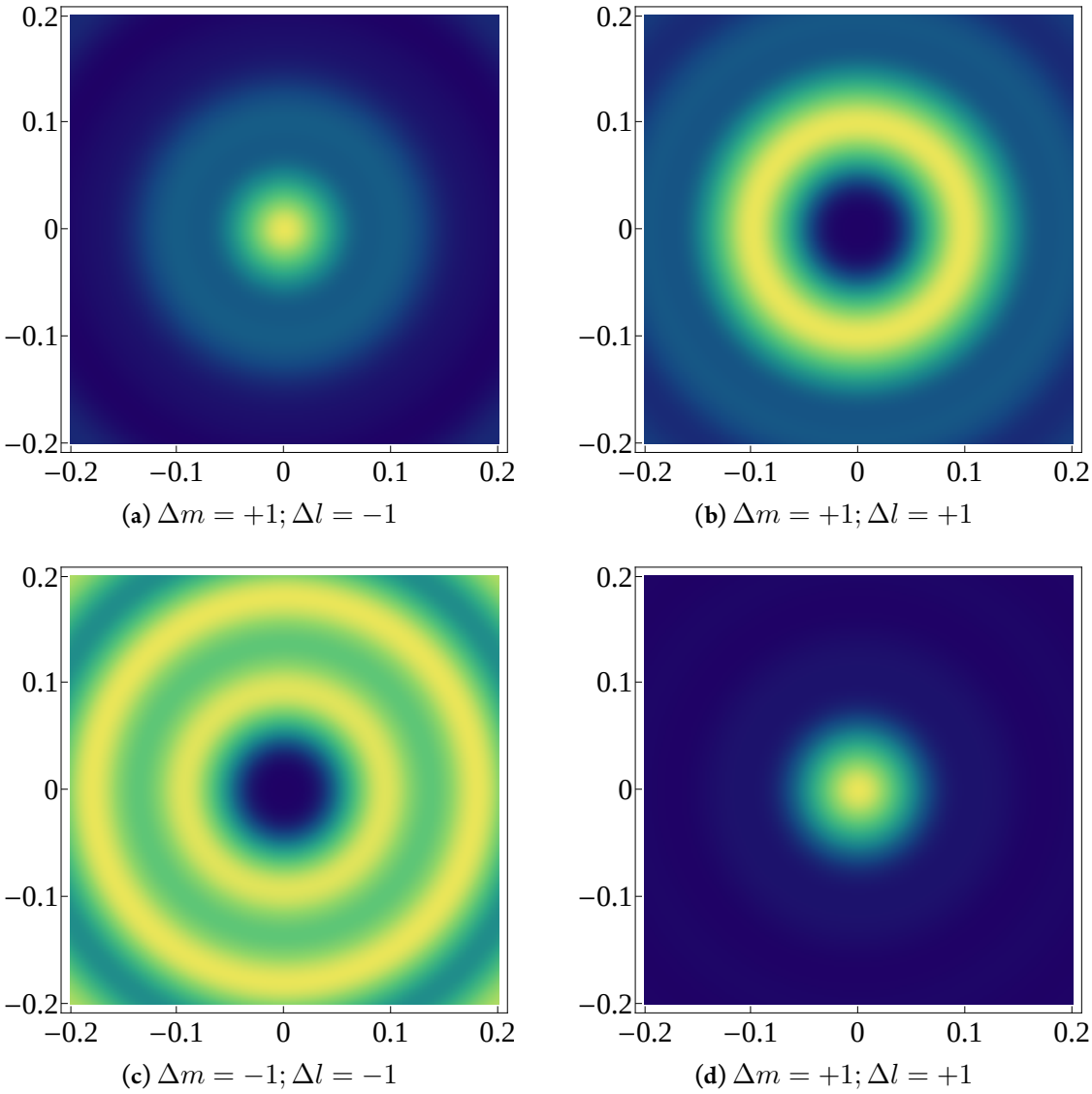

(a) $\Delta m = +1; \Delta l = -1$

(b) $\Delta m = +1; \Delta l = +1$

(c) $\Delta m = -1; \Delta l = -1$

(d) $\Delta m = +1; \Delta l = +1$

Figure 6.3.7: The spatial dependence of the strength of the matrix element for the interaction between a hydrogen-like atom and the electron vortex beam with $l = -1$, across a nanometre scale (see text for relevant parameters). (a) and (b) show the interaction for which $\Delta m = +1$, with $\Delta l = -1$ and $\Delta l = +1$ respectively. (c) and (d) show the interaction for which $\Delta m = -1$, with $\Delta l = -1$ and $\Delta l = +1$ respectively. Plots are normalised such that for each individual plot blue is the lowest value (zero) and yellow is the highest. The relative strengths for each plot may be seen in the line graphs of 6.3.8c

As can be seen in each figure, those interactions for which the orbital angular momentum about the beam axis is conserved - i.e. having $\Delta m = \pm 1$ and $\Delta l = \mp 1$ - are the dominant processes in the centre of the beam, while those that do not conserve orbital angular momentum about the z-axis are the off-axis interactions, as described qualitatively above. In the following we will refer to the former as 'ordinary' interactions, and the latter as 'irregular'. For the case of the incident $l = 0$ beam, shown in Fig. 6.3.5 the ordinary interactions - with $\Delta m = -\Delta l$ - have the same magnitude for both the forward and reverse atomic transition, as do the other, irregular transitions. It is this symmetry that led to the clear and unambiguous dichroism result of Verbeeck *et al.*, in their experiment on magnetised iron films [24]. This symmetry is not apparent in the transitions of the vortex beams with $l = \pm 1$ when comparing the ordinary and irregular transitions within each beam; however when considering the ordinary and irregular forward and reverse transitions of the vortex beams of opposite winding with $l = \pm 1$, the symmetry is again apparent. The ordinary forward transition for the $l = +1$ beam has the same magnitude and spatial profile as the ordinary reverse transition for the $l = -1$ beam, and vice versa, with the same relationships for the irregular transitions, such that $|\mathcal{A}_l^{+1}| = |\mathcal{A}_{-l}^{-1*}|$, as shown for the on-axis dipole interaction in Section 6.3.4. This suggests that future dichroism experiments using electron vortex beams should compare the transition rates between oppositely vortex beams with opposite signs of orbital angular momentum. An experimental scheme for such a dichroism experiment is suggested below.

Fig. 6.3.8 shows the relative magnitude of the square modulus of the matrix element for each interaction with the different vortex beams having $l = 0, \pm 1$. For an $l = 0$ beam it is found that the probability of scattering to either the $\Delta m = +1$ or $\Delta m = -1$ by an ordinary transition is the same, with the corresponding change in l being $\Delta l = -1$ or $\Delta l = +1$ respectively. Similarly, the irregular transitions also have the same probability, though this probability is much smaller than that of the ordinary transitions and is of course zero on-axis. For the $l = 1$ incident beam, the forward ordinary transition has the largest magnitude, and is an order of magnitude larger than the reverse ordinary transition. Similarly, the reverse ordinary transition is the largest of the $l = -1$ beam induced transitions, as expected from the symmetry in the beam interactions discussed above. These are the largest contributions to the overall matrix element for the $l = \pm 1$ beams, and as such will contribute the largest to the signal obtained in an electron energy loss spectroscopy experiment. The other channels will contribute to a background signal, in the experiment proposed below only the small irregular channel with the same Δl as this main signal will contribute to the measured background signal. As can be seen in Fig. 6.3.9, the strengths of the dominant interactions for the vortex beams are significantly larger than (approximately double) the equivalent interactions for the $l = 0$ beam, suggesting that dichroism experiments comparing with incident vortex beams will give stronger signals than the similar experiment with incident plane wave, and post-selection using a vortex analyser, as in [24].

Such a dichroism signal could be measured using the experimental set-up depicted in Fig. 6.3.10.

pixel) the atomic position $\mathbf{R}$ is fixed, so that the factor $e^{i(l-l'\pm)\phi_R}$ contributes only a magnitude factor in each case. Since the interaction is not a coherent process, and the atom may only interact with one p-vortex, the magnitude of $|\mathcal{M}_{\text{dip}}^{l,l'}|^2$ for an interaction at position $\mathbf{R}$ was found by summing $|\mathcal{M}_p^{l,l'}|^2$ for the relevant conditions of m and l, where $|\mathcal{M}_p^{l,l'}|^2$ is the square modulus of the effective operator of Eq. (6.78) for a given p. This was done for $-11 \leq p \leq 11$, as outside this range the modulation factors $J_{l-p}(k_\perp \rho_R)$ lead to negligible contributions for the sampled range of $\mathbf{R}$.

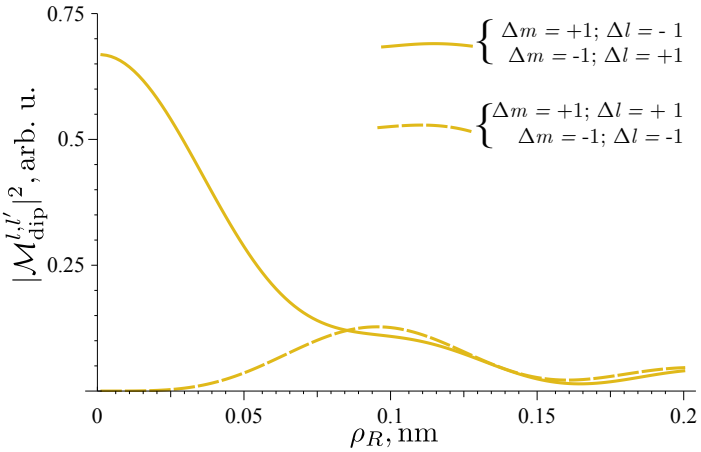

(a) $l = 0$

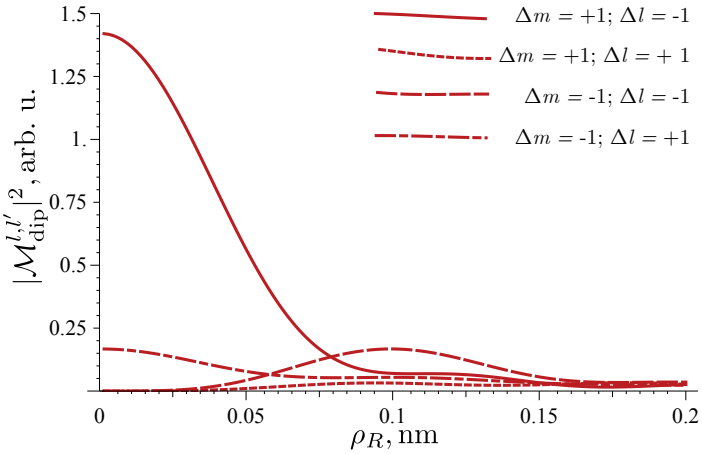

(b) $l = +1$

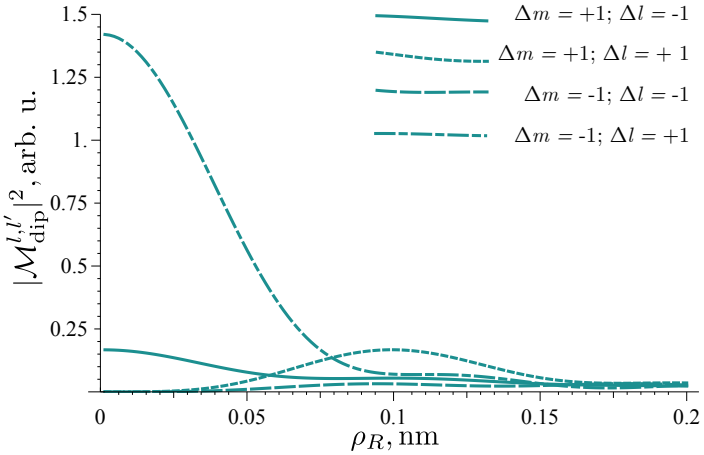

(c) $l = -1$

Figure 6.3.8: The relative strength of the interactions with $\Delta m = \pm 1$ for incident beams with $l = 0, \pm 1$. For the $l = 0$ incident beam it can be seen in (a) that the two ordinary transitions have the same strength and spatial profile, as do the two irregular transitions. The incident vortex beam with $l = \pm 1$ each have a dominant ordinary transition - approximately double the strength of those of the $l = 0$ beam - with the other ordinary and two irregular transitions greatly suppressed. Plots are given in arbitrary units.

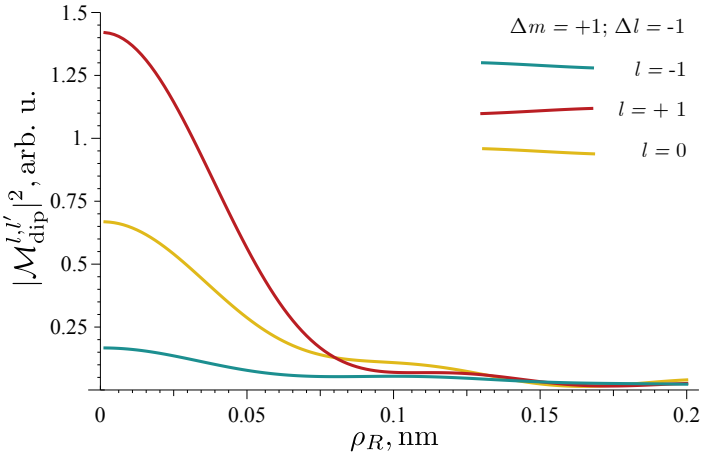

(a) $\Delta m = +1$

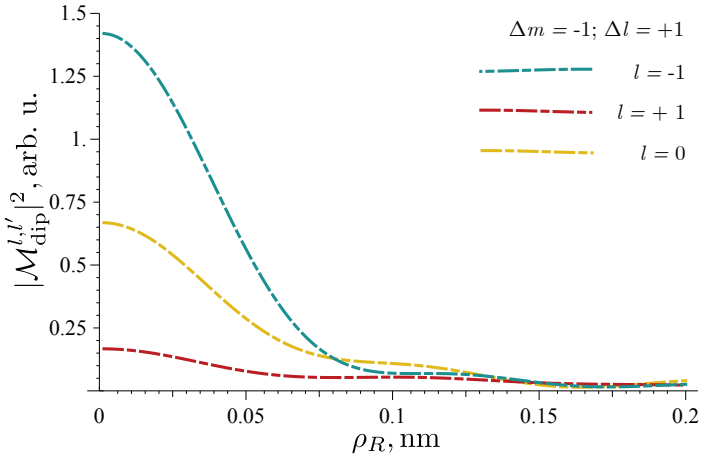

(b) $\Delta m = -1$

Figure 6.3.9: The magnitude and spatial variation of (a) the $\Delta m = +1, \Delta l = -1$ transition, and (b) the $\Delta m = -1, \Delta l = +1$ transition. It can be seen that for the $\Delta m = +1$ atomic transition, the matrix element is an order of magnitude greater for the $l = +1$ beam, and vice-versa for the $\Delta m = -1$ transition.

Using this arrangement, electron energy loss spectroscopy using electron vortex beams could be used to obtain chiral information from various samples. An incident vortex beam of vorticity $l = 1$ is focused via a scanning confocal lensing system onto a point on the sample. The confocal set-up is required to reduce the contributions from neighbouring off-axis atoms that will interact with the vortex through irregular transitions, though these cannot be completely eliminated. The sample will interact with the electron vortex, whether by core-shell excitations or other chiral activity, changing the total orbital angular momentum within the beam. This beam is transmitted through the sample, and passed though a forked holographic mask, acting as vortex analyser. This will decompose the beam into the different vortex states, and the relative integrated intensity of the different vortex states can be measured, and compared with the same experiment performed with a vortex beam of opposite orbital angular momentum. A spatially resolved electron energy loss spectrum will be obtained by scanning the focused probe across a sample to obtain an energy loss map - comparison with the oppositely polarised electron vortex will lead to spatially resolved chiral information about the sample, with the possibility of nanometre resolution.

To illustrate this, consider the $l = 1$ beam interacting with an atom; the dominant interaction will induce a $\Delta m = +1$ transition within the atom, and scatter the vortex state to $l' = 0$. The transmitted beam is now passed through the vortex analyser, splitting the beam into components having vorticity 0, 1 and 2. Since the dominant interaction is that for which $\Delta l = -1$ (but this interaction is weak), it is expected that there will be the largest signal in the post-analyser $l = 1$ channel (i.e. no diffraction), and significant signal in the $l = 0$ channel, with very little having $l = 2$. The signal of interest is that in the $l = 0$ channel, as this contains those electrons that have undergone an interaction with the atom. To obtain an energy loss spectrum, this will be compared with the similar signal obtained using an $l = -1$ incident vortex beam. In this case, the signal of interest is also the post-analyser $l = 0$ signal, as this is comprised of electrons that have been scattered by the sample to $\Delta l = +1$ though an atomic interaction with $\Delta m = -1$, the dominant interaction for the $l = -1$ beam. Comparison of these two signals at various energies will give electron energy loss spectrum results, and characterise the chiral activity of the sample.

An energy loss spectrum obtained in this way depends on the signals in the post-analyser $l = 0$ beam, for both incident beams. In both cases, this beam will be comprised of the dominant, ordinary interaction, and a smaller contribution from the irregular transition having the same Δl but opposite Δm. This irregular contribution arises due to off-axis interactions and may cause issues with resolution if its magnitude becomes comparable to that of the desired ordinary interaction. For the incident $l = +1$ and $l = -1$ beams respectively, Fig. 6.3.11 and Fig. 6.3.12 show the square modulus of the matrix elements contributing to each post-analyser channel, and the sum of these matrix elements. The sum determines the probability that a interaction observable in that channel occurs, and directly relates to the signal that will be measured in that channel, with the measured signal proportional to the spatial integral of the total squared matrix element. By comparing the relative contributions to the total squared matrix element it can be seen that for the desired ordinary interaction in each case the signal will be much stronger, comprising the main part of the total, measured signal. The irregular signal has a maximum at approximately 0.1 nm, due to off axis interactions, and while this will contribute to background signal it should not be significant

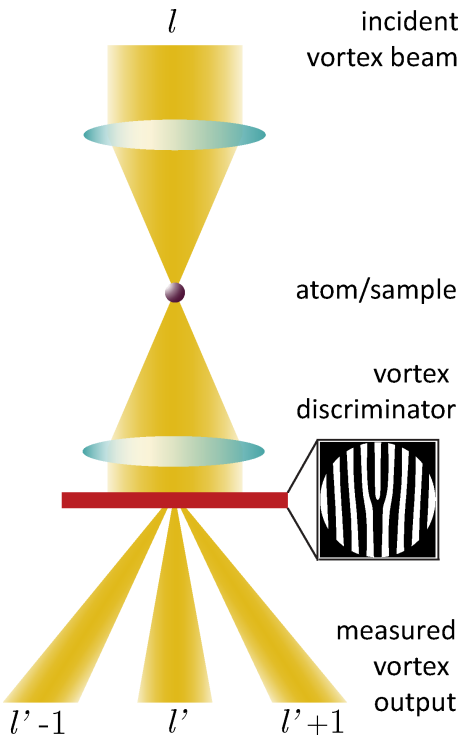

Figure 6.3.10: Suggested experimental set-up for electron energy loss dichroism experiments using electron vortex beams. The sample, shown as a point in this schematic, is illuminated by a focused electron vortex. The transmitted beam is passed through a holographic forked filter, acting as a vortex analyser, so that the beam is split into the different vortex components. Collection of the different vortex components and comparison with those obtained with a beam of opposite vortex polarisation will enable chiral information about the sample to be obtained.

enough to greatly impair the resolution. Thus, this method should be able to provide chiral dichroism spectra at high resolution, with appropriately focused vortex beams. As discussed in Section 1.3.4 the limitations of creating vortex beams with Ångstrom resolution lead to beams that have the central minima washed out [39] - nevertheless, the suggested experiment described here should provide an accessible method for obtaining nanometre resolution electron energy loss chiral dichroism spectra. With the development of specific corrective software for this particular experimental set-up, an increase in resolution may potentially be achievable by utilising the chiral information contained in the other post-analyser channel (though this signal is predicted to be very small), or by correction for the off axis contributions to the total signal. Correction of off-axis contributions will require further simulations to be carried out with more experimentally feasible vortex beam profiles, by expansion into the basis set of the ideal Bessel beams considered here, and also analysis of contributions from the quadrupole and higher multipole terms, though these are expected to be small.

6.4 Comparison of the dipole interaction in the Hamiltonian and wave-function expansions

The selection rules for the interaction of atomic matter with an electron vortex have now been determined using two different methods - a direct multipolar expansion of the interaction Hamiltonian, and the use of an effective operator that has been expanded into a multipolar series. Several key differences have been found using these two methods. We note that the idea of a multipolar expansion in the two cases is not quite the same - in the first case the Hamiltonian is expanded into a 'true' multipolar series, whereas the second method utilised an expansion in powers of $q_\perp$, the in-plane component of the atomic position vector, with the dependence on q_z not included in the expansion. This leads to some, but not all, of the differences between the two methods. Because of this, the full magnitudes of the transition matrix elements for the two methods have not been compared in this analysis, as the selection rules obtained are in quite different formats. For the Hamiltonian expansion method the full matrix element has been derived to achieve the selection rules; for the multipolar expansion method the selection rules are apparent at operator level, before applying the specific atomic states.

The dipole term of the expanded interaction Hamiltonian is found to allow interactions in which zero or one units of orbital angular momentum many be exchanged. The orbital angular momentum of the electron vortex and the centre of mass of the atom combine to form a separate system that may exchange orbital angular momentum with the atom. The combining of the angular momenta of the vortex and the gross atomic motion is also found using the effective operator method when the atom is free to rotate about the beam axis. In this case, the general features of the two sets of selection rules is the same - orbital angular momentum is conserved about the beam axis and the dipole terms in each case may mediate interactions in which one unit is exchanged. The zero order term of the effective operator may be compared with the multipolar expansion dipole interaction in which no units of orbital angular momentum are exchanged - this is not a feature of the effective operator 'dipole' term due to the difference in definition of dipole between

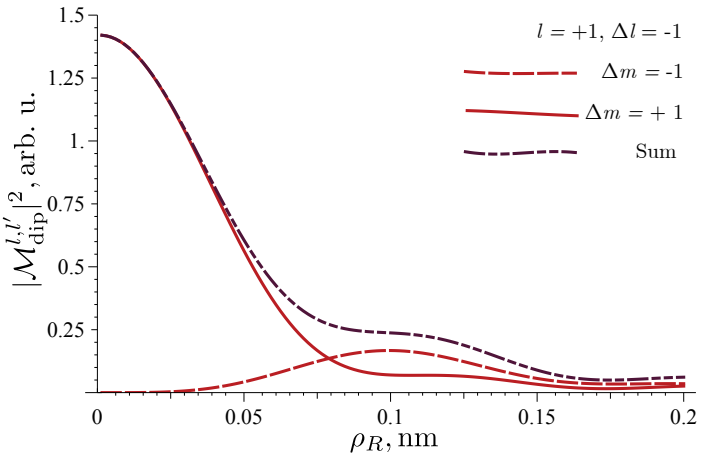

(a) Post-analyser $l = 0$ channel

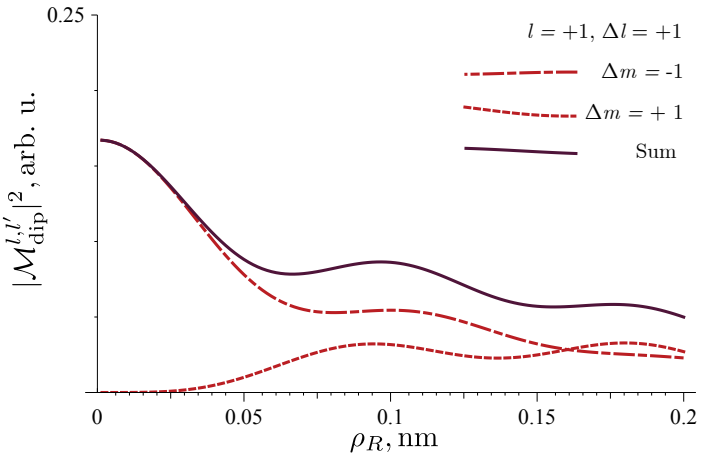

(b) Post-analyser $l = 2$ channel

Figure 6.3.11: The matrix elements of the relevant regular or irregular interactions contribute to the signal observed in the indicated post-vortex analyser channels. The signal is proportional to the integrated matrix element. For the $l = +1$ beam the transition of interest is that with $\Delta l = -1, \Delta m = +1$. This will be observed in the $l = 0$ channel, shown in (a), and the off-axis irregular transition with $\Delta l = -1, \Delta m = -1$ does not contribute a significant amount. The interaction probability contributing to the $l = 2$ channel, shown in (b), is very small so that this dichroism effects are not expected to be apparent in this channel. Plots are given in arbitrary units.

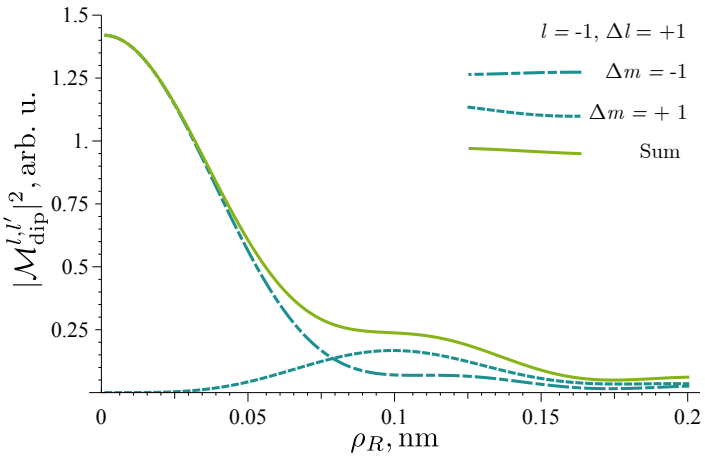

(a) Post-analyser $l = 0$ channel

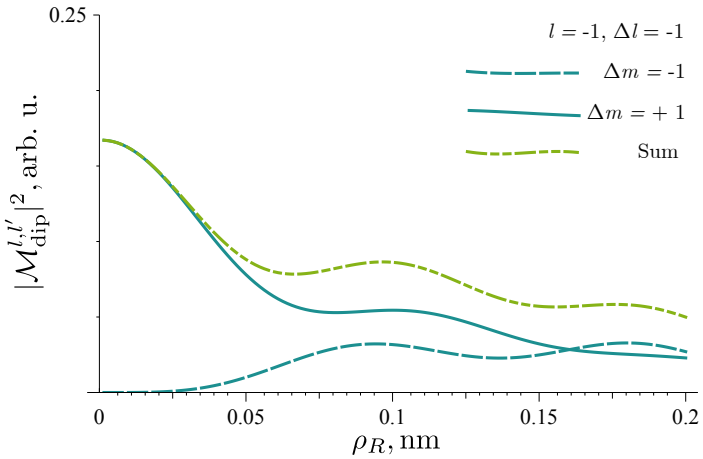

(b) Post-analyser $l = -2$ channel

Figure 6.3.12: The matrix elements of the relevant regular or irregular interactions contribute to the signal observed in the indicated post-vortex analyser channels. The signal is proportional to the integrated matrix element. For the $l = -1$ beam the transition of interest is that with $\Delta l = +1, \Delta m = -1$. This will be observed in the $l = 0$ channel, shown in (a), and the off-axis irregular transition with $\Delta l = -1, \Delta m = +1$ does not contribute a significant amount. The interaction probability contributing to the $l = 2$ channel, shown in (b), is very small so that this dichroism effects are not expected to be apparent in this channel. Plots are given in arbitrary units.

the two methods.

A key difference is the 'dipole' term of the effective operator permits interactions in which any amount of orbital angular momentum may be exchanged. This is found when the atom is fixed at a distance from the axis. This should be reproducible in the multipolar Hamiltonian by calculating the matrix element at different positions $\mathbf{R}$ without integrating the centre of mass states. However in order to obtain any spatial information about the interaction, this must be evaluated on a point-by-point basis. The effective Hamiltonian method allows for more immediate determination of the spatial profile of the interaction.

Using both methods, for the interactions in which exchange is possible, the matrix elements of the "forward" and "reverse" exchanges, $\mathcal{A}_l^{\mathrm{F}}$ and $\mathcal{A}_l^{\mathrm{R}}$ respectively, are found to have magnitudes such that $\mathcal{A}_l^{\mathrm{F}} = \mathcal{A}_{-l}^{\mathrm{R}*}$. As long as there is no net magnetic moment of the atom that would disallow either the forward or reverse transitions (i.e. the atom is in the highest or lowest m state) the transition rate of both would be the same, and no net dichroism would be observed in an EELS experiment such as that demonstrated in [24] using an incident $l = 0$ beam, or that suggested above using oppositely polarised incident vortex beams. The interaction mechanisms for both the Hamiltonian and wavefunction expansions are directly comparable to the action of circularly polarised light on the atom. For the Hamiltonian expansion method, this is apparent in the atomic dipole matrix element $\boldsymbol{\mathcal{D}}$, which shows explicit dependence on circular polarisation, while the operator $\rho_q e^{\pm i\phi_q}$ of the wavefunction expansion may also be expressed in terms of projection onto a circularly polarised basis

$$\rho_q e^{\pm i\phi_q} = x_q \pm i y_q = \mathbf{r}_q \cdot \left(\frac{\hat{\mathbf{x}} \pm i\hat{\mathbf{y}}}{2} \right). \tag{6.91}$$

The advantage of the wavefunction expansion is that the change in interaction with the distance of the atom from the beam axis is readily apparent, via the modulating functions $J_{l-p}(k_\perp \rho_R)$. For the Hamiltonian expansion, the Hamiltonian is dependent on R; this serves to illustrates the limits of the validity of the dipole approximation. The expansion is valid for $|\mathbf{q}| \ll |\mathbf{r}_v - \mathbf{R}|$; when satisfied, the dipole term is then dominant. Outside this limit, however, this dipole Hamiltonian is not applicable, and higher order terms must be considered. The wavefunction multipolar expansion avoids this issue; the atom interacts with p-modes weighted according to the distance from the axis, which dictates the significant multipolar interactions. Due to the asymptotic limit of the Bessel function, which requires $0 < k_\perp q_\perp \ll \sqrt{l+1}$, this approach applies best in the case of small atoms, $|\mathbf{q}| \approx a_0$, and high l. Although $k_\perp a_0 \approx 1$ for the typical 200 keV Bessel beam, $k_\perp$ can be increased by altering the mask shape, such that this method of analysis is applicable for the $l = 1$ beam interacting with the hydrogen atom.

6.5 Analysis and application of the selection rules

The following analysis is applicable to the results of the both the Hamiltonian and wavefunction multipolar expansions, since we find that the forward and reverse transitions contribute the same magnitude to the interaction matrix element. The analysis will be presented in terms of general functions $\mathcal{U}_l^{0,\pm1}$, which represent the magnitudes of the contributions to the matrix element for $\Delta m = 0, \pm 1$ for each of the multipolar expansions, i.e. the $\mathcal{C}_l^{0,\pm1}$ of Eq. (6.34), and the $\mathcal{A}_{l,\Sigma,p,l'}^{\pm1}$ of

Eq. (6.84).

It has been demonstrated experimentally that electron vortex beams can exhibit dichroism in their absorption by matter [24]. This is due to the internal electronic structure of the material under study - whether it has a magnetic moment - and is not due to the structure of the beam itself. A dichroic signal is observed when one vortex polarisation is absorbed preferentially over the other. The transition (or absorption) rate, Γ, is proportional to the modulus square of the matrix element, and the density of the final states ρ_f accessible via the interaction. This is expressed as Fermi's golden rule:

$$\Gamma = \frac{2\pi}{\hbar}|\mathcal{M}_{fi}|^2\hat{\rho}_f. \tag{6.92}$$

The transition rates for electron vortex beams with two different senses of rotation may now be found, using the selection rules of (6.34) and (6.80) (and those for the off-axis case) above. For simplicity, we choose the beams $l = \pm 1$, and examine scattering in both cases to the state $l' = 0$, noting that the process of an $l = 0$ vortex scattering to $l = \pm 1$ is equivalent, and the experimental process in [24]. Additionally, the centre of mass motion can be restricted, as it would be in a solid, for example, so we may write $L = L'$ and examine only the transfer between the vortex beam and the atomic electron.

The hydrogen atom may seem like a very simple model, however the results derived above may be generalised for a many-electron system, such as an iron atom, by considering the total orbital angular momentum of the atomic electron configuration [63]. In the LS coupling regime, the total angular momentum of the atomic electron wavefunction is given by $\mathbf{J} = \mathbf{L} + \mathbf{S}$, with $|L - S| \leq J \leq L + S$ being the relevant orbital angular momentum quantum number, and $-J \leq m_J \leq J$ the associated magnetic quantum number. m_J, the projection onto the atomic z-axis, will be affected by the exchange of orbital angular momentum with the electron vortex. The total angular factors of the multi-electron wavefunction can be described by the product of the spherical harmonics of the occupied states in a hydrogenic model; since the products of spherical harmonics may be written as linear combinations of spherical harmonics the many electron wavefunction can be described as a linear combination of spherical harmonics of the form $Y_j^{m_j}$ [117], for individual electrons with total angular momentum $j = l + s$ and projection m_j. Here, numerical and phase factors arising from the coupling of the atomic electrons will be neglected, without loss of generality. The coefficients of the spherical harmonics describing the multi-electron wavefunction are calculated using Wigner 3-j symbols; the symmetry properties of the 3-j symbols means that there is merely a difference in phase factor between states having m_j and $-m_j$, and the magnitude of the coefficients is the same.

The possible excitations that can be induced by the $l = \pm 1$ electron vortex in the iron L_2 and L_3 edges are summarised in Table 6.5.1. Each forward transition that may be induced in the $l = +1$ interaction has a corresponding reverse transition which may be induced by the $l = -1$ vortex, such that $m_j^{(+l)} = -m_j^{(-1)}$ and $m_J'^{(+l)} = -m_J'^{(-1)}$. The spherical harmonics are normalised such that

$$(-1)^{(\ell-m)}Y_\ell^{-m}(\theta,\phi) = Y_\ell^{m*}(\theta,\phi), \tag{6.93}$$

and this, along with the symmetries of the Wigner 3-j symbols, shows that the strength of the

$l = +1$		$l = -1$	
L_2	$2p_{1/2}(m_j = -1/2) \rightarrow 3d_{3/2}(m_j = +1/2)$	L_2	$2p_{1/2}(m_j = +1/2) \rightarrow 3d_{3/2}(m_j = -1/2)$
	$2p_{1/2}(m_j = +1/2) \rightarrow 3d_{3/2}(m_j = +3/2)$		$2p_{1/2}(m_j = -1/2) \rightarrow 3d_{3/2}(m_j = -3/2)$
L_3	$2p_{3/2}(m_j = -3/2) \rightarrow 3d_{5/2}(m_j = -1/2)$	L_3	$2p_{3/2}(m_j = +3/2) \rightarrow 3d_{5/2}(m_j = +1/2)$
	$2p_{3/2}(m_j = -1/2) \rightarrow 3d_{5/2}(m_j = +1/2)$		$2p_{3/2}(m_j = +1/2) \rightarrow 3d_{5/2}(m_j = -1/2)$
	$2p_{3/2}(m_j = +1/2) \rightarrow 3d_{5/2}(m_j = +3/2)$		$2p_{3/2}(m_j = -1/2) \rightarrow 3d_{5/2}(m_j = -3/2)$
	$2p_{3/2}(m_j = +3/2) \rightarrow 3d_{5/2}(m_j = +5/2)$		$2p_{3/2}(m_j = -3/2) \rightarrow 3d_{5/2}(m_j = -5/2)$

Table 6.5.1: Allowed transitions in the L_2 and L_3 edges for interaction with an electron vortex beam with $l = +1$ and $l = -1$.

forward and reverse transitions contributing to the matrix element will be the same.

The total transition rate of the L_2 and L_3 edges, as observed in [24], is given by the sum of the transitions rates for the possible transitions in each edge. Explicitly, for the L_2 edge, we have

$$\Gamma_{\mathrm{L_2}}^{l=+1} = \frac{2\pi}{\hbar}|\mathcal{U}_l^{+1}|^2\left(|\mathcal{A}_{+1}^{L_2(a)}|^2\hat{\rho}_{3d_{3/2}(m_j=+1/2)} + |\mathcal{A}_{+1}^{L_2(b)}|^2\hat{\rho}_{3d_{3/2}(m_j=+3/2)}\right), \tag{6.94}$$

and

$$\Gamma_{\mathrm{L_2}}^{l=-1} = \frac{2\pi}{\hbar}|\mathcal{U}_l^{-1}|^2\left(|\mathcal{A}_{-1}^{L_2(a)}|^2\hat{\rho}_{3d_{3/2}(m_j=-1/2)} + |\mathcal{A}_{-1}^{L_2(b)}|^2\hat{\rho}_{3d_{3/2}(m_j=-3/2)}\right), \tag{6.95}$$

which, will be equal as long as the densities of final states are the same in each case, i.e. $\hat{\rho}_{3d_{3/2}(m_j=+1/2)} = \hat{\rho}_{3d_{3/2}(m_j=-1/2)}$ and $\hat{\rho}_{3d_{3/2},m_j=+3/2} = \hat{\rho}_{3d_{3/2},m_j=-3/2}$, as it has been established above that $|\mathcal{A}_{+1}^{L_2}| = |\mathcal{A}_{-1}^{L_2}|$, and $|\mathcal{U}_l^{+1}| = |\mathcal{U}_l^{-1}|$. Note that the atomic matrix elements $\mathcal{A}_{L_2}^{\pm1}$ take slightly different forms for the two expansion methods; we have, for the Hamiltonian multipolar expansion:

$$\mathcal{A}_{+1}^{L_2(a)} = \langle 2p_{1/2}, m_j = -1/2 \,|\, \mathbf{q} \,|\, 3d_{3/2}, m_j = +1/2\rangle\,; \tag{6.96a}$$
$$\mathcal{A}_{+1}^{L_2(b)} = \langle 2p_{1/2}(m_j = +1/2) \,|\, \mathbf{q} \,|\, 3d_{3/2}, m_j = +3/2\rangle\,; \tag{6.96b}$$
$$\mathcal{A}_{-1}^{L_2(a)} = \langle 2p_{1/2}, m_j = +1/2 \,|\, \mathbf{q} \,|\, 3d_{3/2}, m_j = -1/2\rangle\,; \tag{6.96c}$$
$$\mathcal{A}_{-1}^{L_2(b)} = \langle 2p_{1/2}, m_j = -1/2 \,|\, \mathbf{q} \,|\, 3d_{3/2}, m_j = -3/2\rangle\,; \tag{6.96d}$$

while in the on-axis case the matrix elements for the effective operator formalism take the form:

$$\mathcal{A}_{+1}^{L_2(a)} = \left\langle 2p_{1/2}, m_j = -1/2 \,\middle|\, e^{i(k_z-k'_z)(z_q+z_R)}\rho_q e^{i\phi_q} \,\middle|\, 3d_{3/2}, m_j = +1/2\right\rangle; \tag{6.97a}$$
$$\mathcal{A}_{+1}^{L_2(b)} = \left\langle 2p_{1/2}(m_j = +1/2) \,\middle|\, e^{i(k_z-k'_z)(z_q+z_R)}\rho_q e^{i\phi_q} \,\middle|\, 3d_{3/2}, m_j = +3/2\right\rangle; \tag{6.97b}$$
$$\mathcal{A}_{-1}^{L_2(a)} = \left\langle 2p_{1/2}, m_j = +1/2 \,\middle|\, e^{i(k_z-k'_z)(z_q+z_R)}\rho_q e^{-i\phi_q} \,\middle|\, 3d_{3/2}, m_j = -1/2\right\rangle; \tag{6.97c}$$
$$\mathcal{A}_{-1}^{L_2(b)} = \left\langle 2p_{1/2}, m_j = -1/2 \,\middle|\, e^{i(k_z-k'_z)(z_q+z_R)}\rho_q e^{-i\phi_q} \,\middle|\, 3d_{3/2}, m_j = -3/2\right\rangle. \tag{6.97d}$$

The operator is more complicated due to the summation in the off-axis case, but the result that $|\mathcal{A}_{+1}^{L_2}| = |\mathcal{A}_{-1}^{L_2}|$ is the same.

This shows there is no inherent dichroism expected due to the interaction on a fundamental level, it is the available density of final states that leads to the dichroic signal observed. It is readily shown that this holds true for higher values of l, when comparing $\Gamma_{\pm l}$, although, as indicated above, there will be difference in the absorption rate when comparing interactions for which $|l_1| \neq |l_2|$. It is clear then that the reason for the dichroism observed by Verbeeck et al [24] is the magnetic nature of the iron used in the experiment. The non-zero value of the magnetic quantum number m causes there to be a difference in the available final states of the atomic electron; the rate of absorption reflects this.

6.6 Comparison with optical vortex results

It has been shown here that, in the dipole approximation, the electron vortex can induce atomic transitions in which the orbital angular momentum projection of the atom changes, i.e. there is some $\Delta m \neq 0$. In the previous chapter it was shown that the optical vortex cannot induce such a transition via the dipole interaction, though the quadrupole interaction allows for indirect exchange through the centre of mass participating. As such, for a stationary atom the interaction may proceed for the electron vortex case, whereas for the optical vortex there will be no transfer possible, as the centre of mass must be free to move [14, 66]. The results of the Hamiltonian expansion for electron vortices are directly comparable to the results obtained for the optical interaction, since the definition of the dipole term is the same in each case - the dipole interaction term has a linear dependence on $\mathbf{q}$ and no other dependence.

Comparing the atom-vortex interaction for the optical vortex and the multipolar Hamiltonian formalism for the election vortex may both be written in the form $\langle e\mathbf{q}\rangle_{fi} \cdot \langle \mathbf{f}_v(\mathbf{r})\rangle$. This suggests that the condition for orbital angular momentum transfer is for $\langle \mathbf{f}_v(\mathbf{r})\rangle$ to exhibit chirality in the form of circular polarisation, as is the case for the electron vortex interaction. The long-range Coulomb interaction is able to couple the dipole moment of the electron to the electric field of the vortex beam through apparent circular polarisation, while the optical vortex interaction only depends of the local value of the vector potential at the electron position, which has no chiral features. We note that the effective operator formalism leading to transfer of orbital angular momentum also shows this circularity, in the form of the factor $\mathbf{r} \cdot \frac{1}{2}(\hat{\mathbf{x}} \pm \hat{\mathbf{y}})$, as mentioned above.

As previously discussed in Section 5.4, the results for the interaction with optical vortices has been confirmed, and the experiment of Verbeeck *et al.* [24] gives experimental confirmation of the results of the electron vortex interactions discussed above for the $l = 0$ case, however experiments so far have not directly confirmed or disproved the feasibility of the experimental set-up described in Section 6.3.5 (other experiments pertaining to dichroism using electron vortices are discussed below).

6.7 Summary

Direct analysis of the Coulomb interaction between an electron vortex and the internal dynamics of the hydrogenic atom has shown that it is possible to transfer orbital angular momentum between the atom and the electron vortex, in contrast to the result of the similar interaction between optical vortices and atomic matter. This difference in behaviour of the optical and electron vortices is important in demonstrating that, despite the similarities due to the vortex structure, the two phenomena are quite distinct. Though the applications and successes of optical vortices will guide the development of the field of electron vortices, there will be many new applications in which optical vortices are not relevant, but electron vortices may be successful. To this end, an experimental configuration has been proposed that would enable the use of electron vortices in electron energy loss spectroscopy to obtain chiral information. This suggestion builds on the previous experimental results of Verbeeck *et al.* [24], who used a non-vortex beam as the incident probe, and a holographic mask as a vortex analyser after interaction with the sample [24], and

simulations by Schattschneider *et al.* [74] who simulated chiral activity of atomic matter by studying the spatial profile of the transmitted intensity after interaction with an vortex probe.

The experiment of Verbeeck *et al.* provides a proof-of principle result that the electron vortex is able to transfer orbital angular momentum to the atom. The theoretical exploration above confirms that the interaction is similar to the action of spin-polarised optical beams on atomic transitions, such as via the x-ray magnetic chiral dichroism effect. The analysis above (for example Fig. 6.3.8a) confirms that, for $l = 0$, the interaction rate of the forward and reverse transitions will be the same. However, if vortex beams are used as probes, the interaction for the desired forward (reverse) transition for the $l = 1$ ($l = -1$) beam is greater than that of the $l = 0$ beam for the same transition, so that the signal should potentially be larger. As shown in Section 6.3.5, relative to the transition of interest, the irregular transitions and additional ordinary transition are suppressed when using a vortex beam as an incident probe, so that the signal to noise ratio obtained using this suggested set-up would be increased over using non-vortex beams as probes.

The dichroism experiments discussed and simulated by Schattschneider *et al.* [74] seek to determine the dichroism activity of atomic matter by examining the spatial intensity variation of the transmitted beam. Their conclusion is that the necessary spatial information is lost, due to effects of the many possibilities of off-axis transitions. This is very different to the experiment outlined here, in which the dichroism effects will become apparent through comparison of vortex components of the transmitted beams. Since, in the experiment proposed here, the transmitted beam is passed though a holographic mask the signal to noise ratio will be increased, as the desired signal is isolated from the rest of the transmitted beam as discussed above, making the dichroism effects much more apparent than the small spatial variations required in [74]. Additionally, the spatial information comes not from the transmitted beam, but from the scanning of the probe across the sample, with the signal obtained from the total integrated intensity at each scan point - or pixel - so this requires a high resolution scanning vortex probe.

7

Spin-Orbit Coupling in the Electron Vortex

The electron vortex, having both spin angular momentum and orbital angular momentum, will exhibit spin-orbit coupling in a similar manner whereby the spin and orbital angular momenta of the bound atomic electron couple to shift the electron energy. In this chapter, the origin of the coupling is derived by applying the Foldy-Wouthuysen transformation to the relativistic Dirac equation, to achieve the non-relativistic limit in which spin-orbit coupling is apparent. The Dirac equation is introduced in Section 7.1 as the relativistic generalisation of the Schrödinger equation. The main features of the solutions are discussed, and the minimal coupling prescription for the interaction with electromagnetic fields is shown to arise naturally from the requirement that the Dirac equation be Lorentz invariant. The Foldy-Wouthuysen transformation is introduced in Section 7.2, and applied to the Dirac equation in the presence of fields to obtain a non-relativistic equation suitable for treating particles with spin. This is shown to have the same form as the Schrödinger-Pauli equation. The spin-orbit interaction term is then applied to the electron vortex to determine the magnitude of the intrinsic spin-orbit coupling of the electron due to its electric field, and to the case of the electron moving past an external potential, such as an ionic impurity.

The investigation into the spin-orbit coupling of the $l = 1$ electron vortex - both the intrinsic coupling and that due to an external field - has been published in [86]

7.1 The Dirac Equation

The Schrödinger equation is, in essence, a wave equation, and is not suitable for a description of particles that have a large enough momentum so as to be considered relativistically. Additionally, the Schrödinger equation does not allow for consideration of the particle spin, so on these two counts it is not sufficient for a full description of electron motion. The Dirac equation extends the

Schrödinger equation in order to overcome these deficiencies. To find such a relativistic formalism, the classical energy relations upon which the Schrödinger equation is based may be replaced by their relativistic counterparts, such that the basic principles of quantum mechanics formalism remain intact [118]. These principles include:

1. The full description of the system is to be contained within the wavefunction ψ, identified as the probability amplitude of the system. The probability density is given as $|\psi|^2 \geq 0$.

2. Physical observables are represented by Hermitian operators, the eigenvalues of which represent a set of possible measurement outcomes of the operator.

3. The wavefunction of any system may be expanded into a suitable linear combination of a complete orthonormal set of states that are each eigenfunctions of a complete set of commuting operators.

4. The time-evolution of the system is expressed in the Schrödinger formalism

$$i\hbar\partial_t\psi = H\psi. \tag{7.1}$$

In addition, in order to satisfy the requirements of special relativity, the theory must also be Lorentz covariant so that Lorentz boosts result in the appropriate transformation laws for scalar, pseudo-scalar, vector and pseudo-vector quantities [119].

Replacing the terms in the relativistic energy momentum relation $E^2 = p^2c^2 + m^2c^4$ with the appropriate quantum mechanical operators gives the Klein-Gordon equation

$$\left(i\hbar\partial_t\right)^2\psi = \left(c^2(-i\hbar\nabla)^2 + c^4m^2\right)\psi \tag{7.2}$$

$$\partial_t^2\psi = \left(c^2\nabla^2 - \frac{c^4}{\hbar^2}m^2\right)\psi. \tag{7.3}$$

using the Einstein summation convention, $\partial_x = (\partial_1, \partial_2, \partial_3)$, with the indices representing the Cartesian unit vector basis. This equation displays the Lorentz covariance required for relativistic motion, however it is not suitable to describe particles having non-zero spin, and as such was originally discarded as a useful equation [118]. The Klein-Gordon equation does have application to spin-0 particles such as the pion or the Higgs boson [118, 120]. Solutions to the free Klein-Gordon equation above have the form of plane waves; however the forms of the probability density derived from application of Noether's theorem is not positive definite, as it is proportional to E, which may take negative values. This apparent inconsistency with point 1 above is resolved by considering those solutions with negative energy as corresponding to anti-particles, having negative energy and charge [118, 119, 121]. The anti-particle solutions have negative energy when interpreted as particle solution propagating forward in time; however when considering anti-particles propagating backwards in time the anti-particle energy is positive, and the meaningful, positive definite probability density and current are recovered [118, 119, 121].

The relativistic quantum mechanical equation suitable for describing the free spin-$\frac{1}{2}$ electron is the Dirac equation, having the form

$$\hat{H}\psi = \left(c\boldsymbol{\alpha}\cdot\mathbf{p} + c^2\beta m\right)\psi \tag{7.4}$$

$$\frac{1}{c}\partial_t^2\psi = \left(-\boldsymbol{\alpha}\cdot\nabla - \frac{ic}{\hbar}\beta m\right)\psi \tag{7.5}$$

where $\boldsymbol{\alpha}$ and β are matrices, determined by the requirement that a free Dirac particle must satisfy the energy-momentum relation. In the Dirac representation $\boldsymbol{\alpha}$ and β are 4×4 matrices, written as

$$\boldsymbol{\alpha} = \begin{pmatrix} 0 & \boldsymbol{\sigma} \\ \boldsymbol{\sigma} & 0 \end{pmatrix}; \qquad \beta = \begin{pmatrix} \mathbb{1}_2 & 0 \\ 0 & -\mathbb{1}_2 \end{pmatrix}, \tag{7.6}$$

with $\boldsymbol{\sigma}$ the vector of Pauli spin matrices and $\mathbb{1}_n$ the $n\times n$ identity matrix. The energy-momentum relations then have the form of the 'square root' of the Klein-Gordon equation, where the matrices allow for the negative and imaginary roots. The Dirac equation is more commonly given in the concise covariant form

$$(i\hbar\gamma^\mu\partial_\mu - cm)\psi = 0 \tag{7.7}$$

with the four-vector derivative $\partial_\mu = (\frac{1}{c}\partial_t, \nabla)$, and $\gamma^\mu = (\beta, \beta\boldsymbol{\alpha})$ the Dirac γ-matrices (see Appendix C.1).

In the Dirac representation there are four linearly independent solutions of the Dirac equation, which have the form of spinors with four components, corresponding to two positive energy particle solutions, and two negative energy anti-particle solutions; the solutions take the form of plane waves

$$\psi = Nue^{-ip^\mu x_\mu}, \tag{7.8}$$

with a normalisation constant n and 4-spinors u written as

$$u_s = \begin{pmatrix} \chi_s \\ \frac{c\boldsymbol{\sigma}\cdot\mathbf{p}}{E+mc^2}\chi_s \end{pmatrix}; \qquad u_{s+2} = \begin{pmatrix} \frac{c\boldsymbol{\sigma}\cdot\mathbf{p}}{|E|+mc^2}\chi_s \\ \chi_s \end{pmatrix}, \tag{7.9}$$

with $s = 1, 2$. Only two components of u are independent; this is indicated by the inclusion of the two independent 2-spinors χ_s:

$$\chi_1 = \begin{pmatrix} 1 \\ 0 \end{pmatrix}; \qquad \chi_2 = \begin{pmatrix} 0 \\ 1 \end{pmatrix}. \tag{7.10}$$

The solutions u_s and u_{s+2} of Eq. (7.9) are identified with the particle and antiparticle solutions respectively. In the non-relativistic limit the quantity $\frac{c\boldsymbol{\sigma}\cdot\mathbf{p}}{E+mc^2}$ has the approximate form

$$\frac{c\boldsymbol{\sigma}\cdot\mathbf{p}}{E+mc^2} \approx \frac{1}{2mc}\boldsymbol{\sigma}\cdot\mathbf{p} = \frac{\boldsymbol{\sigma}\cdot\mathbf{v}}{c} \tag{7.11}$$

which is small, hence these components of u_s and u_{s+2} are termed the 'small components' and may be neglected in the non-relativistic limit so that $u \to \chi$.

It turns out that the two states χ_s represent the projection of the particle spin on the direction of motion, and the four solutions u are eigenfunctions of the helicity operator

$$\Lambda = \frac{\mathbf{\Sigma}\cdot\mathbf{p}}{|\mathbf{p}|} = \frac{\hbar}{2}\begin{pmatrix} \frac{\boldsymbol{\sigma}\cdot\mathbf{p}}{|\mathbf{p}|} & 0 \\ 0 & \frac{\boldsymbol{\sigma}\cdot\mathbf{p}}{|\mathbf{p}|} \end{pmatrix}, \tag{7.12}$$

with eigenvalues $\pm\frac{\hbar}{2}$. Thus the four solutions of the Dirac equation describe the particle and anti-particle excitations, each with two possible helicity states [118, 119, 121]. In the case of propagation in the z-direction only, the helicity eigenstates $\pm\frac{\hbar}{2}$ are identified with the spin-up and spin-down spinors $\chi_{1,2}$ respectively. Even in this restricted case it can be seen that spin and helicity are distinct, since it is always possible to perform a Lorentz boost to a frame in which the momentum is reversed; the helicity will be reversed but the spin will remain the same, as for a massive particle spin is always given in the particle's rest frame [122]. Helicity may also be defined for a particle with total angular momentum J, by letting $\mathbf{\Sigma} \to \mathbf{J} = \mathbf{L} + \mathbf{\Sigma}$. The helicity operator commutes with the Hamiltonian, ensuring helicity is a conserved quantity. Helicity is then a 'good', or 'better' quantum number up to transformation in which $\mathbf{p}$ changes sign, in contrast with spin or total angular momenta, which depend on the frame of reference [121, 122]. In the following discussion of spin-orbit coupling, the term 'spin' is taken to be synonymous with helicity as defined in Eq. (7.12), since we take the non-relativistic limit and define $\mathbf{p} = (0, 0, p_z)$, such that $\Lambda \to \sigma_z$.

In the same manner as with the Schrödinger equation, the interaction with external fields is incorporated in the minimal coupling scheme, with a similar form to that used in Chapter 5. In relativistic quantum mechanics this coupling arises naturally following the requirement that local transformations of solutions to the Dirac equation, of the general form

$$\psi(x) \to e^{i\alpha(x)}\psi(x), \tag{7.13}$$

preserve the Lorentz invariance of the Lagrangian, or Lagrangian density [119, 121]. The Lagrangian density for the Dirac electron reads

$$\mathcal{L} = i\hbar\bar{\psi}\partial_\mu\psi - cm\bar{\psi}\psi, \tag{7.14}$$

where $\bar{\psi} = \psi^\dagger\gamma^0$ is the adjoint spinor, which transforms as

$$\bar{\psi}(x) \to e^{-i\alpha(x)}\bar{\psi}(x). \tag{7.15}$$

The result of this transformation then is an 'extra' term in the Lagrangian density, since for the local function $\partial_\mu\alpha(x) \neq 0$. This violates Lorentz covariance, since the Lagrangian density must take the same form in all reference frames. In order to address this, the introduction of the covariant derivative,

$$\mathcal{D}_\mu = \partial_\mu - \frac{ie}{\hbar}A_\mu, \tag{7.16}$$

requires the introduction of a gauge field $A_\mu = (\frac{\phi}{c}, -\mathbf{A})$, which transforms as

$$A_\mu \to A_\mu + \frac{\hbar}{e}\partial_\mu\alpha. \tag{7.17}$$

which fixes the 'extra term' of the original Lagrangian density. However the energy of the gauge field must also now be included in the Lagrangian density, giving

$$\mathcal{L} = i\hbar\bar{\psi}\gamma^\mu\mathcal{D}_\mu\psi - cm\bar{\psi}\psi - \frac{1}{4\mu_0}F_{\mu\nu}F^{\mu\nu}, \tag{7.18}$$

with $F^{\mu\nu}$ the electromagnetic field tensor. This is the fully covariant Lagrangian of quantum electrodynamics, describing charged, massive spin-$\frac{1}{2}$ particles interacting with the photon field A^μ [119, 121]. The corresponding equation of motion for the particle field in the presence of a gauge field A^μ is then

$$(i\hbar\gamma^\mu\partial_\mu - e\gamma^\mu A_\mu - cm)\psi = 0. \tag{7.19}$$

We are now in a position to consider the non-relativistic limit of the Dirac equation in the presence of fields. This will enable us to describe the spin of the vortex electron using the 2-spinors Eq. (7.10) and the aim is to describe the difference in behaviour of the two spin states in the interaction with an electromagnetic field.

7.2 The Foldy-Wouthuysen Transformation

The Foldy-Wouthuysen theory deals with a unitary transformation applied to the Dirac equation, to yield the non-relativistic limit in such a way that the particle and anti-particle spinor solutions are not mixed. As discussed above (c.f. Eq. (7.11)), in the non-relativistic limit the small components may be neglected, so in essence what we look for in this transformation is to present the Dirac equation in a form that will decouple upper and lower components of the spinor solutions, producing two equations acting on the 2-spinors of the non-relativistic particle and anti particle solutions separately. This allows us to treat the positive and negative energy solutions of the Dirac equation separately, and ensures that transitions between the positive and negative energy states are suppressed, as is the case in the non-relativistic limit [118].

The Dirac equation in the presence of an external field is given by

$$H\psi = i\hbar\frac{\partial\psi}{\partial t} = \left(\beta mc^2 + c\boldsymbol{\alpha}\cdot(\mathbf{p} - e\mathbf{A}) + e\Phi\right)\psi. \tag{7.20}$$

The three terms in the Dirac Hamiltonian are of two different types, designated as 'even' or 'odd'. Even terms, such as βmc^2 and $e\Phi$, are operators that do not couple the large and small spinor components, whereas odd terms facilitate mixing of the spinor components. Since $\boldsymbol{\alpha}$ is odd, $c\boldsymbol{\alpha}\cdot(\mathbf{p} - e\mathbf{A})$ is an odd operator. In applying the Foldy-Wouthuysen transformation, the aim is to determine a new Hamiltonian, H', such that all odd operators are removed. Any operator A acting on a Dirac spinor may be uniquely decomposed into the sum of an odd and even operators A_{even} and A_{odd} [123], such that

$$A = A_{\text{even}} + A_{\text{odd}},$$

with

$$A_{\text{even}} = \frac{1}{2}\left(A + \beta A\beta\right); \qquad A_{\text{odd}} = \frac{1}{2}\left(A - \beta A\beta\right). \tag{7.21}$$

The even and odd operators respectively commute and anticommute with β

$$[\beta, A_{\text{even}}] = 0; \qquad \{\beta, A_{\text{odd}}\} = 0. \tag{7.22}$$

It turns out that there is an exact transformation to obtain an even Hamiltonian H' only in the case of no external fields. For an electron in the presence of external fields application of the Foldy-Wouthyusen transformation yields an expansion of operators in increasing powers of $(mc^2)^{-1}$, such that the magnitude of higher order terms progressively decreases. In this way, odd operators can be removed up to a desired order in $(mc^2)^{-1}$. Here, this will be done up to order $(mc^2)^{-3}$.

7.2.1 The Form of the Foldy-Wouthyusen Transformation

We write the transformation in terms of a time dependant unitary operator $U = e^{iS(t)}$, where $S(t)$ is an odd, self-adjoint operator, the form of which is to be subsequently determined. This is applied to the state function $\psi(\mathbf{r}, t)$ to yield a new, transformed state function

$$\psi'(\mathbf{x}, t) = e^{iS(t)}\psi(\mathbf{x}, t); \tag{7.23}$$

noting that $\psi(\mathbf{r}, t) = e^{-iS(t)}\psi'(\mathbf{r}, t)$, the Hamiltonian H may be written

$$H\psi = i\hbar\partial_t(e^{-iS(t)}\psi') \tag{7.24}$$

$$= i\hbar(\partial_t e^{-iS(t)})\psi' + i\hbar e^{-iS(t)}\partial_t\psi', \tag{7.25}$$

identifying $i\hbar\partial_t\psi' = H'\psi'$, we may rearrange and multiply from the left by $e^{iS(t)}$ to find

$$H'(t) = e^{iS(t)}\left(H(t) - i\hbar\partial_t\right)e^{-iS(t)}. \tag{7.26}$$

This is the essence of the transformation [118]. In application of this transformation, it is convenient to suppress the time and space dependence of the operators. For any linear operators A and B acting in the same vector space we have the relation [123, 124]

$$e^A B e^{-A} = \sum_{n=0}^{\infty} \frac{1}{n!}\Omega_n(A, B), \tag{7.27}$$

where the operator $\Omega_n(A, B)$ is defined as

$$\Omega_n(A, B) = [A, \Omega_{n-1}(A, B)], \tag{7.28}$$

with

$$\Omega_0(A, B) = B, \tag{7.29}$$

so that the function $\Omega_n(A, B)$ consists of $n-1$ nested commutators. This expansion is now applied to Eq. (7.26) to give (see Appendix C.2 for details)

$$H' = H + \hbar \sum_{n=0}^{\infty} \frac{i^n}{(n+1)!} \Omega_n(S, \tfrac{i}{\hbar}[S, H] - \partial t S). \tag{7.30}$$

This expression may be simplified by separating the even and odd operators in Eq. (7.30). We write

$$H = mc^2\beta + T + V, \tag{7.31}$$

where

$$T = c\boldsymbol{\alpha} \cdot (\mathbf{p} - e\mathbf{A}); \qquad V = e\Phi, \tag{7.32}$$

are odd and even operators respectively. We may also define, for any operator A [123, 124]

$$\dot{A} = \partial t A - \frac{i}{\hbar}[A, V]. \tag{7.33}$$

Applying the expansion Eq. (7.30) to Eq. (7.31), we have

$$\begin{aligned} H' &= mc^2\beta + T + V + \sum_{n=0}^{\infty} \frac{i^{n+1}}{(n+1)!} \Omega_n(S, [S, mc^2\beta]) \\ &\qquad + \sum_{n=0}^{\infty} \frac{i^{n+1}}{(n+1)!} \Omega_n(S, [S, T]) - \hbar \sum_{n=0}^{\infty} \frac{i^n}{(n+1)!} \Omega_n(S, [S, \dot{S}]) \\ &= V + mc^2 \sum_{n=0}^{\infty} \frac{i^n}{(n)!} \Omega_n(S, \beta) + \sum_{n=0}^{\infty} \frac{i^n}{(n)!} \Omega_n(S, T) - \hbar \sum_{n=0}^{\infty} \frac{i^n}{(n+1)!} \Omega_n(S, [S, \dot{S}]). \end{aligned} \tag{7.34}$$

Making use of the fact the S is odd, we write

$$H' = V + mc^2\beta \sum_{n=0}^{\infty} \frac{(-2iS)^n}{n!} + \sum_{n=0}^{\infty} \frac{i^n}{n!} \Omega_n(S, T - \tfrac{\hbar}{n+1}\dot{S}), \tag{7.35}$$

which gives the general form of the Foldy-Wouthyusen transformation to be applied to the Dirac Hamiltonian. This transformation will be applied to obtain a Hamiltonian for which all terms up to order $(mc^2)^{-2}$ are even.

7.2.2 Expanding in Powers of $(mc^2)^{-1}$

The Foldy-Wouthuysen transformation will be carried out to order $(mc^2)^{-2}$, so that all odd terms up to order $(mc^2)^{-2}$ are eliminated; however the even terms of $(mc^2)^{-3}$ will be included in the final Hamiltonian. In the non-relativistic limit the terms of order $(mc^2)^{-3}$ are small relative to the energy $E \approx mc^2$, but as will be shown certain of the even $(mc^2)^{-3}$ terms lead to important relativistic corrections to the Schrödinger equation. The Hamiltonian will now be decomposed

into even and odd terms. It can be seen that

$$S^n = \begin{cases} \text{even} & \text{for even } n; \\ \text{odd} & \text{for odd } n, \end{cases}$$

and

$$\Omega_n(S, T - \tfrac{\hbar}{n+1} \ldots (S)) = \begin{cases} \text{even} & \text{for odd } n; \\ \text{odd} & \text{for even } n. \end{cases}$$

This allows the even and odd parts of the Hamiltonian, H'_{even} and H'_{odd} respectively, to be written

$$H'_{\text{even}} = V + mc^2\beta \sum_{n \text{ even}}^{\infty} \frac{(-2iS)^n}{n!} + \sum_{n \text{ odd}}^{\infty} \frac{i^n}{n!} \Omega_n(S, T - \tfrac{\hbar}{n+1}\dot{S}); \tag{7.36}$$

$$H'_{\text{odd}} = mc^2\beta \sum_{n \text{ odd}}^{\infty} \frac{(-2iS)^n}{n!} + \sum_{n \text{ even}}^{\infty} \frac{i^n}{n!} \Omega_n(S, T - \tfrac{\hbar}{n+1}\dot{S}). \tag{7.37}$$

Expanding the full Hamiltonian Eq. (7.35) in powers of $(mc^2)^{-1}$

$$H' = mc^2\beta + \sum_{k=0}^{\infty} \eta_k (mc^2)^{-k}. \tag{7.38}$$

The Hamiltonian will be even up to order K if all terms $(\eta'_0 \ldots \eta'_k \ldots \eta'_K)$ are even. In order to see the odd and even terms of each order in $(mc^2)^{-1}$, the operator S is now written as an expansion in powers of $(mc^2)^{-1}$:

$$S = \sum_{k=1}^{\infty} S_k (mc^2)^{-k} \qquad \text{and} \qquad \dot{S} = \sum_{k=1}^{\infty} \dot{S}_k (mc^2)^{-k}; \tag{7.39}$$

using these relations with Eq. (7.36) and Eq. (7.37) will enable the odd and even terms of the different orders of $(mc^2)^{-1}$ to be determined. Evidently, the Hamiltonian will be even to order K if all odd terms up to and including that order cancel. We now seek S such that all odd terms of order $(mc^2)^0$, $(mc^2)^{-1}$ and $(mc^2)^{-2}$ are zero.

Expanding the odd Hamiltonian Eq. (7.37) up to S^3 and $\dot{S}^2$, will ensure that all odd term up to and including order $(mc^2)^{-2}$ are present:

$$H'_{\text{odd}} = mc^2\beta \left(-2iS + \frac{(-2iS)^3}{3!} \right) + \Omega_0(S, T - \hbar\dot{S}) - \frac{1}{2}\Omega_2(S, T - \tfrac{\hbar}{3}\dot{S}) \ldots \tag{7.40}$$

Collecting terms by order in mc^2, we have

$$H'_{\text{odd}} = \eta_{\text{odd},0} + (mc^2)^{-1}\eta_{\text{odd},1} + (mc^2)^{-2}\eta_{\text{odd},2}, \tag{7.41}$$

with

$$\eta_{\text{odd},0} = -2ic^2\beta S_1 + T; \tag{7.42}$$

$$\eta_{\text{odd},1} = -2ic^2\beta S_2 - \hbar\dot{S}_1; \tag{7.43}$$

$$\eta_{\text{odd},2} = -2ic^2\beta S_3 + \frac{4}{3}ic^2\beta S_1^3 - \hbar\dot{S}_2 - \frac{1}{2}[S_1,[S_1,T]]. \tag{7.44}$$

H_0' will be even if $\eta_{\text{odd},0} = 0$, allowing the form of S_1 to be determined:

$$S_1 = \frac{\beta T}{2i}. \tag{7.45}$$

Similarly, $\eta_{\text{odd},1}$, $\eta_{\text{odd},2}$ must also be zero so that η_1 and η_2 are even. This allows us to find S_2 and S_3:

$$\begin{aligned} S_2 &= -\frac{\hbar\beta\dot{S}_1}{2i} \\ &= \frac{\hbar\dot{T}}{(2i)^2}; \end{aligned} \tag{7.46}$$

and, noting that $(\beta T)^3 = -\beta T^3$ and $[S_1,[S_1,[T]]] = -4(2i)^{-2}\beta T^3$:

$$\begin{aligned} S_3 =& \frac{2}{3}S_1^3 - \frac{\hbar\beta}{2i}\dot{S}_2 - \frac{\beta}{4i}[S_1,[S_1,T]] \\ =& -\frac{2}{3}\beta\frac{T^3}{(2i)^3} + \frac{\hbar^2\ddot{T}}{(2i)^3} + 2\frac{T^3}{(2i)^3} \\ =& \frac{\beta}{(2i)^3}\left(\frac{4}{3}T^3 + \hbar^2\ddot{T}\right). \end{aligned} \tag{7.47}$$

This fixes $\eta_0 + (mc^2)\eta_1 + (mc^2)^2\eta_2$ to be even, so that up to order $(mc^2)^{-2}$, the Hamiltonian is now completely described by the even expansion of Eq. (7.36). As mentioned above the even terms of order $(mc^2)^{-3}$ will also be included in the final Hamiltonian.

7.2.3 The Foldy-Wouthyusen Hamiltonian

Now that the odd terms up to order $(mc^2)^{-2}$ have been transformed away, the Hamiltonian is given by Eq. (7.36) up to order $(mc^2)^{-3}$:

$$\begin{aligned} H' = V + mc^2\beta\left(1 + \frac{(-2iS)^2}{2} + \frac{(-2iS)^4}{4!}\right) + i\Omega_1(S,T) + \\ \frac{i^3}{3!}\Omega_3(S,T) - \frac{i\hbar}{2}\Omega_1(S,\dot{S}) + \mathcal{O}((mc^2)^{-4}); \end{aligned} \tag{7.48}$$

separating the powers of $(mc^2)^{-1}$ gives

$$H' = \eta_0 + (mc^2)^{-1}\eta_1 + (mc^2)^{-2}\eta_2 + (mc^2)^{-3}\eta_{\text{even},3}, \tag{7.49}$$

so that

$$\eta_0 = V; \tag{7.50}$$

$$\eta_1 = -2\beta S_1^2 + i[S_1, T]; \tag{7.51}$$

$$\eta_2 = -2\beta\{S_1, S_2\} + i[S_2, T] + i[S_2, T] - \frac{i\hbar}{2}[S_1, \dot{S}_1]; \tag{7.52}$$

$$\begin{aligned}\eta_{\text{even},3} = &-2\beta\{S_1, S_3\} - 2\beta S_2^2 + \frac{2}{3}\beta S_1^4 + i[S_3, T] \\ &- \frac{i}{6}[S_1, [S_1, [S_1, T]]] - \frac{i\hbar}{2}[S_1, \dot{S}_2] - \frac{i\hbar}{2}[S_2, \dot{S}_2].\end{aligned} \tag{7.53}$$

Substituting S_1, S_2 and S_3 (see Appendix C.3 for details) gives

$$\eta_0 = V; \tag{7.54}$$

$$\eta_1 = \frac{\beta T^2}{2}; \tag{7.55}$$

$$\eta_2 = -\frac{i\hbar}{8}[T, \dot{T}]; \tag{7.56}$$

$$\eta_{\text{even},3} = -\frac{1}{8}\beta T^4 - \frac{\hbar^2}{16}\{T, \ddot{T}\}, \tag{7.57}$$

so that the final transformed Hamiltonian is expressed as

$$H' = mc^2\beta + V + \frac{\beta T^2}{2mc^2} - \frac{i\hbar}{8m^2c^4}[T, \dot{T}] - \frac{1}{8m^3c^6}\beta T^4 - \frac{\hbar^2}{16m^3c^6}\{T, \ddot{T}\} \tag{7.58}$$

What remains is to express this using the definitions of T and V, Eq. (7.32) above. Evaluating the powers, time derivatives, commutators, and anti-commutators of T yields the following results (see Appendix C.4)

$$T^2 = c^2(\mathbf{p} - e\mathbf{A})^2 - 2ec^2\boldsymbol{\Sigma}\cdot\mathbf{B}, \tag{7.59}$$

$$T^4 = c^4(\mathbf{p} - e\mathbf{A})^4 - \hbar^2e^2c^4\mathbf{B}^2 - 2ec^2\left\{(p - eA)^2, \boldsymbol{\Sigma}\cdot\mathbf{B}\right\}, \tag{7.60}$$

$$[T, \dot{T}] = -ie\hbar c^2\nabla\cdot\mathbf{E} + \frac{2iec^2}{\hbar}\boldsymbol{\Sigma}\cdot\Big((\mathbf{p} - e\mathbf{A})\times\mathbf{E} - \mathbf{E}\times(\mathbf{p} - e\mathbf{A})\Big), \tag{7.61}$$

$$\{T, \ddot{T}\} = ec^2\{\mathbf{p} - e\mathbf{A}, \dot{\mathbf{E}}\} + \frac{2iec^2}{\hbar}\boldsymbol{\Sigma}\cdot\Big((\mathbf{p} - e\mathbf{A})\times\dot{\mathbf{E}} + \dot{\mathbf{E}}\times(\mathbf{p} - e\mathbf{A})\Big). \tag{7.62}$$

The Foldy-Wouthyusen Hamiltonian Eq. (7.58) may then be written as

$$\begin{aligned}H' = \beta mc^2 + e\Phi + \beta\frac{(\mathbf{p} - e\mathbf{A})^2}{2m} - \beta\frac{(\mathbf{p} - e\mathbf{A})^4}{8m^3c^2} - \frac{e\hbar^2}{16m^3c^4}\beta\{\mathbf{p} - e\mathbf{A}, \dot{E}\} \\ - \frac{e}{m}\beta\boldsymbol{\Sigma}\cdot\mathbf{B} - \frac{i\hbar e}{8m^3c^4}\beta\boldsymbol{\Sigma}\cdot\Big(\dot{\mathbf{E}}\times(\mathbf{p} - e\mathbf{A}) + (\mathbf{p} - e\mathbf{A})\times\dot{\mathbf{E}}\Big) \\ + \frac{e}{4m^3c^2}\beta\{(\mathbf{p} - e\mathbf{A})^2, \boldsymbol{\Sigma}\cdot\mathbf{B}\} - \frac{e^2\hbar^2}{8m^3c^2}\beta\mathbf{B}^2 - \frac{e\hbar^2}{8m^2c^2}\nabla\cdot\mathbf{E} \\ - \frac{e}{4m^2c^2}\boldsymbol{\Sigma}\cdot(\mathbf{E}\times(\mathbf{p} - e\mathbf{A}) - (\mathbf{p} - e\mathbf{A})\times\mathbf{E}).\end{aligned} \tag{7.63}$$

All terms in Eq. (7.63) are even, so that the upper and lower component of the 4 component Dirac spinor ψ will remain separate after application of H'. This Hamiltonian is now suitable for applying to the Dirac solutions in the non-relativistic limit, as the positive energy particle solutions are not coupled to the negative energy anti-particle solutions. In the non-relativistic limit the spinors u may be written

$$u_s^{\text{NR}} = \begin{pmatrix} \chi_s \\ 0 \end{pmatrix}; \qquad u_{s+2}^{\text{NR}} = \begin{pmatrix} 0 \\ \chi_s \end{pmatrix}. \tag{7.64}$$

This separation allows the 4×4 Hamiltonian matrix of Eq. (7.63), to be written as two different 2×2 matrices acting on bispinors. The upper left portion of Eq. (7.63) acts only on the particle solutions, u_s^{NR}, while the lower right part acts on the anti-particle solutions u_{s+2}^{NR}. We are interested in the electron particle solutions, so we may write β and $\mathbf{\Sigma}$ as

$$\beta = \begin{pmatrix} \mathbb{1}_2 & 0 \\ 0 & -\mathbb{1}_2 \end{pmatrix} \to \mathbb{1}_2; \tag{7.65}$$

$$\mathbf{\Sigma} = \frac{\hbar}{2} \begin{pmatrix} \boldsymbol{\sigma} & 0 \\ 0 & \boldsymbol{\sigma} \end{pmatrix} \to \frac{\hbar}{2}\boldsymbol{\sigma}, \tag{7.66}$$

Similarly, for the anti-particle solutions we have we have $\beta \to -\mathbb{1}_2$ and $\mathbf{\Sigma} \to \frac{\hbar}{2}\boldsymbol{\sigma}$. Applying Eq. (7.65) and Eq. (7.66) to Eq. (7.63) gives

$$\begin{aligned} H' = mc^2 + e\Phi + \frac{(\mathbf{p} - e\mathbf{A})^2}{2m} - \frac{(\mathbf{p} - e\mathbf{A})^4}{8m^3c^2} - \frac{e\hbar}{2m}\boldsymbol{\sigma} \cdot \mathbf{B} - \frac{e\hbar^2}{8m^2c^2}\nabla \cdot \mathbf{E} \\ - \frac{e\hbar}{4m^2c^2}\boldsymbol{\sigma} \cdot (\mathbf{E} \times (\mathbf{p} - e\mathbf{A}) - (\mathbf{p} - e\mathbf{A}) \times \mathbf{E}) - \frac{e\hbar^2}{16m^3c^4}\{\mathbf{p} - e\mathbf{A}, \dot{E}\} \\ - \frac{i\hbar^2 e}{16m^3c^4}\boldsymbol{\sigma} \cdot \left(\dot{\mathbf{E}} \times (\mathbf{p} - e\mathbf{A}) + (\mathbf{p} - e\mathbf{A}) \times \dot{\mathbf{E}}\right) \\ + \frac{e\hbar}{8m^3c^2}\{(\mathbf{p} - e\mathbf{A})^2, \boldsymbol{\sigma} \cdot \mathbf{B}\} - \frac{e^2\hbar^2}{8m^3c^2}\mathbf{B}^2 \end{aligned} \tag{7.67}$$

The first seven terms are familiar as the Pauli equation - the non-relativistic Schrödinger equation in the presence of fields with relativistic corrections [125]. The fourth term represents the correction to the kinetic energy, due to the relativistic mass increase, the fifth is the Zeeman term, the magnetic dipole energy of the electron in a magnetic field, the sixth is the Darwin term, due to Zitterbewegung, or fluctuation about the electron centre of motion causing fluctuations of the potential felt by the electron. The seventh term will be shown to lead to the spin-orbit coupling of the electron; the last four terms are not common in the literature, but represent further, small corrections to the kinetic and potential energy due to high order contributions from the magnetic field and the time derivatives of the electric field [124].

7.4 Spin-orbit interaction

We focus here on the spin-orbit interaction, and on applying this to the electron vortex Bessel beam wavefunction. Using the non-relativistic spinors u_s the vortex wavefunction of a non-relativistic electron with spin -$\frac{1}{2}$ is

$$\Psi_{\pm} = N_l J_l(k_\rho \rho) e^{il\phi} e^{ik_z z} e^{-i\omega t} \chi^{(\pm)} \tag{7.68}$$

$$= \psi \chi^{(\pm)}, \tag{7.69}$$

where the spin state of the vortex electron are given as eigenfunction of the z-component of spin

$$\chi^{(+)} = \begin{pmatrix} 1 \\ 0 \end{pmatrix}; \qquad \chi^{(-)} = \begin{pmatrix} 0 \\ 1 \end{pmatrix}. \tag{7.70}$$

The spin orbit interaction term in the non-relativistic limit, as found above, is

$$\begin{aligned} H_{\text{so}} &= -\frac{e\hbar}{8m^2c^2} \boldsymbol{\sigma} \cdot (\mathbf{E} \times (\mathbf{p} - e\mathbf{A}) - (\mathbf{p} - e\mathbf{A}) \times \mathbf{E}) \\ &= \frac{ie\hbar^2}{8m^2c^2} \boldsymbol{\sigma} \cdot (\mathbf{E} \times \nabla - \nabla \times \mathbf{E}) + \frac{e^2\hbar}{4m^2c^2} \boldsymbol{\sigma} \cdot \mathbf{E} \times \mathbf{A}. \end{aligned} \tag{7.71}$$

These spin-orbit interaction terms will be applied to the finite paraxial Bessel beam electron vortex solutions of Chapter 2, to find the energy difference between the aligned and anti-aligned spin states $\Psi_{\pm}$. This will be investigated in two situations, firstly the intrinsic coupling of the vortex orbital angular momentum and the electron spin, via the electric field, and secondly by an external potential, such as an ionic impurity in an otherwise uniform crystal.

Since we are interested in the effect on the energy of the spin states aligned or anti-aligned with the electron's motion, only a field transverse to this motion will affect the coupling. The cylindrical symmetry of the vortex field and the ion field leads to no azimuthal field components, so that it is the radial field that is important. The intrinsic electric field of the electron vortex is purely radial, and has only radial dependence. The situation with the ionic field is slightly different - this potential has spherical symmetry, so that the magnitude of the radial component changes along the z-axis. The ion will be assumed to be situated at $z = 0$, so that the field increases and then decreases along the length of the beam from $-\frac{L}{2}$ to $\frac{L}{2}$.

The radial component of the intrinsic vortex field and the ionic field may both be written in the general form

$$\mathbf{E} = E_\rho \hat{\boldsymbol{\rho}}. \tag{7.72}$$

The fields we are interested in are Coulombic, so that $\mathbf{A} = 0$, additionally neither of the fields has a time-dependent contribution to the magnetic field, so that $\nabla \times \mathbf{E} = 0$. The spin-orbit interaction may then be written

$$H_{\text{so}} = -\frac{ie\hbar^2}{4m^2c^2} \boldsymbol{\sigma} \cdot E_\rho \hat{\boldsymbol{\rho}} \times \nabla \tag{7.73}$$

$$= \frac{e\hbar}{4m^2c^2} \boldsymbol{\sigma} \cdot E_\rho \hat{\boldsymbol{\rho}} \times \mathbf{p}. \tag{7.74}$$

The operator for the z-component of the orbital angular momentum is given as $\mathbf{L}_z = \hat{\boldsymbol{\rho}} \times \mathbf{p}$, and the spin angular momentum operator is given by $\mathbf{S} = \frac{\hbar}{2}\boldsymbol{\sigma}$, so H_{SO} may be written as

$$H_{\text{SO}} = \frac{e}{2m^2c^2}\frac{1}{\rho}E_\rho \mathbf{S}\cdot\mathbf{L}_z. \tag{7.75}$$

Writing

$$\xi = \frac{e}{2m^2c^2}\frac{1}{\rho}E \tag{7.76}$$

the spin orbit Hamiltonian can be written in the form

$$H_{\text{SO}} = \xi \mathbf{S}\cdot\mathbf{L}_z \tag{7.77}$$

so that the energy shift due to this spin-orbit interaction is found from

$$\Delta E_\pm = \langle \Psi_\pm \,|\, \xi \mathbf{S}\cdot\mathbf{L}_z \,|\, \Psi_\pm \rangle . \tag{7.78}$$

Unlike the well known spin-orbit interaction in atomic physics the orbital angular momentum in the electron vortex is firmly aligned parallel (or anti-parallel) to the z-axis, such that $\mathbf{L} = l\hbar\hat{\mathbf{z}}$. Thus, the result of $\mathbf{S}\cdot\mathbf{L}_z$ is simply the z-component of the spin, multiplied by the orbital angular momentum quantum number:

$$\Delta E_\pm = \langle \Psi_\pm \,|\, \xi S_z L_z \,|\, \Psi_\pm \rangle \tag{7.79}$$

$$= \pm\frac{l}{2}\langle \psi \,|\, \xi \,|\, \psi \rangle . \tag{7.80}$$

This represents the deviation of a particular spin state from the expected kinetic energy, 200eV in the case of the electron vortices to be considered here. The magnitude of the energy splitting between the two spin states is

$$\delta_l = \Delta E_+ - \Delta E_- \tag{7.81}$$

$$= l\langle \psi \,|\, \xi \,|\, \psi \rangle . \tag{7.82}$$

This general expression will now be used to determine the magnitude of the spin-orbit interaction within the electron vortex, as it propagates within its own field, and the external field of an ionic impurity.

7.4.1 Intrinsic Spin-Orbit Coupling

The magnitude of the intrinsic spin-orbit coupling will be determined for the finite electron vortex of Section 2.5. As shown in Chapter 3, the field of the finite vortex is given by

$$\mathbf{E}(\rho) = -\hat{\boldsymbol{\rho}}\frac{e}{\varepsilon_0}\frac{I_z k_\perp^2 m_e}{2\pi e\hbar k_z \mathcal{I}_l}\frac{1}{\rho}\int_0^\rho J_l(k_\perp\rho)\Theta(\rho_{l,1}-\rho)\rho' d\rho'. \tag{7.83}$$

Using this field, and the apertured Bessel beam with Eq. (7.82), the spin-orbit splitting is determined for the electron vortices with $l = 1, 3$ and 10[1]. The results are shown in Table 7.4.1. As can be seen, the magnitude of the splitting is particularly small and, unexpectedly, decreases with increasing l. This is due to the rather complicated l-dependence of the beam wavefunction and the electric field; the peak of the magnetic field occurs at a greater radius than the peak of the amplitude distribution of the beam, and this lag increases with l, so that the overlap between the field and the beam is reduced at higher values of l, leading to the decrease in magnitude of the energy splitting.

Since both the field and $|N_l|^2$ are linearly proportional to the axial current I_z this effect will increase with current. Increasing the current to 1 μA should lead to a coupling energy of order 10^{-7} eV; however at higher current the effect of electron-electron interactions such as the Boersch effect [126] will become significant, as the distance between electrons is now of the order of μm. Additionally, such an increase in current is not possible with current electron microscope technology, for which typical currents are in the range 10^{-12} A - 10^{-9} A [103]. Even this 6-orders of magnitude increase of the spin orbit interaction energy is far below the typical microscope energy resolution, in the range of 0.1-1 eV [126], and this energy spread increases for higher currents due to the Boersch effect. Thus the effect of spin-orbit coupling is determined to have no measurable effect on the energy spread of the electrons, and so will not lead to any decrease in image resolution in the use of non-spin polarised electron vortex beams. We note here that the spin-orbit coupling described above is intrinsic to the single vortex electron, and not a feature of the electron-electron interactions throughout the vortex beam. As discussed in Section 2.5.3 the electrons within the beam are well separated, and direct electron-electron interaction such as the Coulomb repulsion leading to the Boersch effect may be generally neglected in this theoretical treatment. The multi-electron spin orbit coupling within the beam due to the interaction of nearby electrons is thus expected to be small.

This intrinsic spin-orbit coupling is not related to the spin-orbit coupling described by Bliokh *et al.* in the non-paraxial relativistic electron vortex [32]. The spin-orbit interaction described here is a general feature of the electron's motion within its own field, whereas the spin-orbit interaction of Bliokh *et al.* arises as a perturbation in the small components of the spinor solutions describing the relativistic electron vortex in the non-paraxial limit. In the non-relativistic limit, the non-paraxial contributions to Eq. (2.39) are small, and the beam may be described by the paraxial Bessel beam with spin, as has been done above. In the relativistic limit, the full, non-paraxial vortex solution of Eq. (2.39) will be subject to the effect of the intrinsic coupling due to the vortex electric field, and each component of Eq. (2.39) will acquire a spin dependent energy shift.

7.4.2 Spin-Orbit Coupling in an External Field

In cylindrical coordinates the field of a point charge of Ze is given as

$$E_Z = \frac{Ze^2}{4\pi\varepsilon_0}\left(\frac{\rho}{(\rho^2+z^2)^{\frac{3}{2}}}\hat{\boldsymbol{\rho}} + \frac{z}{(\rho^2+z^2)^{\frac{3}{2}}}\hat{\mathbf{z}}\right). \tag{7.84}$$

[1] This was done using Mathematica, to evaluate and integrate the expressions for the electric field. Since the vortex wavefunction is identically zero outside of $\rho_{l,1}$ the numerical integration is exact.

	δ_l^{beam} $(10^{-13}$ eV)	$\delta_l^{\text{external}}$ $(10^{-13}$ eV)
$l = 1$	2.53	$9.32Z$
$l = 3$	1.88	$5.08Z$
$l = 10$	0.894	$2.04Z$

Table 7.4.1: Magnitude of the energy split of the aligned and anti-aligned spin states for the intrinsic spin-orbit coupling, δ_l^{beam}, and spin-orbit coupling in the presence of an external field, δ_l^{beam}.

As discussed above, only the radial part will contribute to the spin-orbit interaction. The energy splitting due to this field calculated for the finite electron vortices with $l = 1, 3$ and 10 is shown in Table 7.4.1. As before, the magnitude of the coupling decreases with increasing l. This effect arises due to the increase in beam radius leading to a smaller overlap between the beam and the electric field of the point charge. The magnitude of the energy splitting due to the coupling is slightly larger than that found for the intrinsic field, but is still very small, so as to be negligible. This indicates that the energy of non-spin-polarised vortex beams will not be significantly disturbed by propagation past charged points or defects in crystals.

8

Discussion and Outlook

This thesis has examined several aspects of the new phenomenon of electron vortex physics. Though many aspects of the physics and dynamics of vortices in wave fields are universal [19–21, 80, 81], others depend on the particular wave field in which the vortex exists [22, 66]. Areas of similarity and disparity between optical and electron vortices have been highlighted throughout this thesis, but the principal differences relate to the behaviour of the vortices in the presence of fields or interacting with matter: the charge of the electron leads to an intrinsic magnetic moment, which modifies the trajectory of the vortex in an external field; the motion of the charged electron generates electric and magnetic fields, which have an axial component particular to the vortex; and the electron and photon interact with matter via a different mechanism, leading to substantial differences between atomic selection rules. In addition, the small wavelength of the electron matter wave means that practical applications of the electron vortex include investigation of the dynamics of vortices on the nanoscale. On the other hand, the linear and angular momenta of the electron vortex have been shown to display the same characteristics as those of the optical vortex, demonstrating the universality of the properties associated with the vortex rather than the vortex-carrying medium.

The main results of this thesis are the demonstration of the fields of the electron vortex, resulting in a general form applicable to all charged Bessel beams. This is also relevant in the study of particle vortices consisting of ions, which, along with atomic vortex beams [127] could have potential applications in etching and lithography. The demonstration of the selection rules of the interaction of an electron with atomic matter was a significant triumph for this thesis, in that it allows a clear interpretation of the experimental results of Verbeeck *et al.* [24] to be made. In addition to allowing the clear interpretation of the published results, and comparison with the well known XMCD effect, the detailed study of the complex spatial dependence of the interaction has also allowed the suggestion of a method by which atomic resolution magnetic spectra may be obtained in the

electron microscope.

The aims of this thesis were to put the study of electron vortices on a sound theoretical footing, in order to better utilise the potentials afforded by the new branch of physics. These aims have been met, in that a theoretical formalism of paraxial, non-relativistic vortex beams has been presented, however there is a great deal more to explore. Some areas of particular interest are outlined below.

8.1 Outlook for Future Research Directions

Application of the electron vortex requires an accurate theory describing the quantum mechanical vortex state. The Bessel states used within this thesis are the simplest form of vortex to treat theoretically, and thus give a good overview of the properties of the electron vortex; however they are not necessarily the most physically relevant states. In general, electron optics is well described using Gaussian beams, and the long range propagation of the electron vortex has been shown to have the behaviour of a Gaussian beam as it passes though focus [25]. On the other hand, the divergence of the electron beam can be made small over the few-hundred nanometer thickness of a sample due to the small convergence angles of the order of mrads [38]; this fact and the application of other techniques, such as the use of annular apertures behaving as axicon lenses [91] may lead to well behaved Bessel beams in the electron microscope. Further experimental work is required to determine the particular ranges of experimental parameters within which the electron may be considered Bessel-like or Laguerre-Gaussian like.

The Laguerre-Gaussian beams give the best approximation to the cavity laser modes relevant for optical vortices [97, 99], and it may well turn out that the practical applications of electron vortices in the electron microscope require a description in terms of Laguerre-Gaussian modes, particularly in regards to propagation through the electron optics system, determining image formation and interpretation. In that case, the result shown here must be adapted to be relevant for such states - whether through a new formalism or an expansion in terms of the complete Bessel function basis states. The general features in such cases are not expected to be drastically different, but for example the intrinsic electromagnetic fields of the vortex will have a different spatial dependence, and the magnitude of the spin orbit coupling will be different. Of particular importance is the spatial dependence of the vortex atom-interactions, specifically the dipole interaction term. This could be determined by expanding the Laguerre-Gaussian vortex state in terms of Bessel functions, and applying the Bessel function addition theorem formalism laid out in Section 6.3, or by a 'brute force' application the Hamiltonian of Section 6.2, calculating numerical values for the matrix element at different values of the centre of mass position vector $\mathbf{R}$. Relative to the Bessel beam of infinite radial extent the charge density of the Laguerre-Gaussian beam is localised near to the beam axis, so that the effect of the off-axis contributions is expected to be reduced, though not eliminated since the Coulomb interaction is long ranged. If this is the case the prospects for chiral spectroscopy as described in Section 6.3.5 are improved, as the noise contributions from off-axis atoms will be reduced.

As was shown in Chapter 4 the orbital angular momentum density of the electron vortex has components in the radial and azimuthal directions. The electron vortex has already been applied in interactions with nanoparticles to show that the vortex beam will induce rotation of the

nanoparticle [27, 28], similar to the optical spanner effect, though the rotation induced in the nanoparticles was hampered by friction forces. The rotation experiments proposed in Section 4.3 would provide a method by which friction could be eliminated, and the interaction between an electron vortex and nanoparticles of various materials could be studied in isolation. Alternatively, friction between various species of nanoparticles on different surfaces could be studied by examining the behaviour under the influence of the electron vortex, using the suspended particle system as a control to quantify the friction involved. Friction on the nanoscale is poorly understood [128], and an important issue for nanomanipulation [129] and many aspects of molecular biophysics [130, 131], so that electron vortices utilised in such a way would become a valuable tool in characterising friction interactions.

The orbital angular momentum of the vortex is not the same as the well known orbital angular momentum of the atomic electron. The orbital angular momentum of the vortex is fixed to be aligned or anti-aligned with the direction of motion of the electron, which in a magnetic field leads to the accumulation of Berry phase along the curved trajectory of the vortex line, as described in Section 1.2.2. The fixed one dimensional nature of the vortex that this represents requires a valid quantum mechanical description - while the z component of the orbital angular momentum takes the same form as that of the spherically symmetric atomic case, what are the relevant raising and lowering operators for orbital angular momentum in the cylindrical geometry? For the Laguerre-Gaussian optical vortex beam such operators have been defined [132], but the relevant operators for the vortex fermions will take a different form. Such operators may be defined for both the Bessel and Laguerre-Gaussian electron vortices, with the Laguerre-Gaussian operators having z-dependence due to their divergence.

A major focus for electron vortex beams is their suitability for use in spectroscopy experiments, as discussed in Section 1.4.1 and Section 6.3.5. There are many technical aspects that affect the potential of electron vortices in such experiments, not least the difficulty of generating highly coherent electron vortices with suitable intensity. If spectroscopy involving electron vortices is to be successful, then new technological implementations of dedicated vortex generators are required. As indicated in Section 1.3, a major obstacle to the generation of high quality atomic scale vortices is the beam coherence, due to the finite size of the electron source. Another issue is that although the holographic mask technique currently produces the most robust vortices, limitations of the technique mean that the intensity of the beam is greatly reduced from typical (non-vortex) electron beams, and so the scattering rate of the inelastic collisions required for core-loss spectroscopy is greatly reduced. Optimisation of the production of electron vortices is necessary for their efficient practical application, and a driving goal of current active research [52, 55].

So far, the most promising spectroscopic applications relate to using electron vortices to determine chiral information within the electron microscope, including chirality that is either magnetic or structural in origin. Both structural and magnetic chirality can be discerned in the electron microscope using current technology - in the case of structural chirality this requires a careful study of the sample from multiple angles [133], whereas for magnetism, energy loss magnetic chiral dichroism (EMCD) is an established technique [134, 135], but requires large scattering angles, making detection difficult. Electron vortices offer improvements over both these techniques - the inherent chirality of the electron vortex means that fewer measurements will be

required to fully characterise the chirality of the structure, and in the case of magnetic dichroism the relevant atom-vortex interaction has been shown to be dipole active, so that smaller scattering angles are required. If suitable vortex beams are made available, then atomic resolution electron energy loss spectroscopy will be achievable by means of the experiment suggested in Section 6.3.5. Such an experiment could be performed in current electron microscopes by careful arrangements of suitable masks within the condenser and objective lenses of an STEM; though atomic resolution may be possible, the nanometre scale vortices currently available still promise high resolution magnetic information. Such experiments must be performed in order to demonstrate the potential, and fuel interest in the necessary technological development. To date, the only experimental endorsement of the application of vortices to spectroscopy applications is the experiment of Verbeeck *et al.* [24]. Magnetic imaging in the electron microscope would be extremely useful in materials characterisation for many applications, including evaluation of spintronic devices. Other than magnetic information, the phase structure of the electron vortex beam also presents the possibility of high resolution phase contrast microscopy, as is important for biological specimens [26, 136, 137] without the need for the introduction of additional phase shifts using absorbing phase plates, and the smooth phase ramp of the electron microscope will lead to an increase in the phase contrast [26].

Further work considering the interactions of the electron vortex with other forms of matter is a priority for determining other potential applications. This includes electron vortex states propagating in semiconductor and metallic and half-metallic materials of varying dimensions, which may lead to developments in spintronics, and novel conductance effects, such as orbital angular momentum dependent densities of states and Hall effects relating to the orbital angular momentum [138, 139]. Additionally, in metallic structures the electron vortex will excite plasmon resonances, and these could potentially include resonant states with orbital angular momentum. The vortex applications are not limited to bulk matter and spintronics - quantum gases may be imaged using electron microscopes [140], and quantised vortices are an important phenomenon in Bose-Einstein condensates [87] so electron or optical vortices might prove the perfect tool with which to prepare and image specified phase states in quantum gases.

8.2 Closing Remarks

The breakthrough of the prediction and subsequent experimental verification of electron vortices is predicted to lead to a great many new applications, some of which have been mentioned above, and some which are yet to be discovered. Though electron vortices bear similarities to the more widely know optical vortices, their material and charge properties lead to a great many differences. While this means that known results cannot just be 'borrowed' from the optics case, it also opens up possibilities of new practical applications and physical phenomena that will further shape the understanding of orbital angular momentum. In short, there remains a lot of work to be done.

A

Optical Vortex Interactions

A.1 Expansion of vector potential about centre of mass

The interaction Hamiltonians Eq. (5.42) and Eq. (5.43) are given in terms of the vector potential at $\mathbf{r}_e = \mathbf{R} + \frac{m_p}{M}\mathbf{q}$ and $\mathbf{r}_p = \mathbf{R} + \frac{m_e}{M}\mathbf{q}$. Expanding $\mathbf{A}(\mathbf{r})$ about $\mathbf{R}$ in a series of terms of increasing overs of $\mathbf{q}$ will enable the Hamiltonians to be written as a multipolar series. Taylor expansion of a vector function $\mathbf{F}(\mathbf{x})$ is achieved by [141]

$$\mathbf{F}(\mathbf{x}+\mathbf{a}) = \mathbf{F}(\mathbf{x}) + (\mathbf{a}\cdot\nabla_{\mathbf{x}'})\,\mathbf{F}(\mathbf{x}')\big|_{\mathbf{x}'=\mathbf{x}} + \frac{(\mathbf{a}\cdot\nabla_{\mathbf{x}'})^2}{2!}\mathbf{F}(\mathbf{x}')\big|_{\mathbf{x}'=\mathbf{x}}\cdots \tag{A.1}$$

For the interaction between the optical vortex vector potential and the atomic electron we need

$$\hat{\mathbf{A}}(\mathbf{R}+\alpha\mathbf{q}) = \hat{\mathbf{A}}(\mathbf{R}) + \alpha\,(\mathbf{q}\cdot\nabla_{\mathbf{r}'})\,\hat{\mathbf{A}}(\mathbf{r}')\big|_{\mathbf{r}'=\mathbf{R}} + \alpha^2\frac{(\mathbf{q}\cdot\nabla_{\mathbf{r}'})^2}{2!}\hat{\mathbf{A}}(\mathbf{r}')\big|_{\mathbf{r}'=\mathbf{R}}\cdots, \tag{A.2}$$

where, for determining the expansion of $\hat{\mathbf{A}}(\mathbf{r}_e)$ and $\hat{\mathbf{A}}(\mathbf{r}_p)$ α may be $\frac{m_p}{M}$ and $-\frac{m_e}{M}$ respectively. Thus, the leading order dipole term is given simply by $\hat{\mathbf{A}}(\mathbf{R})$, with the second order term, $(\mathbf{q}\cdot\nabla_{\mathbf{r}'})\,\hat{\mathbf{A}}(\mathbf{r}')\big|_{\mathbf{r}'=\mathbf{R}}$, identified as leading to the quadrupole interaction term. These will contribute to the interaction Hamiltonian through Δ_A and Σ_A

$$\Delta_A = \hat{\mathbf{A}}(\mathbf{r}_e) - \hat{\mathbf{A}}(\mathbf{r}_p) \tag{5.27}$$

$$\Sigma_A = \frac{m_p}{M}\hat{\mathbf{A}}(\mathbf{r}_e) + \frac{m_e}{M}\hat{\mathbf{A}}(\mathbf{r}_p). \tag{5.28}$$

After the expansion, we have

$$\Delta_A = (\mathbf{q}\cdot\nabla_{\mathbf{r}'})\,\hat{\mathbf{A}}(\mathbf{r}')\big|_{\mathbf{r}'=\mathbf{R}} + (m_p - m_e)\,(\mathbf{q}\cdot\nabla_{\mathbf{r}'})^2\,\hat{\mathbf{A}}(\mathbf{r}')\big|_{\mathbf{r}'=\mathbf{R}} \tag{A.3}$$

$$\Sigma_A = 2\hat{\mathbf{A}}(\mathbf{R}) + \frac{m_p - m_e}{M}\left(\mathbf{q}\cdot\nabla_{\mathbf{r}'}\right)\hat{\mathbf{A}}(\mathbf{r}')\big|_{\mathbf{r}'=\mathbf{R}}; \tag{A.4}$$

so that the only contribution to the dipole interaction are the first terms in Eq. (A.3) and Eq. (A.4), as these will give terms that are linear in $\mathbf{q}$. The other terms in Eq. (A.3) and Eq. (A.4) will lead to terms of second order in $\mathbf{q}$, and contribute to the quadrupole term (see Appendix A.4).

A.2 Electric Dipole Matrix Element

Here, the azimuthal components electric dipole matrix element will be explicitly shown, in order to infer the selection rules for an atomic transition. Writing the dipole matrix element as

$$\langle\hat{\boldsymbol{\varepsilon}}\cdot\mathbf{d}\rangle_{fi} = e\hat{\boldsymbol{\varepsilon}}\cdot\left\langle\psi_q^f(\mathbf{q})\,\middle|\,\mathbf{q}\,\middle|\,\psi_q^f(\mathbf{q})\right\rangle \tag{A.5}$$

and separating into Cartesian coordinates, we have

$$\begin{aligned}\langle\hat{\boldsymbol{\varepsilon}}\cdot\mathbf{d}\rangle_{fi} = eN_{n,\ell,m}N_{n',\ell',m'}\hat{\boldsymbol{\varepsilon}}\cdot\Bigg[&\hat{\mathbf{x}}\mathcal{A}_q^{\pm1}\int_0^{2\pi}e^{i(m-m')\phi_q}\cos\phi_q d\phi_q \\ &+\hat{\mathbf{y}}\mathcal{A}_q^{\pm1}\int_0^{2\pi}e^{i(m-m')\phi_q}\sin\phi_q d\phi_q + \hat{\mathbf{z}}\mathcal{A}_q^{0}\int_0^{2\pi}e^{i(m-m')\phi_q}\phi_q d\phi_q\Bigg]\end{aligned} \tag{A.6}$$

with the factors $\mathcal{A}_q^{0,\pm1}$ containing the integrals over the other spatial variables ρ_q and θ_q:

$$\mathcal{A}^{\pm1} = \int_0^\infty Q_n(\rho_q)Q_{n'}(\rho_q)\rho_q^3 d\rho_q\int_0^\pi P_{\ell'}^{m'}(\cos\theta_q)P_\ell^m(\cos\theta_q)\sin^2\theta_q d\theta_q; \tag{A.7}$$

$$\mathcal{A}^{0} = \int_0^\infty Q_n(\rho_q)Q_{n'}(\rho_q)\rho_q^3 d\rho_q\int_0^\pi P_{\ell'}^{m'}(\cos\theta_q)P_\ell^m(\cos\theta_q)\sin\theta_q\cos\theta_q d\theta_q. \tag{A.8}$$

Calculating the ϕ_q integrals for each case gives the standard result of circular polarisation induced atomic transitions

$$\begin{aligned}\langle\hat{\boldsymbol{\varepsilon}}\cdot\mathbf{d}\rangle_{fi} = eN_{n,\ell,m}N_{n',\ell',m'}\hat{\boldsymbol{\varepsilon}}\cdot\Bigg[&\frac{\hat{\mathbf{x}}+i\hat{\mathbf{y}}}{2}\mathcal{A}_q^{\pm1}\delta_{m,m'-1} \\ &+\frac{\hat{\mathbf{x}}-i\hat{\mathbf{y}}}{2}\mathcal{A}_q^{\pm1}\delta_{m,m'+1} + \hat{\mathbf{z}}\mathcal{A}_q\mathcal{A}_q^0\delta_{m,m'}\Bigg].\end{aligned} \tag{A.9}$$

This is dependent on the polarisation of the light field, and not the topological character of the vortex itself.

A.3 Vector Potential Matrix Element

The second part of the matrix element of Eq. (5.52) has the form

$$\left\langle\hat{A}(\mathbf{R})\right\rangle_{fi} = \langle\psi_{\mathrm{R}}^f(\mathbf{R});n_{\mathrm{OV}}^f|\hat{A}(\mathbf{R})|\psi_{\mathrm{R}}^i(\mathbf{R});n_{\mathrm{OV}}^i\rangle\,. \tag{A.10}$$

This will be explicitly evaluated to determine the effect of the vortex interaction on the centre of mass states. The centre of mass states take the form given in Eq. (5.7), so that

$$\left\langle \hat{A}(\mathbf{R}) \right\rangle_{fi} = -\frac{iE_0}{\omega} \left\langle \psi^f_{\mathrm{R}} \right| J_l(k_\perp \rho_R) e^{ik_z z} e^{il\Phi_R} \left| \psi^i_{\mathrm{R}} \right\rangle \left\langle n^f_{\mathrm{OV}} \right| \hat{a}_{k_\perp, k_z} \left| n^i_{\mathrm{OV}} \right\rangle + \frac{iE_0}{\omega} \left\langle \psi^f_{\mathrm{R}} \right| J_l(k_\perp \rho_R) e^{-ik_z z} e^{-il\Phi_R} \left| \psi^i_{\mathrm{R}} \right\rangle \left\langle n^f_{\mathrm{OV}} \right| \hat{a}^\dagger_{k_\perp, k_z} \left| n^i_{\mathrm{OV}} \right\rangle ; \quad \text{(A.11)}$$

when evaluated, this yields

$$\left\langle \hat{A}(\mathbf{R}) \right\rangle_{fi} = -\frac{iE_0}{\omega} \mathcal{A}_R \Big[\sqrt{n^i_{\mathrm{OV}}} \delta(K_z - K'_z + k_z) \delta_{(L, L'-l)} \delta_{(n^f_{\mathrm{OV}}, n^i_{\mathrm{OV}}-1)} - \sqrt{n^i_{\mathrm{OV}} + 1} \delta(K_z - K'_z - k_z) \delta_{(L, L'+l)} \delta_{(n^f_{\mathrm{OV}}, n^i_{\mathrm{OV}}+1)} \Big], \quad \text{(A.12)}$$

as the selection rules for the interaction, with

$$\mathcal{A}_R = \int_0^\infty R^i(\rho_R) R^f(\rho_R)(\rho_R) J_l(k_\perp \rho_R) \rho_R d\rho_R. \quad \text{(A.13)}$$

The first term in Eq. (A.12) indicates the absorption of a vortex photon by the centre of mass, while the second term is that of emission of a vortex photon. Angular and linear momentum is conserved in each case, and it can be seen that the angular momentum of the centre of mass is allowed to change - rotation about the centre of mass may be induced by interaction with an optical vortex.

A.4 The Quadrupole Transition Matrix Element

In order to examine the selection rules arising from the quadrupole term, the transition matrix element of the quadrupole terms identified in Section A.1 is calculated explicitly. To do this, all quantities will be expressed using Cartesian coordinates so that derivatives of unit vectors are not an unnecessary complication. We write the position vector as

$$\mathbf{q} = \hat{\mathbf{x}} \rho_q \sin(\theta_q) \cos(\phi_q) + \hat{\mathbf{y}} \rho_q \sin(\theta_q) \sin(\phi_q) + \hat{\mathbf{z}} \rho_q \cos(\theta_q);$$

and the vector potential operator as

$$\hat{\mathbf{A}}(\mathbf{R}) = \hat{\mathbf{A}}(x_R, y_R, z_R) = -\hat{\boldsymbol{\varepsilon}} i \frac{E_0}{\omega} J_l(k_\perp \sqrt{x_R^2 + y_R^2}) \Big(e^{ik_z z_R} e^{il \arctan(y_R, x_R)} \hat{a}_k + e^{-ik_z z_R} e^{-il \arctan(y_R, x_R)} \hat{a}^\dagger_k \Big).$$

The expansion of Eq. (A.2) will now be explicitly evaluated up to second order (giving terms of order $\mathbf{q}$), so as to determine the quadrupole interaction Hamiltonian, and examine the selection rules for orbital angular momentum exchange. The first two terms of Eq. (A.2) are, in Cartesian coordinates,

$$\hat{\mathbf{A}}(\mathbf{R}+\alpha\mathbf{q}) = \hat{\mathbf{A}}(\mathbf{R}) + \alpha\rho_q \sin(\theta_q)\cos(\phi_q)\partial_x\hat{\mathbf{A}}(x,y,z)\Big|_{\mathbf{R}} + \alpha\rho_q \sin(\theta_q)\sin(\phi_q)\partial_y\hat{\mathbf{A}}(x,y,z)\Big|_{\mathbf{R}} + \alpha\rho_q \cos(\theta_q)\partial_z\hat{\mathbf{A}}(x,y,z)\Big|_{\mathbf{R}} : \quad \text{(A.14)}$$

The final term, the ∂_z component, is evaluated simply as

$$\begin{aligned}\partial_z\hat{\mathbf{A}}(x,y,z)\Big|_{\mathbf{R}} &= -\hat{\boldsymbol{\varepsilon}} i\frac{E_0}{\omega}\left(ik_z J_l\left(k_\perp\sqrt{x_R^2+y_R^2}\right)e^{ik_z z_R}e^{il\arctan(y_R,x_R)}\hat{a}_k \right.\\ &\qquad \left. + ik_z J_l\left(k_\perp\sqrt{x_R^2+y_R^2}\right)e^{-ik_z z_R}e^{-il\arctan(y_R,x_R)}\hat{a}_k^\dagger\right)\\ &= \hat{\boldsymbol{\varepsilon}}\frac{E_0}{\omega}\left(k_z J_l(k_\perp\rho_R)e^{ik_z z_R}e^{il\Phi_R}\hat{a}_k + k_z J_l(k_\perp\rho_R)e^{-ik_z z_R}e^{-il\Phi_R}\hat{a}_k^\dagger\right);\end{aligned}$$

however the ∂_x and ∂_y terms are slightly more complicated; looking first at the x terms, we have

$$\begin{aligned}\partial_x\hat{\mathbf{A}}(x,y,z)\Big|_{\mathbf{R}} &= -\hat{\boldsymbol{\kappa}}_1\partial_x J_l\left(k_\perp\sqrt{x^2+y^2}\right)e^{il\arctan(y,x)}\\ &\qquad + \hat{\boldsymbol{\kappa}}_2\partial_x J_l\left(k_\perp\sqrt{x^2+y^2}\right)e^{-il\arctan(y,x)}\Big|_{\mathbf{R}},\end{aligned}$$

with $\hat{\boldsymbol{\kappa}}_1 = i\frac{E_0}{\omega}e^{ik_z z}\hat{a}_k\hat{\boldsymbol{\varepsilon}}$ and $\hat{\boldsymbol{\kappa}}_2 = i\frac{E_0}{\omega}e^{-ik_z z}\hat{a}_k^\dagger\hat{\boldsymbol{\varepsilon}}$. This gives

$$\begin{aligned}\partial_x\hat{\mathbf{A}}(x,y,z)\Big|_{\mathbf{R}} &= -\hat{\boldsymbol{\kappa}}_1\left(e^{il\arctan(y,x)}\left(\frac{k_\perp x}{\sqrt{x^2+y^2}}J_l'(k_\perp\sqrt{x^2+y^2})\right)\right.\\ &\qquad \left. + ilJ_l(k_\perp\sqrt{x^2+y^2})e^{il\arctan(y,x)}\partial_x\arctan(y,x)\right)\Big|_{\mathbf{R}}\\ &\quad + \hat{\boldsymbol{\kappa}}_2\left(e^{-il\arctan(y,x)}\left(\frac{k_\perp x}{\sqrt{x^2+y^2}}J_l'(k_\perp\sqrt{x^2+y^2})\right)\right.\\ &\qquad \left. - ilJ_l(k_\perp\sqrt{x^2+y^2})e^{-il\arctan(y,x)}\partial_x\arctan(y,x)\right)\Big|_{\mathbf{R}}.\end{aligned}$$

The derivatives of the $\arctan(y,x)$ function are

$$\partial_x\arctan(y,x) = \frac{y}{x^2+y^2}; \qquad \partial_y\arctan(y,x) = -\frac{x}{x^2+y^2}. \qquad \text{(A.15)}$$

Thus, we now have

$$\begin{aligned}\partial_x\hat{\mathbf{A}}(x,y,z)\Big|_{\mathbf{R}} &= \hat{\boldsymbol{\kappa}}_1\left(e^{il\arctan(y_R,x_R)}\left(\frac{k_\perp x_R}{\sqrt{x_R^2+y_R^2}}J_l'\left(k_\perp\sqrt{x_R^2+y_R^2}\right)\right)\right.\\ &\qquad \left. + \frac{ily_R}{x_R^2+y_R^2}J_l\left(k_\perp\sqrt{x_R^2+y_R^2}\right)e^{il\arctan(y_R,x_R)}\right)\\ &\quad - \hat{\boldsymbol{\kappa}}_2\left(e^{-il\arctan(y_R,x_R)}\left(\frac{k_\perp x_R}{\sqrt{x_R^2+y_R^2}}J_l'\left(k_\perp\sqrt{x_R^2+y_R^2}\right)\right)\right.\\ &\qquad \left. - \frac{ily_R}{x_R^2+y_R^2}J_l\left(k_\perp\sqrt{x_R^2+y_R^2}\right)e^{-il\arctan(y_R,x_R)}\right);\end{aligned}$$

returning to cylindrical coordinates gives

$$\begin{aligned}\partial_x \hat{\mathbf{A}}(x,y,z)\Big|_{\mathbf{R}} &= -i\frac{E_0}{\omega}\hat{\boldsymbol{\varepsilon}} \\ &\times \left[e^{il\Phi_R} e^{ik_z z_R} \hat{a}_k \left(k_\perp \cos\Phi_R J_l'\left(k_\perp \rho_R\right) + \frac{il\sin(\Phi_R)}{\rho_R} J_l\left(k_\perp \rho_R\right) \right) \right. \\ &\left. - e^{-il\Phi_R} e^{-ik_z z_R} \hat{a}_k^\dagger \left(k_\perp \cos\Phi_R J_l'\left(k_\perp \rho_R\right) - \frac{il\sin(\Phi_R)}{\rho_R} J_l\left(k_\perp \rho_R\right) \right) \right] \end{aligned} \tag{A.16}$$

as the x derivative of the vector potential. Similar treatment of the y term gives

$$\begin{aligned}\partial_y \hat{\mathbf{A}}(x,y,z)\Big|_{\mathbf{R}} &= -i\frac{E_0}{\omega}\hat{\boldsymbol{\varepsilon}} \\ &\times \left[e^{il\Phi_R} e^{ik_z z_R} \hat{a}_k \left(k_\perp \sin\Phi_R J_l'\left(k_\perp \rho_R\right) - \frac{il\cos(\Phi_R)}{\rho_R} J_l\left(k_\perp \rho_R\right) \right) \right. \\ &\left. - e^{-il\Phi_R} e^{-ik_z z_R} \hat{a}_k^\dagger \left(k_\perp \sin\Phi_R J_l'\left(k_\perp \rho_R\right) + \frac{il\cos(\Phi_R)}{\rho_R} J_l\left(k_\perp \rho_R\right) \right) \right]; \end{aligned} \tag{A.17}$$

so that finally, up to second order in the expansion, we have

$$\begin{aligned}\hat{\mathbf{A}}(\mathbf{R}+\alpha\mathbf{q}) &= \hat{\mathbf{A}}(\mathbf{R}) \\ &- \frac{i\alpha E_0 \hat{\boldsymbol{\varepsilon}}}{\omega} \Bigg\{ \rho_q \sin(\theta_q)\cos(\phi_q) \\ &\quad \times \left[e^{il\Phi_R} e^{ik_z z_R} \hat{a}_k \left(k_\perp \cos\Phi_R J_l'\left(k_\perp \rho_R\right) + \frac{il\sin(\Phi_R)}{\rho_R} J_l\left(k_\perp \rho_R\right) \right) \right. \\ &\quad \left. - e^{-il\Phi_R} e^{-ik_z z_R} \hat{a}_k^\dagger \left(k_\perp \cos\Phi_R J_l'\left(k_\perp \rho_R\right) - \frac{il\sin(\Phi_R)}{\rho_R} J_l\left(k_\perp \rho_R\right) \right) \right] \\ &\quad + \rho_q \sin(\theta_q)\sin(\phi_q) \\ &\quad \times \left[e^{il\Phi_R} e^{ik_z z_R} \hat{a}_k \left(k_\perp \sin\Phi_R J_l'\left(k_\perp \rho_R\right) - \frac{il\cos(\Phi_R)}{\rho_R} J_l\left(k_\perp \rho_R\right) \right) \right. \\ &\quad \left. - e^{-il\Phi_R} e^{-ik_z z_R} \hat{a}_k^\dagger \left(k_\perp \sin\Phi_R J_l'\left(k_\perp \rho_R\right) + \frac{il\cos(\Phi_R)}{\rho_R} J_l\left(k_\perp \rho_R\right) \right) \right] \\ &\quad - \rho_q \cos(\theta_q) \\ &\quad \times \left[\left(k_z J_l(k_\perp \rho_R) e^{ik_z z_R} e^{il\Phi_R} + k_z J_l(k_\perp \rho_R) e^{-ik_z z_R} e^{-il\Phi_R} \right) \right] \Bigg\} \end{aligned} \tag{A.18}$$

as the expanded vector potential about $\mathbf{R}$.

A.4.1 The Quadrupole Interaction Hamiltonian

The quadrupole term of the interaction Hamiltonian is found from the terms in Eq. (5.37) that are second order in $\mathbf{q}$. Two such terms arise, the second terms of Eq. (A.3) and Eq. (A.4). The focus here will be the quadrupole term directly affecting the atomic electron, i.e. that from Eq. (A.4),

since the other contribution will be very small. Thus, we have

$$\hat{H}_{\mathrm{OV}}^{\mathrm{int}(q)} = \frac{e(m_p - m_e)}{m_p m_e} \mathbf{p}_q \cdot (\mathbf{q} \cdot \nabla) \hat{\mathbf{A}}(\mathbf{R}) \tag{A.19}$$

as the quadrupole interaction of interest. Once again, the momentum operator is written as the commutator of the atomic electron Hamiltonian and position operators, and the matrix element is found to lead to selection rules:

$$\mathcal{M}_{\mathrm{OV}}^{\mathrm{quad}} = \frac{ie}{\hbar} \frac{(m_p - m_e)}{m_p m_e} (\mathcal{E}_f - \mathcal{E}_i) \left\langle \psi_q^f(\mathbf{q}); \psi_{\mathrm{R}}^f(\mathbf{R}); n_{\mathrm{OV}}^f \right| \mathbf{q} \cdot (\mathbf{q} \cdot \nabla) \hat{\mathbf{A}}(\mathbf{R}) \left| \psi_q^i(\mathbf{q}); \psi_{\mathrm{R}}^i(\mathbf{R}); n_{\mathrm{OV}}^i \right\rangle, \tag{A.20}$$

separating the polarisation vector $\hat{\boldsymbol{\varepsilon}}$ from the optical potential once again, we have

$$\mathcal{M}_{\mathrm{OV}}^{\mathrm{quad}} = \frac{ie}{\hbar} \frac{(m_p - m_e)}{m_p m_e} (\mathcal{E}_f - \mathcal{E}_i) \left\langle \psi_q^f(\mathbf{q}); \psi_{\mathrm{R}}^f(\mathbf{R}); n_{\mathrm{OV}}^f \right| \hat{\varepsilon}_i q^i q_j \partial^j \hat{A}(\mathbf{R}) \left| \psi_q^i(\mathbf{q}); \psi_{\mathrm{R}}^i(\mathbf{R}); n_{\mathrm{OV}}^i \right\rangle, \tag{A.21}$$

A.4.2 Quadrupole Selection Rules

The point of interest here is the possibility of transfer of orbital angular momentum between the optical vortex and the atomic electron. As such, the orbital angular momentum selection rules will be explicitly evaluated via the azimuthal integration of the matrix element of Eq. (A.21). The atomic position operator and vector potential gradient are expanded in Cartesian coordinates, so that any dependence on the circular polarisation of the optical vortex field is made clear. The selection rules found after integration over ϕ_q and Φ_R are found to be:

$$\begin{aligned}
\mathcal{M}_{\mathrm{OV}}^{\mathrm{quad}} = {} & \frac{i\pi e(m_p - m_e)}{\hbar m_p} N_{n,\ell,m} N_{n',\ell',m'} (\mathcal{E}_f - \mathcal{E}_i) \\
& \times \hat{\boldsymbol{\varepsilon}} \cdot \Bigg\{ \left(\frac{\hat{\mathbf{x}} + i\hat{\mathbf{y}}}{2} \right) \Bigg[\sqrt{n_{\mathrm{OV}}^i} \Big((A + iB) \delta_{(m,m')} \delta_{(L,L'+1-l)} \\
& \qquad + (A - iB) \delta_{(m,m'+2)} \delta_{(L,L'-1-l)} \Big) \delta_{(n_{\mathrm{OV}}^f, n_{\mathrm{OV}}^i - 1)} \\
& \quad - \sqrt{n_{\mathrm{OV}}^i + 1} \Big((A^* - iB^*) \delta_{(m,m')} \delta_{(L,L'+1+l)} \\
& \qquad + (A^* + iB^*) \delta_{(m,m'+2)} \delta_{(L,L'-1+l)} \Big) \delta_{(n_{\mathrm{OV}}^f, n_{\mathrm{OV}}^i + 1)} \\
& \quad + 2\sqrt{n_{\mathrm{OV}}^i} C \delta_{(m,m'+1)} \delta_{(L,L'-l)} \delta_{(n_{\mathrm{OV}}^f, n_{\mathrm{OV}}^i - 1)} \\
& \qquad - 2\sqrt{n_{\mathrm{OV}}^i + 1} C^* \delta_{(m,m'+1)} \delta_{(L,L'+l)} \delta_{(n_{\mathrm{OV}}^f, n_{\mathrm{OV}}^i + 1)} \Bigg] \\
& + \left(\frac{\hat{\mathbf{x}} + i\hat{\mathbf{y}}}{2} \right) \Bigg[\sqrt{n_{\mathrm{OV}}^i} \Big((A - iB) \delta_{(m,m')} \delta_{(L,L'-1-l)} \\
& \qquad + (A + iB) \delta_{(m,m'-2)} \delta_{(L,L'+1-l)} \Big) \delta_{(n_{\mathrm{OV}}^f, n_{\mathrm{OV}}^i - 1)} \\
& \quad - \sqrt{n_{\mathrm{OV}}^i + 1} \Big((A^* + iB^*) \delta_{(m,m')} \delta_{(L,L'-1+l)}
\end{aligned}$$

$$
\begin{aligned}
&+ (A^* - iB^*)\delta_{(m,m'-2)}\delta_{(L,L'+1+l)}\Big)\delta_{(n^f_{\rm OV},n^i_{\rm OV}+1)} \\
&+ 2\sqrt{n^i_{\rm OV}}C\delta_{(m,m'-1)}\delta_{(L,L'-l)}\delta_{(n^f_{\rm OV},n^i_{\rm OV}-1)} \\
&\quad - 2\sqrt{n^i_{\rm OV}+1}C^*\delta_{(m,m'-1)}\delta_{(L,L'+l)}\delta_{(n^f_{\rm OV},n^i_{\rm OV}+1)}\Big] \\
&+\hat{\mathbf{z}}\Big[\sqrt{n^i_{\rm OV}}\Big((A'+iB')\delta_{(m,m'-1)}\delta_{(L,L'+1-l)} \\
&\quad - (A'+iB')\delta_{(m,m'+1)}\delta_{(L,L'-1-l)}\Big)\delta_{(n^f_{\rm OV},n^i_{\rm OV}-1)} \\
&- \sqrt{n^i_{\rm OV}+1}\Big((A'^*-iB'^*)\delta_{(m,m'-1)}\delta_{(L,L'+1+l)} \\
&\quad - (A'^*-iB'^*)\delta_{(m,m'+1)}\delta_{(L,L'-1+l)}\Big)\delta_{(n^f_{\rm OV},n^i_{\rm OV}+1)} \\
&+ 2\sqrt{n^i_{\rm OV}}C'\delta_{(m,m')}\delta_{(L,L'-l)}\delta_{(n^f_{\rm OV},n^i_{\rm OV}-1)} \\
&\quad - 2\sqrt{n^i_{\rm OV}+1}C'^*\delta_{(m,m')}\delta_{(L,L'+l)}\delta_{(n^f_{\rm OV},n^i_{\rm OV}+1)}\Big]\Big\} \quad \text{(A.22)}
\end{aligned}
$$

where A, A', B,B', C and C' are the non-azimuthal factors from the integration:

$$
\begin{aligned}
A &= k_\perp \int_0^\infty Q_{n'}(\rho_q)Q_n(\rho_q)\rho_q^4 d\rho_q \int_0^\pi P_{\ell'}^{m'}(\cos\theta_q)P_\ell^m(\cos\theta_q)\sin^3\theta_q d\theta_q \\
&\qquad \int_0^\infty R^i(\rho_R)R^f(\rho_R)J_l'(k_\perp\rho_R)\rho_R d\rho_R \delta(K_z - K_z' - k_z) \\
A' &= k_\perp \int_0^\infty Q_{n'}(\rho_q)Q_n(\rho_q)\rho_q^4 d\rho_q \int_0^\pi P_{\ell'}^{m'}(\cos\theta_q)P_\ell^m(\cos\theta_q)\sin^2\theta_q\cos\theta_q d\theta_q \\
&\qquad \int_0^\infty R^i(\rho_R)R^f(\rho_R)J_l'(k_\perp\rho_R)\rho_R d\rho_R \delta(K_z - K_z' + k_z) \\
B &= il \int_0^\infty Q_{n'}(\rho_q)Q_n(\rho_q)\rho_q^4 d\rho_q \int_0^\pi P_{\ell'}^{m'}(\cos\theta_q)P_\ell^m(\cos\theta_q)\sin^3\theta_q d\theta_q \\
&\qquad \int_0^\infty R^i(\rho_R)R^f(\rho_R)J_l(k_\perp\rho_R) d\rho_R \delta(K_z - K_z' - k_z) \\
B' &= il \int_0^\infty Q_{n'}(\rho_q)Q_n(\rho_q)\rho_q^4 d\rho_q \int_0^\pi P_{\ell'}^{m'}(\cos\theta_q)P_\ell^m(\cos\theta_q)\sin^2\theta_q\cos\theta_q d\theta_q \\
&\qquad \int_0^\infty R^i(\rho_R)R^f(\rho_R)J_l(k_\perp\rho_R) d\rho_R \delta(K_z - K_z' + k_z) \\
C &= -k_z \int_0^\infty Q_{n'}(\rho_q)Q_n(\rho_q)\rho_q^4 d\rho_q \int_0^\pi P_{\ell'}^{m'}(\cos\theta_q)P_\ell^m(\cos\theta_q)\sin^2\theta_q\cos\theta_q d\theta_q \\
&\qquad \int_0^\infty R^i(\rho_R)R^f(\rho_R)J_l(k_\perp\rho_R) d\rho_R \delta(K_z - K_z' - k_z) \\
C' &= -k_z \int_0^\infty Q_{n'}(\rho_q)Q_n(\rho_q)\rho_q^4 d\rho_q \int_0^\pi P_{\ell'}^{m'}(\cos\theta_q)P_\ell^m(\cos\theta_q)\sin\theta_q\cos^2\theta_q d\theta_q \\
&\qquad \int_0^\infty R^i(\rho_R)R^f(\rho_R)J_l(k_\perp\rho_R) d\rho_R \delta(K_z - K_z' + k_z).
\end{aligned}
$$

These quadrupole selection rules are rather more complicated than the dipole case. The orbital angular momentum projection of the atomic electron is allowed to change by one or two units in

this quadrupole interaction, but once again, the circular polarisation of the optical vortex plays a key role. For the linearly polarised field - $\hat{\mathbf{z}}$-polarised - the atomic electron may exchange one unit of angular momentum with the centre of mass, such that $\Delta m = \pm 1$. It can be seen that this does not depend on the vortex field, as both these processes are allowed for both absorption and emission of a vortex photon by the centre of mass, and here, only the centre of mass may directly exchange orbital angular momentum with the vortex. This is also the case for the interactions involving a circularly polarised field, in which exchanges of $\Delta m = \pm 2$ are possible. The centre of mass may exchange $l\hbar$ orbital angular momentum with the vortex, and the atomic electron may exchange one unit with the centre of mass, and one with the polarisation angular momentum of the field, giving a total change of $\Delta m = \pm 2$. The centre of mass of the atom may also exchange angular momentum with the spin polarisation of the photon. All the interactions described above rely on centre of mass motion.

If the interacting photon were not a vortex photon, then the exchange processes between the centre of mass and the atomic electron would still be possible. The quadrupole term allows the centre of mass and atomic electron angular momenta to couple directly (the weaker dipole term of Eq. (5.47) allows coupling between the electron and centre of mass such that $\Delta m = \pm 1$ and $\Delta L = \mp 2$, with the 'extra' unit from the circular polarisation of the photon). If the light field were not circularly polarised, then exchange of one unit would still be possible. However, the presence of orbital angular momentum l in the light field does not directly affect the atomic electron.

B

Electron Vortex Interactions

B.1 Calculation of Dipole Selection Rules

Here, the Coulomb matrix element of Eq. (6.27) will be explicitly evaluated. We write the shorthand

$$\left\langle \frac{(\mathbf{r}_v - \mathbf{R})}{|\mathbf{r}_v - \mathbf{R}|^3} \right\rangle_{fi} = \left\langle \psi_v^f(\mathbf{r}_v); \psi_p^f(\mathbf{R}) | \frac{(\mathbf{r}_v - \mathbf{R})}{|\mathbf{r}_v - \mathbf{R}|^3} | \psi_v^i(\mathbf{r}_v); \psi_p^i(\mathbf{R}) \right\rangle . \tag{B.1}$$

from Eq. (6.30) we have

$$\frac{(\mathbf{r}_v - \mathbf{R})}{|\mathbf{r}_v - \mathbf{R}|^3} = \frac{1}{[\mathcal{F} - \mathcal{G}\cos(\Phi_v - \Phi_R)]^{\frac{3}{2}}} \left[\left(\frac{\hat{\mathbf{x}} + i\hat{\mathbf{y}}}{2} \right) \left(\rho_v e^{-i\Phi_v} - \rho_R e^{-i\Phi_R} \right) + \left(\frac{\hat{\mathbf{x}} - i\hat{\mathbf{y}}}{2} \right) \left(\rho_v e^{i\Phi_v} - \rho_R e^{i\Phi_R} \right) \right] \tag{B.2}$$

Making the substitution $y = \Phi_v - \Phi_R$ allows for mixing of the orbital angular momentum of the electron vortex and the centre of mass motion, and requires generic integrals of the form

$$\mathcal{Y}_\alpha^{(\beta)} = \int_0^{2\pi} \frac{e^{i(l-l'+\alpha)y}}{(\mathcal{F}(\rho_v, z_v, \rho_R, z_R) - \mathcal{G}(\rho_v, \rho_R)\cos(\Phi_v - \Phi_R))^{\frac{\beta}{2}}} dy, \tag{6.31}$$

so that the integral over $d\Phi_v$ is now replaced by the integral over dy. For the dipole terms, α takes the values $0, \pm 1$. The full matrix element becomes

$$\left\langle \frac{(\mathbf{r}_v - \mathbf{R})}{|\mathbf{r}_v - \mathbf{R}|^3} \right\rangle_{fi} = \mathcal{N} \int d^3R \int d\rho_v \int dz_v$$

$$\times \Bigg[\left(\frac{\hat{\mathbf{x}} + i\hat{\mathbf{y}}}{2} \right) \left(\mathcal{I}_v \mathcal{J} \mathcal{R} \mathcal{Y}^3_{-1} - \mathcal{I} \mathcal{J} \mathcal{R}_R \mathcal{Y}^3_0 \right) e^{i(l+L-l'-L'-1)\Phi_R}$$

$$\left(\frac{\hat{\mathbf{x}} - i\hat{\mathbf{y}}}{2} \right) \left(\mathcal{I}_v \mathcal{J} \mathcal{R} \mathcal{Y}^3_{+1} - \mathcal{I} \mathcal{J} \mathcal{R}_R \mathcal{Y}^3_0 \right) e^{i(l+L-l'-L'+1)\Phi_R}$$

$$\hat{\mathbf{z}} \left(\mathcal{I} \mathcal{J}_z \mathcal{R} \mathcal{Y}^3_0 - \mathcal{I} \mathcal{J} \mathcal{R}_z \mathcal{Y}^3_0 \right) e^{i(l+L-l'-L')\Phi_R} \Bigg] \quad \text{(B.3)}$$

where the factors from the relevant wavefunctions have been written using the following shorthand:

$$\mathcal{F} = \rho_v^2 + \rho_R^2 + (z_v - z_R)^2, \quad \text{(B.4a)}$$

$$\mathcal{G} = 2\rho_v \rho_R, \quad \text{(B.4b)}$$

$$\mathcal{I}_v = J_l(k_\perp \rho_v) J_{l'}(k'_\perp \rho_v) \rho_v, \quad \text{(B.4c)}$$

$$\mathcal{I} = J_l(k_\perp \rho_v) J_{l'}(k'_\perp \rho_v), \quad \text{(B.4d)}$$

$$\mathcal{J} = e^{i(k_z - k'_z) z_v} dz_v, \quad \text{(B.4e)}$$

$$\mathcal{J}_z = e^{i(k_z - k'_z) z_v} z_v dz_v, \quad \text{(B.4f)}$$

$$\mathcal{R} = R^i(\rho_R) R^f(\rho_R, z_R) e^{i(K_R - K'_R)\rho_R} e^{i(K_z - K'_z) z_R}, \quad \text{(B.4g)}$$

$$\mathcal{R}_R = R^i(\rho_R) R^f(\rho_R) e^{i(K_R - K'_R)\rho_R} e^{i(K_z - K'_z) z_R} \rho_R, \quad \text{(B.4h)}$$

$$\mathcal{R}_z = R^i(\rho_R) R^f(\rho_R) e^{i(K_R - K'_R)\rho_p} e^{i(K_z - K'_z) z_R} z_R, \quad \text{(B.4i)}$$

$$\mathcal{N} = N^i_v N^f_v N^i_R N^f_R. \quad \text{(B.4j)}$$

In order to examine the possibility of orbital angular momentum transfer, we may now evaluate the azimuthal integral over Φ_R, to find

$$\left\langle \frac{\mathbf{r}_v - \mathbf{R}}{|\mathbf{r}_v - \mathbf{R}|^3} \right\rangle_{fi} = \mathcal{B}^{(-1)}_l \left(\hat{\mathbf{x}} + i\hat{\mathbf{y}} \right) \delta_{[(L+l),(L'+l'+1)]}$$

$$+ \mathcal{B}^{(+1)}_l \left(\hat{\mathbf{x}} - i\hat{\mathbf{y}} \right) \delta_{[(L+l),(L'+l'-1)]} + \mathcal{B}^{(0)}_l \hat{\mathbf{z}} \delta_{[(L+l),(L'+l')]} \quad \text{(6.32)}$$

with the factors $\mathcal{B}_l$ containing the non-azimuthal factors integrated over the remaining degrees of freedom

$$\mathcal{B}^{(-1)}_l = \frac{2\pi\mathcal{N}}{2} \int d^3R \int d\rho_v \int dz_v \left(\mathcal{I}_v \mathcal{J} \mathcal{R} \mathcal{Y}^3_{-1} - \mathcal{I} \mathcal{J} \mathcal{R}_p \mathcal{Y}^3_0 \right) \quad \text{(B.5a)}$$

$$\mathcal{B}^{(+1)}_l = \frac{2\pi\mathcal{N}}{2} \int d^3R \int d\rho_v \int dz_v \left(\mathcal{I}_v \mathcal{J} \mathcal{R} \mathcal{Y}^3_{+1} - \mathcal{I} \mathcal{J} \mathcal{R}_p \mathcal{Y}^3_0 \right) \quad \text{(B.5b)}$$

$$\mathcal{B}^{(0)}_l = 2\pi\mathcal{N} \int d^3R \int d\rho_v \int dz_v \left(\mathcal{I} \mathcal{J}_z \mathcal{R} \mathcal{Y}^3_0 - \mathcal{I} \mathcal{J} \mathcal{R}_z \mathcal{Y}^3_0 \right) \quad \text{(B.5c)}$$

It can be seen that $|\mathcal{B}^{(+1)}_l| = |\mathcal{B}^{(-1)*}_l|$.

B.2 Calculation of Quadrupole Selection Rules

Here, we find the selection rules for the quadrupole potential terms using the same method as in Appendix B.1. The quadratic interaction potential terms are

$$\hat{H}_{\text{Int}}^{\text{quad}} = \frac{e^2}{8\pi\varepsilon_0}\left[\frac{(m_p^2 - m_e^2)}{M}\frac{\mathbf{q}^2}{|\mathbf{r}_v - \mathbf{R}|^3} + 3\frac{(m_e^4 - m_p^4)}{M}\frac{(\mathbf{q}\cdot(\mathbf{r}_v - \mathbf{R}))^2}{|\mathbf{r}_v - \mathbf{R}|^5}\right] \tag{6.26}$$

which is expanded in vector components as

$$\begin{aligned}\hat{H}_{\text{Int}}^{\text{quad}} = \frac{e^2}{8\pi\varepsilon_0}\frac{\rho_q^2}{M}\Bigg[\frac{3(m_e^4 - m_p^4)}{|\mathbf{r}_v - \mathbf{R}|^5}\Big(&\sin^2\theta_q\rho_v^2\cos^2(\phi_q - \Phi_v) + \sin^2\theta_q\rho_R^2\cos^2(\phi_q - \Phi_R)\\ &- 2\sin^2\theta_q\rho_r\rho_v\cos(\phi_q - \Phi_v)\cos(\Phi_q - \Phi_R)\\ &+ 2\sin\theta_q\cos\theta_q\rho_v(z_v - z_R)\cos(\phi_q - \Phi_v)\\ &- 2\sin\theta_q\cos\theta_q\rho_R(z_v - z_R)\cos(\phi_q - \Phi_R)\\ &+ \cos^2\theta_q(z_v - z_R)^2\Big) + \frac{(m_p^2 - m_e^2)}{|\mathbf{r}_v - \mathbf{R}|^3}\Bigg]\end{aligned} \tag{B.6}$$

Expanding the azimuthal angular functions into exponential functions, so that the orbital angular momentum exchange will be apparent, we have

$$\begin{aligned}\hat{H}_{\text{Int}}^{\text{quad}} = \frac{e^2}{8\pi\varepsilon_0}\frac{\rho_q^2}{M}\Bigg[\frac{3(m_e^4 - m_p^4)}{|\mathbf{r}_v - \mathbf{R}|^5}\Big(&\frac{1}{4}\sin^2\theta_q\rho_v^2\left(e^{2i(\phi_q - \Phi_v)} + e^{-2i(\phi_q - \Phi_v)} + 1\right)\\ &+ \frac{1}{4}\sin^2\theta_q\rho_R^2\left(e^{2i(\phi_q - \Phi_R)} + e^{-2i(\phi_q - \Phi_R)} + 1\right)\\ &- \frac{1}{2}\sin^2\theta_q\rho_R\rho_v\big(e^{i(2\phi_q - \Phi_R - \Phi_v)} + e^{-i(2\phi_q - \Phi_R - \Phi_v)}\\ &\qquad + e^{i(\Phi_R - \Phi_v)} + e^{-i(\Phi_R - \Phi_v)}\big)\\ &- \sin\theta_q\cos\theta_q\rho_v(z_v - z_r)\left(e^{i(\phi_q - \Phi_v)} + e^{-i(\phi_q - \Phi_v)}\right)\\ &- \sin\theta_q\cos\theta_q\rho_R(z_v - z_r)\left(e^{i(\phi_q - \Phi_R)} + e^{-i(\phi_q - \Phi_R)}\right)\\ &+ \cos^2\theta_q(z_v - z_r)^2\Big) + \frac{(m_p^2 - m_e^2)}{|\mathbf{r}_v - \mathbf{R}|^3}\Bigg]\end{aligned} \tag{B.7}$$

As before we have,

$$\frac{1}{|\mathbf{r}_v - \mathbf{R}|^3} = \frac{1}{[\mathcal{F} + \mathcal{G}\cos(\Phi_v - \Phi_R)]^{\frac{3}{2}}} \tag{B.8}$$

and similarly

$$\frac{1}{|\mathbf{r}_v - \mathbf{R}|^5} = \frac{1}{[\mathcal{F} + \mathcal{G}\cos(\Phi_v - \Phi_R)]^{\frac{5}{2}}} \tag{B.9}$$

so that we can once again make the substitution $y = \Phi_v - \Phi_R$, and make use of the integrals of Eq. (6.31). Evaluating the full matrix element gives the following Kronecker delta functions that

form the basis of the selection rules:

$$\begin{aligned}\mathcal{M}_{\mathrm{EV}}^{\mathrm{quad}} = \frac{3e^2\pi^2(m_e^4 - m_p^4)}{\varepsilon_0}\Bigg[&\delta_{(l+L),(l'+L'+2)}\delta_{m,m'-2}\Bigg(\frac{\xi_v^3\xi_R^1\xi_q\eta^0\tau^{3,0}\mathcal{Y}_{-2}^5}{4} + \frac{\xi_v^1\xi_R^3\xi_q\eta^0\tau^{3,0}\mathcal{Y}_0^5}{4} \\ &\qquad - \frac{\xi_v^2\xi_R^2\xi_q\eta^0\tau^{3,0}\mathcal{Y}_{-1}^5}{2}\Bigg) \\ &\delta_{(l+L),(l'+L'-2)}\delta_{m,m'+2}\Bigg(\frac{\xi_v^3\xi_R^1\xi_q\eta^0\tau^{3,0}\mathcal{Y}_2^5}{4} + \frac{\xi_v^1\xi_R^3\xi_q\eta^0\tau^{3,0}\mathcal{Y}_0^5}{4} \\ &\qquad - \frac{\xi_v^2\xi_R^2\xi_q\eta^0\tau^{3,0}\mathcal{Y}_1^5}{2}\Bigg) \\ &+\delta_{(l+L),(l'+L'+1)}\delta_{m,m'-1}\Big(\xi_v^2\xi_R^1\xi_q\eta^1\tau^{2,1}\mathcal{Y}_{-1}^5 - \xi_v^1\xi_R^2\xi_q\eta^1\tau^{2,1}\mathcal{Y}_0^5\Big) \\ &+\delta_{(l+L),(l'+L'-1)}\delta_{m,m'+1}\Big(\xi_v^2\xi_R^1\xi_q\eta^1\tau^{2,1}\mathcal{Y}_1^5 - \xi_v^1\xi_R^2\xi_q\eta^1\tau^{2,1}\mathcal{Y}_0^5\Big) \\ &\delta_{(l+L),(l'+L')}\delta_{m,m'}\Bigg(\frac{\xi_v^3\xi_R^1\xi_q\eta^0\tau^{3,0}\mathcal{Y}_0^5}{4} + \frac{\xi_v^1\xi_R^3\xi_q\eta^0\tau^{3,0}\mathcal{Y}_0^5}{4} \\ &\qquad - \frac{\xi_v^2\xi_R^2\xi_q\eta^0\tau^{3,0}\mathcal{Y}_{-1}^5}{2} - \frac{\xi_v^2\xi_R^2\xi_q\eta^0\tau^{3,0}\mathcal{Y}_1^5}{2} \\ &\qquad + \xi_v^1\xi_R^1\xi_q\eta^2\tau^{1,2}\mathcal{Y}_0^5\Big)\Bigg] \\ &+\frac{3e^2\pi^2(m_p^2 - m_e^2)}{\varepsilon_0}\delta_{(l+L),(l'+L')}\delta_{m,m'}\xi_v^1\xi_R^1\xi_q\eta^0\tau^{1,0}\mathcal{Y}_0^3 \end{aligned} \tag{B.10}$$

with the non-azimuthal integrated factors given by

$$\xi_v^{(n)} = \int_0^\infty J_l(k_\perp\rho_v)J_{l'}(k'_\perp\rho_v)\rho_v^n d\rho_v \tag{B.11a}$$

$$\xi_R^{(n)} = \int_0^\infty R^i(\rho_v)R^f\rho_R^n d\rho_R \tag{B.11b}$$

$$\xi_q = \int_0^\infty \mathcal{Q}_n(\rho_q)\mathcal{Q}_{n'}(\rho_q)\rho_q^4 d\rho_q \tag{B.11c}$$

$$\eta_z^{(n)} = \int_{-\infty}^\infty\int_{-\infty}^\infty e^{i(k_z-k'_z)z_v}e^{i(K_z-K'_z)z_R}(z_v - z_R)^n dz_v dz_R \tag{B.11d}$$

$$\tau^{(n,n')} = \int_0^\pi P_\ell^m(\cos\theta_q)P_{\ell'}^{m'}(\cos\theta_q)\sin^n\theta_q\cos^{n'}\theta_q d\theta_q \tag{B.11e}$$

B.3 Nucleus-Vortex Coulomb Interaction

The second term of the interaction Hamiltonian of Eq. (6.38) will not affect the internal electron state of the atom, but it may induce transitions between different states of the atomic nucleus. In particular we are interested in the transfer of orbital angular momentum, and so we will look for changes in the rotational states of the nucleus. We have

$$\mathcal{M}_{fi}^R = -\left\langle\psi_q^i;\psi_R^i;\psi_v^i\right|\frac{e^2}{4\pi\varepsilon_0}\frac{1}{|\mathbf{r}_v - \mathbf{R}|}\left|\psi_q^f;\psi_R^f;\psi_v^f\right\rangle \tag{B.12}$$

Since both ψ_R^i and ψ_v^i are specified in the same coordinate frame no transformation is necessary. Once again, we have

$$|\mathbf{r}_v - \mathbf{R}| = \sqrt{\rho_v^2 + \rho_R^2 + (z_v - z_R)^2 - \rho_v \rho_R \cos(\Phi_v - \Phi_R)} \tag{B.13}$$

$$= \left[\mathcal{F} + \mathcal{G}\cos\left(\Phi_v - \Phi_R\right)\right]^{\frac{1}{2}}, \tag{B.14}$$

with the functions $\mathcal{F}$ and $\mathcal{G}$ that same as previously give in Eq. (B.4a) and Eq. (B.4b). The azimuthal factors of the matrix element are then given by

$$\mathcal{M}_{fi}^R \propto \int_0^{2\pi} d\phi_q \int_0^{2\pi} d\Phi_R \int_0^{2\pi} d\Phi_v \frac{e^{i(\ell-\ell')\phi_q} e^{i(L-L')\Phi_R} e^{i(l-l')\Phi_v}}{\left[\mathcal{F} + \mathcal{G}\cos\left(\Phi_v - \Phi_R\right)\right]^{\frac{1}{2}}}. \tag{B.15}$$

Again, the substitution $y = \Phi_v - \Phi_R$ is made, and the matrix element is written in terms of the integrals of Eq. (6.31). Evaluating this gives the selection rule

$$\mathcal{M}_{fi}^R = \frac{e^2\pi}{\varepsilon_0} \Theta_{R,v,y} \Theta_q \delta_{m,m'} \delta_{l+L,l'+L'} \tag{B.16}$$

where expressions for $\Theta_{R,v,y}$ and Θ_q are given in Appendix B.7.1, and since the atomic electron wavefunction is not affected, we have $2\pi\Theta_q = 1$.

B.4 The Matrix Element After First Expansion

The effective operator of Eq. (6.49) may be directly integrated to find the full selection rules of the interaction for the special case when the atom is free to rotate about the beam axis. This is carried out by integration with the atomic states using the same technique as before, the y-integrals of Eq. (6.31). The relevant factors to be integrated are, as before, the azimuthal terms for both the vortex and atomic electron wavefunctions, along with the Coulomb interaction factor. Allowing the nuclear coordinate to act as a dynamical variable we have, from the effective operator and the relevant states

$$\mathcal{M}_{fi} \propto \int_0^{2\pi} \int_0^{2\pi} \frac{e^{i(p-p')\Phi_v'} e^{i(m-m')\phi_q}}{|\mathbf{r}_v' - \mathbf{q}|} d\Phi_v' d\phi_q. \tag{B.17}$$

Similar to above, the Coulomb interaction may be expanded as

$$\frac{1}{|\mathbf{r}_v' - \mathbf{q}|} = \frac{1}{\left(\rho_v'^2 + z_v'^2 + \rho_q^2 - z_v'\rho_q\cos\theta_q - \rho_v'\rho_q\sin\theta_q\cos(\Phi_v' - \phi_q)\right)^{\frac{1}{2}}} \tag{B.18}$$

$$= \frac{1}{\left(\mathcal{F}' - \mathcal{G}'\cos(\Phi_v' - \phi_q)\right)^{\frac{1}{2}}} \tag{B.19}$$

So that the azimuthal integral becomes

$$\mathcal{M}_{fi} \propto \int_0^{2\pi} \frac{e^{-i(p-p')y'}}{\left(\mathcal{F}' + \mathcal{G}'\cos(\Phi_v' - \phi_q)\right)^{\frac{1}{2}}} \int_0^{2\pi} e^{i(m+p-m'-p')\phi_q} d\phi_q \tag{B.20}$$

where the substitution $y' = \Phi'_v - \phi_q$ has been made in the same manner as before, and

$$\mathcal{F}'(\rho'_v, \rho_q, z'_v, \theta_q) = \rho'^2_v + z'^2_v + \rho^2_q \tag{B.21}$$

$$\mathcal{G}'(\rho'_v, \rho_q, \theta_q) = \rho'_v \rho_q \sin\theta_q. \tag{B.22}$$

The full matrix element is then

$$\mathcal{M}_{fi} = \frac{e^2}{\varepsilon_0\sqrt{2\pi}} \left(\sum_{p=\infty}^{\infty} \Theta_R^{l,l',p,p'} \Theta_{q,v',y'}^{p,p'} \delta_{l+L-p,l'+L'-p'} \delta_{m+p,m'+p'} + \Theta_{R,v,y}\Theta_q \delta_{m,m'} \delta_{(l+L),(l'+L')} \right), \tag{B.23}$$

where the factors Θ_R, $\Theta_{q,v',y'}$, $\Theta_{R,v,y}$ and Θ_q are numerical factors arising from integrating over the remaining spatial degrees of freedom, and the matrix element of the Coulomb interaction between the vortex electron and the nucleus has been included (see Appendix B.3). Full expressions for the Θ factors are given in Appendix B.7.1 and Appendix B.7.2. The vortex-nucleus interaction contributes a channel in which the orbital angular momentum of the atomic electron may not change, but the rotational state of the nucleus may exchange angular momentum with the vortex. For the interaction in which the exchange with the atomic electron is possible, the selection rule of orbital angular momentum conservation are

$$m - m' = -(p - p'). \tag{B.24}$$

This selection rule only pertains to the particular p vortex wave that the atomic electron interacts with. This may be related to the original orbital angular momentum of the vortex beam l only if the initial and final orbital angular momentum states of the centre of mass are known. As before, we consider the centre of mass in an orbital angular momentum eigenstate, with initial and final states having L and L' units of angular momentum respectively. Eq. (6.51) contains the relevant factor for these centre of mass eigenstates, and when integrated over the centre of mass coordinates we find the selection rule

$$l - l' + L - L' = p - p' \tag{B.25}$$

such that the full selection rule of the interaction is found to show the same general orbital angular momentum conservation as that obtained in Section 6.2 using the multipolar expansion of the interaction Hamiltonian, namely

$$\Delta l + \Delta L = -\Delta m; \tag{B.26}$$

however, this is much less restrictive regarding the change of orbital angular momentum of the atom. This selection rule encompasses all possible transitions, from all multipolar contributions, since as yet no information regarding the multipolar nature of the transition has been obtained. This general expression of orbital angular momentum conservation does not specify which transitions are dipole allowed. In order to find this, a further wavefunction expansion is made.

We note here that, for the case when the atom position $\mathbf{R}$ is not a dynamical variable and the atom is held fixed, there is no selection rule relating Δl and Δm. In these situations, the orbital angular momentum transfer to the atom may take any value, as $-\infty \leq p \leq \infty$, and the change in orbital angular momentum of the beam is similarly unbounded. The consequences of this are

explored in Section 6.3.4 and Section 6.3.5 for the dipole terms of the interaction found from the multipolar expansion.

B.5 Fourier Transform of Effective Operator

The effective operator may be expressed in terms of the total linear momentum transfer $\mathbf{Q}(\beta)$ between the beam and the atomic electron:

$$\begin{aligned}\mathbf{Q}(\beta) &= \mathbf{k}' - \mathbf{k} \\ &= \sqrt{(\mathbf{k}-\mathbf{k}')^2} = \sqrt{\mathbf{k}^2 + \mathbf{k}'^2 - 2\mathbf{k}\cdot\mathbf{k}'} \\ &= \sqrt{k^2 + k'^2 - 2k_\perp k'_\perp \cos(\beta) - 2k_z k'_z}\end{aligned} \tag{B.27}$$

where $\beta = \phi'_k - \phi_k$. Writing the effective operator in this is accomplished in a way that recalls the method for Fourier transform of the Coulomb potential [142]. From Eq. (6.62)

$$I_q^{p,p',u,u'} = \int d^3r'_s . e^{i(k_z - k'_z)z'_s} J_{p-u}(k_\perp q_\perp) J_{p'-u'}(k'_\perp q_\perp) \frac{J_u(k_\perp \rho'_s) J_{u'}(k'_\perp \rho'_s)}{|\mathbf{r}'_s|} \times e^{i(p-u-p'+u')\phi_q} e^{i(u-u')\Phi'_s} \tag{6.62}$$

we may write the effective operator as a function of $\mathbf{Q}$. In order to do so, the Bessel functions may be written in integral form using:

$$J_\nu(z) = \frac{1}{2\pi i^\nu} \int_0^{2\pi} e^{iz\cos(\alpha)} e^{i\nu\alpha} d\alpha. \tag{2.28}$$

Writing the Bessel functions $J_u(k_\perp \rho'_s) J_{u'}(k'_\perp \rho'_s)$ in integral form gives

$$J_u(k_\perp \rho'_s) J_{u'}(k'_\perp \rho'_s) = \frac{1}{4\pi^2 i^u (-i)^{u'}} \int_0^{2\pi} e^{ik_\perp \rho'_s \cos(\alpha)} e^{iu\alpha} d\alpha \int_0^{2\pi} e^{-ik'_\perp \rho'_s \cos(\alpha')} e^{-iu'\alpha} d\alpha' \tag{B.28}$$

where the function $J_{u'}(k'_\perp \rho'_s)$ has been written in terms of a complex conjugate. The angles α and α' may be identified with the angles between the position vector ρ'_s and the transverse momenta, $k_\perp$ and $k'_\perp$ respectively, so as to allow the scalar product to be written later:

$$J_u(k_\perp \rho'_s) J_{u'}(k'_\perp \rho'_s) = \frac{1}{4\pi^2 i^u (-i)^{u'}} \int_0^{2\pi} e^{ik_\perp \rho'_s \cos(\phi_k - \Phi'_s)} e^{iu(\phi_k - \Phi'_s)} d\phi_k \int_0^{2\pi} e^{-ik'_\perp \rho'_s \cos(\phi'_k - \Phi'_s)} e^{-iu'(\phi'_k - \Phi'_s)} d\phi'_k \tag{B.29}$$

Combining this with Eq. (6.62) gives

$$I_q^{p,p',u,u'} = J_{p-u}(k_\perp q_\perp) J_{p'-u'}(k'_\perp q_\perp) e^{i(p-u-p'+u')\phi_q} \frac{1}{4\pi^2 i^u (-i)^{u'}}$$

$$\times \int d^3r'_s \int_0^{2\pi} d\phi_k \int_0^{2\pi} d\phi'_k e^{ik_\perp \rho'_s \cos(\phi_k - \Phi'_s)} e^{-ik'_\perp \rho'_s \cos(\phi'_k - \Phi'_s)}$$
$$\times \frac{e^{i(k_z - k'_z)z'_s} e^{i(u-u')\Phi'_s}}{|\mathbf{r}'_s|} e^{iu(\phi_k - \Phi'_s)} e^{-iu'(\phi'_k - \Phi'_s)}$$
$$= J_{p-u}(k_\perp q_\perp) J_{p'-u'}(k'_\perp q_\perp) e^{i(p-u-p'+u')\phi_q} \frac{1}{4\pi^2 i^u (-i)^{u'}}$$
$$\times \int d^3r'_s \int_0^{2\pi} d\phi_k \int_0^{2\pi} d\phi'_k \frac{e^{i(\mathbf{k}-\mathbf{k}')\cdot\mathbf{r}'_s}}{|\mathbf{r}'_s|} e^{iu\phi_k} e^{-iu'\phi'_k} \quad \text{(B.30)}$$

Using this the linear momentum transfer vector $\mathbf{Q}(\beta)$, we may write

$$I_q^{p,p',u,u'} = J_{p-u}(k_\perp q_\perp) J_{p'-u'}(k'_\perp q_\perp) e^{i(p-u-p'+u')\phi_q} \frac{1}{4\pi^2 i^u (-i)^{u'}}$$
$$\times \int d^3r'_s \int_0^{2\pi} d\beta \int_0^{2\pi} d\phi_k \frac{e^{-i\mathbf{Q}(\beta)\cdot\mathbf{r}'_s}}{|\mathbf{r}'_s|} e^{i(u-u')\phi_k} e^{-iu\beta}$$
$$= J_{p-u}(k_\perp q_\perp) J_{p'-u}(k'_\perp q_\perp) e^{i(p-p')\phi_q} \frac{\delta_{u,u'}}{2\pi} \int d^3r'_s \int_0^{2\pi} d\beta \frac{e^{-i\mathbf{Q}(\beta)\cdot\mathbf{r}'_s}}{|\mathbf{r}'_s|} e^{-iu\beta} \quad \text{(B.31)}$$

This now has a similar form as the Fourier transform of the Coulomb potential. Evaluating this using the standard result [142]

$$\tilde{f}(\mathbf{k}) = \frac{1}{(2\pi)^{3/2}} \int d^3x \frac{1}{|\mathbf{x}|} e^{-i\mathbf{k}\cdot\mathbf{x}} = \sqrt{\frac{2}{\pi}} \frac{1}{k^2}, \quad \text{(B.32)}$$

gives

$$I_q^{p,p',u,u} = J_{p-u}(k_\perp q_\perp) J_{p'-u}(k'_\perp q_\perp) e^{i(p-p')\phi_q} \frac{\delta_{u,u'}}{\sqrt{2\pi^3}} \int_0^{2\pi} d\beta \frac{e^{-iu\beta}}{\mathbf{Q}(\beta)}. \quad \text{(6.63)}$$

B.6 Summation over p, p' and u

In order to achieve the multipolar expansion, the asymptotic limit of the Bessel function is applied. Since this is valid for Bessel functions of positive order only, it is necessary to write the expanded wavefunctions in such a was that they are always of positive order, even for $p < 0$. This leads to the conditions on p, p' and u, as given in Table 6.3.1. Applying these conditions leads to a set of eighteen restricted sums over p, p' and u:

$$\Sigma^{p,p',u} = \sum_{u=0}^{\infty} \Bigg(\sum_{p=0,p\geq u}^{\infty} \sum_{p'=0,p'\geq u}^{\infty} J_{p-u}(k_\perp q_\perp) J_{p'-u}(k_\perp q_\perp)$$
$$+ \sum_{p=0,p\geq u}^{\infty} \sum_{p'=0,p'<u}^{\infty} (-1)^{|p'-u|} J_{p-u}(k_\perp q_\perp) J_{|p'-u|}(k_\perp q_\perp)$$
$$+ \sum_{p=0,p\geq u}^{\infty} \sum_{p'=-\infty}^{-1} (-1)^{|p'-u|} J_{p-u}(k_\perp q_\perp) J_{|p'-u|}(k_\perp q_\perp)$$
$$+ \sum_{p=0,p<u}^{\infty} \sum_{p'=0,p'\geq u}^{\infty} (-1)^{|p-u|} J_{|p-u|}(k_\perp q_\perp) J_{p'-u}(k_\perp q_\perp)$$

$$
\begin{aligned}
&+\sum_{p=0,p<u}^{\infty}\sum_{p'=0,p'<u}^{\infty}(-1)^{|p-u|+|p'-u|}J_{|p-u|}(k_\perp q_\perp)J_{|p'-u|}(k_\perp q_\perp)\\
&+\sum_{p=0,p<u}^{\infty}\sum_{p'=-\infty}^{-1}(-1)^{|p-u|+|p'-u|}J_{|p-u|}(k_\perp q_\perp)J_{|p'-u|}(k_\perp q_\perp)\\
&+\sum_{p=-\infty}^{-1}\sum_{p'=0,p'\geq u}^{\infty}(-1)^{|p-u|}J_{|p-u|}(k_\perp q_\perp)J_{p'-u}(k_\perp q_\perp)\\
&+\sum_{p=-\infty}^{-1}\sum_{p'=0,p'<u}^{\infty}(-1)^{|p-u|+|p'-u|}J_{|p-u|}(k_\perp q_\perp)J_{|p'-u|}(k_\perp q_\perp)\\
&\qquad\sum_{p=-\infty}^{-1}\sum_{p'=-\infty}^{-1}(-1)^{|p-u|+|p'-u|}J_{|p-u|}(k_\perp q_\perp)J_{|p'-u|}(k_\perp q_\perp)\Bigg)\\
&+\sum_{u=-\infty}^{-1}\Bigg(\sum_{p=0}^{\infty}\sum_{p'=0}^{\infty}J_{p-u}(k_\perp q_\perp)J_{p'-u}(k_\perp q_\perp)\\
&\qquad+\sum_{p=0}^{\infty}\sum_{p'=-\infty,p'\geq u}^{-1}J_{p-u}(k_\perp q_\perp)J_{p'-u}(k_\perp q_\perp)\\
&\quad+\sum_{p=0}^{\infty}\sum_{p'=-\infty,p'<u}^{-1}(-1)^{|p'-u|}J_{p-u}(k_\perp q_\perp)J_{|p'-u|}(k_\perp q_\perp)\\
&\qquad+\sum_{p=-\infty,p\geq u}^{-1}\sum_{p'=0}^{\infty}J_{p-u}(k_\perp q_\perp)J_{p'-u}(k_\perp q_\perp)\\
&\quad+\sum_{p=-\infty,p\geq u}^{-1}\sum_{p'=-\infty,p'\geq u}^{-1}J_{p-u}(k_\perp q_\perp)J_{p'-u}(k_\perp q_\perp)\\
&+\sum_{p=-\infty,p\geq u}^{-1}\sum_{p'=-\infty,p'<u}^{-1}(-1)^{|p'-u|}J_{p-u}(k_\perp q_\perp)J_{|p'-u|}(k_\perp q_\perp)\\
&\quad+\sum_{p=-\infty,p<u}^{-1}\sum_{p'=0}^{\infty}(-1)^{|p-u|}J_{|p-u|}(k_\perp q_\perp)J_{p'-u}(k_\perp q_\perp)\\
&+\sum_{p=-\infty,p<u}^{-1}\sum_{p'=-\infty,p'\geq u}^{-1}(-1)^{|p-u|}J_{|p-u|}(k_\perp q_\perp)J_{p'-u}(k_\perp q_\perp)\\
&+\sum_{p=-\infty,p<u}^{-1}\sum_{p'=-\infty,p'<u}^{-1}(-1)^{|p-u|+|p'-u|}J_{|p-u|}(k_\perp q_\perp)J_{|p'-u|}(k_\perp q_\perp)\Bigg).
\end{aligned}
\tag{B.33}
$$

The Bessel functions written in each term above are now each of positive order, and are suitable for expanding in powers of $q_\perp$. Applying the asymptotic limit of Eq. (6.65) gives

$$
\begin{aligned}
\Sigma^{p,p',u}=\sum_{u=0}^{\infty}\Bigg(&\sum_{p=0,p\geq u}^{\infty}\sum_{p'=0,p'\geq u}^{\infty}\frac{1}{\Gamma(p-u+1)\Gamma(p'-u+1)}\left(\frac{k_\perp q_\perp}{2}\right)^{p+p'-2u}\\
&+\sum_{p=0,p\geq u}^{\infty}\sum_{p'=0,p'<u}^{\infty}\frac{(-1)^{|p'-u|}}{\Gamma(p-u+1)\Gamma(|p'-u|+1)}\left(\frac{k_\perp q_\perp}{2}\right)^{p-u+|p'-u|}
\end{aligned}
$$

$$
\begin{aligned}
&+\sum_{p=0,p\geq u}^{\infty}\sum_{p'=-\infty}^{-1}\frac{(-1)^{|p'-u|}}{\Gamma(p-u+1)\Gamma(|p'-u|+1)}\left(\frac{k_\perp q_\perp}{2}\right)^{p-u+|p'-u|}\\
&+\sum_{p=0,p<u}^{\infty}\sum_{p'=0,p'\geq u}^{\infty}\frac{(-1)^{|p-u|}}{\Gamma(|p-u|+1)\Gamma(p'-u+1)}\left(\frac{k_\perp q_\perp}{2}\right)^{|p-u|+p'-u}\\
&+\sum_{p=0,p<u}^{\infty}\sum_{p'=0,p'<u}^{\infty}\frac{(-1)^{|p-u|+|p'-u|}}{\Gamma(|p-u|+1)\Gamma(|p'-u|+1)}\left(\frac{k_\perp q_\perp}{2}\right)^{|p-u|+|p'-u|}\\
&+\sum_{p=0,p<u}^{\infty}\sum_{p'=-\infty}^{-1}\frac{(-1)^{|p-u|+|p'-u|}}{\Gamma(|p-u|+1)\Gamma(|p'-u|+1)}\left(\frac{k_\perp q_\perp}{2}\right)^{|p-u|+|p'-u|}\\
&+\sum_{p=-\infty}^{-1}\sum_{p'=0,p'\geq u}^{\infty}\frac{(-1)^{|p-u|}}{\Gamma(|p-u|+1)\Gamma(p'-u+1)}\left(\frac{k_\perp q_\perp}{2}\right)^{|p-u|+p'-u}\\
&+\sum_{p=-\infty}^{-1}\sum_{p'=0,p'<u}^{\infty}\frac{(-1)^{|p-u|+|p'-u|}}{\Gamma(|p-u|+1)\Gamma(|p'-u|+1)}\left(\frac{k_\perp q_\perp}{2}\right)^{|p-u|+|p'-u|}\\
&\quad\sum_{p=-\infty}^{-1}\sum_{p'=-\infty}^{-1}\frac{(-1)^{|p-u|+|p'-u|}}{\Gamma(|p-u|+1)\Gamma(|p'-u|+1)}\left(\frac{k_\perp q_\perp}{2}\right)^{|p-u|+|p'-u|}\\
&+\sum_{u=-\infty}^{-1}\left(\sum_{p=0}^{\infty}\sum_{p'=0}^{\infty}\frac{1}{\Gamma(p-u+1)\Gamma(p'-u+1)}\left(\frac{k_\perp q_\perp}{2}\right)^{p+p'-2u}\right.\\
&\quad+\sum_{p=0}^{\infty}\sum_{p'=-\infty,p'\geq u}^{-1}\frac{1}{\Gamma(p-u+1)\Gamma(p'-u+1)}\left(\frac{k_\perp q_\perp}{2}\right)^{p+p'-2u}\\
&\quad+\sum_{p=0}^{\infty}\sum_{p'=-\infty,p'<u}^{-1}\frac{(-1)^{|p'-u|}}{\Gamma(p-u+1)\Gamma(|p'-u|+1)}\left(\frac{k_\perp q_\perp}{2}\right)^{p-u+|p'-u|}\\
&\quad+\sum_{p=-\infty,p\geq u}^{-1}\sum_{p'=0}^{\infty}\frac{1}{\Gamma(p-u+1)\Gamma(p'-u+1)}\left(\frac{k_\perp q_\perp}{2}\right)^{p+p'-2u}\\
&\quad+\sum_{p=-\infty,p\geq u}^{-1}\sum_{p'=-\infty,p'\geq u}^{-1}\frac{1}{\Gamma(p-u+1)\Gamma(p'-u+1)}\left(\frac{k_\perp q_\perp}{2}\right)^{p+p'-2u}\\
&\quad+\sum_{p=-\infty,p\geq u}^{-1}\sum_{p'=-\infty,p'<u}^{-1}\frac{(-1)^{|p'-u|}}{\Gamma(p-u+1)\Gamma(|p'-u|+1)}\left(\frac{k_\perp q_\perp}{2}\right)^{p-u+|p'-u|}\\
&\quad+\sum_{p=-\infty,p<u}^{-1}\sum_{p'=0}^{\infty}\frac{(-1)^{|p-u|}}{\Gamma(|p-u|+1)\Gamma(p'-u+1)}\left(\frac{k_\perp q_\perp}{2}\right)^{|p-u|+p'-u}\\
&\quad+\sum_{p=-\infty,p<u}^{-1}\sum_{p'=-\infty,p'\geq u}^{-1}\frac{(-1)^{|p-u|}}{\Gamma(|p-u|+1)\Gamma(p'-u+1)}\left(\frac{k_\perp q_\perp}{2}\right)^{|p-u|+p'-u}\\
&\left.+\sum_{p=-\infty,p<u}^{-1}\sum_{p'=-\infty,p'<u}^{-1}\frac{(-1)^{|p-u|+|p'-u|}}{\Gamma(|p-u|+1)\Gamma(|p'-u|+1)}\left(\frac{k_\perp q_\perp}{2}\right)^{|p-u|+|p'-u|}\right)
\end{aligned}
\tag{B.34}
$$

In order to determine the particular terms in the full multipole expansion, the specific relationships between p, p' and u that give the desired powers of $q_\perp$ are found for each multipole term. These relationships are specified in Table 6.3.2, Table 6.3.3 and Table 6.3.4 for the zero order, dipole and quadrupole terms respectively.

B.7 Matrix element factors

In the following, the explicit expressions for the integrals arising in the evaluation of the matrix element are given. These are from the non-azimuthal factors of the wavefunctions in each case, and the precise value depend on the particular initial and final states of the electron vortex, atomic electron and nuclear wavefunctions.

B.7.1 Integral Factors for Nucleus-Vortex Coulomb Interaction

The matrix element of the Coulomb interaction between the electron vortex and the atomic nucleus is given in Appendix B.3. The relevant integral factors take the following form:

$$\Theta_{R,v,y} = N_R N'_R N_l N_{l'} \int_0^\infty d\rho_R \int_{-\infty}^\infty dz_R \int_0^\infty d\rho_v \int_{-\infty}^\infty dz_v \int_0^{2\pi} \times \frac{R^{f*}(\rho_R) R^i(\rho_R) J_l(k_\perp \rho_v) J_{l'}(k'_\perp \rho_v)}{[\mathcal{F} + \mathcal{G}\cos y]^{\frac{1}{2}}} \times e^{i(K_\perp - K'_\perp)\rho_R} \rho_R \rho_v e^{i(K_z - K'_z) z_R} e^{i(k_z - k'_z) z_v} e^{i(l-l')y}; \quad \text{(B.35)}$$

$$\Theta'_q = N_{n,\ell,m} N_{n',\ell',m'} \int_0^\infty d\rho_q \mathcal{Q}^{f*}_{n'}(\rho_q) \mathcal{Q}^i_n(\rho_q) \rho_q^2 \int_0^\pi d\theta_q P^m_\ell(\cos\theta_q) P^{m'}_{\ell'}(\cos\theta_q) \sin\theta_q. \quad \text{(B.36)}$$

Θ'_q is simply the overlap integral of the radial and polar functions of two hydrogenic electron states. Since the nucleus-vortex interaction cannot affect the internal state of the atom the set of quantum numbers n, l, m for initial and final hydrogenic states must be the same and we have $2\pi\Theta'_q = 1$.

B.7.2 Integral factors for First Effective Operator

After the first expansion of the electron vortex wavefunction about the atomic nucleus, the matrix element and selection rules may be directly evaluated. This is shown in Appendix B.4, with the relevant integral factors given as:

$$\Theta_R^{l,l',p,p'} = N_R N'_R N_l N_{l'} \int_0^\infty d\rho_R \rho_R R^{f*}(\rho_R) R^i(\rho_R) J_{l-p}(k_\perp \rho_R) J_{l'-p'}(k'_\perp \rho_R) \times \int_{-\infty}^\infty dz_R e^{i(K_z + k_z - K'_z - k'_z) z_R}; \quad \text{(B.37)}$$

$$\Theta^{p,p'}_{q,v',y'} = N_{n,\ell,m} N_{n',\ell',m'} \int_0^\infty d\rho'_v \int_{-\infty}^\infty dz'_v \int_0^\infty d\rho_q \int_0^\pi d\theta_q \times \mathcal{Q}^{f*}_{n'}(\rho_q) \mathcal{Q}^i_n(\rho_q) \frac{J_p(k_\perp \rho'_v) J_{p'}(k'_\perp \rho'_v)}{[\mathcal{F}' + \mathcal{G}'\cos(y')]^{\frac{1}{2}}} \rho_q^2 \rho_v \sin\theta_q \times P^m_\ell(\cos\theta_q) P^{m'}_{\ell'}(\cos\theta_q) e^{i(p-p')y'} e^{i(k_z - k'_z) z'_v}. \quad \text{(B.38)}$$

B.7.3 Integral Factors for Zero Order Term

The matrix element and selection rules of the zero order term found in Section 6.3.3 have the following factors arising after the integration over the non-azimuthal degrees of freedom of the atomic electron and nucleus, as well as the integral over the total momentum transfer:

$$\Theta_q^{\text{ZO}} = N_{n,\ell,m} N_{n',\ell',m'} \int_0^\infty d\rho_q \int_0^\pi d\theta_q \mathcal{Q}_{n'}^{f*}(\rho_q) \mathcal{Q}_n^i(\rho_q) P_\ell^m(\cos\theta_q) P_{\ell'}^{m'}(\cos\theta_q) \times \rho_q^2 \sin\theta_q e^{i(k_z - k_z')\rho_q \cos\theta_q} \tag{B.39}$$

$$\Theta_R^{l,l',p} = 2\pi N_R N_R' N_l N_{l'} \int_{-\infty}^\infty dz_R \int_0^\infty d\rho_R \rho_R J_{l-p}(k_\perp \rho_R) J_{l'-p}(k_\perp \rho_R) \times R^{f*}(\rho_R) R^i(\rho_R) e^{i(K_z + k_z - K_z' - k_z')z_R} \tag{B.40}$$

B.7.4 Integral Factors for Dipole Term

For the dipole terms of Section 6.3.4, there are two different matrix elements illustrated - one for the case when the atom is located along the beams axis, and one for the off-axis case. The dipole matrix element of the atomic electron, and so Θ_q^{dip}, is common to each of them, whereas Θ_R and $\Theta_R^{l,l',p,\pm}$ apply to the on-axis and off-axis scenarios respectively.

$$\Theta_q^{\text{dip}} = N_{n,\ell,m} N_{n',\ell',m'} \int_0^\infty d\rho_q \int_0^\pi d\theta_q \mathcal{Q}_{n'}^{f*}(\rho_q) \mathcal{Q}_n^i(\rho_q) P_\ell^m(\cos\theta_q) P_{\ell'}^{m'}(\cos\theta_q) \times \rho_q^3 \sin\theta_q \cos\theta_q e^{i(k_z - k_z')\rho_q \cos\theta_q} \tag{B.41}$$

$$\Theta_R = N_R N_R' \int_0^\infty d\rho_R R^{f*}(\rho_R) R^i(\rho_R) \rho_R \int_{-\infty}^\infty dz_R e^{i(K_z + k_z - K_z' - k_z')z_R} \tag{B.42}$$

$$\Theta_R^{l,l',p,\pm} = N_R N_R' N_l N_{l'} \int_{-\infty}^\infty dz_R \int_0^\infty d\rho_R \rho_R J_{l-p}(k_\perp \rho_R) J_{l'-p\pm1}(k_\perp \rho_R) \times R^{f*}(\rho_R) R^i(\rho_R) e^{i(K_z + k_z - K_z - k_z)z_R} \int_0^{2\pi} e^{i(l-l'-p+p\mp1)} \tag{B.43}$$

Due to the relationship between Bessel functions of positive and negative order given by (2.29) we have $|\Theta_R^{l,l',p,\pm}| = |\Theta_R^{-l,-l',-p,\mp}|$.

C

Relativistic Quantum Mechanics

C.1 The Dirac γ Matrices

The γ-matrices are useful in writing a fully Lorentz covariant form of the Dirac equation and other relativistic field quantities, including the Lagrangian for quantum electrodynamics. The γ-matrices form the 4-dimensional (three space and one time) representation of the Lorentz algebra for Lorentz boosts and rotations of spin-$\frac{1}{2}$ particles. [119]. In the Dirac representation the four γ-matrices are defined as

$$\gamma^0 = \begin{pmatrix} \mathbb{1}_2 & 0 \\ 0 & -\mathbb{1}_2 \end{pmatrix}; \qquad \gamma^i = \begin{pmatrix} 0 & \sigma^i \\ -\sigma^i & 0 \end{pmatrix} \tag{C.1}$$

or, equivalently, $\gamma^\mu = (\beta, \beta\boldsymbol{\alpha})$. Though this notation is suggestive, the γ-matrices themselves are not 4-vectors - instead the matrices act on true 4-vectors to give a Lorentz invariant quantity [119].

The commutation and anti-commutation of the γ-matrices are their defining characteristics - they must satisfy the algebra of the Lorentz group, in order to represent Lorentz transformations. We have

$$\{\gamma^\mu, \gamma^\nu\} = 2g^{\mu\nu}\mathbb{1}_4 \tag{C.2}$$

where the metric tensor $g^{\mu\nu}$ is given as

$$g^{\mu\nu} = \begin{pmatrix} 1 & 0 & 0 & 0 \\ 0 & -1 & 0 & 0 \\ 0 & 0 & -1 & 0 \\ 0 & 0 & 0 & -1 \end{pmatrix}. \tag{C.3}$$

The Lorentz transformations are then defined elegantly by the commutators of the γmatrices, so

that we may write boosts and rotations respectively in the form [118, 119]

$$S^{0j} = \frac{i}{4}[\gamma^0, \gamma^j] = -\frac{i}{2}\begin{pmatrix} \sigma^j & 0 \\ 0 & -\sigma^j \end{pmatrix} \tag{C.4a}$$

$$S^{ij} = \frac{i}{4}[\gamma^i, \gamma^j] = \frac{\hbar}{2}\varepsilon^{ijk}\Sigma^k \tag{C.4b}$$

with ε^{ijk} the Levi-Civita permutation symbol, and $\boldsymbol{\Sigma}$ the spin operator for Dirac particles

$$\boldsymbol{\Sigma} = \frac{\hbar}{2}\begin{pmatrix} \boldsymbol{\sigma} & 0 \\ 0 & \boldsymbol{\sigma} \end{pmatrix}. \tag{C.5}$$

The γ-matrices are Hermitian, however the generators of Lorentz transformations Eq. (C.4) are not meaning that the transformation generators $S^{\mu\nu}$ are not unitary, so that transformed quantities are no longer Hermitian [118, 119]. This means that, for a Dirac spinor $\psi^\dagger\psi \neq 1$ after a Lorentz boost. In order to resolve this, the adjoint Dirac spinor is introduced

$$\bar{\psi} = \psi^\dagger\gamma^0. \tag{C.6}$$

While the Dirac spinor ψ transforms as

$$\psi \to \Lambda\psi = e^{-\frac{i}{2}\delta S^{\mu\nu}}\psi, \tag{C.7}$$

for some small parameter δ, the adjoint spinor transforms as

$$\bar{\psi} \to (\psi^\dagger\Lambda^\dagger)\gamma^0 = \psi^\dagger e^{\frac{i}{2}\delta S^{\mu\nu\dagger}}\gamma^0. \tag{C.8}$$

From Eq. (C.4), the following relations can be found:

$$S^{0j\dagger} = -S^{0j}, \qquad S^{ij\dagger} = S^{ij};$$
$$\{S^{0j}, \gamma^0\} \qquad [S^{0j}, \gamma^0] = 0;$$

and it can then be seen that $S^{\mu\nu\dagger}\gamma^0 = \gamma^0 S^{\mu\nu}$. So that the quantity $\bar{\psi}\psi$ transforms as

$$\begin{aligned}
\bar{\psi}\psi \to &(\psi^\dagger\Lambda^\dagger)\gamma^0\Lambda\psi \\
&= \psi^\dagger\left(1\frac{i}{2}\delta S^{\mu\nu\dagger}\right)\gamma^0\left(1 - \frac{i}{2}\delta S^{\mu\nu}\right)\psi \\
&= \psi^\dagger\gamma^0\left(1 + \frac{i}{2}\delta S^{\mu\nu}\right)\left(1 - \frac{i}{2}\delta S^{\mu\nu}\right)\psi \\
&= \psi^\dagger\gamma^0\Lambda^{-1}\Lambda\psi \\
&= \bar{\psi}\psi
\end{aligned}$$

Thus $\bar{\psi}\psi$ is a Lorentz scalar, invariant under transformations. Similarly it can be shown [119] that

$\bar{\psi}\partial_\mu\psi$ is a Lorentz vector, so that the Lagrangian density for the Dirac field ψ is written

$$\mathcal{L} = i\hbar\bar{\psi}\partial_\mu\psi - c^2 m\bar{\psi}\psi. \tag{C.9}$$

On applying the Euler-Lagrange equations for $\bar{\psi}$ and ψ this yields the field equations of motion; respectively the Dirac equation of Eq. (7.7) or the adjoint Dirac equation

$$i\partial_\mu\bar{\psi}\gamma^\mu + m\bar{\psi} = 0. \tag{C.10}$$

C.2 Applying The Foldy-Wouthuysen Transformation

The Foldy-Wouthuysen transformation takes the form

$$H'(t) = e^{iS(t)}\left(H(t) - i\hbar\partial_t\right)e^{-iS(t)}. \tag{C.11}$$

This will now be written into a convenient form, and applied to the Dirac Hamiltonian in the presence of fields. In application of this transformation it is convenient to suppress the time and space dependence of the operators. For any linear operators A and B acting in the same vector space we have the relation [123, 124]

$$e^A B e^{-A} = \sum_{n=0}^{\infty}\frac{1}{n!}\Omega_n(A,B) \tag{C.12}$$

where the operator $\Omega_n(A,B)$ is defined as

$$\Omega_n(A,B) = [A, \Omega_{n-1}(A,B)] \tag{C.13}$$

with

$$\Omega_0(A,B) = B \tag{C.14}$$

so that the function $\Omega_n(A,B)$ consists of $n-1$ nested commutators. This is now applied to Eq. (C.11). For the term $e^{iS(t)}H(t)e^{-iS(t)}$ we have simply

$$e^{iS(t)}H(t)e^{-iS(t)} = \sum_{n=0}^{\infty}\frac{i^n}{n!}\Omega_n(S,H). \tag{C.15}$$

The second term $e^{iS(t)}i\hbar\partial_t e^{-iS(t)}$ is slightly more tricky, but noting that

$$e^{iS}\partial_t e^{-iS} = -ie^{iS}\partial_t S e^{-iS} \tag{C.16}$$

suggests that we may look for an expansion in terms of $\Omega_n(S,\partial_t S)$. By comparing the first few terms in the expansions of ∂_t and $\partial_t S$, up to $n=2$,

$$\Omega_0(S,\partial_t) = \partial_t = 0 \qquad \Omega_0(S,\partial_t S) = \partial_t S$$
$$\Omega_1(S,\partial_t) = [S,\partial_t] = -\partial_t S \qquad \Omega_1(S,\partial_t S) = [S,\partial_t S]$$

$$\Omega_2(S,\partial_t) = -[S,\partial_t S] = -\Omega_1(S,\partial_t S) \qquad \Omega_2(S,\partial_t S) = [S,[S,\partial_t S]]$$

it is clear to see that

$$\Omega_n(S,\partial_t) = -\Omega_{n-1}(S,\partial_t S); \tag{C.17}$$

so that we may write

$$\begin{aligned} e^{iS}\partial_t e^{-iS} &= \sum_{n=0}^{\infty} \frac{i^n}{n!}\Omega_n(S,\partial_t) \\ &= -\sum_{n=0}^{\infty} \frac{i^n}{n!}\Omega_{n-1}(S,\partial_t S) \\ &= -\sum_{n=0}^{\infty} \frac{i^{n+1}}{(n+1)!}\Omega_n(S,\partial_t S). \end{aligned}$$

Putting this together with Eq. (C.11) and Eq. (C.15) gives

$$H' = \sum_{n=0}^{\infty} \frac{i^n}{n!}\Omega_n(S,H) - \hbar\sum_{n=0}^{\infty} \frac{i^n}{(n+1)!}\Omega_n(S,\partial tS); \tag{C.18}$$

this can be consolidated into a single summation:

$$\begin{aligned} H' &= H + \sum_{n=1}^{\infty} \frac{i^n}{n!}\Omega_{n-1}(S,[S,H]) - \hbar\sum_{n=0}^{\infty} \frac{i^n}{(n+1)!}\Omega_n(S,\partial tS) \\ &= H + \hbar\sum_{n=0}^{\infty} \frac{i^n}{(n+1)!}\Omega_n(S,\tfrac{i}{\hbar}[S,H] - \partial tS), \end{aligned} \tag{C.19}$$

giving the full expansion in terms of the original Hamiltonian H.

C.3 The Foldy-Wouthuysen Hamiltonian

Application of the Foldy-Wouthuysen transformation has resulted in an expansion in powers of $(mc^2)^{-1}$, for which all terms of order $(mc^2)^{-2}$ and below are now even. This Hamiltonian has the form

$$H' = mc^2\beta + V + (mc^2)^{-1}\eta_1 + (mc^2)^{-2}\eta_2 + (mc^2)^{-3}\eta_{\text{even},3} \tag{7.49}$$

where the operator coefficients are given in terms of the transformation matrices S_n:

$$\eta_1 = -2\beta S_1^2 + i[S_1,T] \tag{7.51}$$

$$\eta_2 = -2\beta\{S_1,S_2\} + i[S_2,T] + i[S_2,T] - \frac{i\hbar}{2}[S_1,\dot{S}_1] \tag{7.52}$$

$$\begin{aligned} \eta_{\text{even},3} = &-2\beta\{S_1,S_3\} - 2\beta S_2^2 + \frac{2}{3}\beta S_1^4 + i[S_3,T] \\ &- \frac{i}{6}[S_1,[S_1,[S_1,T]]] - \frac{i\hbar}{2}[S_1,\dot{S}_2] - \frac{i\hbar}{2}[S_2,\dot{S}_2]. \end{aligned} \tag{7.53}$$

The transformation matrices have been determined by the reduction of the odd operators of order $(mc^2)^0$, $(mc^2)^{-1}$, and $(mc^2)^{-2}$, the S operators are given by

$$S_1 = \frac{\beta T}{2ic^2} \tag{7.45}$$

$$S_2 = \frac{\hbar \dot{T}}{(2i)^2} \tag{7.46}$$

$$S_3 = \frac{\beta}{(2i)^3}\left(\frac{4}{3}T^3 + \hbar^2 \ddot{T}\right). \tag{7.47}$$

so that substituting Eq. (7.45)-Eq. (7.47) into Eq. (7.50)-(7.53) will give the Foldy-Wouthuysen Hamiltonian in terms of the odd and even operators T and V from the original Hamiltonian. Substituting the Beginning with η_1, we have

$$\begin{aligned} \eta_1 &= -2\beta\left(\frac{\beta T}{2i}\right)^2 + \frac{i}{2i}[\beta T, T] \\ &= \frac{\beta T^2}{2}, \end{aligned} \tag{C.20}$$

since β anti-commutes with the odd operator T. η_2 becomes

$$\begin{aligned} \eta_2 &= \frac{2\hbar\beta}{(2i)^3}\{\beta T, \dot{T}\} - \frac{i\hbar}{2(2i)^2}[\beta T, \beta \dot{T}] - \frac{i\hbar}{(2i)^2}[\dot{T}, T] \\ &= -\frac{i\hbar}{8}[T, \dot{T}]; \end{aligned} \tag{C.21}$$

and finally,

$$\begin{aligned} \eta_3 = &-\frac{2\beta}{m^3(2i)^4}\left\{\beta T, \frac{4}{3}\beta T^3 + \hbar\beta\ddot{T}\right\} - \frac{2\hbar^2\beta}{m^3(2i)^4}\dot{T} + \frac{2}{3}\frac{\beta}{m^3(2i)^4}(\beta T)^4 \\ &+ \frac{i}{m^3(2i)}\left[\frac{4}{3}\beta T^3 + \hbar^2\beta\ddot{T}, T\right] - \frac{i}{6m^3(2i)^3}[\beta T, [\beta T, [\beta T, T]]] \\ &+ \frac{i\hbar^2}{2m^3(2i)^3}[\beta T, \ddot{T}] + \frac{i\hbar^2}{2m^3(2i)^3}[\dot{T}, \beta\dot{T}] \\ = &-\frac{1}{8}\beta T^4 - \frac{\hbar^2}{16}\beta\{T, \ddot{T}\}. \end{aligned}$$

where we have made use of the fact that even powers of T are even operators, and that β commutes with even operators. The final form of the Foldy-Wouthuysen Hamiltonian is then

$$H' = mc^2\beta + V + \frac{\beta T^2}{2mc^2} - \frac{i\hbar}{8m^2c^4}[T, \dot{T}] - \frac{1}{8m^3c^6}\beta T^4 - \frac{\hbar^2}{16m^3c^6}\{T, \ddot{T}\} \tag{C.22}$$

C.4 Powers, time derivatives, commutators and anti-commutators

Here, explicit expressions for the operators T^2, T^4, $[T, \dot{T}]$ and $\{T, \ddot{T}\}$ are found by substituting for T from the original Hamiltonian, Eq. (7.20). We have

$$T = \boldsymbol{\alpha}\cdot(\mathbf{p} - e\mathbf{A}), \qquad V = e\Phi; \tag{7.32}$$

and it will also be necessary to make use of the relationships [123, 124]

$$(\boldsymbol{\alpha}\cdot\mathbf{C})(\boldsymbol{\alpha}\cdot\mathbf{D}) = \mathbf{C}\cdot\mathbf{D} + \frac{2i}{\hbar}\boldsymbol{\Sigma}\cdot\mathbf{C}\times\mathbf{D}; \tag{C.23}$$

$$\boldsymbol{\Sigma} = \frac{\hbar}{4i}\boldsymbol{\alpha}\times\boldsymbol{\alpha} = \frac{\hbar}{2}\begin{pmatrix}\boldsymbol{\sigma} & 0\\ 0 & \boldsymbol{\sigma}\end{pmatrix}; \tag{C.24}$$

$$\mathbf{p}\times\mathbf{C} + \mathbf{C}\times\mathbf{p} = -i\hbar\nabla\times\mathbf{C}. \tag{C.25}$$

C.4.1 Powers

The Foldy-Wouthuysen Hamiltonian of Eq. (7.58) has even powers of T, which are even operators. Squaring the odd operator T gives

$$\begin{aligned} T^2 &= (c\alpha\cdot(\mathbf{p}-e\mathbf{A}))^2 \\ &= c^2(\mathbf{p}-e\mathbf{A}) - iec^2\boldsymbol{\Sigma}\cdot(\mathbf{p}\times\mathbf{A}+\mathbf{A}\times\mathbf{p}) \\ &= c^2(\mathbf{p}-e\mathbf{A}) - iec^2\boldsymbol{\Sigma}\cdot\mathbf{B}. \end{aligned} \tag{C.26}$$

Squaring this to obtain T^4 gives

$$\begin{aligned} T^4 &= \left(c^2(\mathbf{p}-e\mathbf{A}) - iec^2\boldsymbol{\Sigma}\cdot\mathbf{B}\right)^2 \\ &= c^4(\mathbf{p}-e\mathbf{A})^4 + e\hbar^2c^4(\boldsymbol{\Sigma}\cdot\mathbf{B})^2 - e\hbar c^4\left\{(\mathbf{p}-e\mathbf{A})^2, \boldsymbol{\Sigma}\cdot\mathbf{B}\right\}. \end{aligned} \tag{C.27}$$

C.4.2 Time Derivatives

The first and second order time derivative of T are required in the transformed Hamiltonian. Using the definition Eq. (7.33) we have

$$\begin{aligned} \dot{T} &= \frac{i}{\hbar}[V,T] - \partial_t T \\ &= \frac{i}{\hbar}[e\Phi, c\boldsymbol{\alpha}\cdot(\mathbf{p}-e\mathbf{A})] + \partial_t(c\boldsymbol{\alpha}\cdot(\mathbf{p}-e\mathbf{A})) \\ &= ec\boldsymbol{\alpha}\cdot(\Phi\nabla - \nabla\Phi) - ec\boldsymbol{\alpha}\dot{\mathbf{A}} \\ &= ec\boldsymbol{\alpha}\cdot\mathbf{E} \end{aligned} \tag{C.28}$$

Using Eq. (7.33) a second time to obtain the second order time derivative gives

$$\begin{aligned} \ddot{T} &= \frac{i}{\hbar}[V,\dot{T}] + \partial_t\dot{T} \\ &= \frac{i}{\hbar}[e\Phi, ec\boldsymbol{\alpha}\cdot\mathbf{E}] - \partial_t(ec\boldsymbol{\alpha}\cdot\mathbf{E}) \\ &= ec\boldsymbol{\alpha}\cdot\dot{\mathbf{E}} \end{aligned} \tag{C.29}$$

C.4.3 Commutator and Anti-Commutator

The product of T and $\dot{T}$ is an even operator. Evaluating the commutator between the two gives

$$[T,\dot{T}] = [c\boldsymbol{\alpha}\cdot(\mathbf{p}-e\mathbf{A}), ec\boldsymbol{\alpha}\cdot\mathbf{E}]$$

$$
\begin{aligned}
&= ec^2(\mathbf{p}\cdot\mathbf{E} - \mathbf{E}\cdot p) + iec^2\boldsymbol{\Sigma}\cdot(\mathbf{p}\times\mathbf{E} - \mathbf{E}\times\mathbf{p}) - e^2c^2(\mathbf{A}\cdot\mathbf{E} - \mathbf{E}\cdot A) \\
&\quad - ie^2c^2\boldsymbol{\Sigma}\cdot(\mathbf{A}\times\mathbf{E} - \mathbf{E}\times\mathbf{A}) \\
&= ec^2[(\mathbf{p} - e\mathbf{A}), \mathbf{E}] + iec^2\boldsymbol{\Sigma}\cdot((\mathbf{p} - e\mathbf{A})\times\mathbf{E} - \mathbf{E}\times(\mathbf{p} - e\mathbf{A}))\,. \qquad \text{(C.30)}
\end{aligned}
$$

Similarly, the anti-commutator between T and $\ddot{T}$ gives the even operator

$$
\begin{aligned}
\{T, \ddot{T}\} &= \left\{c\alpha\cdot(\mathbf{p} - e\mathbf{A}), ec\boldsymbol{\alpha}\cdot\dot{\mathbf{E}}\right\} \\
&= ec\boldsymbol{\alpha}\cdot(\mathbf{p} - e\mathbf{A})(\boldsymbol{\alpha}\cdot\dot{\mathbf{E}}) + ec(\boldsymbol{\alpha}\cdot\dot{\mathbf{E}})\alpha\cdot(\mathbf{p} - e\mathbf{A}) \\
&= ec\{\mathbf{p} - e\mathbf{A}, \dot{\mathbf{E}}\} + iec\boldsymbol{\Sigma}\cdot\Big((\mathbf{p} - e\mathbf{A})\times\dot{\mathbf{E}} + \dot{\mathbf{E}}\times(\mathbf{p} - e\mathbf{A})\Big) \qquad \text{(C.31)}
\end{aligned}
$$

D

Conferences

In 2013 I attended two conferences specifically relating to the orbital angular momentum of light and electrons, namely the *Spin Orbit Interaction for Light and Matter Waves* workshop at the Max-Planck-Institut für Physik Komplexer Systeme, Dresden, Germany and the *Second International Conference on Optical Angular Momentum* conference held at The Burrell Collection, Glasgow, Scotland. I found these conferences particularly inspiring, and I greatly appreciated the passionate and varied discussions I was a part of at these meetings. It was also inspiring to meet with the distinguished authors of seminal articles in the field with which I was already familiar, and to discover new works and appreciate the richness of the field. The knowledge gained in attending these conferences has directly contributed to this thesis. Reproduced below are the conference photographs from both meetings. As can be seen, the sun shone on both these events.

Figure D.0.1: Conference photo of the *Spin Orbit Interaction for Light and Matter Waves* workshop at the Max-Planck-Institut für Physik Komplexer Systeme, Dresden, Germany, 15th-19th April 2013.

Figure D.0.2: *Conference photo of the Second International Conference on Optical Angular Momentum* conference held at The Burrell Collection, Glasgow, Scotland, 3rd-5th June 2013.

List of Abbreviations and Symbols

Abbreviations

BFP	Back Focal Plane
EELS	Electron energy loss spectroscopy
EMCD	Energy loss magnetic circular dichroism
FFP	Front focal plane
FIB	Focused ion beam
FWHM	Full width at half maximum
STEM	Scanning transmission electron microscopy
TEM	Transmission electron microscopy
XMCD	X-ray magnetic circular dichroism

Mathematical Symbols

α	Index
α	Maximum angle of entrance
α	General variable
α	Dirac α matrix
$\alpha(x)$	Gauge transformation parameter
α_c	Convergence angle
α_o	Objective aperture angle
$\alpha_{l,n}$	nth zero of Bessel function $J_l(x)$
β	Index
β	General variable
β	Angle between intial and final wavevectors
β	Dirac β matrix
γ	Index
γ^μ	Dirac γ matices
Γ	Integrated vortex circulation strength
Γ	Transition rate
$\Gamma(x)$	Gamma function
δ_l	Spin-orbit interaction energy shift
$\delta_{l,l'}$	Kronecker delta
$\delta(x)$	Dirac delta distribution
Δ	Normalised orbital angular momentum dichroism signal
Δ_A	See p.82
Δ_ϕ	See p.82
$\Delta\theta$	Phase shift of beam in magnetic field
$\Delta\phi$	Observable beam rotation in magnetic field
ΔE	Energy spread of beam
Δf	Axial displacement between two focal points
Δl	Change in orbital angular momentum
ΔR	FWHM of vortex node
η	Foldy-Wouthuysen transformation

	expansion coefficient
$\xi_z^{(n)}$	See p.160
$\hat{\boldsymbol{\varepsilon}}$	Unit wave polarisation vector
ε_0	Vacuum permittivity
ε^{ijk}	Levi-Civita tensor
$\Theta(x)$	Heaviside step function
Θ'_q	See p.167
Θ_q^{dip}	See p.168
Θ_q^{ZO}	See p.168
$\Theta_{q,v',y}^{p,p'}$	See p.168
Θ_R	See p.168
$\Theta_{R,v,y}$	See p.167
$\Theta_R^{l,l',p,p'}$	See p.167
$\Theta_R^{l,l',p}$	See p.168
$\Theta_R^{l,l',p,\pm}$	See p.168
$\boldsymbol{\kappa}_{1,2}$	See p.152
λ	Wavelength
Λ	Helicity operator
μ	Reduced mass
μ	index
μ_0	Vacuum permeability
ν	Index
ξ	Spin orbit interaction parameter (see p.141)
$\xi_q^{(n)}, \xi_R^{(n)}, \xi_v^{(n)}$	See p.160
$\boldsymbol{\Pi}_\gamma(\mathbf{r})$	Generalised field momentum
$\hat{\boldsymbol{\rho}}$	Unit vector in ρ direction
$\hat{\rho}_f$	Density of available final states
$\rho_{l,n}$	Radius of nth Bessel zero for $J_l(k_\perp \rho)$
$\tilde{\rho}_{\text{A}}(\mathbf{r})$	Charge density of atom
$\tilde{\rho}_l(\mathbf{r})$	Charge density of Bessel beam
$\tilde{\rho}_l^\circ(\mathbf{r})$	Charge density of apertured Bessel beam
σ	Photon spin ($\sigma = \pm 1$)
$\boldsymbol{\sigma}$	Vector of Pauli spin matrices
$\boldsymbol{\Sigma}$	Spin operator
Σ_A	See p.82
$\tau^{(n,n')}$	See p.160
ϕ	Scalar potential
$\hat{\boldsymbol{\phi}}$	Unit vector in ϕ direction
ϕ_l	l-dependent rotation in magnetic field
ϕ_s	Separation angle of hologram
	reconstructed beams
Φ	Bessel function expansion angle
Φ'	Bessel function expansion angle
$\Phi(\mathbf{r})$	Coulomb potential for electron vortex
χ_s	Spin spinor
χ_S	Phase shift due to spherical aberrations
ψ	General wavefield
$\bar{\psi}$	Adjoint Dirac spinor
ψ_{atom}	Atomic wavefunction product state
$\psi_{f,i}(\mathbf{r})$	Initial (i) or final (f) wavefunction
$\psi_l(\mathbf{r})$	Vortex wavefunction
$\psi_l(\mathbf{r}_v)$	Vortex wavefunction
$\psi_q(\mathbf{q})$	Atomic electron wavefunction
$\psi_R(\mathbf{R})$	Atomic centre of mass wavefunction
ψ_l°	Apertured Bessel-type wavefunction
ψ_l^{B}	Bessel-type wavefunction
ψ_p	Plane wave wavefunction
Ψ	Non-relativistic spinor vortex solution
Ψ	Bessel function expansion angle
Ψ'	Bessel function expansion angle
Ψ_l	Relativistic Bessel electron wavefunction
ω	(Angular) mode frequency
ω_L	Larmor frequency
ω_c	Cyclotron frequency ($2\omega_L$)
Ω	Nanoparticle rotation frequency
Ω_n	See p.135
∇_T	Transverse Laplacian
$\mathbb{1}_n$	$n \times n$ identity matrix
a	Index
a	General variable
a_0	Bohr radius
A	Linear operator
A, A'	See p.155
A_μ	Gauge field 4-vector
$\mathbf{A}(\mathbf{r})$	Vector potential
$\mathcal{A}_q^\pm, \mathcal{A}_q^0$	See p.150
$\mathcal{A}_l^{\pm 1}$	See p.108
$\mathcal{A}_l^{\text{F, R}}$	Matrix element factors for forward (F) and reverse (R) transitions
$\mathcal{A}_{l,\Sigma p,l'}^{\pm 1}$	See p.109
$\mathcal{A}_{l,l',p}^{\pm 1}$	See p.109
$\mathcal{A}_R$	See p.151

b Index

b General variable

B Linear operator

B, B' See p.155

$\mathbf{B}(\mathbf{r})$ Magnetic field

B_ϕ Azimuthal component of magnetic field

B_z Axial component of magnetic field

$\mathcal{B}_l^{\pm 1,0}$ See p.158

c Speed of light in vaccuum

c Index

c General variable

C Path of integration

C, C' See p.155

C_θ Elliptical polarisation conversion coefficient

C_C Coefficient of chromatic aberration

C_S Coefficient of spherical aberration

CD Chiral dicroism signal

$\mathcal{C}_l^{\pm 1,0}$ See p.95

d Resolution of scanning probe

d Grating separation

$\mathbf{d}$ Atomic electron dipole moment $e\mathbf{q}$

$d\mathbf{s}$ Path element

$d\mathbf{S}$ Surface element

dV Volume element

∂_x Partial derivative with respect to x

∂_μ 4-vector derivative

$\mathcal{D}$ Electric dipole matrix element (see p.94)

$\mathcal{D}_\mu$ Covariant derivative

e Electron charge

E Average beam energy

$\mathbf{E}(\mathbf{r})$ Electric field vector

$\mathbf{E}^{\text{NP}}$ Non-paraxial vortex electric field vector

E_0 Electron rest energy

E_0 Optical electric field amplitude

E_ρ Radial component of electric field

$\mathcal{E}$ Energy of a free electron

$\mathcal{E}_{i,f}$ Atomic electron energy; initial (i), final (f)

f Lens focal length

$\mathbf{F}$ General vector function

$F^{\mu\nu}$ Electromagnetic field tensor

$F_R^{l,l',p,p'}$ See p.100

${}_pF_q[\{a_1 \dots a_p\}; \{b_1 \dots b_q\}; z]$ Generalised hypergeometric function

$\mathcal{F}$ See p.158

$\mathcal{F}'$ See p.162

$g^{\mu\nu}$ Metric tensor

$\mathcal{G}$ See p.158

$\mathcal{G}'$ See p.162

h Height

$\hbar$ Reduced Planck's constant

H' Transformed Foldy-Wouthyusen Hamiltonian

$H_0^{(q)}$ Unperturbed atomic electron Hamiltonian

$H_0^{(R)}$ Unperturbed centre of mass Hamiltonian

$H_{\text{int}}^{\text{B}}$ Electron vortex-atom interaction Hamiltonian, atomic nucleus states

$H_{\text{int}}^{\text{CM}}$ Electron vortex-atom interaction Hamiltonian, centre of mass states

H^{EV} Full Hamiltonian for electron vortex-atom system

$H_{\text{int}}^{\text{dip, quad, hex}}$ Dipole, quadrupole, hexapole electron vortex-atom interaction Hamiltonians

H_{SO} Spin-orbit interaction Hamiltonian

H_0^{OV} Unperturbed optical vortex Hamiltonian

$H_{\text{int}}^{\text{OV}}$ Hamiltonian for optical vortex-atom interaction

$H_{\text{int}}^{\text{OV}(q)}$ Hamiltonian for optical vortex-atom interaction, affecting atomic electron

$H_{\text{dip}}^{\text{OV}(q)}$ Dipole interaction Hamiltonian affecting atomic electron

$H_{\text{quad}}^{\text{OV}(q)}$ Quadrupole interaction Hamiltonian affecting atomic electron

$H_{\text{int}}^{\text{OV}(R)}$ Hamiltonian for optical vortex-atom interaction, affecting centre of mass

I Moment of inertia

$I(\mathbf{r})$ Interference pattern

$I_{\sigma=\pm 1}$ Transmitted intensity

$I_q^{p,p'}$ See p.100

I_z Axial current

$\mathcal{I}$ See p.158

$\mathcal{I}_l$ Dimensionless Bessel moment (see p.52)

$\mathcal{I}_v$ See p.158

$\mathbf{j}(\mathbf{r})$ Normalised probability current density

$\mathbf{J}$ Total angular momentum vector

J Total angular momentum quantum number

$\mathbf{J}(\mathbf{r})$ Probability current density

$J_l(x)$ Bessel function of the first kind, of order l

$\tilde{\mathbf{J}}(\mathbf{r})$ Charge current density of Bessel beam

$\tilde{\mathbf{J}}^\circ(\mathbf{r})$ Charge current density of apertured Bessel beam

$\mathcal{J}$ See p.158

$\mathcal{J}_z$ See p.158

k Wavenumber

k Index

$\mathbf{k}(k_\rho, k_\phi, k_z)$ Wavevector

$\mathbf{k}(k_x, k_y, k_z)$ Wavevector

k_z Axial wavevector

$\mathbf{k}_\perp$ Transverse wavevector

$k_\perp$ Transverse wavenumber

K Maximum index

$\mathbf{K}(K_\rho, K_\phi, K_z)$ Centre of mass wavevector

$K_q^{p,p',u}$ See p.103

$K_\perp$ Centre of mass transverse wavevector

l, l' Orbital angular momentum quantum number

ℓ, ℓ' Atomic electron orbital angular momentum quantum number

L Length of finite Bessel beam

L Axial length of cylindrical surface

L Centre of mass orbital angular momentum quantum number

L Angular momentum transfer per electron

L Total orbital angular momentum quantum number

$\mathbf{L}$ Total angular momentum vector

$\mathbf{L}$ Angular momentum operator

L^{CM} Full Lagrangian for electron vortex-atom system with centre of mass states

L^{EV} Full Lagrangian for electron vortex-atom system

L^{OV} Full Lagrangian for optical vortex-atom system

L_0^{atom} Unpertubed atomic Lagrangian

L_0^{OV} Unpertubed optical vortex Lagrangian

$L_{\text{int}}^{\text{OV}}$ Interaction Lagrangian for optical vortex-atom system

L_{TR} Rate of angular momentum transfer

$\mathbf{L}_{\text{EV}}$ Total angular momentum of electron vortex

$\mathbf{L}_{\text{OV}}$ Total angular momentum of optical vortex

$\mathcal{L}$ Lagrangian density

$\boldsymbol{\mathcal{L}}$ Angular momentum density

$\boldsymbol{\mathcal{L}}_{\text{EV}}$ Angular momentum density of electron vortex

$\boldsymbol{\mathcal{L}}_{\text{OV}}$ Angular momentum density of optical vortex

$\langle \mathcal{L}_z \rangle$ Angular momentum expectation value in the presence of fields

m Mass (usually electron)

m Atomic electron magnetic quantum number

m_e Electron mass

m_p Proton mass

m_J Total angular momentum magnetic quantum number

$\mathcal{M}_{fi}$ Matrix element

$\mathcal{M}_{\text{OV}}^{\text{quad}}$ Quadrupole matrix element for optical vortex-atom interaction

$\mathcal{M}_{\text{dip}}^{l,l'}$ Matrix element for dipole interaction

$\mathcal{M}_{\text{ZO}}^{\text{on-axis}}$ Matrix element for on-axis dipole interaction

$\mathcal{M}_{\text{ZO}}^{l,l'}$ Matrix element for zero order interaction

n index, integer

n Atomic electron principal quantum number

n_1, n_2 Refractive index

$n_{\text{OV}}^{i,f}$ Photon occupation; initial (i), final (f)

$N_l, N_l^i, N_{l'}^f$ Normalisation factor for vortex electron

$N_{n,\ell,m}$ Normalisation factor for atomic electron

$\mathcal{N}$ See p.158

$\mathcal{O}$ Effective operator after expansion

$\mathcal{O}'$ Effective operator second expansion

$\mathcal{O}'_{\text{dip}}$ Dipole effective operator

$\mathcal{O}'_{\text{quad}}$ Quadrupole effective operator

$\mathcal{O}'_{\text{ZO}}$ Zero-order effective operator

p Radial index for Laguerre-Gaussian beam

p, p' Index

p General variable

$\mathbf{p}_\alpha$ Generalised coordinate momentum

$\mathbf{p}_p$ Atomic proton momentum

$\mathbf{p}_q$ Atomic electron momentum

$\mathbf{p}_v$ electron vortex momentum

$\langle P_\perp \rangle$ Expectation value of transverse momentum

$P_\ell^m(\cos\theta)$ Generalised Laguerre polynomial

$\boldsymbol{\mathcal{P}}$ Linear momentum density

$\boldsymbol{\mathcal{P}}_{\text{EV}}$ Linear momentum density of electron vortex

$\boldsymbol{\mathcal{P}}_{\text{OV}}$ Linear momentum density of optical vortex

q q-plate charge

$\mathbf{q}(\rho_q, \phi_q, \theta_q)$ Position vector of atomic electron (relative to atomic nucleus)

$q_\perp$ In-plane atomic electron radius, $\rho_q \sin\theta_q$

$\mathbf{Q}(\beta)$ Total wavevector transfer

$Q_n(\mathbf{q})$ Radial state of atomic electron

$\mathbf{r}(\rho, \phi, z)$ Position vector

$\mathbf{r}(x, y, z)$ Position vector

$\mathbf{r}_e(\rho_e, \phi_e, z_e)$ Position vector of atomic electron (relative to beam origin)

$\mathbf{r}_p(\rho_p, \phi_p, z_p)$ Position vector of atomic proton

$\mathbf{r}'_s(\rho'_s, \phi'_s, z'_s)$ Electron vortex position relative to atomic electron

$\mathbf{r}_R(\rho_R, \phi_R, z_R)$ Position vector of centre of mass

$\mathbf{r}_v(\rho_v, \phi_v, z_v)$ Position vector of vortex electron

$\mathbf{r}'_v(\rho'_v, \phi'_v, z'_v)$ Electron vortex position relative to atomic nucleus

$\mathbf{r}_\perp$ Transverse position vector

r_c^A Confusion radius for axial astigmatism

r_c^C Confusion radius for chromatic aberrations

r_c^S Confusion radius for spherical aberrations

R Nanoparticle radius

R_c Radius of peak intensity of vortex beam

R_{max} Maximum radius of holographic aperture

$R(\rho_R)$ Radial state of centre of mass wavefunction

$\mathcal{R}$ See p.158

$\mathcal{R}_R$ See p.158

$\mathcal{R}_z$ See p.158

S Total spin quantum number

S Foldy-Wouthuysen transformation operator

$\mathbf{S}$ Spin angular momentum vector

$S^{\mu\nu}$ Lorentz transformation

$\mathcal{S}$ Poynting vector

t Time

T Odd operator

u, u' Index

$u_{s,s+2}$ Dirac spinor solutions

$u_{s,s+2}^{\text{NR}}$ Non-relativistic spinor solutions

$u(\rho), u(\rho, z)$ Spatial mode function

u^{B} Spatial mode function of Bessel beam

u^{LG} Spatial mode function of Laguerre-Gaussian beam

$\mathcal{U}_l^{0,\pm1}$ General matrix element factors

$\mathbf{v}$ Velocity

V Volume

V Even operator

$V_\beta(\mathbf{r}_\alpha)$ Coulomb potential

w_0 Minimum Gaussian beam waist

w_B Characteristic Gaussian beam waist in a magnetic field

$w(z)$ Gaussian Beam waist

$\hat{\mathbf{x}}$ Unit vector in x direction

y Angle difference between vortex and centre of mass

y' Angle difference between vortex and atomic electron

$\hat{\mathbf{y}}$ Unit vector in y direction

$Y_l(x)$ Bessel function of the second kind, of order l

$Y_l^m(\theta, \phi)$ Spherical harmonic function

$\mathcal{Y}_\alpha^{(\beta)}$ See p.158

z_R Rayleigh range

Z Atomic number

$Z_l(x)$ General Bessel function

References

[1] L. Allen, M. Beijersbergen, R. Spreeuw, and J. Woerdman. Orbital angular momentum of light and the transformation of Laguerre-Gaussian laser modes. *Physical Review A*, **45**(11):8185–8189, (1992).

[2] P. Coullet, L. Gil, and F. Rocca. Optical vortices. *Optics Communications*, **73**(5):403–408, (1989).

[3] L. Allen, S. M. Barnett, and M. J. Padgett. *Optical Angular Momentum*. Institute of Physics Pub., Bristol, 2003.

[4] D. L. Andrews. *Structured Light and its Applications: An Introduction to Phase-Structured Beams and Nanoscale Optical Forces*. Academic Press, Burlington, 2008.

[5] H. He, M. E. Friese, N. R. Heckenberg, and H. Rubinsztein-Dunlop. Direct observation of transfer of orbital angular momentum to absorbing particles from a laser beam with a phase singularity. *Physical Review Letters*, **75**(5):826–829, (1995).

[6] K. Dholakia, M. Macdonald, and G. Spalding. Optical tweezers : the next generation. *Physics World*, **15**:31–35, (2002).

[7] D. G. Grier. A revolution in optical manipulation. *Nature*, **424**:810–816, (2003).

[8] K. Ladavac and D. G. Grier. Microoptomechanical pumps assembled and driven by holographic optical vortex arrays. *Optics Express*, **12**(6):1144–1149, (2004).

[9] P. Galajda and P. Ormos. Complex micromachines produced and driven by light. *Applied Physics Letters*, **78**(2):249–251, (2001).

[10] A. M. Yao and M. J. Padgett. Orbital angular momentum: origins, behavior and applications. *Advances in Optics and Photonics*, **3**:161–204, (2011).

[11] S. Fürhapter, A. Jesacher, S. Bernet, and M. Ritsch-Marte. Spiral phase contrast imaging in microscopy. *Optics Express*, **13**(3):689–694, (2005).

[12] M. Baránek and Z. Bouchal. Rotating vortex imaging implemented by a quantized spiral phase modulation. *Journal of the European Optical Society Rapid Publications*, **8**:13017, (2013).

[13] G. Molina-Terriza, J. P. Torres, and L. Torner. Twisted photons. *Nature Physics*, **3**(5):305–310, (2007).

[14] S. J. Van Enk and G. Nienhuis. Commutation rules and eigenvalues of spin and orbital angular momentum of radiation fields. *Journal of Modern Optics*, **41**(5):963–977, (1994).

[15] S. M. Barnett and L. Allen. Orbital angular momentum and nonparaxial light beams. *Optics Communications*, **110**:670–678, (1994).

[16] A. O'Neil, I. MacVicar, L. Allen, and M. J. Padgett. Intrinsic and extrinsic nature of the orbital angular momentum of a light beam. *Physical Review Letters*, **88**(5):053601, (2002).

[17] A. Mair, A. Vaziri, G. Weihs, and A. Zeilinger. Entanglement of the orbital angular momentum states of photons. *Nature*, **412**(6844):313–316, (2001).

[18] A. Z. Khoury and P. Milman. Quantum teleportation in the spin-orbit variables of photon pairs. *Physical Review A*, **83**(6):060301, (2011).

[19] I. Bialynicki-Birula, Z. Bialynicka-Birula, and C. Śliwa. Motion of vortex lines in quantum mechanics. *Physical Review A*, **61**(3):032110, (2000).

[20] I. Bialynicki-Birula and Z. Bialynicka-Birula. Motion of vortex lines in nonlinear wave mechanics. *Physical Review A*, **65**(1):014101, (2001).

[21] I. Bialynicki-Birula, T. Mloduchowski, T. Radozycki, and C. Śliwa. Vortex lines in motion. *Acta Physica Polonica A*, **100**(29 Supplement):1–10, (2001).

[22] K. Y. Bliokh, Y. Bliokh, S. Savel'ev, and F. Nori. Semiclassical dynamics of electron wave packet states with phase vortices. *Physical Review Letters*, **99**(19):190404, (2007).

[23] M. Uchida and A. Tonomura. Generation of electron beams carrying orbital angular momentum. *Nature*, **464**(7289):737–9, (2010).

[24] J. Verbeeck, H. Tian, and P. Schattschneider. Production and application of electron vortex beams. *Nature*, **467**(7313):301–304, (2010).

[25] B. J. McMorran, A. Agrawal, I. M. Anderson, A. A. Herzing, H. J. Lezec, J. J. McClelland, and J. Unguris. Electron vortex beams with high quanta of orbital angular momentum. *Science*, **331**:192–195, (2011).

[26] A. Jesacher, S. Fürhapter, S. Bernet, and M. Ritsch-Marte. Shadow Effects in Spiral Phase Contrast Microscopy. *Physical Review Letters*, **94**(23):233902, (2005).

[27] J. Verbeeck, H. Tian, and G. Van Tendeloo. How to manipulate nanoparticles with an electron beam? *Advanced Materials*, **2012**:1–4, (2012).

[28] T. Gnanavel, J. Yuan, and M. Babiker. Observation of gold nanoparticles movements under sub-10 nm vortex electron beams in an aberration corrected TEM. In D. J. Stokes and J.L. Hutchison, editors, *Proccedings of the European Microscopy Congress*, number ii. Royal Microscopical Society, Oxford, (2012).

[29] J. F. Nye and M. V. Berry. Dislocations in wave trains. *Proceedings of the Royal Society A*, **336**(1605):165–190, (1974).

[30] M. V. Berry and M. R Dennis. Knotted and linked phase singularities. *Proceedings of the Royal Society A*, **457**:2251–2263, (2001).

[31] M. V. Berry and M. R. Dennis. Knotting and unknotting of phase singularities: Helmholtz waves, paraxial waves and waves in 2+1 spacetime. *Journal of Physics A: Mathematical and General*, **34**(42):8877–8888, (2001).

[32] K. Bliokh, M. Dennis, and F. Nori. Relativistic electron vortex beams: Angular momentum and spin-orbit interaction. *Physical Review Letters*, **107**(17):174802, (2011).

[33] V. Bagrov and D. Gitman. Non-Volkov solutions for a charge in a plane wave. *Annalen der Physik*, **14**(8):467–478, August (2005).

[34] C. C. Leary, D. Reeb, and M. G. Raymer. Self-spin-controlled rotation of spatial states of a Dirac electron in a cylindrical potential via spin–orbit interaction. *New Journal of Physics*, **10**(10):103022, (2008).

[35] D. V. Karlovets. Electron with orbital angular momentum in a strong laser wave. *Physical Review A*, **86**(6):062102, (2012).

[36] R. Van Boxem, J. Verbeeck, and B. Partoens. Spin effects in electron vortex states. *Europhysics Letters*, **102**(4):40010, (2013).

[37] R.F. Egerton. *Physical Principles of Electron Microscopy: An Introduction to TEM, SEM, and AEM*. Springer, Edmonton, 2005.

[38] L. Reimer. *Transmission Electron Microscopy: Physics of Image Formation and Microanalysis*. Springer, Berlin, (1997).

[39] J. Verbeeck, P. Schattschneider, S. Lazar, M. Stöger-Pollach, S. Löffler, A. Steiger-Thirsfeld, and G. Van Tendeloo. Atomic scale electron vortices for nanoresearch. *Applied Physics Letters*, **99**(20):203109, (2011).

[40] P. Schattschneider, M. Stöger-Pollach, S. Löffler, A. Steiger-Thirsfeld, J. Hell, and Jo Verbeeck. Sub-nanometer free electrons with topological charge. *Ultramicroscopy*, **115**:21–25, (2012).

[41] M. W. Beijersbergen, R. P. C. Coerwinkel, and M. Kristensen. Helical-wavefront laser beams produced with a spiral phaseplate. *Optics Communications*, **112**:321–327, (1994).

[42] G. Turnbull, D.A. Robertson, G.M. Smith, L. Allen, and M. J. Padgett. The generation of free-space Laguerre-Gaussian modes at millimetre-wave frequencies by use of a spiral phaseplate. *Optics Communications*, **127**(4-6):183–188, (1996).

[43] K. Sueda, G. Miyaji, N. Miyanaga, and M. Nakatsuka. Laguerre-Gaussian beam generated with a multilevel spiral phase plate for high intensity laser pulses. *Optics Express*, **12**(15):3548, (2004).

[44] B. E. A. Saleh and M. C. Teich. *Fundamentals of Photonics*. Wiley Interscience, New York, (1991).

[45] W.-H. Lee. Binary computer generated holograms. *Applied Optics*, **18**:3661, (1979).

[46] N. R. Heckenberg, R. McDuff, C. P. Smith, H. Rubinsztein-Dunlop, and M. J. Wegener. Laser beams with phase singularities. *Optical and Quantum Electronics*, **24**(9):951–962, (1992).

[47] N. R. Heckenberg, R McDuff, C P Smith, and a G White. Generation of optical phase singularities by computer-generated holograms. *Optics Letters*, **17**(3):221, (1992).

[48] L. Clark, S. M. Lloyd, M. Babiker, and J. Yuan. Electron beams with a twist. *Journal of Physics: Conference Series*, **371**:012005, (2012).

[49] P. E. Batson, N. Dellby, and O. L. Krivanek. Sub-ångstrom resolution using aberration corrected electron optics. *Nature*, **418**(6898):617–20, (2002).

[50] J. Verbeeck, P. Schattschneider, S. Lazar, M. Stöger-Pollach, and S. Löffler. Atomic scale electron vortices for nanoresearch (supplementary material). *Applied Physics Letters*, **99**:1–6, (2011).

[51] J. Verbeeck, H. Tian, and A. Béché. A new way of producing electron vortex probes for STEM. *Ultramicroscopy*, **113**:83–87, February (2012).

[52] P. Schattschneider, M. Stöger-Pollach, and J. Verbeeck. Novel vortex generator and mode converter for electron beams. *Physical Review Letters*, **109**(8):084801, (2012).

[53] M. W. Beijersbergen and L. Allen. Astigmatic laser mode converters and transfer of orbital angular momentum. *Optics Communications*, **96**:123–132, (1993).

[54] L. Marrucci, C. Manzo, and D. Paparo. Optical spin-to-orbital angular momentum conversion in inhomogeneous anisotropic media. *Physical Review Letters*, 96(16):163905, April 2006.

[55] L. Marrucci, E. Karimi, S. Slussarenko, B. Piccirillo, E. Santamato, E. Nagali, and F. Sciarrino. Spin-to-orbital optical angular momentum conversion in liquid crystal "q-plates": Classical and quantum applications. *Molecular Crystals and Liquid Crystals*, **561**:48–56, (2012).

[56] E. Karimi, L. Marrucci, V. Grillo, and E. Santamato. Spin-to-Orbital Angular Momentum Conversion and Spin-Polarization Filtering in Electron Beams. *Physical Review Letters*, **108**(4):044801, (2012).

[57] V. Grillo, L. Marrucci, E. Karimi, and R. Zanella. Quantum simulation of a spin polarization device in an electron microscope. *Arxiv preprint arXiv:1301.3938*.

[58] T. Kohashi, M. Konoto, and K. Koike. High-resolution spin-polarized scanning electron microscopy (spin SEM). *Journal of Electron Microscopy*, **59**(1):43–52, (2010).

[59] M. V. Berry. Waves and Thom's theorem. *Advances in Physics*, **25**:1–26, (1976).

[60] T. C. Petersen, M. Weyland, D. M. Paganin, T. P. Simula, S. A. Eastwood, and M. J. Morgan. Electron vortex production and control using aberration induced diffraction catastrophes. *Physical Review Letters*, **110**(3):033901, (2013).

[61] M. R. Dennis, R. P. King, B. Jack, K. O'Holleran, and M. J. Padgett. Isolated optical vortex knots. *Nature Physics*, **6**(2):118–121, (2010).

[62] P. Schattschneider and J. Verbeeck. Theory of free electron vortices. *Ultramicroscopy*, **111**:1461–1468, (2011).

[63] R.D. Cowan. *The Theory of Atomic Structure and Spectra*. University of California Press, Berkeley, (1981).

[64] C. T. Chen, Y. U. Idzerda, H. J. Lin, N. V. Smith, G. Meigs, E. Chaban, G. H. Ho, E. Pellegrin, and F. Sette. Experimental confirmation of the x-ray magnetic circular dichroism sum rules for iron and cobalt. *Physical Review Letters*, **75**(1):152–155, (1995).

[65] S. Lloyd, M. Babiker, and J. Yuan. Quantized orbital angular momentum transfer and magnetic dichroism in the interaction of electron vortices with matter. *Physical Review Letters*, **108**(7):074802, (2012).

[66] S. M. Lloyd, M. Babiker, and J. Yuan. Interaction of electron vortices and optical vortices with matter and processes of orbital angular momentum exchange. *Physical Review A*, **86**(2):023816, (2012).

[67] J. Yuan, S. M. Lloyd, and M. Babiker. Chiral specific electron vortex beam spectroscopy. *Arxiv preprint arXiv:1303.5322v3*, (2013).

[68] M. Babiker, C. Bennett, D. Andrews, and L. Dávila Romero. Orbital angular momentum exchange in the interaction of twisted light with molecules. *Physical Review Letters*, **89**(14):143601, (2002).

[69] D. L. Andrews, L. C. Dávila Romero, and M. Babiker. On optical vortex interactions with chiral matter. *Optics Communications*, **237**:133–139, (2004).

[70] R. Jáuregui. Rotational effects of twisted light on atoms beyond the paraxial approximation. *Physical Review A*, **70**(3):033415, (2004).

[71] A. Alexandrescu, E. Di Fabrizio, and D. Cojoc. Electronic and centre of mass transitions driven by Laguerre–Gaussian beams. *Journal of Optics B: Quantum and Semiclassical Optics*, **7**(4):87–92, (2005).

[72] J. C. Idrobo and S. J. Pennycook. Vortex beams for atomic resolution dichroism. *Journal of Electron Microscopy*, **60**(5):295–300, (2011).

[73] Peter Schattschneider, B. Schaffer, I. Ennen, and J. Verbeeck. Mapping spin-polarized transitions with atomic resolution. *Physical Review B*, **85**(13):134422, (2012).

[74] P. Schattschneider, M. Löffler, S.and Stöger-Pollach, and J. Verbeeck. Is magnetic chiral dichroism feasible with electron vortices? *Arxiv preprint arXiv:1304.7976v3*, pages 1–4, (2013).

[75] Z. Mohammadi, C. P. Van Vlack, S. Hughes, J. Bornemann, and R. Gordon. Vortex electron energy loss spectroscopy for near-field mapping of magnetic plasmons. **20**(14):1351–1353, (2012).

[76] F. García de Abajo and M. Kociak. Probing the photonic local density of states with electron energy loss spectroscopy. *Physical Review Letters*, **100**(10):106804, (2008).

[77] U. Hohenester, H. Ditlbacher, and J. Krenn. Electron-energy-loss spectra of plasmonic nanoparticles. *Physical Review Letters*, **103**(10):106801, (2009).

[78] S. Löffler and P. Schattschneider. Elastic propagation of fast electron vortices through crystals. *Acta Crystallographica Section A*, **68**(4):443–447, (2012).

[79] A. Lubk, L. Clark, G. Guzzinati, and J. Verbeeck. Topological analysis of paraxially scattered electron vortex beams. *Physical Review A*, **87**(3):033834, (2013).

[80] M. V. Berry and M. R. Dennis. Topological events on wave dislocation lines: birth and death of loops, and reconnection. *Journal of Physics A*, **40**(1):65–74, (2007).

[81] M. V. Berry and M. R. Dennis. Reconnections of wave vortex lines. *European Journal of Physics*, **33**(3):723–731, (2012).

[82] G. M. Gallatin and B. J. McMorran. Propagation of vortex electron wave functions in a magnetic field. *Physical Review A*, **86**(1):012701, (2012).

[83] C. Greenshields, R. L. Stamps, and S. Franke-Arnold. Vacuum Faraday effect for electrons. *New Journal of Physics*, **14**(10):103040, (2012).

[84] K. Y. Bliokh, P. Schattschneider, J. Verbeeck, and F. Nori. Electron vortex beams in a magnetic field: A new twist on Landau levels and Aharonov-Bohm states. *Physical Review X*, **2**(4):041011, (2012).

[85] G. Guzzinati, P. Schattschneider, K. Y. Bliokh, F. Nori, and J. Verbeeck. Observation of the Larmor and Gouy rotations with electron vortex beams. *Physical Review Letters*, **110**(9):093601, (2013).

[86] S. M. Lloyd, M. Babiker, J. Yuan, and C. Kerr-Edwards. Electromagnetic vortex fields, spin, and spin-orbit interactions in electron vortices. *Physical Review Letters*, **109**(25):254801, December (2012).

[87] Kenichi K. and Makoto T. Quantised vortices in atomic bose–einsten condensates. In M. Tsubota and W. P. Halperin, editors, *Progress in Low Temperature Physics: Quantum Turbulence*, volume 16 of *Progress in Low Temperature Physics*, pages 351 – 403. Elsevier, 2009.

[88] I. Ivanov. Creation of two vortex-entangled beams in a vortex-beam collision with a plane wave. *Physical Review A*, **85**(3):033813, (2012).

[89] M.L. Boas. *Mathematical Methods in the Physical Sciences*. Wiley, 2006.

[90] J. Durnin, J. J. Miceli Jr, and J. H. Eberly. Diffraction-free beams. *Physical Review Letters*, **58**(15):1499–1501, (1987).

[91] D. McGloin and K. Dholakia. Bessel beams: Diffraction in a new light. *Contemporary Physics*, **46**(1):15–28, (2005).

[92] J. W. Goodman. *Introduction To Fourier Optics*. McGraw-Hill physical and quantum electronics series. Roberts & Company Publishers, 2005.

[93] M. Abramowitz and I. A. Stegun. *Handbook of Mathematical Functions: With Formulas, Graphs, and Mathematical Tables*. Dover Publ., (1964).

[94] I.S. Gradshteĭn, I.M. Ryzhik, and A. Jeffrey. *Table of Integrals, Series and Products*. Academic Press, 1965.

[95] R. P. MacDonald, S. A. Boothroyd, T. Okamoto, J. Chrostowski, and B. A. Syrett. Interboard optical data distribution by Bessel beam shadowing. *Optics Communications*, **122**:169–177, (1996).

[96] H. Kogelnik and T. Li. Laser beams and resonators. *Proceedings of the IEEE*, **54**(10):1312–1329, (1966).

[97] M. Lax, W. H. Louisell, and W. B. McKnight. From Maxwell to paraxial wave optics. *Physical Review A*, **11**(4):1365–1370, (1975).

[98] T. Takenaka, M. Yokota, and O. Fukumitsu. Propagation of light beams beyond the paraxial approximation. *Journal of the Optical Society of America A*, **2**(6):826, (1985).

[99] M. Padgett. An experiment to observe the intensity and phase structure of Laguerre–Gaussian laser modes. *American Journal of Physics*, **64**(1):77–82, (1996).

[100] D. J. Griffiths. *Introduction To Quantum Mechanics, Second Edition*. Pearson Education, 2005.

[101] M. V. Berry. Quantal phase factors accompanying adiabatic changes. *Proceedings of the Royal Society of London*, **392**(1802):45, (1984).

[102] M. V. Berry. The geometric phase. *Scientific American*, **259**:26–34, Dec (1988).

[103] D. B. A. Williams and C. B. Carter. *Transmission Electron Microscopy: A Textbook for Materials Science I: Basics*. Springer, 1996.

[104] Y. Aharonov and D. Rohrlich. *Quantum Paradoxes*. Wiley, (2008).

[105] K. Volke-Sepúlveda, V. Garcés-Chávez, S. Chávez-Cerda, J. Arlt, and K. Dholakia. Orbital angular momentum of a high-order Bessel light beam. *Journal of Optics B*, **4**:82–89, (2002).

[106] A. Alexandrescu, D. Cojoc, and E. Di Fabrizio. Mechanism of Angular Momentum Exchange between Molecules and Laguerre-Gaussian Beams. *Phyical Review Letters*, **96**:243001, (2006).

[107] F. Araoka, T. Verbiest, K. Clays, and A. Persoons. Interactions of twisted light with chiral molecules: An experimental investigation. *Physical Review A*, **71**(5):055401, (2005).

[108] W. Löffler, D. Broer, and J. Woerdman. Circular dichroism of cholesteric polymers and the orbital angular momentum of light. *Physical Review A*, **83**(6):065801, (2011).

[109] C. Cohen-Tannoudji, J. Dupont-Roc, and G. Grynberg. *Photons and Atoms: Introduction to Quantum Electrodynamics*. Wiley-Interscience publication. Wiley, 1989.

[110] S. J. Van Enk. Selection rules and centre-of-mass motion of ultracold atoms. *Journal of the European Optical Society*, **6**:445–457, (1994).

[111] Simon A.R. Horsley and Mohamed Babiker. Röntgen quantum phase shift: A semiclassical local electrodynamical effect? *Physical Review Letters*, **95**:010405, (2005).

[112] K. Y. Bliokh, M.l Alonso, E. Ostrovskaya, and A. Aiello. Angular momenta and spin-orbit interaction of nonparaxial light in free space. *Physical Review A*, **82**(6):063825, (2010).

[113] L. L. D. Landau and E. E. M. Lifshitz. *Quantum Mechanics: Non-Relativistic Theory*. Butterworth-Heinemann Limited, (1977).

[114] B. G. Korenev. *Bessel Functions and Their Applications*. Taylor & Francis, 2004.

[115] G.B. Arfken and H.J. Weber. *Mathematical methods for physicists*. Harcourt/Academic Press, (2001).

[116] Michael V. Berry. Much ado about nothing: optical distortion lines (phase singularities, zeros, and vortices). In S. M. Soskin, editor, *Proceedings of SPIE International Conference on Singular Optics*, volume 3487, pages 1–5, (1998).

[117] E. U. Condon and G. Shortley. *The Theory of Atomic Spectra*. eighth edition, (1963).

[118] J. D. Bjorken and S. D. Drell. *Relativistic quantum mechanics*. International series in pure and applied physics. McGraw-Hill, (1964).

[119] M.E.A. Peskin and D.V.A. Schroeder. *An Introduction To Quantum Field Theory*. Advanced book classics. Addison-Wesley Publishing Company, (1995).

[120] S. De Leo and P. Rotelli. Quaternion Higgs and the electroweak gauge group. *International Journal of Modern Physics A*, **10**(30):4359–4370, (1995).

[121] F. Halzen and A. D. Martin. *Quarks and Leptons: An Introductory Course in Modern Particle Physics*. Wiley, (1984).

[122] M. Chaichian and R. Hagedorn. *Symmetries in Quantum Mechanics: From Angular Momentum to Supersymmetry*. Institute of Physics Publishing, (1998).

[123] F.A. Reuse. *Electrodynamique et Optique Quantiques*. Presses Polytechniques et Universitaires Romandes, (2007).

[124] Y. Hinschberger and P.-A. Hervieux. Foldy–Wouthuysen transformation applied to the interaction of an electron with ultrafast electromagnetic fields. *Physics Letters A*, **376**:813–819, (2012).

[125] W. Greiner. *Quantum Mechanics: An Introduction*. Springer Verlag, 2001.

[126] D.E. Newbury. Electron beam-specimen interactions in the analytical electron microscope. In J. Goldstein, D.C. Joy, and A.D. Romig, editors, *Principles of Analytical Electron Microscopy*. Springer, New York, 1986.

[127] A. G. Hayrapetyan, O. Matula, A. Surzhykov, and S. Fritzsche. Bessel beams of two-level atoms driven by a linearly polarized laser field. *The European Physical Journal D*, **67**(8):167, (2013).

[128] Y. Mo, K. T Turner, and I. Szlufarska. Friction laws at the nanoscale. *Nature*, **457**(7233):1116–9, (2009).

[129] M. R. Falvo, G. Clary, and A. Helser. Nanomanipulation experiments exploring frictional and mechanical properties of carbon nanotubes. *Microscopy and Microanalysis*, **4**:504–512, (1998).

[130] V. Bormuth, V. Varga, J. Howard, and E. Schäffer. Protein friction limits diffusive and directed movements of kinesin motors on microtubules. *Science*, **325**(5942):870–873, (2009).

[131] B. N. Balzer, M. Gallei, M. V. Hauf, M. Stallhofer, L. Wiegleb, A. Holleitner, M. Rehahn, and T. Hugel. Nanoscale friction mechanisms at solid-liquid interfaces. *Angewandte Chemie (International ed. in English)*, **52**(25):6541–6544, (2013).

[132] G. Nienhuis and L. Allen. Paraxial wave optics and harmonic oscillators. *Physical Review A*, **48**:656–665, (1993).

[133] T. Ohsuna, Z. Liu, S. Che, and O. Terasaki. Characterization of chiral mesoporous materials by transmission electron microscopy. *Small (Weinheim an der Bergstrasse, Germany)*, **1**(2):233–237, (2005).

[134] P. Schattschneider, S. Rubino, C. Hébert, J. Rusz, J. Kunes, P. Novák, E. Carlino, M. Fabrizioli, G. Panaccione, and G. Rossi. Detection of magnetic circular dichroism using a transmission electron microscope. *Nature*, **441**(7092):486–488, (2006).

[135] P. Schattschneider, S. Rubino, M. Stoeger-Pollach, C. Hébert, J. Rusz, L. Calmels, and E. Snoeck. Energy loss magnetic chiral dichroism: A new technique for the study of magnetic properties in the electron microscope (invited). *Journal of Applied Physics*, **103**(7):07D931, (2008).

[136] K. Nagayama and R. Danev. Phase contrast electron microscopy: Development of thin-film phase plates and biological applications. *Philosophical transactions of the Royal Society of London B*, **363**(1500):2153–2162, (2008).

[137] F Krumeich, E Müller, and R a Wepf. Phase-contrast imaging in aberration-corrected scanning transmission electron microscopy. *Micron*, **49**:1–14, (2013).

[138] K. Y. Bliokh. Geometrical optics of beams with vortices: Berry phase and orbital angular momentum Hall effect. *Physical Review Letters*, **97**(4):043901, (2006).

[139] K. Y. Bliokh and F. Nori. Relativistic Hall effect. *Physical Review Letters*, **108**(12):120403, (2012).

[140] T. Gericke, P. Würtz, D. Reitz, T. Langen, and H. Ott. High-resolution scanning electron microscopy of an ultracold quantum gas. *Nature Physics*, **4**(12):949–953, (2008).

[141] M. Schwartz. *Vector Analysis with Applications to Geometry and Physics*. Harper, (1960).

[142] S. Hassani. *Mathematical Physics: A Modern Introduction to Its Foundations*. Springer-Verlag, New York, 1999.